GEODYNAMICS OF THE LATE ARCHEAN WAWA SUBPROVINCE GREENSTONE BELTS, SUPERIOR PROVINCE, CANADA

A Thesis Submitted to the Collage of

Graduate Studies and Research

in Partial Fulfilment of the Requirements

for the Degree of Doctor of Philosophy

in the Department of Geological Sciences

University of Saskatchewan

Saskatoon

by

Ali Polat

FALL 1998

UNIVERSITY OF SASKATCHEWAN

College of Graduate Studies and Research

SUMMARY OF DISSERTATION

Submitted in partial fulfilment

of the requirements for the

DEGREE OF DOCTOR OF PHILOSOPHY

by

Ali Polat

Department of Geological Sciences
University of Saskatchewan

Fall 1998

Examining Committee:

Dr. R.B. McKercher	Dean/Associate Dean, Dean's Designate, Chair College of Graduate Studies and Research
Dr. J.F. Basinger	Chair of Advisory Committee, Department of Geological Sciences
Dr. R. Kerrich	Supervisor, Department of Geological Sciences
Dr. R. Renaut	Department of Geological Sciences
Dr. Y. Pan	Department of Geological Sciences
Dr. M.R. Stauffer	Department of Geological Sciences
Dr. E. Tomusiak	Department of Physics and Engineering Physics

External Examiner:

Dr. J. Dostal
Department of Geology
St. Mary's University
Halifax, Nova Scotia
B3H 3C3

Geodynamics of the late Archean Wawa Subprovince Greenstone belts, Superior Province, Canada

The late Archean (ca. 2.80-2.68 Ga) Schreiber-Hemlo and White River-Dayohessarah greenstone belts of the Superior Province, Canada, are collages of komatiite to tholeiitic, transitional and alkaline basalt ocean plateau sequences; tholeiitic and calc-alkaline basalt to rhyolite volcanic island arc sequences; and arc-derived, syn-kinematic siliciclastic trench turbidites accreted along a SSE-facing convergent plate margin through compressional and transpressional collisions. These subduction-accretion complexes were collectively intruded by the syn-kinematic high-La/Yb_n, high-Al, high-Na slab-derived granitoids, syn-kinematic mantle wedge-derived gabbros, and late- to post-kinematic lamprophyres.

A rich compositional diversity of komatiites and basalts is present in ocean plateau sequences. The diverse major and trace element compositions of ocean plateau sequences are consistent with a mantle plume that was chemically heterogenous. Mafic to felsic volcanic arc sequences are characterized by coeval tholeiitic and calc-alkaline magma series with variable major and trace element systematics. Both the tholeiitic and calc-alkaline suites were derived from metasomatized subarc mantle wedge sources. Slab melting was a major source of the felsic suite with garnet ± clinopyroxene ± hornblende residual in the source.

The Schreiber-Hemlo and White River-Dayohessarah greenstone belts have undergone three major phases of deformation. The earliest phase of deformation (D_1) is defined by primarily rotated thrust faults: D_1 reflects tectonic imbrication of oceanic plateaus, island arcs, and arc-derived turbidites in a subduction-accretion complex. D_2 transpression resulted in generation of broken formations and a tectonic mélange. The significance of D_3 in the study area is thought to be subprovince accretion.

The amalgamation processes of the lithotectonic assemblages in the late Archean Schreiber-Hemlo and White River-Dayohessarah greenstone belts are comparable to those of Phanerozoic subduction-accretion complexes, such as the Circum-Pacific, the western north American Cordilleran, and the Altaid orogenic belts, suggesting that subduction-accretion processes significantly contributed to the growth of the continental crust in the late Archean. The episodic growth of the late Archean Superior Province continental crust may have resulted from major plume activities associated with mantle overturn and major orogenies (MOMO).

BIOGRAPHICAL

July, 1963	Born in Denizli, Turkey
June, 1988	B.Sc., Geology, Istanbul Technical University, Turkey
August, 1992	M. Sc., Geology, University of Houston, Texas, USA

HONOURS

Teaching Fellowship, University of Saskatchewan, Canada, 1997-1998

Teaching assistantship, University of Houston, Texas, USA, Texas, USA, 1990-1992

Phillips Petroleum, Academic Scholarship, University of Houston, Texas, USA, 1990-1992

Ms. Norris International Student Scholarship, University of Houston, Texas, USA, 1991

PUBLICATIONS

(1) **A. Polat.** (1988) Evidence for Plaeo- to Neo-tectonic Transition in the Buyuk Polat-Yarimsogut region (Sungurlu-Corum) and Origin of the Kirikkale-Erbaa Fault Zone. *Turkish Association of Petroleum Geologists*, **11**, 127-140.

(2) **A. Polat.** (1994) Structural Analysis of the Aladag Mélange Complex, Eastern Taurides. *Bulletin of Technical University of Istanbul*, **47**, 291-508.

(3) **A. Polat**, and J.F. Casey. (1995) Structural record of the Emplacement of the Pozanti-Karsanti ophiolite onto the Menderes-Taurus Block in the Late Cretaceous, Eastern Taurides, Turkey. *Journal of Structural Geology*, **17**, 1673-1688.

(4) **A. Polat**, J.F. Casey, and R. Kerrich. (1996): Geochemical Characteristics of Accreted

UNIVERSITY OF SASKATCHEWAN
COLLEGE OF GRADUATE STUDIES AND RESEARCH

Saskatoon

CERTIFICATION OF THESIS WORK

We, the undersigned, certify that **Ali POLAT,** candidate for the degree of Doctor of Philosophy has presented a thesis with the following title: ***"Geodynamics of The Late Archean Wawa Subprovince Greenstone Belts, Superior Province, Canada".*** We consider that the thesis is acceptable in form and content, and that the candidate through an oral examination held on May 28, 1998 demonstrated a satisfactory knowledge of the field covered by the thesis.

External Examiner: Dr. J. Dostal
St. Mary's University

Internal Examiners:

College of Graduate Studies and Research, University of Saskatchewan
50 Murray Building, 3 Campus Drive, Saskatoon SK S7N 5A4
Telephone: (306) 966-5751 Facsimile: (306) 966-5756 E-mail: Gradstudies@usask.ca

PERMISSION TO USE

In presenting this thesis in partial fulfilment of the requirements for a Postgraduate degree from the University of Saskatchewan, I agree that the Libraries of this University may make it freely available for inspection. I further agree that permission for copying of this thesis in any manner, in whole or in part, for scholarly purposes may be granted by the professor or professors who supervised my thesis work, or in their absence, by the Head of Department or the Dean of the College in which my thesis work was done. It is understood that any copying or publication or use of this thesis or parts thereof financial gain shall not be allowed without my written permission. It is also understood that due recognition shall be given to me and to the University of Saskatchewan in any scholarly use which may be made of any material in my thesis.

Request for permission to copy or to maker other use of material in this thesis in whole or part should be addressed to:

Head of the Department of Geological Sciences
University of Saskatchewan
Saskatoon, Saskatchewan S7N 5E2

ABSTRACT

The late Archean (ca. 2.80-2.68 Ga) Schreiber-Hemlo and White River-Dayohessarah greenstone belts of the Superior Province, Canada, are collages of komatiite to tholeiitic, transitional and alkaline basalt ocean plateau sequences; tholeiitic and calc-alkaline basalt to rhyolite volcanic island arc sequences; and arc-derived, syn-kinematic siliciclastic trench turbidites accreted along a SSE-facing convergent plate margin through compressional and transpressional collisions. These subduction-accretion complexes were collectively intruded by the syn-kinematic high-La/Yb_n, high-Al, high-Na slab-derived granitoids, syn-kinematic mantle wedge-derived gabbros, and late- to post-kinematic lamprophyres.

A rich compositional diversity of komatiites and basalts is present in ocean plateau sequences. The diverse major and trace element compositions of ocean plateau sequences are consistent with a mantle plume that was chemically heterogenous. Mafic to felsic volcanic arc sequences are characterized by coeval tholeiitic and calc-alkaline magma series with variable major and trace element systematics. Both the tholeiitic and calc-alkaline suites were derived from metasomatized subarc mantle wedge sources. Slab melting was a major source of the felsic suite with garnet ± clinopyroxene ± hornblende residual in the source.

The Schreiber-Hemlo and White River-Dayohessarah greenstone belts have undergone three major phases of deformation. The earliest phase of deformation (D_1) is defined by primarily rotated thrust faults: D_1 reflects tectonic imbrication of oceanic plateaus, island arcs, and arc-derived turbidites in a subduction-accretion complex. D_2 transpression resulted in generation of broken formations and a tectonic mélange. The significance of D_3 in the study area is thought to be subprovince accretion.

The amalgamation processes of the lithotectonic assemblages in the late Archean

Schreiber-Hemlo and White River-Dayohessarah greenstone belts are comparable to those of Phanerozoic subduction-accretion complexes, such as the Circum-Pacific, the western north American Cordilleran, and the Altaid orogenic belts, suggesting that subduction-accretion processes significantly contributed to the growth of the continental crust in the late Archean. The episodic growth of the late Archean Superior Province continental crust may have resulted from major plume activities associated with mantle overturn and major orogenies (MOMO).

ACKNOWLEDGEMENTS

I would like to express my sincere gratitude to my supervisor Rob Kerrich for his intellectual guidance and financial support for this study. I have greatly benefited from his encouragement to develop independent thinking, and to critically evaluate conventional wisdom on the geology of Archean greenstone belts. I will rely upon these traits in my future geological studies.

I would like to thank my committee members, Drs. M. Satuffer, Y. Pan, R. Renaut, and E. Tomusiak, my external examiner Dr. J. Dostal, and the Chairman of the Advisory Committee, Dr. J. Basinger, for their kindness and sincere help during the preparation of this thesis.

It was certainly great for me to work with Dr. D.A. Wyman, I would like to thank him for his help throughout this study. Drs. A.M.C. Sengor and Dr. T. Kusky are gratefully acknowledged for their encouragement and discussion on varies aspects of Geology. Special thanks goes to P. Hollings and B. Morgan for their help during field and lab studies, respectively. Emotionally special thanks extended to Mr. Cenan Gurgan for his financial support during my language studies in England, without his help it would have been impossible for me to carry out this study.

Finally, I would like to express my sincere gratitude to my wife, Mevlude Polat, and my little son, Hasan Huseyin Polat, and my parents Hasan Huseyin and Saime Polat, for their extraordinary patience, love, and support.

TABLE OF CONTENTS

CHAPTER 3. GEOCHEMISTRY OF ULTRAMAFIC-MAFIC OCEAN FLOOR SEQUENCES

CHAPTER 4. PETROGENESIS OF SUBDUCTION-RELATED MAFIC TO FELSIC VOLCANIC ROCKS

LIST OF TABLES

Page

LIST OF FIGURES

LIST OF APPENDICES

Page

ABBREVIATIONS AND ACRONYMS

Rocktypes

MORB	Mid-Ocean Ridge Basalt
E-MORB	Enriched Mid-Ocean Ridge Basalt
N-MORB	"Normal" Mid-Ocean Ridge Basalt
OIB	Ocean Island Basalt
OPB	Ocean Plateau basalt
AUK	Aluminum-undepleted komatiites
ADK	Aluminum-depleted komatiites
Syn-COLG	Sny-collisional granitoids
I-type	Igneous type
S-type	Supracrustal or sedimentary type
A-type	Anorogenic type
TTG	Tonalite-trondjhemite-granodiorite
TTGM	Tonalite-granodiorite-granite monzonite
MMGS	Monzodiorite-nonzonite-granodiorite-syenite
GMG	Garnet-muscovite-granite
VAG	Volcanic arc granitoids
ORG	Ocean-ridge granitoids
WPG	Within-plate granitoids

Mantle Reservoirs and Structure

HIMU	High μ ($^{238}U/^{204}Pb$)
DMM	Depleted MORB Mantle
EM1	Enriched Mantle component 1
EM2	Enriched Mantle component 2

SDC	Subduction Derived Component
RSC	Residual Slab Component
MOHO	Seismically defined boundary at the lower crust-mantle transition
D'	670 km Transition Zone
D''	Core - Mantle Boundary at 2900 km
CMB	Core - Mantle Boundary

Structural Geology

LSHFZ	Lake Superior Hemlo-Fault Zone
D_1	Deformation phase 1
D_2	Deformation phase 2
D_3	Deformation phase 3
S_1	Foliation developed during deformation phase 1
S_2	Foliation developed during deformation phase 2
L_1	Foliation developed during deformation phase 1
L_2	Foliation developed during deformation phase 2
F_1	Fault developed during deformation phase 1
F_2	Fault developed during deformation phase 2
δ	Delta structures
σ	Sigma structure
S-C	Schistosity-Cisaillement (shear)

Metallogenic

VMS	Volcanic Hosted Massive Sulphide Deposit

Analytical

ICP MS	Inductively coupled plasma mass spectrometer
ICP AES	Inductively Coupled Plasma Atomic Emission Spectrometry
AES	Atomic Emission Spectrometry
XRF	X-ray Fluorescence
AAS	Atomic Absorption Spectrometry
INAA	Instrumental Neutron Activation Analysis
RSD	Relative standard deviation
XRF	X-ray fluorescence
SSMS	Spark source mass spectrometry

Geochemistry

REE	Rare Earth Elements (La-Lu)
LREE	Light Rare Earth Elements (La-Sm)
MREE	Middle Rare Earth Elements (Sm-Gd)
HREE	Heavy Rare Earth Elements (Gd-Lu)
LILE	Large Ion Lithophile Elements (Sr, K, Rb, Ba, Th, Ta)
HFSE	High Field Strength Elements (Nb, Ta, Ce, P, Zr, Hf, Ti, Y)
PGE	Platinum group elements
La/Yb_n	Chondrite normalized ratio
Th/La_{pm}	Primitive mantle normalized ratio
Ti/Ti*	Normalized anomaly calculated with respect to adjacent elements on a

	primitive mantle normalized plot
Mg#	$Mg/(Mg+Fe^{2+})$, where Fe^{2+} is assumed to be 90 % of the total Fe content
LOI	Loss on Ignition

Orogeny

MOMO Mantle overturn and major orogenies

Time

Ma	Million years
Ga	1,000 Ma

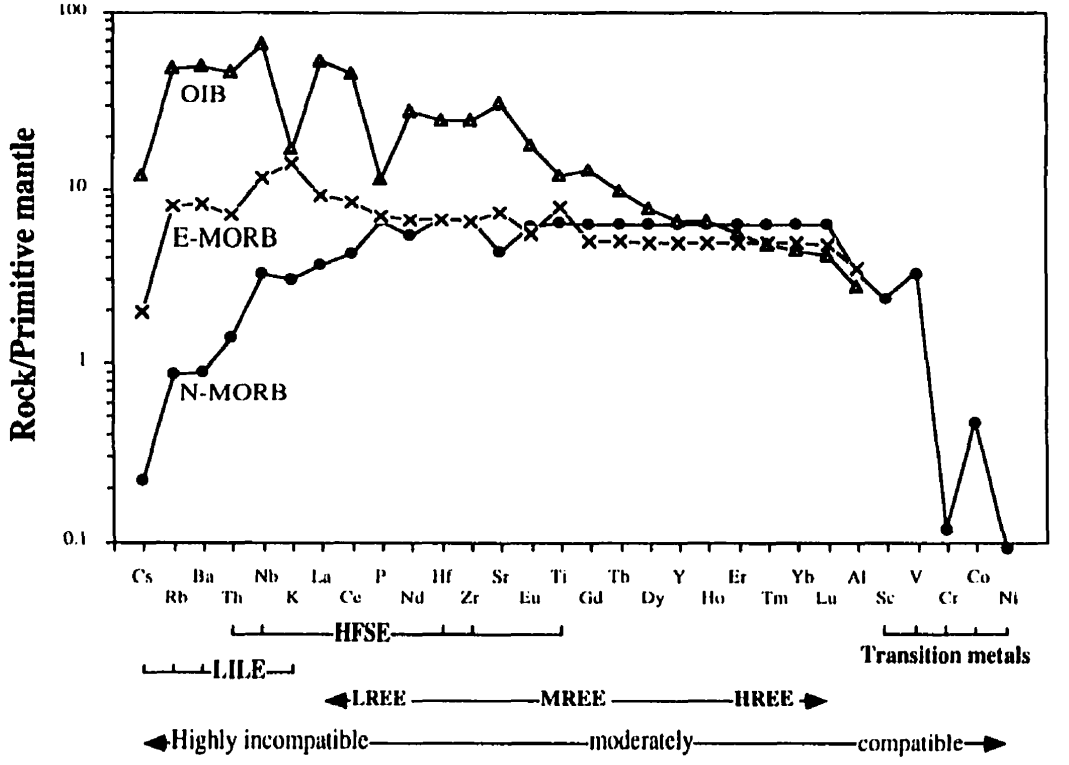

XRF					○	●			●			○	●		●				○						●			●		●	
INAA				○			●	●		○	○			●			○						●			●		●			● reliable
AA,ICP-AES		●	●			●						○	●		●											●	●	●	●	●	
ID, TIMS				●			●	●		●	●	●	●			●	●	●		●	●	●	●	●							○ less reliable
ICP-MS	●	●	●	○	●		●	●	●	●	●	●	●	●	●	●	●	●	●	●	●	●	●	●		●	●	●	●	●	

Introductory Figure for trace element geochemistry: Primitive mantle-normalized diagrams for NMORB, EMORB, and OIB illustrating the position of the LILE, HFSE, REE, and transition metals in the incompatiblity squence of Sun and McDonough (1989). The lower panel indicates those elements can reliably be determined in ultramafic to mafic volcanic rocks by specified analystical techniques. Open circles signify potental problems arising from detection limits.

CHAPTER 1. INTRODUCTION AND SCOPE

1-1. Geological significance of 2.75-2.60 Ga greenstone-granitoid terranes

The time window of 2.75-2.60 Ga is unusual in geological history in terms of coeval voluminous intra-oceanic ultramafic to mafic volcanism, emplacement of voluminous high La/Yb_n, high-Al tonalite-trodhjemite-granodiorites (TTG), deposition of thick greywacke turbidite sequences, and formation of the earliest giant volcanogenic massive sulphide (VMS) and mesothermal gold deposits. Collectively, these events are thought to reflect widespread terrane accretion, and rapid crustal growth (Hoffman, 1989; Kerrich and Wyman, 1989; Stein and Hofmann, 1994; Windley, 1995; Taylor and McLennan, 1995; Kerrich and Wyman, 1996). Voluminous ultramafic (komatiites, komatiitic basalts) and mafic (Mg-, to Fe-tholeiites) volcanic rocks were erupted globally between ca. 2750 and 2680 Ma. These ultramafic to mafic sequences are believed to be derived from mantle plumes originating either at the 670 kilometre transition zone between the upper and lower mantles, or at the core mantle boundary (McDonough and Ireland, 1993; Nisbet et al., 1993; Stein and Hofmann, 1994). The intrusion of voluminous high La/Yb_n, high-Al TTG has been attributed to slab melting at Archean subduction zones (Martin, 1986; 1993; Drummond and Defant, 1990; Feng and Kerrich, 1992). These events are collectively considered as part of the late Archean super-continent cycle, involving accretion of oceanic plateaus, island arcs and continental fragments, closure of

ocean basins (e.g., global oceans, and back-arc basins), rifting of magmatic arcs, and arc-plume interaction (Taylor and McLennan, 1995; Kerrich and Wyman, 1996; Dostal and Mueller, 1997).

All these Archean tectonic, magmatic, sedimentological, metamorphic, and metallogenic processes are extensively preserved in the 3.1 to 2.6 Ga greenstone-granitoid terranes of the Superior Province of Canada (Card, 1986; Card and Ciesielski,1990; Thurston and Chievers, 1990; Thurston et al., 1991; Desrochers et al., 1993). The Superior Province, the largest Archean craton globally (~1,572,000 km^2), was built by the amalgamation of subprovinces, including plutonic, volcanic-plutonic (greenstone-granitoid), high-grade gneissic, and sedimentary subprovinces, in the interval 2.74-2.65 Ga to an ancient cratonic nucleus, the north Caribou terrane of the Sachigo Subprovince (Fig. 1.1; Card and Ciesielski, 1986; Card, 1990; Thurston et al., 1991; Percival et al., 1994). Extensive geochronological studies on pre-, syn-, and post-kinematic igneous rocks of these subprovinces suggest that the assembly of the subprovinces was diachronous from north to south (Thurston, 1990; Williams, 1990; Percival et al., 1994).

1-2. Geological characteristics of the Archean Superior Province greenstone belts

Greenstone belts in the Archean Superior Province are kilometre to 100 km scale areas of supracrustal rocks within composite greenstone-granitoid terranes, with tectonic or intrusive boundaries. They have generally undergone poly-phase deformation characterized by isoclinal and sheath folds, thrust and strike-slip faults, and diverse lineations and foliations. A greenstone belt may consist of one or more lithotectonic assemblages, characterized by stratified volcanic and/or sedimentary rock units built during a discrete interval of time in a common depositional or volcanic setting (Thurston, 1991). Volcanic sequences are composed of variable proportions of metamorphosed

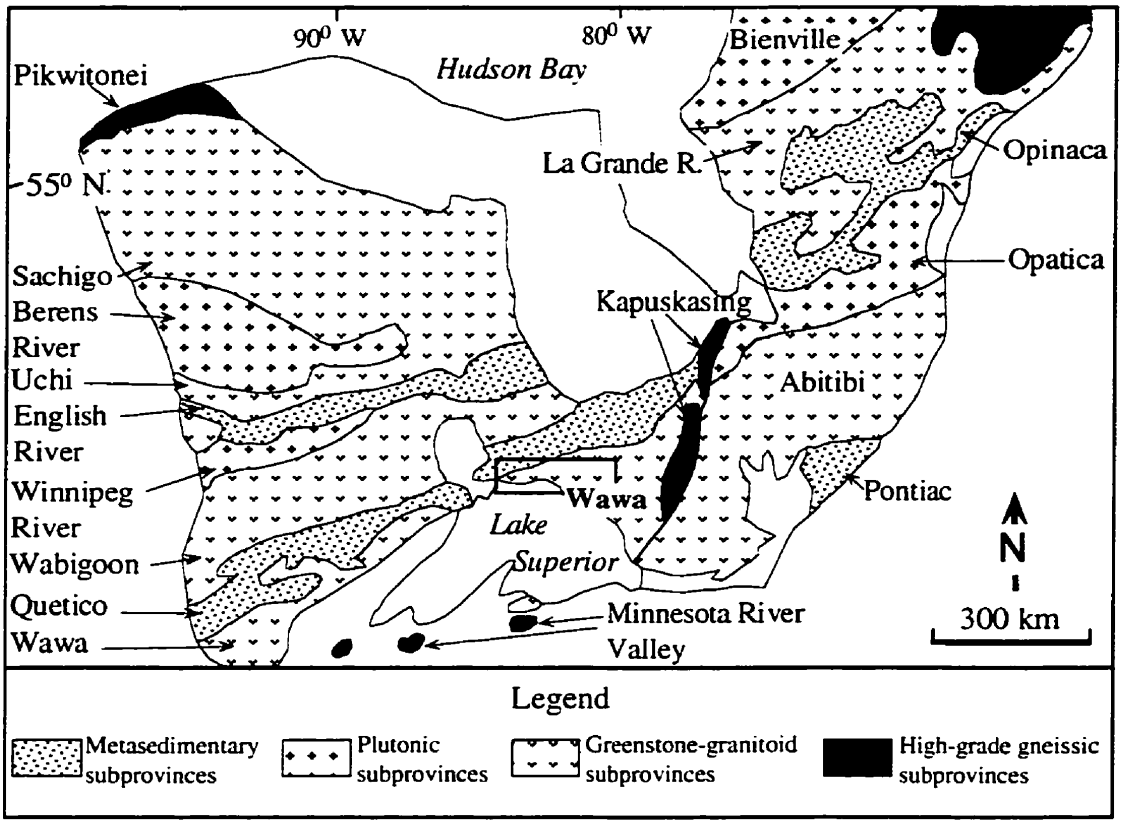

Figure 1.1. Subprovince map of the Superior Province (modified after Card, 1990). Rectangle shows the locations of the Schreiber-Hemlo and White River-Dayohessarah greenstone belts.

ultramafic-mafic, intermediate, and felsic rocks. Sedimentary rocks are predominantly metamorphosed, proximal to distal siliciclastic turbidites. Small volumes of chemical sedimentary rocks, such as iron formation, carbonates, and cherts occur sporadically within volcanic sequences. Stratigraphic relationships between different lithological units are commonly obscure and often marked by shear zones. These volcanic and sedimentary litho-tectonic assemblages were intruded by syn- to post-kinematic, mantle- to crustally-derived mafic to felsic intrusive rocks (Feng and Kerrich, 1992; Sutcliffe et al., 1993).

Thurston and Chievers (1990) recognized four types of litho-stratigraphic sequences in the Superior Province greenstone belts: (1) quartz and carbonate-bearing platform sequences; (2) mafic-ultramafic ocean floor volcanic sequences; (3) mafic (tholeiitic to calc-alkaline) to felsic arc volcanic sequences; and (4) Timmiskaming type fluviatile sediments and associated calc-alkaline to alkaline volcanic sequences.

The greenstone belts are typically metamorphosed to greenschist or amphibolite facies, and metamorphic grade tends to increase towards the contact with TTG plutons. Siliciclastic sedimentary rocks are either separated from volcanic rocks by faults or, less commonly, unconformably overlie them (Thurston, 1991).

It has been suggested that structural, lithological, and geochemical characteristics of the Archean Superior Province greenstone belts are comparable to those of Phanerozoic collisional belts, providing a window into Archean convergent plate margin geological processes (Hoffman, 1989; Card 1990; Thurston and Chievers, 1990; Sleep, 1992; Feng et al., 1993; Desrochers et al., 1993; Windley, 1995; Kusky and Vearncombe, 1997).

1-3. Previous studies and outstanding problems

Given the presence of giant volcanogenic massive sulphide (VMS) and gold deposits, and iron formations, the geology of the Superior Province greenstone belts has been extensively studied (Hofmann, 1989, 1991; Wyman and Kerrich, 1989; Kimura et

al., 1993; Desrochers et al., 1993; Percival et al., 1994). More recently, advanced, high-precision trace element analytical techniques, including ICP-MS, with very low detection limits, have been utilized to characterize the petrogenesis of volcanic and intrusive rocks, and the provenance of siliciclastic sedimentary rocks (Fowler and Jensen, 1988; Feng and Kerrich, 1992a,b; Laflèche et al., 1992; Xie et al., 1993; Barrie et al., 1992; Fan and Kerrich, 1997). Similarly, modern structural analysis have been carried out to understand the tectonic histories of the greenstone belts (Arias and Helmstaedt, 1990; Lacroix and Sawyer, 1995).

Most of these studies were conducted in the Abitibi subprovince. Several geological studies have also been conducted in the Schreiber-Hemlo and White River-Dayohessarah greenstone belts (Walker, 1967; Hugon, 1984; Muir and Elliot, 1987; Muir, 1982, 1986; Carter, 1988; Corfu and Muir, 1989a,b; Williams et al., 1991; Pan et al., 1991; Pan and Fleet, 1994; Kuhns et al., 1994; Stott et al., 1994). Given the presence of the giant Hemlo Au-deposit, most of these studies focused on the Hemlo area (Hugon, 1984; Muir and Elliott, 1987; Muir, 1982, 1986; Corfu and Muir, 1989a,b; Pan and Fleet, 1989; Pan et al., 1991; Pan and Fleet, 1994; Kuhns et al., 1994). Structural studies in the Schreiber-Hemlo and White River-Dayohessarah greenstone belts have mostly been focused along the Lake Superior-Hemlo Fault Zone (LSHFZ) to determine the relationship between deformation and lode gold deposits (Hugon, 1984; Muir and Elliot, 1987; Kuhns et al., 1994). Corfu and Muir (1989a,b) carried out U/Pb geochronological studies on volcanic and plutonic rocks of the Hemlo-Black River and Heron Bay assemblages to determine the timing of volcanism and plutonism. Pan and others (1991) investigated the provenance of sedimentary rocks in the Hemlo-Heron Bay area, based on trace element geochemistry. However, there are only a few modern geochemical and structural studies in the Schreiber-Hemlo and White River-Dayohessarah greenstone belts of the Wawa subprovince distal from Hemlo.

There are several first order unresolved problems regarding the petrogenesis of Archean komatiite-tholeiite sequences, tholeiitic to calc-alkaline mafic to felsic volcanic sequences, and the tectonic evolution of Archean greenstone belts in general. These fundamental questions include:

(1) What are the mantle source characteristics of komatiites and associated Mg-, to Fe-tholeiites?

(2) What were the geodynamic settings in which komatiitic and basaltic flows erupted?

(3) Were Al-undepleted and Al-depleted komatiites derived from similar or different mantle sources?

(4) Did komatiites and associated tholeiites have similar petrogenetic origins?

(5) How do alteration and metamorphism affect the trace element characteristics of komatiites and associated tholeiites?

(6) Was Archean arc magmatism different or similar to Phanerozoic counterparts?

(7) What was the residual mineralogy during slab and wedge melting in Archean subduction zones?

(8) What is the relationship between Archean plume and arc magmatism?

(9) How did Archean subduction zones differ from Phanerozoic counterparts?

(10) What are the geological relationships between siliciclastic turbidites and interleaved komatiite-basalt sequences?

(11) Why are there no high-pressure low temperature (HP/LT) facies metamorphic rocks (blueschist-eclogites) in Archean greenstone belts?

(12) Why are Archean mélanges apparently not as abundant as Phanerozoic counterparts?

(13) How is gold mineralization linked to greenstone belt geodynamics? and

(14) How did Archean continental crust grow?

1-4. Design and methodology

In an attempt to resolve some of the questions posed above, this thesis involves structural and geochemical studies of volcanic and intrusive rocks, and siliciclastic turbidite sequences in the late Archean (2.75-2.69 Ga) Schreiber-Hemlo and White River-Dayohessarah greenstone belts of the Wawa subprovince, Superior Province of Canada. To understand the structural evolution of these belts requires detailed field investigations, including mapping, determination of field relationships between various lithological units (e.g., turbidites and volcanic sequences), characterization of the nature of various deformation phases, construction of detailed cross-sections, and documentation of the systematic orientation of planar and linear structures. Consequently, detailed structural analysis of the Schreiber-Hemlo and White River-Dayohessarah greenstone belts was undertaken to understand the tectonic origin of these belts.

Addressing the fundamental questions regarding the petrogenesis (e.g., mantle source characteristics, melting and fractionation processes) of igneous rocks, and the provenance of siliciclastic sedimentary rocks requires determination of trace elements, specifically rare earth elements (REE: La-Lu), high field strength elements (HFSE: Th, Nb,Ta, Zr, Hf, Ti, Y), and transition metals (Cr, Ni, Co, Sc, V), through high precision analyses. The advent of inductively coupled plasma-mass spectrometry (ICP-MS) permits for the first time high-precision analyses of all REE, HFSE, and transition metals, simultaneously at low levels (ppb). Except for turbidites and some granitoid intrusions in the Hemlo and Heron Bay areas (Pan et al., 1991), there is no high precision trace element data for volcanic rocks of the Schreiber-Hemlo and White River-Dayohessarah greenstone belts. Accordingly, to gain insights to the petrogenesis of volcanic rocks and the provenance of sedimentary rocks of the Schreiber-Hemlo and White River-Dayohessarah greenstone belts a detailed geochemical study has been undertaken in this thesis.

To conduct geochemical investigations using high precision analysis of trace

elements by ICP-MS, requires in turn significant development work of sample preparation protocols, and ICP-MS instrumental conditions. This analytical work conducted at the University of Saskatchewan, has been published in several papers and Ph. D. theses (Appendix 1.1; see Feng, 1992; Fan, 1995; Xie, 1996).

1-5. Structure of the thesis

Chapter 2 presents the geological setting of the Wawa subprovince within the framework of the Superior Province. This also includes detailed description of the geology of the Schreiber-Hemlo and White River-Dayohessarah greenstone belts in the Wawa subprovince. Chapter 3 deals with the geochemistry of ocean floor mafic-ultramafic volcanic sequences in the two greenstone belts. The geochemical characteristics of mafic to felsic, tholeiitic to calc-alkaline volcanic sequences of the belts are addressed in Chapter 4. This is followed by the geochemistry of tonalite-trondhjemite-granodiorite (TTG) intrusions, mafic (gabbroic) to felsic (tonalitic) sills, and siliciclastic sedimentary rocks (Chapter 5). Chapter 6 discusses the structural characteristics and mélange formation in the Schreiber-Hemlo greenstone belt. In the concluding chapter (Chapter 7) the geological characteristics of the Schreiber-Hemlo and White River-Dayohessarah greenstone belts are compared with those of Archean, Proterozoic, and Phanerozoic greenstone belts, in an attempt to understand Archean geodynamics, and crustal growth processes through the Earth's history. Future directions in greenstone belt studies are also suggested in this chapter.

CHAPTER 2. GEOLOGICAL SETTING

2-1.Wawa subprovince

The greenstone-granitoid Wawa subprovince extends from the Vermilion district of Minnesota in the west to the Kapuskasing structural zone in the east (Figs. 1.1, 2.1; Williams et al., 1991). Its northern boundary lies in tectonic contact against structurally overlying metasedimentary rocks of the Quetico subprovince. The southern boundary of the subprovince is marked by the Batchawana fault zone in the east, and is obscured beneath Lake Superior. The western end of the subprovince is bordered by the Proterozoic Trans-Hudson orogen. The Great Lakes Tectonic Zone separates the Wawa subprovince from the Marquette greenstone belt, and the Minnesota Valley gneiss terrane to the south. Williams et.al. (1991) proposed that at least three stages of supracrustal development are preserved in the Wawa subprovince at approximately 2.89, 2.75, and 2. 70 Ga.

The subprovince is composed of two linear concentrations, or zones of greenstone belts: (1) one along its northern border with the Quetico subprovince, comprising the Shebandowan, Schreiber-Hemlo, Manitouwadge-Hornepayne, White River, Dayohessarah, and Kabinakagami greenstone belts; and (2) a second in the south-central portion of the subprovince, including the Mishibishu, Michipicoten, and Gamitagama greenstone belts (Fig. 2.1). These supracrustal zones are composed dominantly of mafic volcanic rocks, with subordinate ultramafic, intermediate, and felsic flows. Sedimentary rocks are predominantly siliciclastic turbiditic wackes and shales, with minor conglomerates, iron formations, cherts, and carbonates. The two linear concentrations of

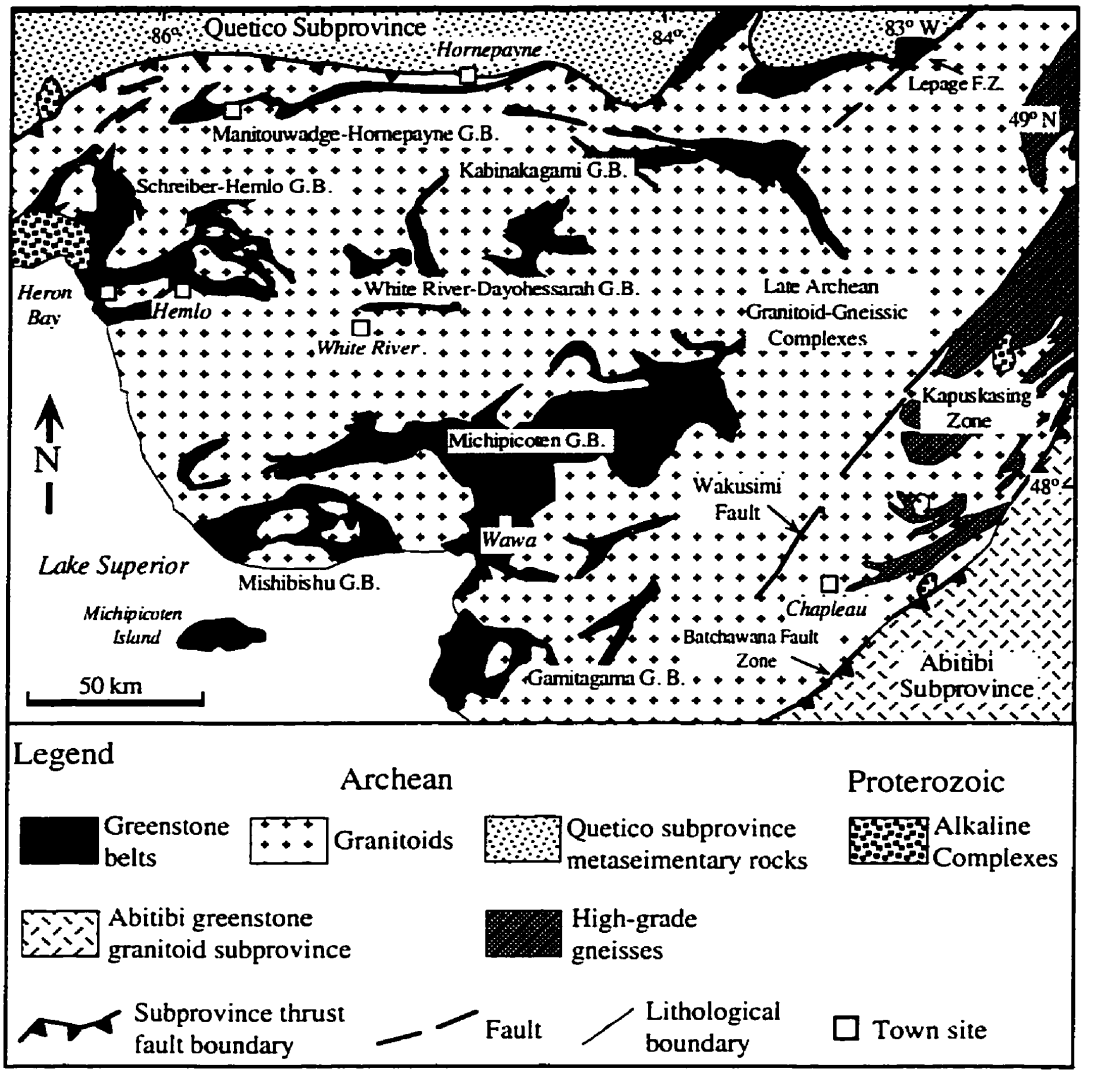

Figure 2.1. Regional geological map of the eastern Wawa Subprovince, indicating greenstone belts (G.B.) in the Hemlo, Manitouwadge, Hornepayne, Heron Bay, White River, Wawa, and Chapleau areas (modified after Williams et al., 1991).

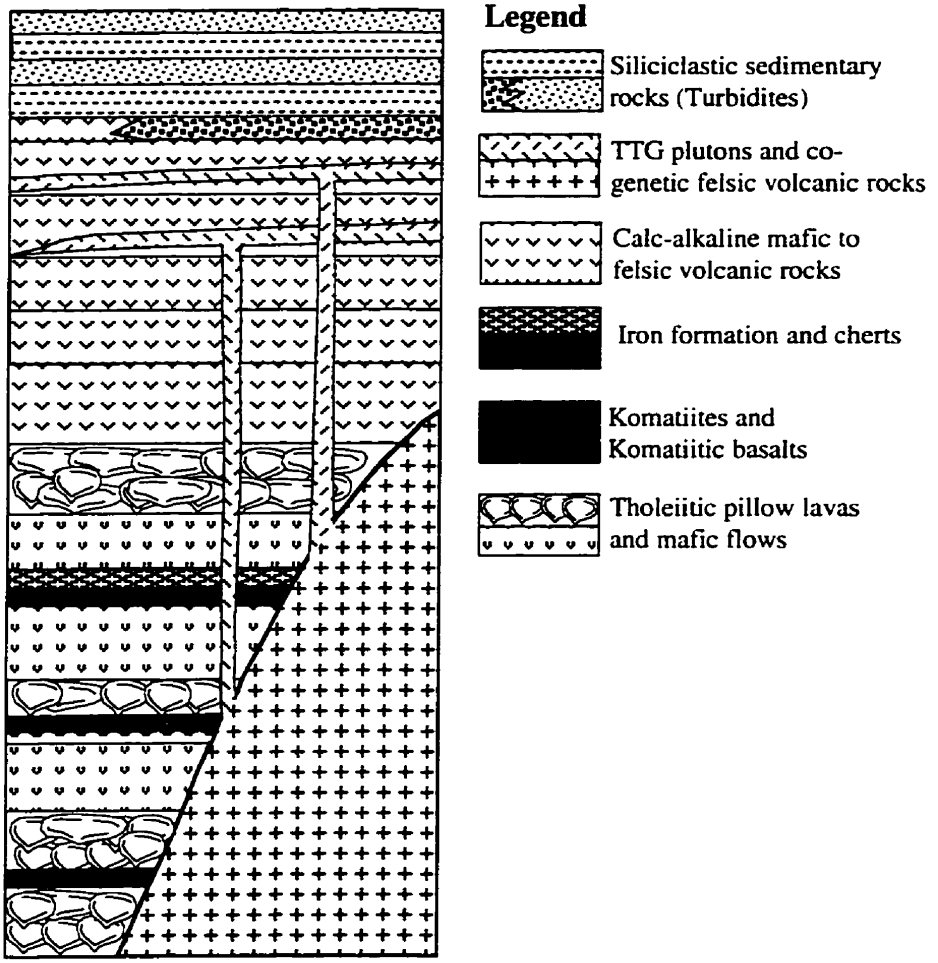

Figure 2.2. Simplified tectono-stratigraphic section for the Schreiber-Hemlo and White River-Dayohessarah greenstone belts. Lithological boundaries may also be tectonic (modified after Williams et al., 1991).

greenstone belts are separated by domains of tonalite-trondhjemite-granodioritic (TTG) plutonic rocks. For the Wawa subprovince as a whole, geological relationships between lithotectonic assemblages and greenstone belts suggest that the various greenstone belts were tectonically assembled prior to the coalescence of the subprovinces of the Superior Province (Williams et al., 1991).

Contacts between various volcanic-volcanic, and volcanic-sedimentary units are for the most part obscured, or are characterized by strike-slip or thrust faults. Generally, lithotectonic assemblages of Mg-, to Fe-tholeiites are structurally or stratigraphically overlain by sub-marine to sub-aerial calc-alkaline basalts, andesites, dacites, and rhyolites (Fig. 2.2; Williams et al., 1991). Unconformities occur where assemblages were juxtaposed along shallow to steeply-dipping shear zones, and were subjected to recumbent folding. In the following sections, the major geological characteristics of the Schreiber-Hemlo and White River-Dayohessarah greenstone belts are presented to provide an improved understanding of the origin and geodynamic setting of these greenstone belts.

2-2. Schreiber-Hemlo greenstone belt

The Schreiber-Hemlo greenstone belt is located in the northeastern portion of the Wawa Subprovince (Figs. 2.1, 2.3; Williams et al., 1991). The belt is composed of tectonic slices of 2775-2700 Ma volcanic and 2705-2695 Ma siliciclastic sedimentary (turbidite) rocks, which are collectively intruded by 2720-2680 Ga TTG plutons and ca. 2690 Ma lamprophyre dykes (see Wyman and Kerrich, 1989; Williams et al., 1991).

Corfu and Muir (1989a) recognized three episodes of felsic magmatism, including TTG plutons and associated rhyolites: (1) ages of 2772 Ma for felsic flows at the Hemlo gold site; (2) 2720 Ma for the Pukaskwa batholith; and (3) 2678 Ma, the Gowan Lake pluton (Fig. 2.4).

Volcanic rocks are dominantly tholeiitic pillow basalts, and 10 cm to 1.5 m thick

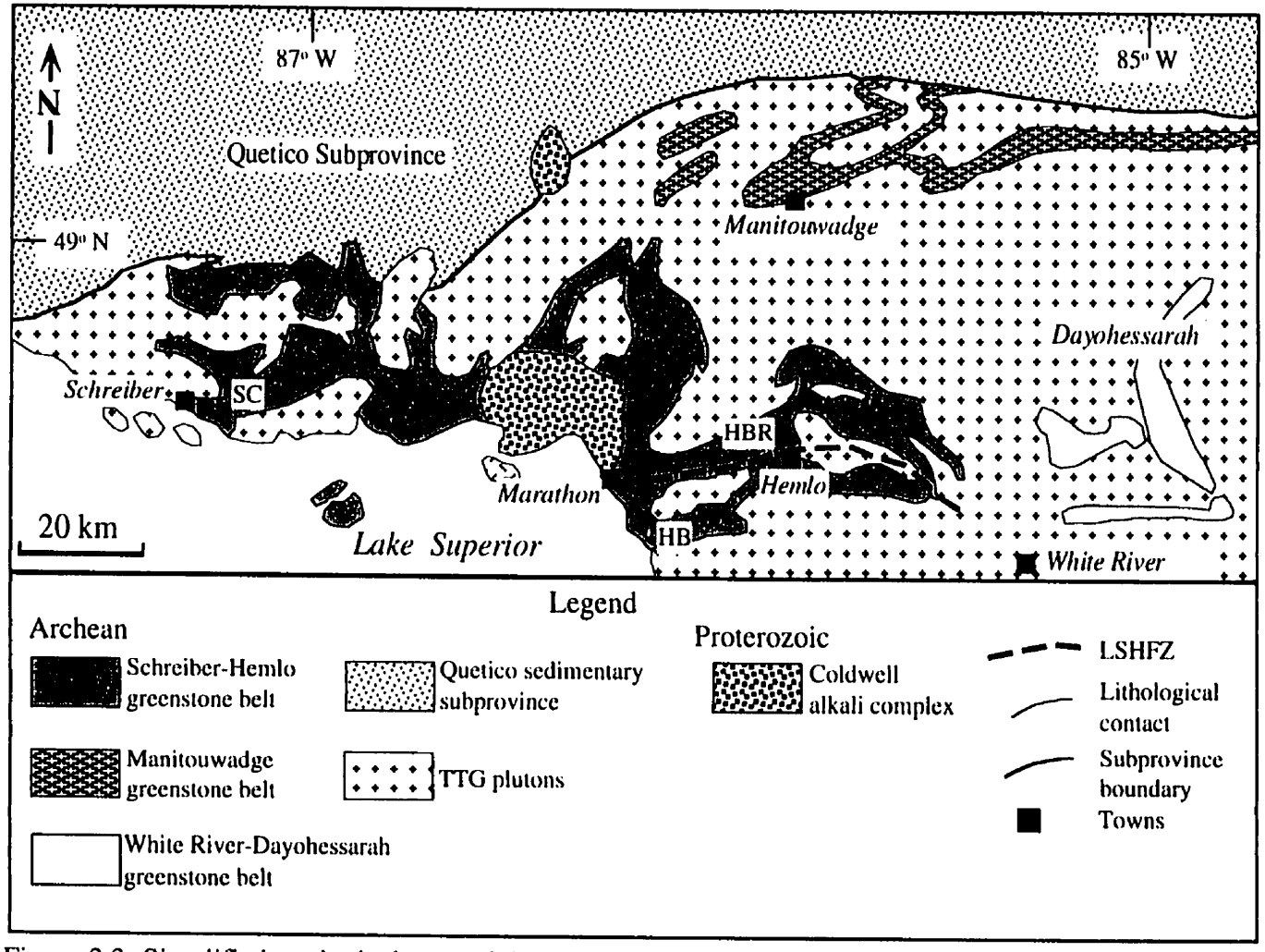

Figure 2.3. Simplified geological map of the Schreiber-Hemlo and White River Dayohessarah greenstone belts. Lithological boundaries may also be tectonic (modified after Williams et al., 1991). TTG: Tonalite trondhjemite-granodiorite; SC: Schreiber assemblage, HBR: Hemlo-Black River assemblage, HB: Heron Bay assemblage.

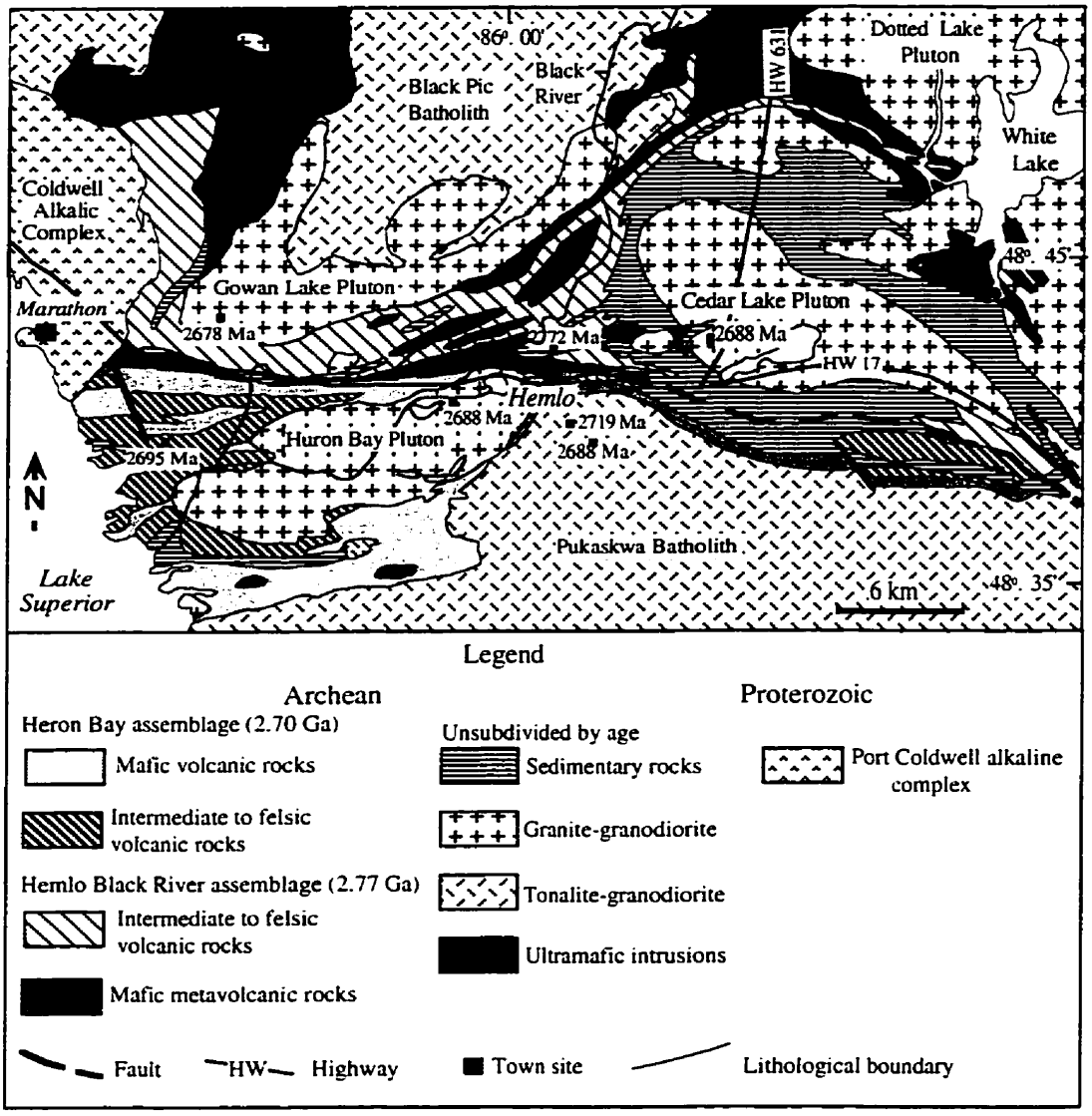

Figure 2.4. Geological map of the Heron Bay and Hemlo areas (modified after Williams et al., 1991). Ages were determined by Corfu and Muir (1989a, b).

basaltic flows, with sporadic komatiites having well preserved spinifex texture. Pillows range from 15 cm to 2 m in size. Andesites, rhyolites, dacites and pyroclastic rocks tend to occur at the upper tectono-stratigraphic sections.

Sedimentary rocks include inter-bedded, turbiditic sandstones, siltstones, and shales. The thickness of beds ranges from a few mm to 1 m. Sandstones tend to be thicker than inter-bedded shales and siltstones. Conglomerates are minor, primarily occurring in turbidite channels. Syn-sedimentary slump folds and cross-bedding are well exposed along the shore of Lake Superior; they are spatially associated with turbidite channel structures. These turbidites are composed dominantly of T_{c-e} (convolute lamination, pelagic shales) sections of the Bouma sequence, consistent with a distal depositional environment (see Bouma, 1962).

The Schreiber-Hemlo greenstone belt is divided into three lithotectonic assemblages by Williams et al. (1991): the Schreiber, Hemlo-Black River, and Heron Bay. The Schreiber and Hemlo-Black River assemblages are separated by the Proterozoic Coldwell alkali complex (Fig. 2.3). The Hemlo-Black River and Heron Bay assemblages are located to the north and south of the right lateral Lake Superior-Hemlo fault zone, respectively (Figs. 2.3, 2.4). These three assemblages are composed of similar volcanic and siliciclastic sedimentary rocks.

The Schreiber and Heron Bay assemblages of the belt are relatively less metamorphosed, at lower greenschist facies, compared to the Hemlo-Black River assemblage. Primary igneous textures and pillow geometries of volcanic rocks, and sedimentary structures of turbidites, such as cross bedding, flute cast and channel structures, grading, convolute lamination, are preserved outside shear zones.

2-1. White River-Dayohessarah greenstone belt

The White River-Dayohessarah greenstone belt is located between the Schreiber-

Hemlo greenstone belt to the west and the Kabinakagami greenstone belt to the east (Figs. 2.1, 2.3). The belt is defined by disconnected supracrustal units exposed in the White River and Dayohessarah Lake areas (Fig. 2.5). In comparison to the Schreiber-Hemlo belt, the White River-Dayohessarah belt is characterized by aerially less extensive supracrustal rocks (Fig. 2.5; Williams et al., 1991; Stott et al., 1994). This greenstone belt has not been subdivided into distinctive lithotectonic assemblages. In the White River area it is composed of discontinuously exposed mafic to felsic volcanic and siliciclastic sedimentary rocks best exposed along Highway 631 in a zone of a few km wide and approximately ten km long. Structurally, the Dayohessarah section of the belt is a southwest-northeast trending, crescent-shaped synform, several km wide and about 35 km long (Fig. 2.5; Stott et al., 1994).

Supracrustal rocks of the White River-Dayohessarah belt are composed of ultramafic to felsic volcanic and siliciclastic sedimentary rocks like those of the Schreiber-Hemlo belt. The northern end of the belt is composed of amphibolite facies rocks and appears to trend eastward. The southern edge of the belt consists of several hundred metre scale xenoliths of amphibolite facies mafic volcanic rocks as enclaves within the TTG batholiths of the White River area. The supracrustal units of the belt in both areas were intruded by granitic to tonalitic plutonic rocks. Contacts between the supracrustal units and bordering plutonic rocks range from tectonic to intrusive.

At least three phases of deformation, characterized by open to isoclinal poly-deformed folds, ductile thrust shears, steeply dipping foliations, boudinage, and normal faults, have been recorded in the belt. It is not clear from field relations whether or not the White River-Dayohessarah greenstone belt is an eastern continuation of the Schreiber-Hemlo greenstone belt. Trace element data in this study is used to evaluate the relationship between the two belts.

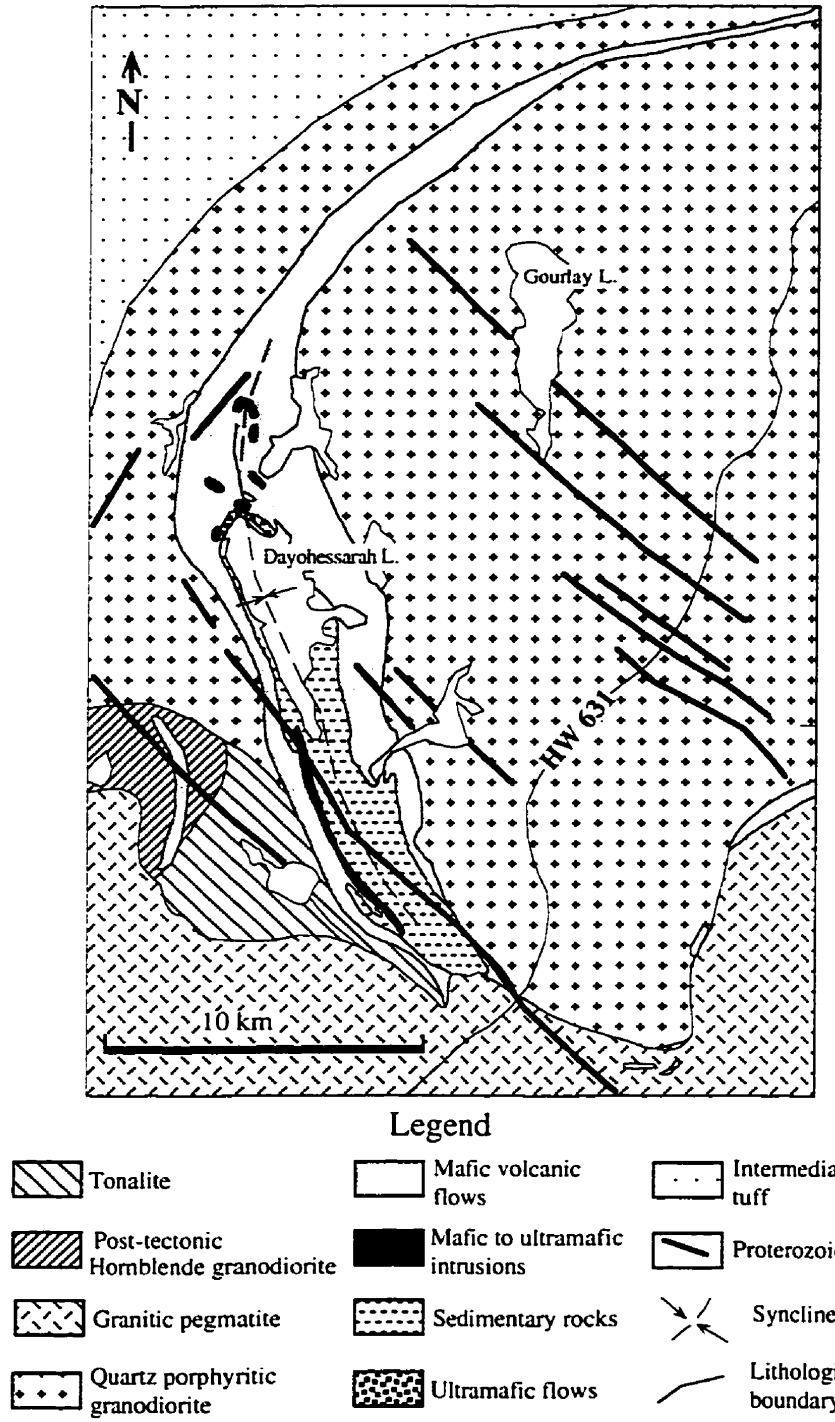

Figure 2.5. Geological map of the Dayohessarah greenstone belt (modified after Stott et al., 1994).

CHAPTER 3. GEOCHEMISTRY OF ULTRAMAFIC-MAFIC OCEAN FLOOR VOLCANIC SEQUENCES

3-1. Introduction

The geochemical characteristics of Archean komatiites and associated basalts are of particular interest for understanding early mantle evolution, petrogenesis, and geodymanic processes (Sun and Nesbitt, 1978; Nesbitt et al., 1979; Cattel and Arndt, 1987; Jochum et al., 1991; Xie and Kerrich, 1994; Dostal and Mueller, 1997). It is widely accepted that komatiites are the product of high temperature (~1600 °C) partial melting, and their origin has been attributed to anomalously hot plumes rising from the deep mantle (Fyfe, 1978; Storey et al., 1991; Campbell and Griffiths, 1992; Herzberg, 1992; Nisbet et al., 1993; Arndt, 1994).

Large tracts of within-plate oceanic basalts are an important component of greenstone-granitoid dominated subprovinces within the Archean Superior Province (Thurston and Chivers, 1990; Hoffman, 1991). These oceanic basalts are locally associated with komatiites, and are thought also to be the products of mantle plumes (Jarvis and Campbell, 1983; Campbell and Griffiths, 1992; Arndt, 1994; Condie, 1994). Geochemically these basalts are Mg-, to Fe-tholeiites in composition, and possess near-flat rare earth element (REE) patterns (Thurston, 1990; Laflèche et al., 1992; Xie et al., 1993). They are distinct from more evolved arc basalts that have the combination of LREE enrichment with negative Nb and Ti anomalies (see Chapter 4; Laflèche et al., 1992), or komatiites and basalts erupted through, and contaminated by, continental crust as in the

Archean Yilgarn block, western Australia (Arndt and Jenner, 1986; Sun et al, 1991; Perring et al., 1996).

Modern oceanic basalts erupted from plumes, such as the Hawaiian and Icelandic plumes, contain several mantle components as identified from isotopic studies (Zindler and Hart, 1986; Hemond et al. 1993; Hanan and Graham, 1996; Hofmann, 1997). Similarly, late Cretaceous ocean plateau basalts (OPB), such as Ontong Java, Broken Ridge, and Gorgona, also have diverse geochemical characteristics (Mahoney et al., 1993; Mahoney et al., 1995; Kerr et al., 1996). These isotopically different mantle components also have distinctive trace element systematics (Saunders et al., 1988; Sun and McDonough, 1989; Weaver, 1991).

Identifying different mantle components in ultramafic and mafic liquids erupted from Archean plumes is more difficult than for Phanerozoic counterparts in that Sr and Pb isotopic signatures typically have been disrupted. Similarly, several key incompatible elements such as Rb, Ba, Pb, K, and Sr used to identify distinct mantle components in modern ocean island basalts also have been disturbed (Weaver, 1991). There is only sparse He isotope data from rare glass inclusions in volcanic flows, but significant Sm-Nd isotope data for crustal recycling into the late Archean mantle (cf. Shirey and Hanson, 1986; Richard et al., 1996).

Accordingly, this chapter presents high precision ICP-MS trace element data for compositionally diverse but stratigraphically related komatiites and associated basalts from the late Archean (~2.75 Ga) Schreiber-Hemlo and White River-Dayohessarah greenstone belts of the Wawa Subprovince in the Archean Superior Province (Fig. 3.1). Included are komatiites and basalts with LREE depletion, flat REE's, and positively fractionated REE's. Based on the data this study attempts to resolve different mantle components in the plume from which the lavas are inferred to have been derived.

Given the fact that most rocks in Archean greenstone belts have undergone poly-

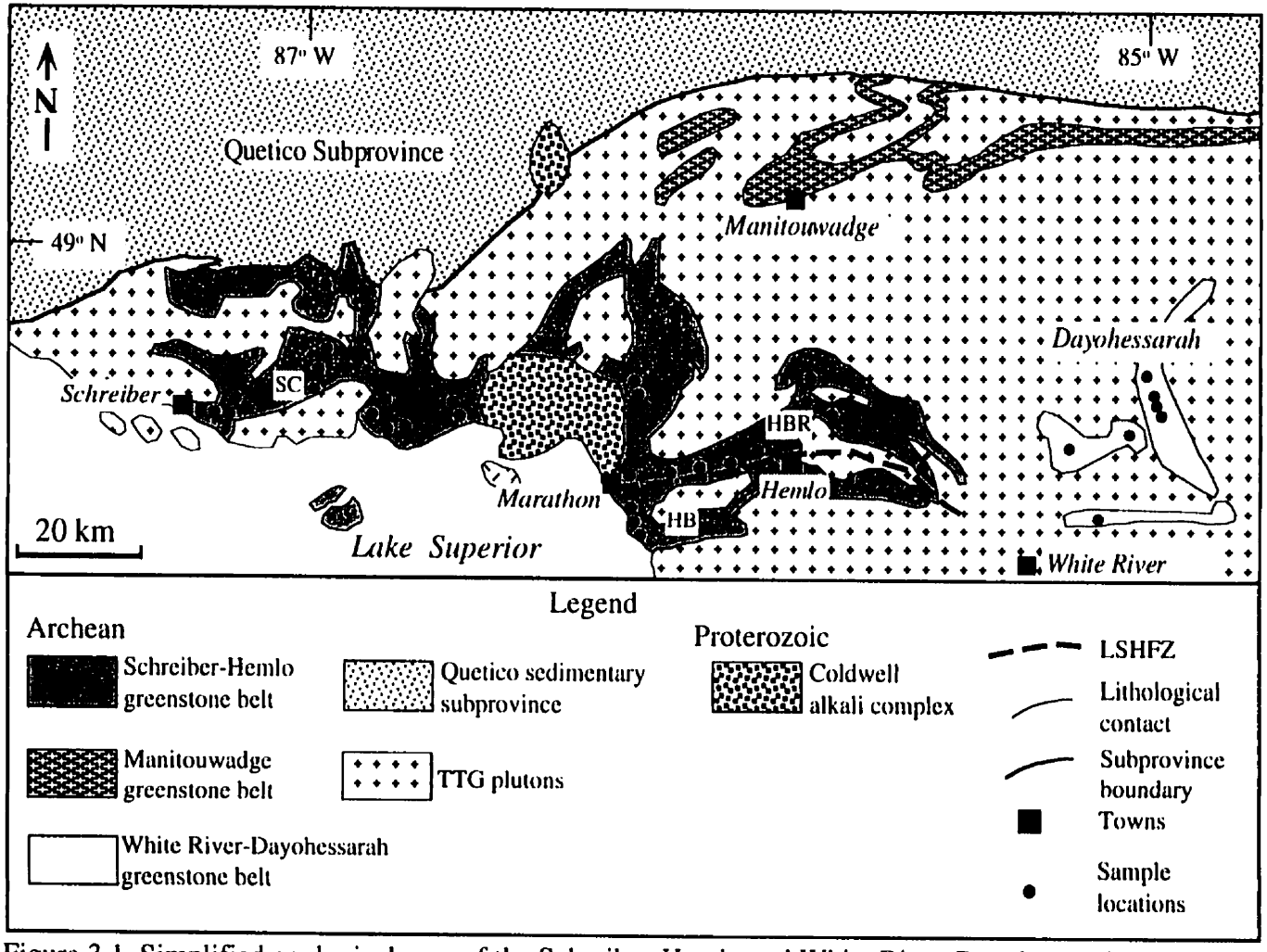

Figure 3.1. Simplified geological map of the Schreiber-Hemlo and White River-Dayohessarah greenstone belts. Lithological boundaries may also be tectonic (modified after Williams et al., 1991). TTG: Tonalite trondhjemite-granodiorite; SC: Schreiber assemblage, HBR: Hemlo-Black River assemblage, HB: Heron Bay assemblage.

phase deformation and greenschist to amphibolite facies metamorphism, some elements may have been mobile. For this reason, emphasis is placed on high field strength elements (HFSE: Th, Nb, Ta, Zr, Hf, Ti, Y), rare earth elements (REE: La-Lu), and transition metals (e.g., Sc, Ni, Cr, V), which are considered to be relatively immobile during sea-floor alteration and metamorphism up to amphibolite facies grade (Winchester and Floyd, 1977; Ludden et al., 1982; Jochum et al., 1991; Condie, 1994 and references therein). The abundances, and inter-element relations of these elements can then be used for geochemical characterization of volcanic sequences of the Schreiber-Hemlo and Dayohessarah greenstone belts.

3-2. Petrography

Komatiites and komatiitic basalts of the Schreiber-Hemlo and White River-Dayohessarah greenstone belts are characterized by diverse petrographic textures, ranging from spinifex to olivine cumulate, typical of these ultramafic flows, but the former is predominant. Spinifex blades range from a few mm to 10 cm in length. Supracrustal sequences have undergone greenschist facies metamorphism and deformation. However, locally volcanic rocks including komatiites are relatively fresh, and contain olivine crystals and well-preserved original igneous textures. In the least altered flows, partly serpentinized olivine is the dominant mineral, whereas in their more metamorphosed counterparts, tremolitic amphibole, talc, and serpentine are abundant. Carbonatization is absent to insignificant in all specimens analyzed. A few per cent of chromite in komatiites, and magnetite in basalts is present. Basaltic volcanic rocks range from undeformed pillow basalts and massive flows to intensely deformed amphibolites. In greenschist facies rocks, chlorite and epidote are the dominant minerals, whereas in their amphibolite facies equivalents, hornblende and actinolitic amphiboles, plagioclase, and epidote ± quartz ± garnet are predominant.

3-3. Sampling procedures, location, and analytical methods

Samples for geochemical analyses were obtained from the least altered outcrops of volcanic flows in the Dayohessarah Lake, Hemlo, Heron Bay, Terrace Bay and Schreiber areas in the Schreiber-Hemlo and White River-Dayohessarah greenstone belts (Fig. 3.1). All samples were powdered using an agate mill. Major elements and Zr were analyzed by XRF (see Potts, 1987). Trace elements, including REE (La-Lu), HFSE (Th, Nb, Ta, Zr, Hf, Y) and transition metals (Cr, Ni, Co, Sc), were analyzed by ICP-MS at the University of Saskatchewan, using a Perkin Elmer Elan 5000 and the protocol of Jenner et al. (1990) and Longerich et al. (1990). Wet chemical operations were conducted under clean-lab conditions, and all acids were distilled. All samples were analyzed twice using both HF-HNO_3 acid dissolution and Na_2O_2 sinter techniques to circumvent potential problems associated with HFSE and REE in refractory minerals (Appendix 3.1). An inter-comparison was made between HF-HNO_3 dissolution and Na_2O_2 sinter techniques for a representative set of samples. Excepting Zr and Hf, there is a close correspondence between results from the two techniques. The Na_2O_2 sinter technique yielded Zr concentrations closer to that of XRF than HF-HNO_3 (Appendix 3.1). This result is interpreted to reflect undissolved refractory minerals in the HF-HNO_3 attack. Analyses of acids, distilled deionized water, and procedural blanks yield levels of < 10 ppb of HFSE and REE. The ICP-MS protocol involves external calibration, standard additions, and the reference materials BIR-1 and BHVO-1 (see Appendices 1.1, 3.1; Xie and Kerrich, 1995; Fan and Kerrich, 1997). Pure elemental standards in solution were employed for external calibration and standard additions. Standard additions were used to overcome possible matrix effects; each unknown was run unspiked and spiked with pure elemental standards. The detection limits (in ppm) defined as 3σ of the procedural blank, for some critical

elements are as follows: Th (0.01), Nb (0.006), Hf (0,008), Zr (0.004), La (0.01), Nd (0.04), and Sm (0.03). The precision for these elements ranges from 1 to 10 %, and accuracies are approximately 5 % (Appendix 3.1; Element ratios are normalized to primitive mantle such that zero fractionation represents 1 (e.g., $Nb/Th_n=1$). Zr/Zr*, Hf/Hf*, Nb/Nb* and Ti/Ti* ratios are calculated following the method of Taylor and McLennan (1985). Major element oxides were 100±0.5 wt. %. The data are reported on a volatile free basis.

3-4. Geochemical results

Based on the definition of komatiites of Arndt and Nesbitt (1982), ultramafic lavas of the late Archean Schreiber-Hemlo and White River-Dayohessarah greenstone belts are divided into komatiites (MgO > 18 wt.%) and komatiitic basalts (13< MgO <18 wt.%). Both of the principal types of komatiites, Al-depleted and Al-undepleted, are present (Table 3.1; Appendix 3.2). On binary plots of MgO versus elements incompatible or compatible in olivine, komatiitic basalts plot co-linearly with komatiites within each group, signifying that the komatiitic basalts are likely fractionation products of komatiitic liquids (Figs. 3.2, 3.3).

Basalts have less than 12 wt.% MgO; and range from Mg-, and Fe-tholeiites to alkali basalts (Figs. 3.2, 3.3; Appendix 3.1). The total population of mafic volcanic rocks can be divided into three major groups based on REE fractionations as has been done for diverse basalts in Archean greenstone belts generally, and Phanerozoic Ocean Plateau basalts (OPB) specifically (Floyd, 1989; Allan et al., 1994; Condie, 1994; Kerr et al., 1996). The three groups are: Group I; La/Sm_n=0.54-0.88; Group II; La/Sm_n=0.93-1.25; and Group III; La/Sm_n=1.4-2.7 (Fig. 3.4; Tables 3.2, 3.3; Appendix 3.3). In each major group, two or three sub-populations may be identified based on Th/Nb, HFSE/REE and

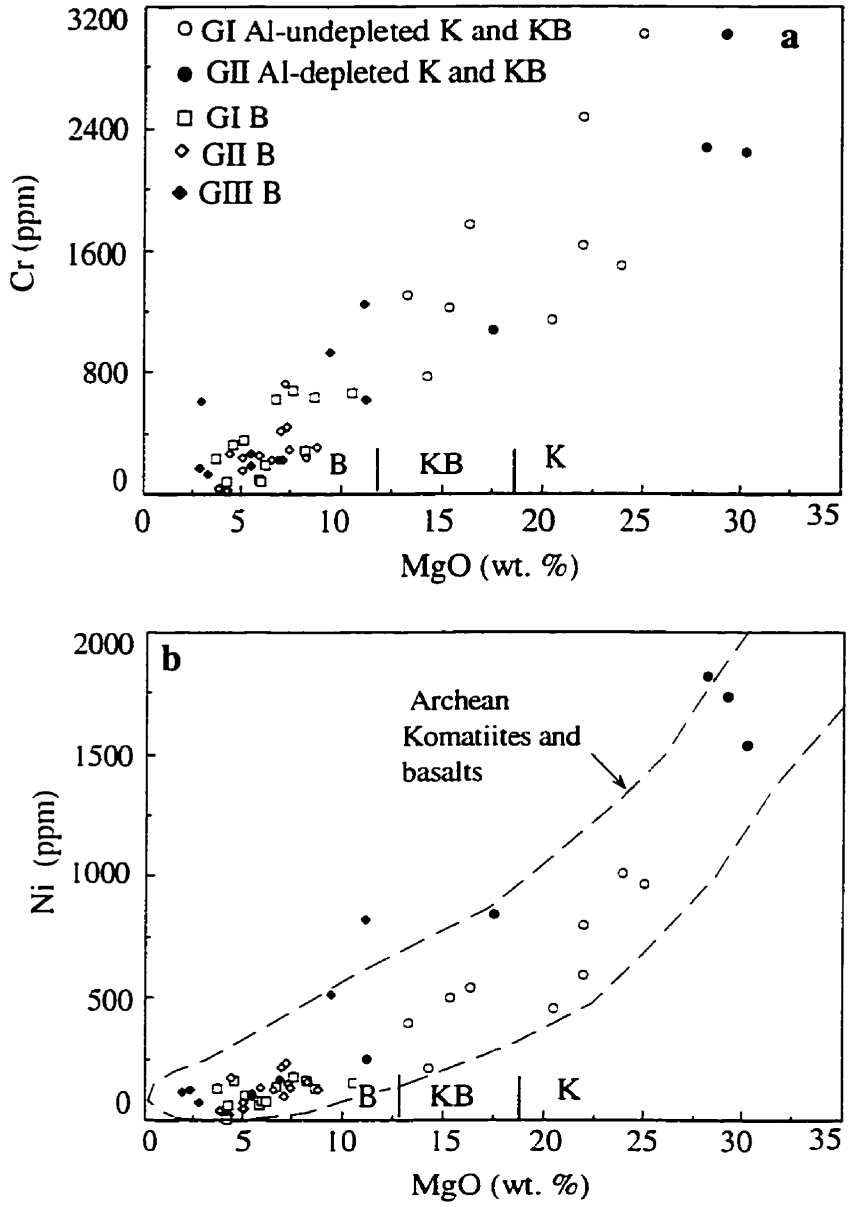

Figure 3.2. Variation diagrams of Cr and Ni vs MgO for komatiites, komatiitic basalts, and basalts of the Schreiber-Hemlo and White River-Dayohessarah greenstone belts. K=Komatiite, KB=Komatiitic basalt, B=Basalt; GI=Group I, GII=Group II, GIII=Group III. The field for Archean komatiites and basalts from Arndt (1991).

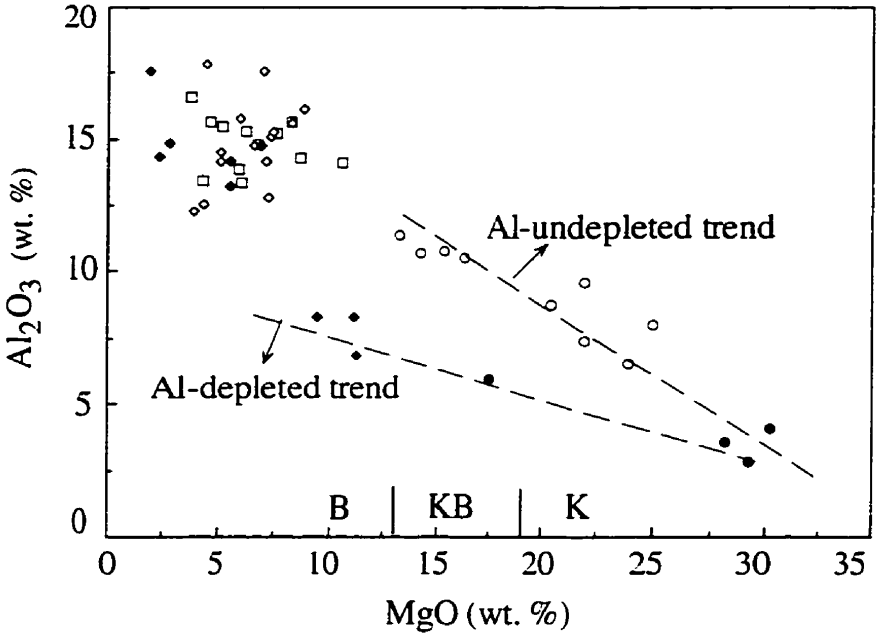

Figure 3.3. Variation diagram of Al_2O_3 vs MgO for komatiites, komatiitic basalts. Abbreivations as in Figure 3.2.

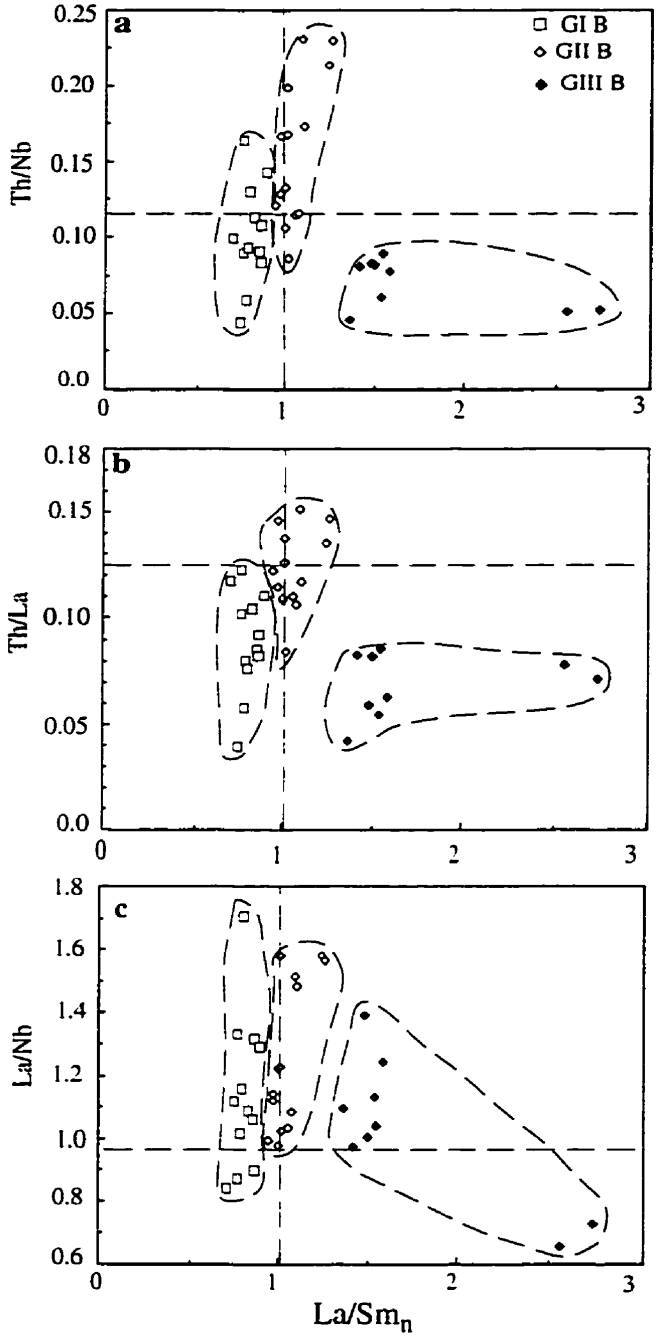

Figure 3.4. Th/Nb, Th/La, and La/Nb vs La/Sm$_n$ variation diagrams showing the three distinctive groups of basalts in the Schreiber-Hemlo and White River-Dayohessarah greenstone belts. Abbreviations as in Figure 3.2. Dashed-lines represent the primitive mantle values.

Th/LREE inter-element relations (Tables 3.2, 3.3; Appendix 3.3). The principal geochemical characteristics of these groups are described in turn below. Several inter-element ratios are expressed as values normalized to primitive mantle, designated subscript n, such that the primitive mantle ratio would be 1.

3-4-1. Group I Al-undepleted komatiites and komatiitic basalts

Group I ultramafic volcanic rocks are Al-undepleted komatiites and komatiitic basalts (MgO=13.5-25 wt.%, Ni=210-1020 ppm, Cr=775-3030 ppm, Al_2O_3=6.5-11 wt.%) [Table 3.1; Appendix 2.2; see Sun and Nesbitt, 1979; Nesbitt et al., 1979; Arndt and Nesbitt, 1982]. Sample DH96-9 appears to be the most pristine; it has near-chondritic Al_2O_3/TiO_2(20), Zr/Y (2.45), and Nb/Ta (17) ratios (cf. Sun and McDonough, 1989). They are characterized by moderate variations of Al_2O_3/TiO_2 (12-23), Ti/Zr (60-105), and Zr/Y (2.3-4.4) ratios, with variably depleted to flat LREE, and flat to slightly enriched HREE patterns (La/Sm_n=0.54-1.2, Gd/Yb_n=0.92-1.3) [Fig. 3.5; Table 3.1; Appendix 3.2]. In addition, they systematically show the following geochemical features: (1) moderately negative to minor positive normalized fractionation of Nb with respect to Th and La (Nb/Nb*=0.6-1.1); (2) positive fractionation of Zr and Hf with respect to MREE (Zr/Zr*=1-1.3, Hf/Hf=1.2); and (3) Zr/Hf (36-47) ratios are variably greater than the primitive mantle value of 36 (Fig. 3.5; Table 3.1; see Sun and McDonough, 1989). The magnitude of negative Nb anomalies, however, does not correlate with LREE concentrations; for example, those with lower La/Sm_n ratios tend to have larger negative Nb anomalies than enriched counterparts. Accordingly, increasingly negative Nb anomalies are not accompanied by progressive gain of Th and LREE, or decreasing Ni and Cr, and hence cannot result from crustal contamination (e.g., SC96-8, SC95-53; Appendix 3.2). Collectively, these compositional features conform to the Al-undepleted

Table 3.1. Summary of significant compositional values and inter-element ratios of komatiites and komatiitic basalts of the Schreiber-Hemlo and White River-Dayohessarah greenstone belts.

	Al-undepleted komatiites	Al-undepleted Komattitic basalts	Al-depleted Komatiites	Al-depleted Komatiitic basalts
SiO_2 (wt.%)	44-48	47-51	41-42	49
MgO	20-25	13-16	28-30	17.5
TiO_2	0.4-0.5	0.6-0.9	0.6-0.9	1.1
Fe_2O_3	11.2-14.4	12-16	20-22	14.9
Cr (ppm)	1142-3028	775-1770	2250-3022	1081
Ni	460-1017	209-546	1544-1822	845
Th	0.1-0.20	0.23-0.50	0.23-0.73	0.44
La	0.6-1.6	2.2-5.0	3.0-7.4	4.17
Nb	0.6-1.5	1.7-4.0	2.6-8.6	5.9
Zr	20-38	41-66	29-71	59
Y	8-12	15-21	5-7	14
$(La/Yb)_{cn}$	0.45-1.2	1.1-1.6	3.9-7.4	2.8
$(La/Sm)_{cn}$	0.54-1.0	0.9-1.2	1.4-2.1	0.97
$(Gd/Yb)_{cn}$	0.90-1.2	1.15-1.3	2.2-2.4	2.42
Al_2O_3/TiO_2	19-23	12-19	3-7	5
Zr/Hf	35-47	35-36	37-39	33
Nb/Ta	10-18	13-17	17	17
Ti/Zr	60-105	73-88	76-120	113
Zr/Y	2.3-4.4	2.7-3.3	5.8-10	4.2
Nb/Nb*	0.63-1.14	0.65-0.85	1.05-1.25	1.47
Eu/Eu*	0.4-1.2	0.8-1.5	0.60-1.26	1.0
Zr/Zr*	1.0-1.3	0.9-1.2	0.76-1.0	0.85
Hf/Hf*	1.1-1.2	1.0-1.2	0.75-1.0	0.90

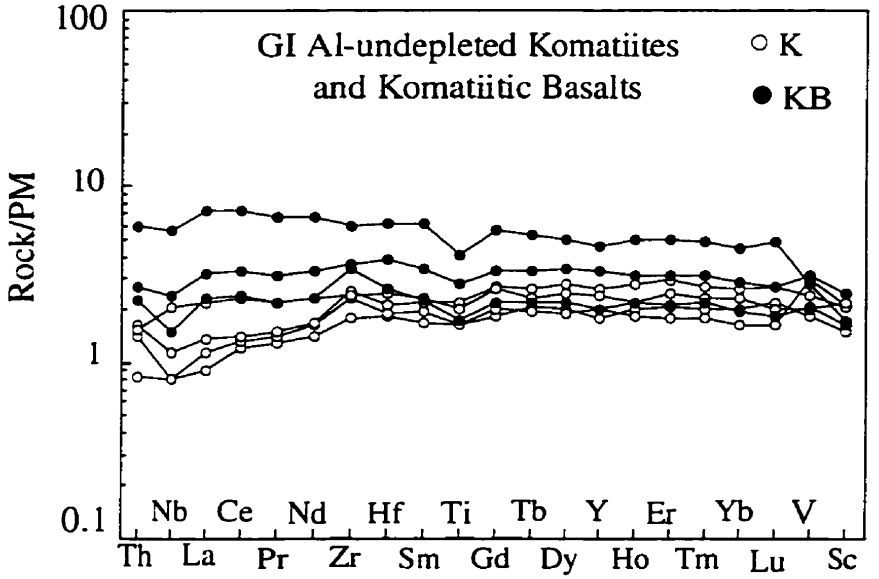

Figure 3.5. Primitive mantle-normalized trace element diagram for Al-undepleted komatiites and komatiic basalts. Abbreivations as in Figure 3.2. Normalizing values from Sun and McDonough (1989).

komatiites at Munro and Tisdale Townships (see Sun and Nesbitt, 1978; Nesbitt et al., 1979; Arndt and Nesbitt, 1982; Xie et al., 1993).

3-4-2. Group II Al-depleted komatiites and komatiitic basalts

Komatiites and komatiitic basalts of Group II (MgO=17.5-30 wt. %, Ni=845-1820 ppm, Cr=1080-3020 ppm) are distinctive in terms of low Al_2O_3/TiO_2 (3-7) ratios and Al_2O_3 (3-6 wt. %) contents (Fig. 3.3; Table 3.1; Appendix 3.2). Together with positively fractionated REE's these features are consistent with Al-depleted komatiites (Figs. 3.2, 3.6a; Table 3.1; Nesbitt et al., 1979; Arndt and Nesbitt, 1982; Jahn et al., 1982; Arndt, 1994). They tend to have higher Fe_2O_3 contents than their Al-undepleted counterparts (14-22 wt.% versus 11-16 wt.%). Ratios of Zr/Hf (33-39) and Nb/Ta (17) are close to chondritic, whereas Zr/Y ratios are super-chondritic (4.2-10).

On a primitive mantle normalized diagram, the significant features of these komatiites and komatiitic basalts are: (1) enrichment of LREE's over MREE's and HREE's (La/Sm_n=1.0-2.1, Gd/Yb_n=2.2-2.4; La/Yb_n=2.8-3.9); (2) depletion of Th with respect to La and Nb, generating high Nb/Th_n (1.3-1.4) but low Th/La_n (0.61-0.85) ratios; (3) enrichment of Nb with respect to Th and La, resulting in moderately positive Nb (Nb/Nb*=1.1-1.47) anomalies; and (4) negative to zero anomalies of Zr and Hf (Zr/Zr*=0.76-1.0, Hf/Hf*=0.75-1.0) [Fig. 3.6a; Table 3.1; Appendix 3.2].

3-4-3. Group I basalts

Group I basalts include a range of primitive Mg-, to evolved Fe-tholeiites (MgO=4-11 wt. %, Fe_2O_3=12-20 wt.%). The most primitive have near-chondritic Ti/Zr (92-120) ratios, and define an iron enrichment trend to the less primitive Fe-tholeiites. Magnesian

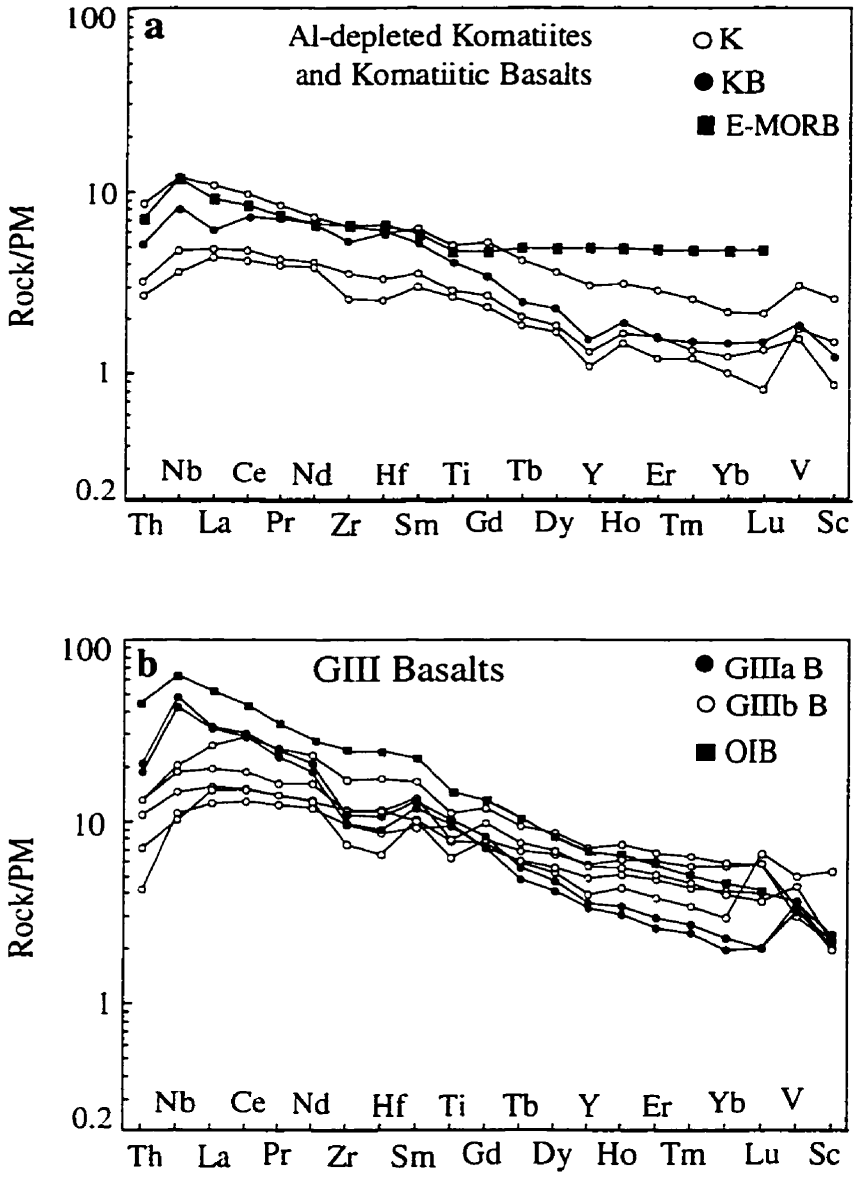

Figure 3.6. Primitive mantle-normalized trace element diagrams for Group II Al-depleted komatiites and komatiitic basalts, and Group III transitional to alkaline basalts. E-MORB and OIB vaules from Sun and McDonough (1989). Abbreviations as in Fig. 3.2.

tholeiites have consistently greater contents of the compatible elements Cr, Co, and Ni, but lower concentrations of incompatible elements including Ti, P, Nb and Zr than Fe-tholeiites (Table 3.2; Appendix 3.3). Mg-tholeiites have near-chondritic Al_2O_3/TiO_2 ratios whereas in Fe-tholeiites this ratio is sub-chondritic (Appendix 3.3).

On a primitive mantle-normalized diagram the group is characterized by LREE depleted patterns but flat HREE, where La/Sm_n=0.7-0.9 and Gd/Yb_n=0.95-1.17 (Fig. 3.7). Absolute REE concentrations are lowest in the Mg tholeiites and highest in the Fe-tholeiites; however, the slopes of the patterns do not change with increasing REE abundance (Fig. 3.7; Appendix 3.3).

Notwithstanding coherent REE patterns, Group I basalts have complex Th-Nb-La inter-element relationships. Most samples have small to pronounced depletions of Th with respect to La, where Th/La_n=0.32-0.99. Three distinctive populations may be distinguished based on Th-Nb-La systematics: Group Ia basalts are characterized by smooth Th-Nb-La patterns (Nb/Nb*=0.9-1.1); Ib basalts possess negative Nb anomalies (Nb/Nb*=0.71-0.78); whereas Ic basalts have positive Nb anomalies (Nb/Nb*=1.2-1.5) [Fig. 3.7; Table 3.2; Appendix 3.3].

3-4-4. Group II basalts

Basalts classified as Group II are the most abundant type of volcanic rocks in the Wawa Subprovince. Like Group I, Group II basalts range from Mg-, to more evolved Fe-tholeiites, where the most MgO-rich flows have near chondritic Al_2O_3/TiO_2 ratios, and higher abundances of Cr, Co, and Ni, but lower Ti, P, Nb and Zr contents (Table 3.2). Similarly, these basalts have near-flat REE patterns, where La/Sm_n=0.95-1.1; Gd/Yb_n=1.1-1.2, and Fe-tholeiites have higher abundances of REE but similar patterns as

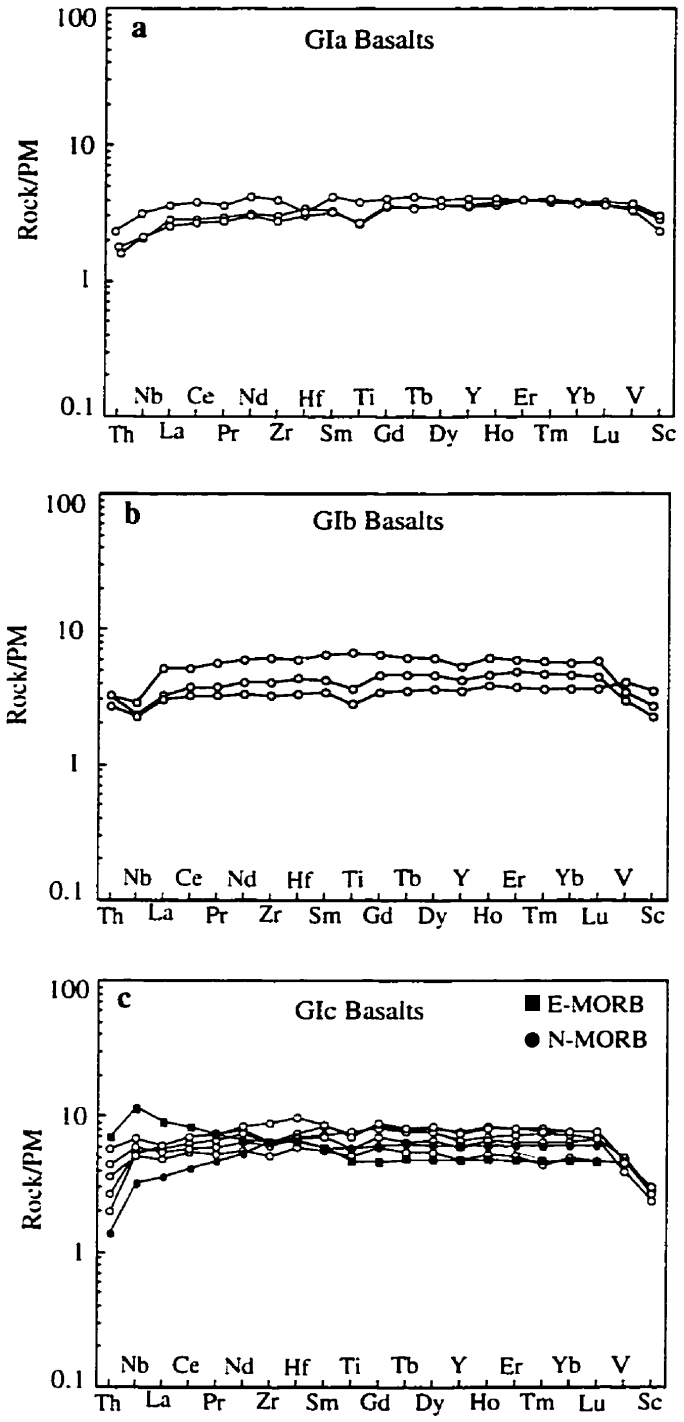

Figure 3.7. Primitive mantle-normalized trace element diagrams for Group I tholeiitic basalts. Normalizing, N-MORB, and E-MORB values from Sun and McDonough (1989). Abbreviations as in Figure 3.2.

Table 3.2. Summary of significant compositional values and inter-element ratios of Group I and Group II basalts of the Schreiber-Hemlo and White River-Dayohessarah greenstone belts.

	G Ia	GIb	GIc	GIIa	GIIb
SiO_2 (wt.%)	47-51	49-52	47-53	48-55	48-53
MgO	4.6-10.6	3.7-8.2	4.2-5.9	4.3-7.4	4.4-8.8
TiO_2	0.6-1.1	0.6-1.5	1.1-1.7	0.8-2.4	0.7-1.2
Fe_2O_3	12-14	10.8-13	11.3-2	12-17	10.5-14
Cr (ppm)	327-667	231-682	82-360	20-435	215-724
Ni	129-162	129-161	62-98	18-147	92-231
Th	0.14-0.36	0.23-0.27	0.17-0.38	0.37-1.54	0.39-0.55
La	1.74-2.45	2.1-3.5	3.3-4.15	3.0-14.4	2.674.27
Nb	1.5-3.2	1.6-2.1	3.7-4.9	2.94-13.3	2.2-3.9
Zr	31-66	36-69	58-101	54-244	46-73
Y	16-25	16-24	22-35	20-66	16-26
$(La/Yb)_{cn}$	0.65-0.94	0.56-0.74	0.86-1.10	1.1-1.45	1.06-1.67
$(La/Sm)_{cn}$	0.78-0.86	0.76-0.90	0.69-0.86	0.95-1.1	0.97-1.25
$(Gd/Yb)_{cn}$	0.94-1.1	0.95-1.17	1.1-1.2	1.1-1.24	1.08-1.20
Al_2O_3/TiO_2	13-25	11-25	8-14	5-18	13-22
Zr/Hf	30-44	34-38	31-34	27-40	29-37
Nb/Ta	16-24	15-16	16-20	14-18	13-18
Ti/Zr	100-113	100-127	92-146	60-109	81-109
Zr/Y	1.9-2.6	2.3-2.9	2.1-2.9		
Nb/Nb*	0.90-1.1	0.72-0.78	1.16-1.5	0.85-1.0	0.57-0.9
Eu/Eu*	0.9-1.0	0.9-0.96	0.9-1.0	0.82-1.0	0.84-1.0
Zr/Zr*	0.9-1.0	0.97-1.0	0.8-1.0	0.87-1.1	0.89-1.1
Hf/Hf*	0.8-1.0	0.97-1.0	0.9-1.1	0.97-1.1	1.0-1.2

Mg-counterparts (Fig. 3.8; Table 3.2 Appendix 3.3). Two outliers have slightly fractionated REE patterns (La/Sm_n=1.25; Gd/Yb_n=1.35; HE19, HE95-9; Appendix 3.3).

Based on Th-Nb-La inter-element relations, Group II basalts may be divided into two populations: Group IIa basalts define consistently smooth patterns, reflected by Nb/Nb* (1.0-1.1) values close to unity, whereas IIb basalts have systematically large negative Nb (Nb/Nb*=0.6-0.86) anomalies (Fig. 3.8; Appendix 3.3). Group IIa is mostly Fe-tholeiites with similar flat normalized patterns to IIb but at 5 to 20 times the primitive mantle. They have lower and more variable MgO contents, but higher TiO_2, Fe_2O_3, P_2O_5, Zr, Hf and total REE concentrations than their IIa counterparts. Group IIb is dominantly Mg-tholeiites, with uniform trace and major element contents, and possess flat normalized REE patterns coherent at 4 to 6 times the primitive mantle (Figs. 3.8).

3-4-5. Group III basalts

These basalts are defined on the basis of their pronounced positively fractionated rare earth element patterns (La/Yb_n=2.6-16) [Fig. 3.6b; Table 3.3]. Relative to basalts of Groups I and II, they have higher contents of incompatible elements at a given MgO value, and similarly greater incompatible/compatible element ratios (e.g., Zr/Y=4.8-7.5), but low Al_2O_3/TiO_2 ratios (Table 3.3; Appendix 3.3). They are transitional to alkaline in character (cf. Winchester and Floyd, 1977; Chen et al., 1991).

Two populations are present both on the basis of major and trace element compositions, as well as Th-La-Nb systematics. Group IIIa have generally lower Al_2O_3 (5-8 wt.%) contents and Al_2O_3/TiO_2 (4) ratios, lower P_2O_5 (0.14), but greater Cr (925-1230 ppm) and Ni (510-820 ppm), and more fractionated REE and lower HREE abundances (La/Sm_n=2.5-2.7; Gd/Yb_n=3.6; Fig. 3.6b; Table 3.3). In contrast, Group

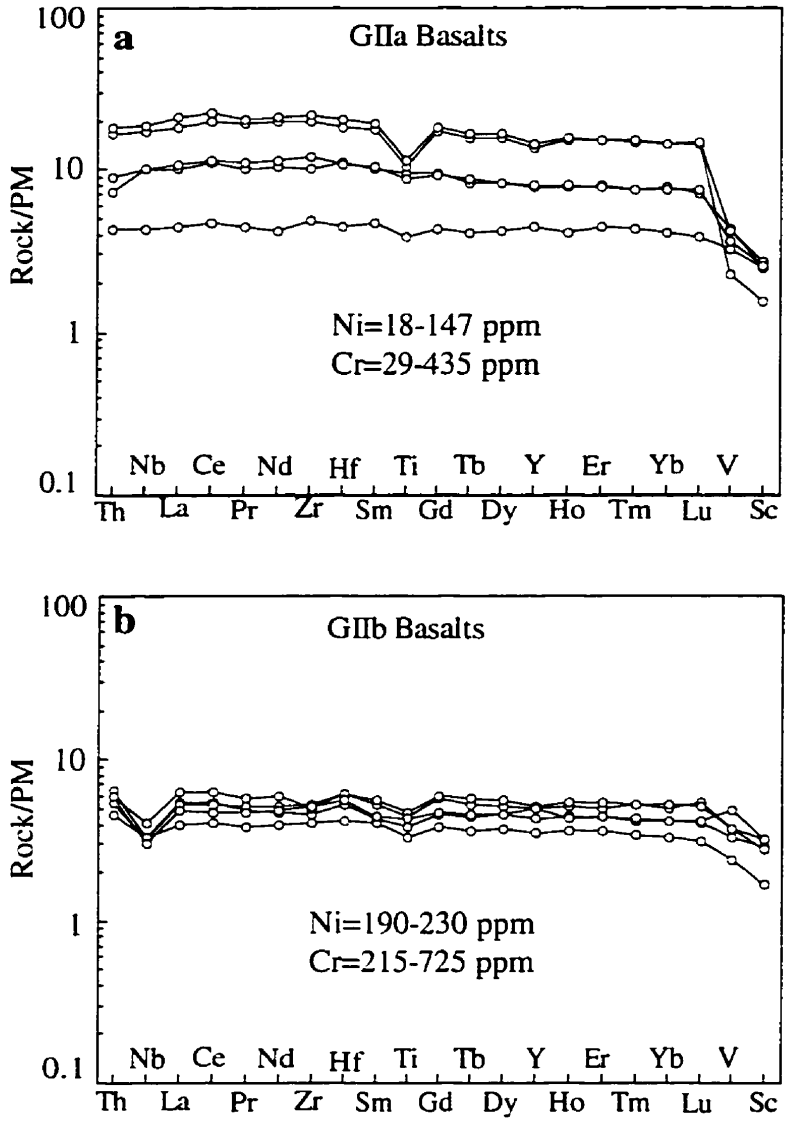

Figure 3.8. Primitive mantle-normalized trace element diagrams for Group II tholeiitic basalts. Abbreviations as in Fig. 3.2.

Table 3.3. Summary of significant compositional values and inter-element ratios of Group III basalts of the Schreiber-Hemlo and White River-Dayohessarah greenstone belts.

	G IIIa	GIIIb
SiO_2 (wt.%)	47-48	48-52
MgO	9.5-11.2	4.4-11.3
TiO_2	2.1-2.2	1.7-2.6
Fe_2O_3	15.7-17.7	8.4-15.5
Cr (ppm)	925-1238	131-618
Ni	508-819	70-244
Th	1.6-1.8	0.36-1.12
La	22-23	8.6-16.5
Nb	30-35	7.3-14.6
Zr	109-120	83-206
Y	15-16	18-36
$(La/Yb)_{cn}$	14.5-16	2.6-5.3
$(La/Sm)_{cn}$	2.6-2.7	1.4-1.6
$(Gd/Yb)_{cn}$	3.6	1.4-2.6
Al_2O_3/TiO_2	4	4-13
Zr/Hf	37-39	36-43
Nb/Ta	18	17-30
Ti/Zr	110-114	64-121
Zr/Y	7.3-7.5	4.6-5.7
Nb/Nb*	1.75-1.85	1.0-1.3
Eu/Eu*	0.9-1.0	0.9-1.1
Zr/Zr*	0.65-0.66	0.65-1.0
Hf/Hf*	0.61-0.64	0.57-1.0

IIIb possesses generally higher Al_2O_3 (6.8-17 wt.%) contents and Al_2O_3/TiO_2 (4-13) ratios, lower Cr (130-610 ppm) and Ni (70-244 ppm), and less fractionated REE's (La/Sm_n=1.4-1.6; Gd/Yb_n=1.4-2.50 (Fig. 3.6b; Appendix 3.3). Moderately negative to zero Zr and Hf anomalies are a distinctive feature of Group III volcanic flows as a whole, in common with the associated Al-depleted komatiites and komatiitic basalts.

Thorium-Nb- LREE systematics of the sub-populations have some features in common but others that differ. Both sub-groups show LREE enrichment coupled with Th depletion over La (Th/La_n=0.57-0.63 IIIa; 0.33-0.66 IIIb). However, Group IIIa has a stronger positive anomaly of Nb with respect to Th and La, whereas patterns for Group IIIb peak at La or Ce, and have smoothly convex-up depletions through La, Nb and Th (Fig. 3.7b; Nb/Nb*=1.75-1.85 versus 1.1-1.5).

Because Th, Nb and LREE behave differently during alteration, the coherency of the convex-up patterns from Th through Nb, peaks at La-Ce and decrease through Ho and MREE is unlikely an effect of alteration, which would result in high Nb/La ratios (Fig. 3.6b). Similarly, Th-Nb-La inter-element relations rule out any significant continental contamination which would result in Th/Nb_n and Th/La_n greater than unity, and negative Nb anomalies. Similar trace element patterns, have been documented from the Hawaiian islands and volcanic rocks in the early Proterozoic Trans-Hudson orogenic belt interpreted as ocean island basalts, yet these lack negative Zr and Hf anomalies (Chen et al., 1991; West et al., 1992; Stern et al., 1995).

3.5. Discussion

In order to characterize the petrogenesis of komatiites and basalts of the late Archean Schreiber-Hemlo and Dayohessarah greenstone belts, we address in turn questions of possible effects of hydrothermal alteration, crustal contamination, and fractional

crystallization on composition in general, and Nb anomalies specifically. The petrogenesis, inter-element relationships, and the depth of melt segregation for various types of komatiites and basalts are considered. Finally, we attempt to identify mantle components contributing to these volcanic suites, the origin of the different components, and their implications for the development of the late Archean mantle.

3-5-1. Hydrothermal alteration

Variable element mobility is a possibility for Archean volcanic rocks that have undergone seafloor hydrothermal alteration, greenschist to amphibolite facies metamorphism, and locally polyphase deformation. Evidence signifying limited mobility of Th, REE (except Eu), and HFSE in rocks analyzed for this study includes the following: (1) Relative abundances of these elements do not correlate with the degree of alteration and metamorphism; for example, undeformed pillow basalts with recognizable original igneous textures and equivalents that have been metamorphosed to lower amphibolite facies grade have similar absolute REE abundances; (2) for Munro-type komatiites, and MgO tholeiites, key inter-element ratios such as Al_2O_3/TiO_2, Ti/Zr, and Zr/Y are near chondritic, as observed elsewhere (see Sun and Nesbitt, 1978; Nesbitt et al., 1979); (3) for komatiites, elements generally considered as least mobile conform to the olivine control line (cf. Arndt, 1994); (4) Th-Nb-La inter-element relationships, as defined by the Nb/Nb* ratio, and La/Sm_n ratios do not correlate with LOI (Loss on Ignition; Fig. 3.9); (5) there is no significant enrichment or depletion of groups of elements that behave coherently during alteration; and (6) chondrite-normalized REE and primitive mantle-normalised diagrams of given suites of basalts associated in the field exhibit consistent and coherent patterns for HFSE, REE and Th.

Similar conclusions concerning the relative immobility of Al, Ti, Ni, REE and

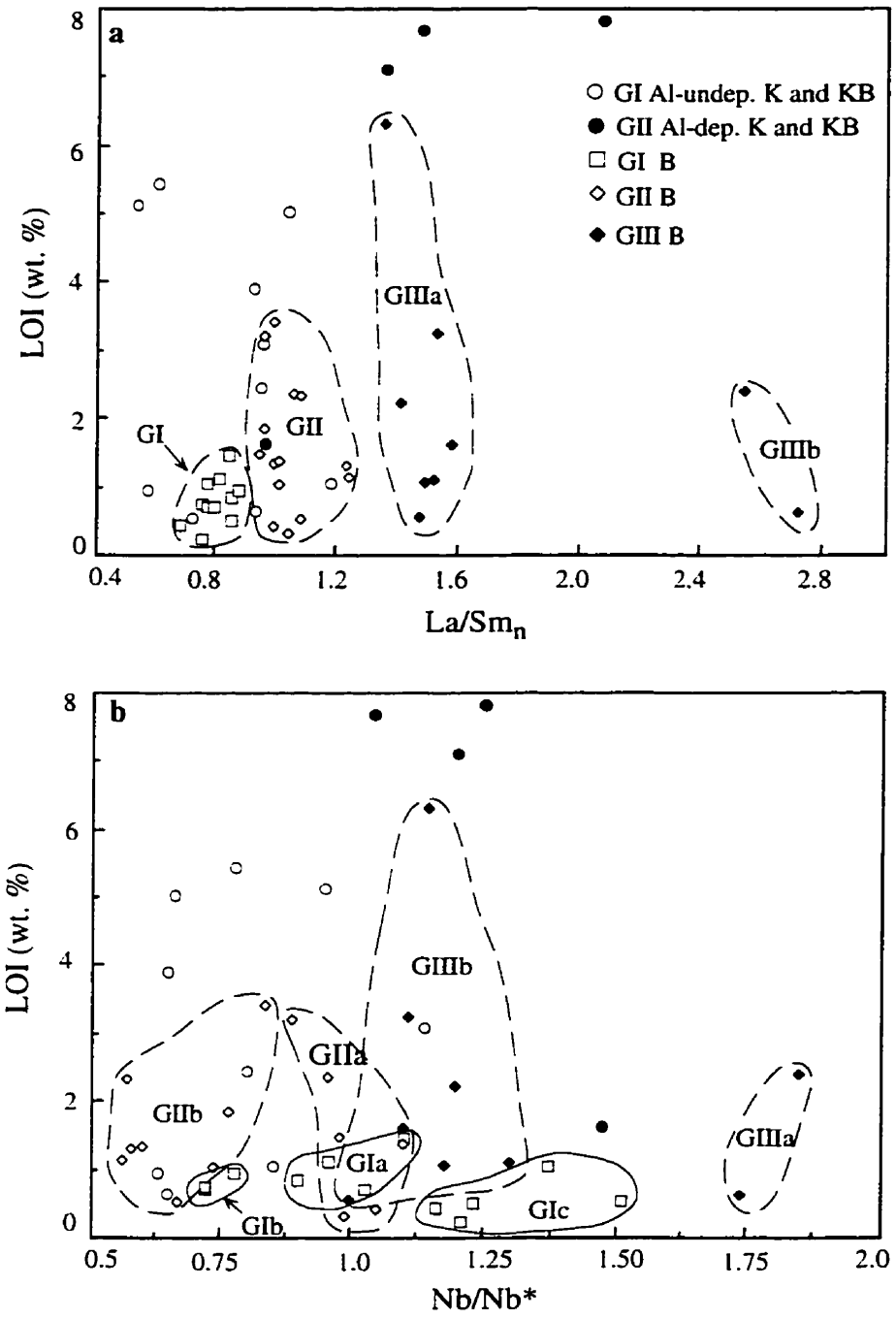

Figure 3.9. LOI (Loss on ignition) vs La/Sm$_n$ and Nb/Nb* variation diagrams, suggusting that LREE fractionation and inter-element ratios do not correlate with alteration and metamorphism. Abbreviations as in Fig. 3.2.

HFSE in ancient volcanic rocks that have experienced alteration under conditions of low water/rock ratios have been reached by numerous workers in the Superior Province specifically (Ludden et al., 1982; Laflèche et al., 1992; Xie and Kerrich, 1994), and other Archean terranes in general (Sun and Nesbitt, 1976; Nesbitt et al., 1979; Jochum et al., 1991; Bickle and Nisbet, 1993; Arndt, 1994). Thus emphasis is placed on Al, Ti, Y, HFSE, REE, and Th that are relatively immobile during secondary processes (see Condie, 1990).

3-5-2. Crustal contamination

Contamination by continental crust is a possibility, especially for magnesian magmas with high liquidus temperatures (Arndt and Jenner, 1986; Perring et al., 1996). We consider geological, stratigraphic, geochronological, and geochemical characteristics of the greenstone belts to address the possibility of crustal contamination.

The basic tectono-stratigraphy in the Schreiber-Hemlo and Dayohessarah greenstone belts is of ultramafic-mafic submarine volcanic rocks tectono-stratigraphically overlain by bimodal, calc-alkaline arc volcanic rocks and associated trench-fore-arc turbidites. These relationships suggest an intra-oceanic arc geodynamic setting formed through the initiation of a subduction zone at the margins of ocean plateau(s) (Polat et al., 1996a). The granitoids in the region are younger than the greenstone belts they engulf (Williams et al., 1991; Corfu and Muir, 1989a,b).

The presence of positive Nb anomalies, high Cr, Ni, and MgO contents, low Al_2O_3/TiO_2, La/Sm_n, and Th/La_n ratios in Group Ic basalts, and Group II komatiites, komatiitic basalts and alkali basalts rule out the contamination of these lavas by continental crust. Negative Nb anomalies in some Group I komatiites and komatiitic basalts, and Groups Ib and IIb tholeiitic basalts could reflect crustal contamination. However, SiO_2,

MgO, Ni, Cr, Co, Th, and LREE contents in these lavas do not correlate with the magnitude of negative Nb anomalies, nor are negative Nb anomalies associated consistently with negative Ti anomalies, (Appendices 3.2, 3.3 Fig. 3.10) as for crustally contaminated 2.7 Ga komatiites and basalts in the Archean Yilgarn Craton, western Australia, where komatiites and associated basalts lavas were erupted through an older sialic basement (Redman and Keays, 1985; Arndt and Jenner, 1986; Barley, 1986; Sun et al., 1989). For example, Group IIb basalts tend to have higher MgO (4.2-8.8 versus 3.9-7.4 wt.%) and Ni (92-230 versus 18-150 ppm), but lower LREE (La=2.7-4.4 versus 3-14.5 ppm) and Th (0.4-0.55 versus 0.4-1.4 ppm) contents, but larger negative Nb (Nb/Nb*=0.56-0.9 versus 0.96-1.1) anomalies than their Group IIa counterparts (Table 3.2; Appendix 3.3).

In contrast to the crustally contaminated 2.7 Ga komatiites and basalts of the Yilgarn Craton, the komatiites and associated basalt sequences within the Wawa and Abitibi subprovinces of the Superior Province formed in intra-oceanic tectonic settings, likely as oceanic plateaus (Thurston, 1990; Polat et al., 1996a; 1998a,b). These intra-oceanic volcanic assemblages were amalgamated along subduction zones, and then were intruded by slab-derived granitoids as arc axes prograded through the subduction-accretion complexes, suggesting that the geodymanic evolution of the Wawa and Abitibi greenstone belts is comparable to Phanerozoic Circum-Pacific accreted terranes of ocean islands, plateaus, and subduction accretion complexes (Hoffman, 1989, 1991; Taira et al., 1992; Polat et al., 1996a). Collectively, geodynamic, stratigraphic, and geochemical characteristics of the Schreiber-Hemlo and White River-Dayohessarah greenstone belts are inconsistent with continental rift or flood basalt origin, involving interaction with an older sialic crustal basement.

3-5-3. Fractional crystallization

Variations of MgO and alteration insensitive elements in komatiites and komatiitic basalts of the study area arose probably from fractionation or accumulation of olivine, as indicated by compliance to the olivine control line in variation diagrams (Figs. 3.2; 3.3; see Arndt, 1994). Clinopyroxene fractionation may have occurred in the komatiitic basalts; however, its extent would have been limited as indicated by uniformly flat HREE over a range of absolute REE abundances (Fig. 3.5; Rollinson, 1993; Skulski et al., 1994). Niobium is compatible in Fe-Ti oxide minerals, but these are unlikely to be fractionating phases in ultramafic liquids.

In tholeiitic basalts high MgO, Ni and Cr contents may have resulted from the mixture of komatiitic liquids and more evolved mafic magmas, or from interaction between a plume and surrounding mantle (cf. Campbell and Griffiths, 1992; Arndt, 1991), whereas low MgO, Ni and Cr basalts may have derived from high MgO equivalents through fractional crystallization (Figs. 3.2, 3.3; cf. Arndt, 1991). Fowler and Jensen (1988) modelled the evolution of Mg-, to Fe-tholeiites in the Kinojevis group, Abitibi belt: they found that the compositional range could be accounted for by fractional crystallization of olivine, and minor clinopyroxene, plagioclase, and Fe-Ti oxides (Figs. 3.10, 3.11). The limited variation of La/Sm_n ratios over a wide range of MgO contents suggest that there was no significant LREE fractionation as a result of fractional crystallization (Appendix 3.3; Fig. 3.10). Similarly, fractional crystallization of clinopyroxene in these basalts is limited by a narrow range of Gd/Yb_n and uniform Sc and CaO contents over a range of REE abundances (Appendix 3.3; Figs. 3.10, 3.11).

Relatively uniform La/Sm_n and Gd/Yb_n ratios, and Sc contents over a large range of Nb from negative to zero to positive anomalies in Groups I and II tholeiites is inconsistent with clinopyroxene fractionation control on the Th-Nb-La systematics (Figs. 3.10, 3.11).

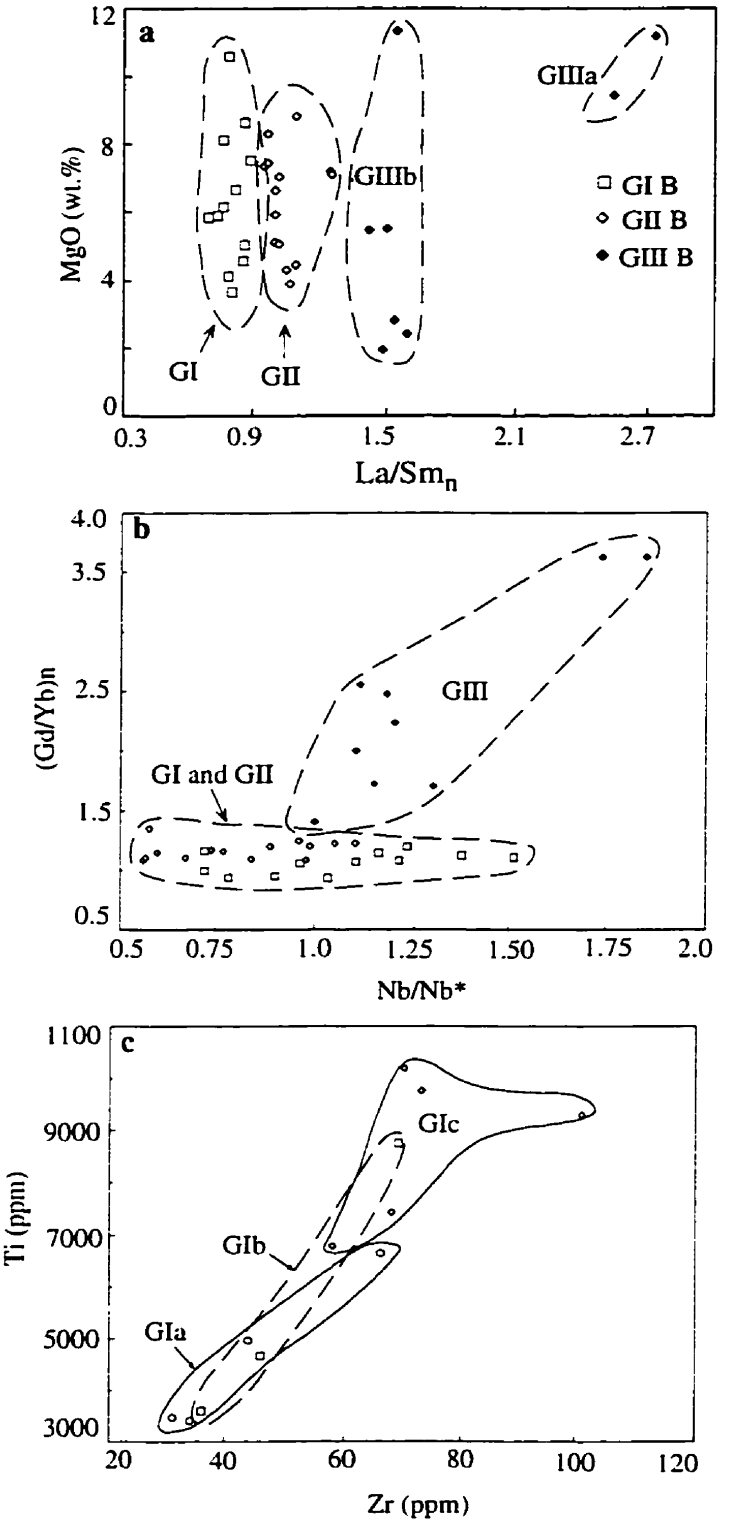

Figure 3.10. MgO vs La/Sm$_n$, Gd/Yb$_n$ vs Nb/Nb*, and Ti vs Zr variation diagrams for basalts. Diagram (c) summizes the Mg-, and Fe-tholeiite fractionation trend for G I basalts.

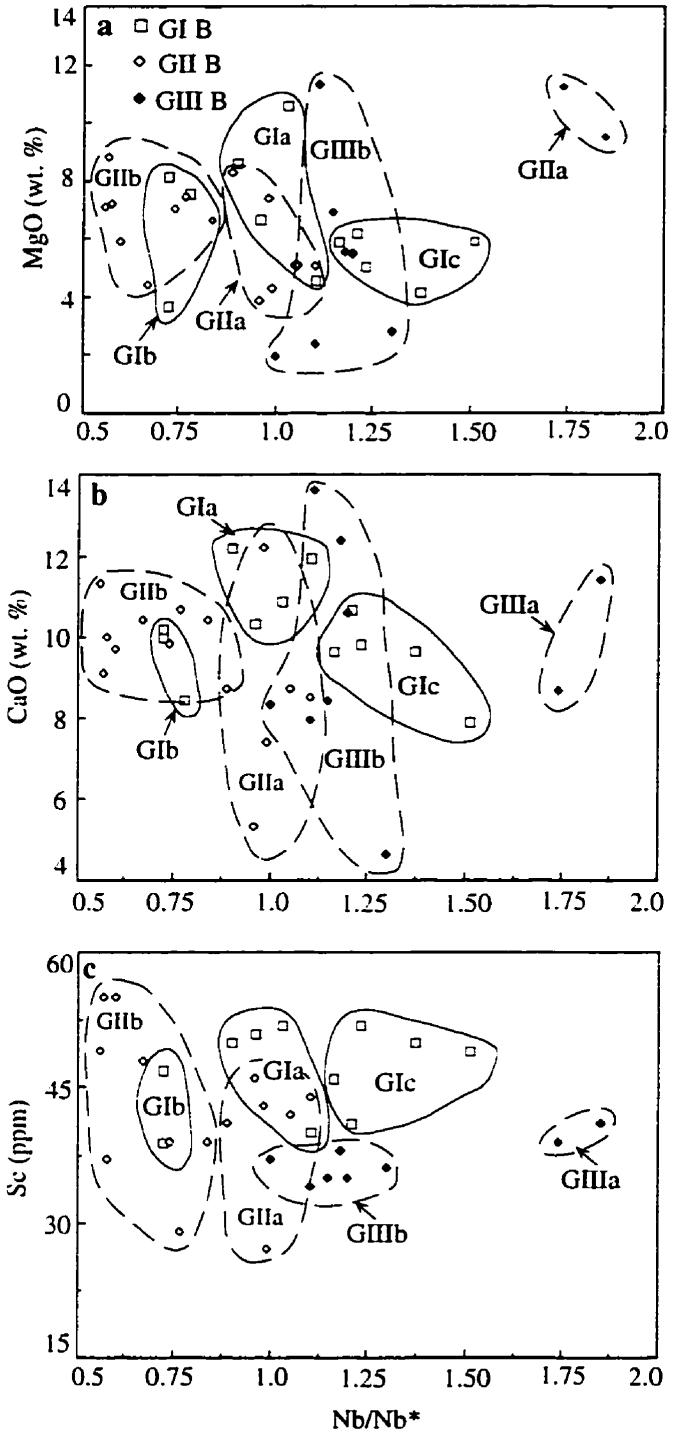

Figure 3.11. MgO, CaO, and Sc vs Nb/Nb* variation diagrams for the three groups of basalts. Abbreviations as in Fig. 3.2.

The lack of large Eu anomalies rules out significant plagioclase accumulation or fractionation. Fe-Ti oxides may accommodate Nb, yet there is no correlation of Nb/Nb* with Fe_2O_3, or TiO_2 contents (Appendix 3.3). Consequently, Th-Nb-La inter-element ratios in the komatiites, komatiitic basalts, and basalts are independent of olivine, clinopyroxene, plagioclase, or Fe-Ti oxide fractionation or accumulation. Hence they must represent a signature of the mantle source (Figs. 3.10, 3.11). These relationships are summarized in Figure 3.10c using Ti and Zr as monitors of the Mg-Fe fractionation trend. For example, Group I basalts show a continuous trend of compositions from primitive Mg-tholeiites to more evolved Fe-tholeiites. Within all sub-groups the trend is accompanied by higher absolute abundances of Th, Nb, REE, Ti and Zr, yet neither the REE fractionations nor Nb-anomalies correlate with absolute abundances of these elements (Fig. 3.11c; Appendix 3.3).

3-5-4. Types of komatiites

There are two principal types of komatiites. Aluminum-undepleted komatiites are characterized by near-chondritic ratios of Al_2O_3/TiO_2, Ti/Zr, and Zr/Y, with flat HREE, and LREE depletion. Aluminum-depleted komatiites have lower Al_2O_3 contents and Al_2O_3/TiO_2 ratios, with generally positively fractionated REE (Sun and Nesbitt, 1976; Nesbitt and Sun, 1976; Nesbitt et al., 1979; Jahn et al., 1982). They are sometimes referred to as Munro-type and Barberton-type, respectively (see Arndt, 1994 for a review). Xie et al. (1993) described a variant of Al-undepleted komatiite from Tisdale township in the late Archean Abitibi greenstone belt. These are characterized by slightly sub-chondritic Al_2O_3/TiO_2 (13-17) ratios, CaO/Al_2O_3=1-1.3, flat REE patterns, and lower Ni contents relative to the Munro-type Al-undepleted komatiites. Both the Al-undepleted and depleted types of komatiites are represented in the Schreiber-Hemlo and

Dayohessarah greenstone belts.

Various models have been proposed for the petrogenesis of komatiites. Initially, it was suggested that komatiites formed by high degree (60-80 %) partial melting of mantle peridotite at relatively low pressure (Viljoen and Viljoen, 1969; Arndt, 1977). Subsequently, low degrees of partial melting at high pressures was advocated, based on the argument of density contrasts between komatiitic liquid and residual crystals (Beswick, 1982; Nisbet, 1982). On the basis of recent experimental studies it has been suggested that komatiites may form by low degrees of partial melting at high pressures (Herzberg and Ohtani, 1988; Miller et al., 1991; Herzberg, 1992). Miller et al. (1991) suggested that the ultimate sources of komatiitic magmas are solid diapirs originating from great depths in the mantle sources anomalously hotter by ~700 °C than the source of mid-ocean ridge basalts (MORB) that when adiabatically decompressed produce high-Mg liquids. Herzberg (1992) suggested that komatiites of Gorgona, Munro, and Barberton types may have formed by < 50 % melting at different depths, based on their major element compositions. From a consideration of fluid dynamics, Campbell et al. (1989) proposed that Archean komatiites may have formed by melting in the high temperature axis of a plume which originated from the lower mantle or mantle-core boundary, whereas basalts derived are from the plume head that had entrained upper mantle.

Given the spatial association of the two types of komatiites in the neighbouring Schreiber-Hemlo and Dayohessarah greenstone belts we interpret these to have been derived from a compositionally heterogeneous mantle plume that underwent dynamic partial melting, resulting in melt segregation at different depths (see Chapter 2; below). The formation of both Al-undepleted and -depleted komatiites in the same greenstone belts also has been documented in other Archean terranes, suggesting a common mantle plume for the two types of komatiites (see Jahn et al., 1982; Cattel and Arndt, 1987; Xie et al., 1993; Puchtel et al., 1993).

3-5-5. Komatiite Zr(Hf)/MREE fractionations

Xie et al. (1993) reported small to significantly positive Zr (Hf)/MREE fractionations, with Zr/Hf<36 in Munro type Al-undepleted komatiites, zero anomalies in Tisdale undepleted komatiites, but systematically negative anomalies with Zr/Hf~36 in Al-depleted in Boston township komatiites. Based on high pressure experimental partition coefficients (D) for HFSE and REE between liquids and different mantle phases, they interpreted the Zr(Hf) anomalies in Al-depleted komatiites as reflecting deep melt segregation in a plume with residual majorite garnet at depths of > 400 km. Zero anomalies in Tisdale komatiites were interpreted as melt segregation in the upper mantle, and for Munro type komatiites positive anomalies tentatively as Mg-silicate perovskite accumulation or residue in the source of mantle plume at depths > 700 km, with melt segregation at shallower levels. Lahaye et al. (1995) also found negative Zr anomalies in Al-depleted Barberton komatiites.

Komatiites in the Schreiber-Hemlo and White River-Dayohessarah greenstone belts show some similarities in Zr(Hf) anomalies to those reported by Xie et al. (1993), and some differences: zero to variably positive anomalies of Zr in Group I Al-undepleted komatiite, and zero to negative anomalies in Group II Al-depleted komatiites (Fig. 3.12). Notwithstanding uncertainties in the significance of the positive Zr anomalies, the results are here interpreted as segregation of ultramafic liquids at different depths from a heterogeneous mantle plume, with the Al-depleted komatiites representing deeper melting in the majorite garnet field.

3-5-6. Types of basalts

Areally extensive tracts of Mg-, and Fe-tholeiites with near-flat REE patterns are abundant in the Superior Province (Ludden et al., 1982; Fowler and Jensen, 1989; Thurston, 1990; Barrie et al., 1991). Compositionally similar volcanic sequences are also

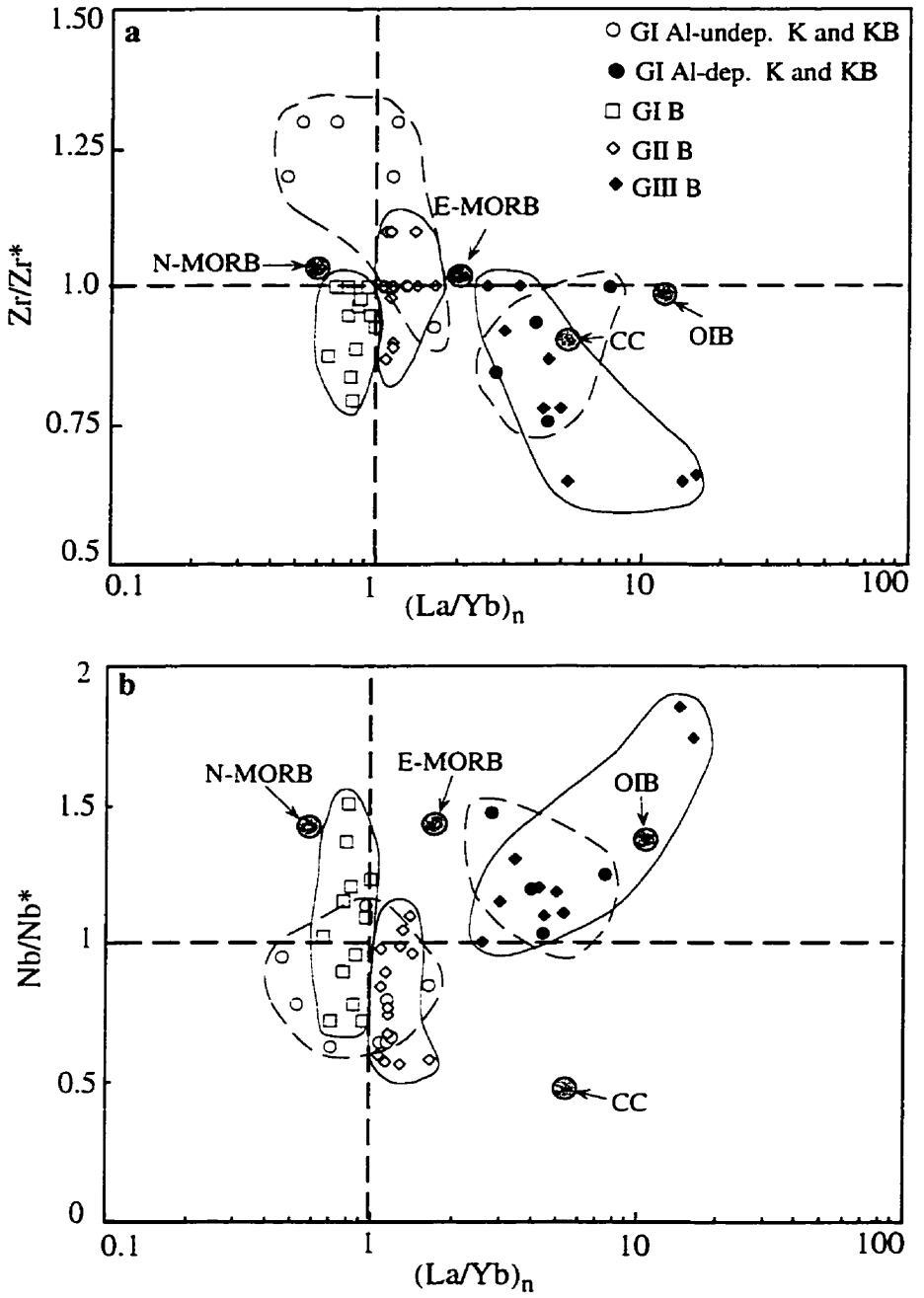

Figure 3.12. Zr/Zr* and Nb/Nb* vs La/Yb_n variation diagrams for komatiites, komatiitic basalts, and basalts. PM, N-MORB, E-MORB, and OIB values are from Sun and McDonough (1989). Bulk continental crust values from Taylor and McLennan (1985). Dashed lines are primitive mantle values. Abbreviations as in Fig. 3.2. CC: Continental crust.

common in greenstone belts of other Archean cratons including the Yilgarn (Redman and Keays, 1985; McCuaig et al., 1994), Wyoming (Snyder et al., 1990) and Limpopo (Rollinson and Lowry, 1992). Based on their areally extensive nature, the absence of crustal contamination, and the lack of volcanogenic sediments that are typically associated with arcs, Thurston (1990) interpreted these volcanic sequences in the Superior Province as intra-oceanic mafic plains. Groups I and II Mg-, to Fe-tholeiites of the Schreiber-Hemlo and Dayohessarah greenstone belts are of this affinity and geodynamic setting.

Floyd (1989) contrasted the morphology and lava composition of oceanic plateau basalts (OPB) with ocean island basalts (OIB). The former are areally extensive tholeiites with relatively subdued morphology, comprising large igneous provinces (LIPs), and are the oceanic counterparts of continental flood basalts. In contrast, ocean islands have topographically pronounced volcanic edifices, and generally include tholeiitic, transitional, and alkali basalts.

Several Phanerozoic oceanic plateaus are dominated by tholeiitic basalts with flat REE patterns, as in the Schreiber-Hemlo and Dayohessarah greenstone belts. Examples include the Nauru Basin, and Ontong-Java (Fig. 3.13; Floyd, 1989; Mahoney et al., 1993; Tejda et al., 1996). Basalts of other oceanic plateaus, such as Kerguelen, Broken Ridge, Naturaliste, east Mariana basin, North Atlantic, and Umu, have a spectrum of REE abundances from depleted to enriched (Castillo et al., 1994; Mahoney et al., 1995; Fretzdorff et al., 1996). In these plateau basalts there are also a spectrum of Nb anomalies. Mantle sources for basalts of the Wawa Subprovince and for OPB are discussed below.

Transitional to alkaline basalts with strongly fractionated REE are sparse in the Superior Province and other Archean terranes (McCuaig et al., 1994; Condie, 1994). The HREE fractionation, coupled with negative Zr and Hf anomalies, and generally high Fe contents in common with associated komatiites and komatiitic basalts, signify that Group

III basaltic liquids segregated deep in the mantle in the presence of residual majorite garnet, or may be shallower level fractionation products of Al-depleted komatiitic liquids. Group IIIb basalts are similar to Fe-tholeiites spatially associated with Al-depleted komatiites, and have pronounced REE fractionation and variable negative Zr anomalies similar to those of Boston township in the Abitibi greenstone belt (Xie et al., 1993).

3-5-7. Mantle sources

There are four principal mantle source components defined from Sr-Nd-Pb systematics. These are depleted MORB mantle (DMM) the major source of MORB, and three enriched components termed EM1, EM2, and HIMU (high $\mu=^{238}U/^{204}Pb$). EM1 and EM2 are likely oceanic crust and sediment processed through subduction zones and recycled into the mantle, whereas HIMU is dominantly recycled oceanic crust (see Hofmann and White, 1982; Zindler and Hart, 1986; Hofmann, 1997). Hart (1988) suggested a fifth mantle component termed FOZO, for focal zone in Sr-Nd-Pb isotope co-ordinates. In recent reviews relatively undepleted mantle has been proposed to reside either below D´ (670 km seismic discontinuity) [Hofmann, 1997], or in the transition zone, the C-component of Hanan and Graham (1996).

Phanerozoic and recent OPB and OIB form in plumes that incorporate one or more of the enriched components, and possibly less depleted mantle, mixed with DMM in the upper mantle (Floyd, 1989; Mahoney et al., 1993, 1995; Hemond et al., 1993; Fretzdorff et al. 1996). Saunders et al. (1988) developed a trace element model for oceanic basalts. In Ce/Nb versus Th/Nb co-ordinates MORB forms an array between DMM and HIMU, and OIB plot between the HIMU end members, DMM, and a component enriched in Th relative to Nb (Fig. 3.13). They defined a residual slab component (RSC) with positive Nb anomalies contributing significantly to HIMU-OIB's and a slab-derived component (SDC) having negative Nb anomalies, corresponding to the high Th/Nb component. This

approach elegantly accounts for the variations in Th-Nb-LREE found in the Wawa volcanic sequences (Fig. 3.13).

Major and trace element characteristics of komatiites and basalts in the late Archean Schreiber-Hemlo and Dayohessarah greenstone belts are consistent with geochemically diverse mantle compositions (Appendices 3.2, 3.3). Based on primitive mantle normalized diagrams, Th-Nb-La systematics, and HFSE/HFSE inter-element relations, three distinctive mantle source components can be identified within the volcanic sequences of these belts: (1) a depleted mantle component represented by LREE depleted Al-undepleted komatiites and Fe-, and Mg-tholeiites (Group I); (2) a trace element undepleted mantle component corresponding to some of the Al-undepleted komatiites and Group II Fe-, and Mg tholeiites, with flat REE patterns; and (3) an enriched mantle component that is represented by REE enriched Al-depleted komatiites, komatiitic basalts and transitional to alkaline basalts (Group III).

Negative Nb anomalies in Al-undepleted komatiites, and Groups Ib and IIb basalts may have resulted from the mixture of SDC and depleted mantle source components (Fig. 13; cf. Saunders et al., 1988). Positive Nb anomalies in G Ic basalts, and G III komatiites and associated basalts likely stem from an RSC. There is probably a continuous variation between the three components given that the total population plots on mixing lines between N-MORB and OIB in Zr/Nb versus Y/Nb and Zr/Nb versus Ce/Y co-ordinates, and the Ta/Th-Hf/Th and Tb/Th ternary diagram. Phanerozoic OPB's also plot on these mixing lines, and between DDM. RSC (HIMU), and SDC on Ce/Nb versus Th/Nb diagram (Figs. 3.13-3.15; cf. Saunders et al., 1988; Floyd, 1989; Joron and Treuil, 1989).

We stress a number of points: (1) a depleted mantle component is required by the prevalent 2.7 Ga ε-Nd values of +1 to +4 for the sub-Superior mantle (Shirey, 1990; see

Figure 3.13. Ce/Nb vs Th/Nb variation diagrams (cf. Saunders et al., 1988). Fields for Umu Volcanic field (UVF), Nauru Basin oceanic plateau (NOBP), Broken Ridge oceanic plateau (BROP), Ontong Java oceanic plateau (OJOP), and Iceland plume are from Fretzdorff et al. (1996), Floyd (1989), Mahoney et al. (1995), and Hemond et al. (1993), respectively. Solid lines represent the simple mixing relations between depleted mantle [DMM], slab residue component [SRC] and slab derived component [SDC]. Dashed line indicate simple melt extraction path and origin of DDM, SDC, and RSC (modified after Saunders et al., 1988). PM, N-MORB, E-MORB and OIB values from Sun and McDonough (1989). Bulk continental crust (CC) values after Taylor and McLennan (1985).

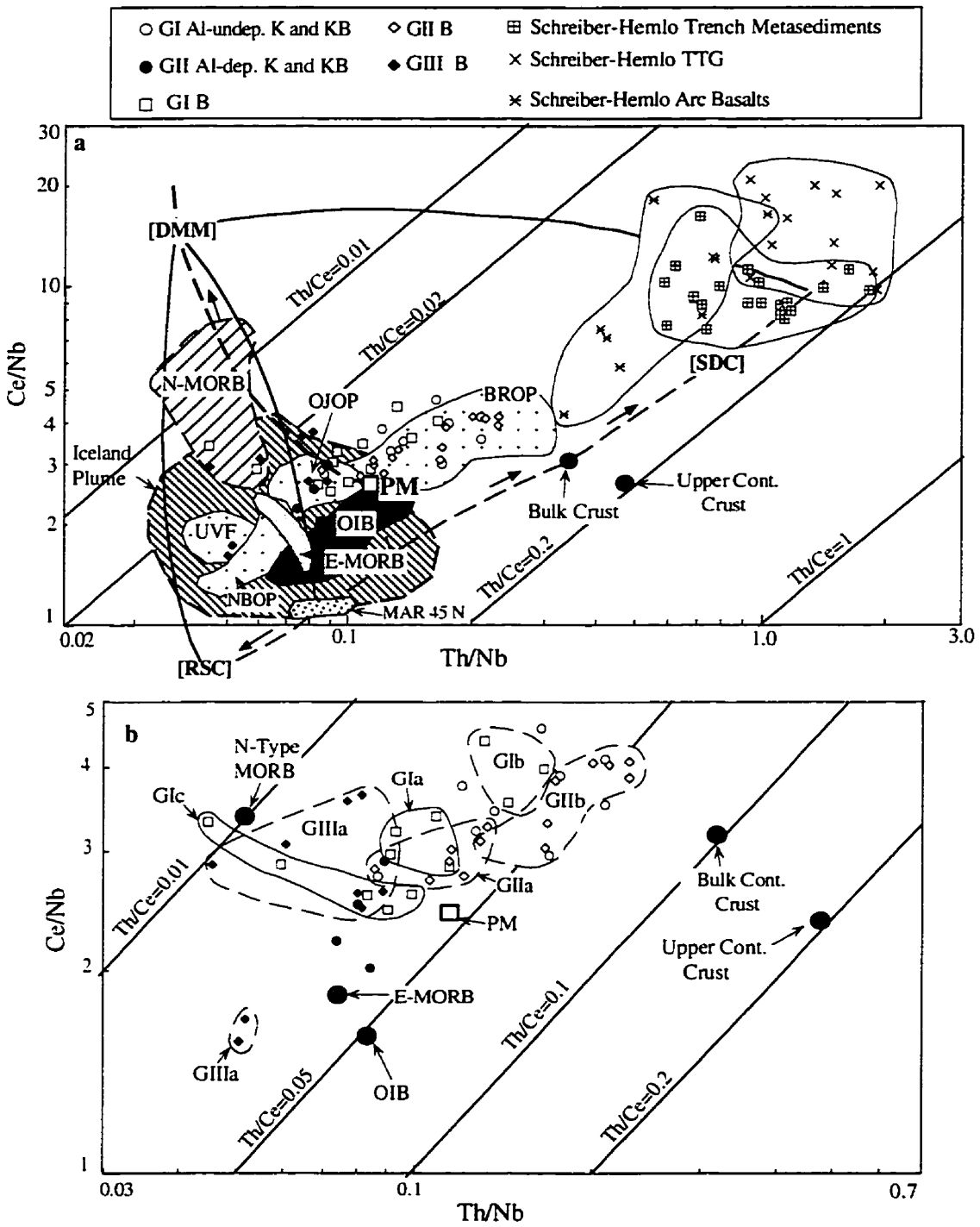
○ GI Al-undep. K and KB
◇ GII B
⊞ Schreiber-Hemlo Trench Metasediments
● GII Al-dep. K and KB
◆ GIII B
× Schreiber-Hemlo TTG
□ GI B
⁎ Schreiber-Hemlo Arc Basalts
a
[DMM]
Th/Ce=0.01
Th/Ce=0.02
N-MORB
OJOP
BROP
[SDC]
Iceland Plume
PM
OIB
UVF
E-MORB
NBOP
MAR 45 N
Bulk Crust
Upper Cont. Crust
Th/Ce=0.2
Th/Ce=1
[RSC]
Ce/Nb
Th/Nb
30
20
10
5
4
3
2
1
0.02
0.1
1.0
3.0
b
N-Type MORB
GIc
GIa
GIb
GIIb
GIIIa
GIIa
PM
E-MORB
OIB
Bulk Cont. Crust
Upper Cont. Crust
Th/Ce=0.01
Th/Ce=0.05
Th/Ce=0.1
Th/Ce=0.2
Ce/Nb
Th/Nb
5
4
3
2
1
0.03
0.1
0.7

below); (2) Shirey and Hanson (1986) have presented clear trace element and isotopic evidence for crustal recycling in the Rainy Lake area of the Superior Province; (3) trace element data plot on mixing lines between MORB, RSC (HIMU), and SDC, as for modern oceanic plateau basalts (Figs. 3.12-3.15); and (4) to the authors knowledge this is only the second time a HIMU-like signature has been identified in Archean basalts and komatiites (cf. McDonough and Ireland, 1993).

Notwithstanding similar LREE depleted patterns, Group I komatiites and tholeiites have subtly but consistently different Zr/REE relations, suggesting either different mantle components or residual minerals for these ultramafic and mafic lavas, or a combination of the two. Lower La/Sm_n ratios in the komatiites (0.54-0.60 versus 0.7-0.9) are consistent with a more depleted mantle source than basalts (Fig. 3.5; Appendices 3.2, 3.3). The spectrum of LREE fractionations in the Al-undepleted komatiites and komatiitic basalts is greater than in counterparts at Pyke Hill where no komatiitic basalts are present (La/Sm_n=0.54-1.2 versus 0.4-0.65; Arndt and Nesbitt, 1982; Xie et al., 1993). The range could reflect a number of possible processes including more clinopyroxene fractionation in the komatiitic basalts, mixing with GIb basalts, or dynamic melting (cf. Elliot, 1991; Arndt et al., 1997). The variably LREE depleted character of Groups Ia and Ic basalts is not interpreted in terms of an Archean equivalent to mid ocean ridge environments. Tholeiitic basalts and picrites with incompatible element depletion are known from Cretaceous plateaus in the western Pacific and Gorgona (Castillo et al., 1994; Kerr et al., 1996). Specifically Hemond et al. (1993) argue that the strongly LREE depleted picrites in Iceland are a distinct component of the Iceland plume, rather than entrained North Atlantic MORB.

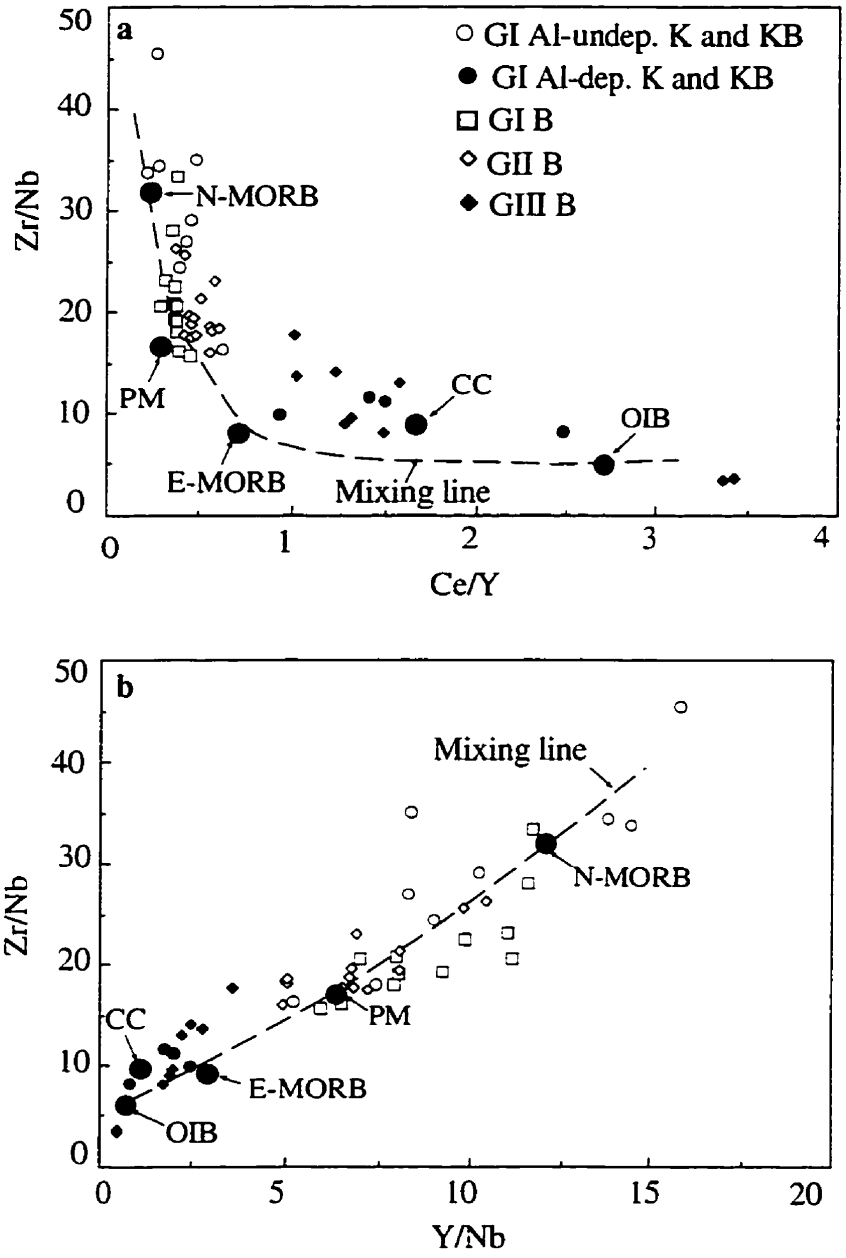

Figure 3.14. (a) Zr/Nb vs Ce/Y and (b) Zr/Nb vs Y/Nb variation diagrams for komatiites, komatiitic basalts, and basalts. Abbreviations as in Fig. 3.13.

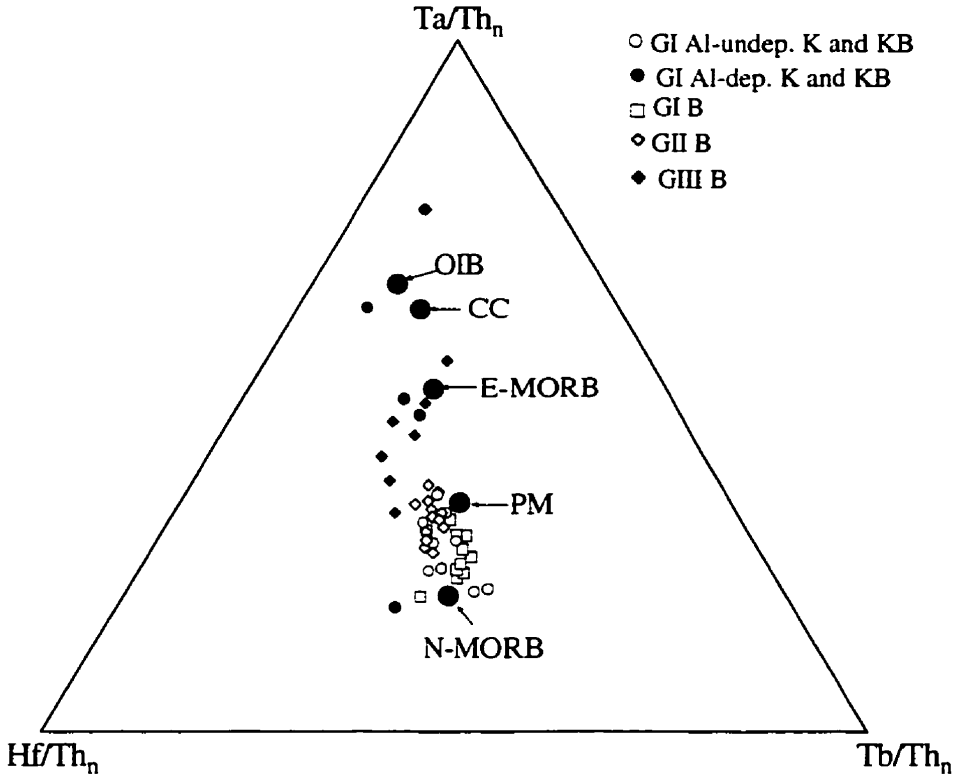

Figure 3.15. Ta/Th$_n$-Hf/Th$_n$-Tb/Th$_n$ ternary variation diagram for komatiites komatiitic basalts, and basalts. Abbreviations as in Figure 3.13 (after Joron and Treuil, 1989).

3-5-8. Nb anomalies

Negative Nb anomalies in Groups I Al-undepleted komatiites, and Ib and IIb tholeiitic basalts may either reflect mantle source characteristics, or have resulted from secondary petrogenetic processes. Bach et al. (1996) described MORB like basalts from the northern Chile ridge with unusual depletion of Nb and Ta relative to La. They rule out re-equilibration reactions between basaltic liquids and olivine, orthopyroxene and spinel, as proposed by Kelemen et al. (1993) for arc basalts, because Nb depletion would be accompanied by co-depletion of Ti, Zr, and Hf, but this is not observed. Nb/La fractionation could result from accessory minerals such as rutile, titanite and amphibole, but these are unlikely to be present in depleted MORB mantle or the mantle source of Groups Ib and IIb basalts. Bach et al. (1996) also ruled out Nb/La fractionation by dynamic melting as this would require high degrees of melting, which is inconsistent with the major element composition of the North Chile Ridge basalts. They attributed the high La/Nb and La/Ta ratios to a previous melt extraction at very low degree partial melting. All of the processes discussed above generate basalts with a significant range of La/Nb ratios, and in the case of the North Chile Ridge basalts no fractionation of Nb and Th. In contrast Groups Ib and IIb basalts are characterized by fractionated Nb from Th and La, and coherent patterns (Figs. 3.7,3.8; Table 3.2). Consequently, it is likely that the Nb depletion is a property of the mantle source.

Klein and Karsten (1995) and Karsten et al. (1996) reported Nb-depleted basalts, with respect to both Th and La, from the southern Chile Ridge. They attributed this to the contamination of the MORB mantle source by slab-derived components (SDC=Nb/Nb*<1) through subduction zone processes. The depletion of Nb(Ta) with respect to Th and La in Group Ib and IIb basalts are comparable to those of the southern Chile Ridge. Collectively, the moderate to significant negative Nb anomalies both in Fe-, and Mg-tholeiites may indicate the recycling of a slab-derived component (SDC) into the

mantle (Fig. 3.13; cf. Saunders et al., 1988; Klein and Karsten, 1995; Karsten et al., 1996).

Fractionated patterns in Group II Al-depleted komatiites and transitional to alkaline basalts may signify a number of processes. Majorite garnet accounts for some of the fractionation of REE, and negative Zr(Hf) anomalies (cf. Xie et al., 1993). The presence of minor to significant positive Nb anomalies in Group II komatiites and IIIa basalts suggests that the mantle source was enriched in Nb with respect to Th and La (Appendices 3.2, 3.3). If the trace element systematics of these volcanic rocks have similar significance as those of modern HIMU-OIB, they may signify a stored and reactivated residual slab component (RSC=Nb/Nb*>1), represented by oceanic crust processed through a subduction zone and incorporated into mantle plume, with deep melt segregation (see Hofmann and White, 1982; Sun and McDonough, 1989; Weaver, 1991; McDonough, 1991).

Because of their similar partition coefficients, Nb, La, and Th are less likely to be fractionated from one another during the genesis of oceanic lavas (Sun and McDonough, 1989). Accordingly, the presence of both Nb-depleted and -enriched komatiites and basalts in the Schreiber-Hemlo and White River-Dayohessarah greenstone belts may be attributed to recycling of respectively SDC and RSC deep into the mantle. The subduction of arc-derived Archean siliciclastic sediments also may have played an important role in the generation of negative Nb anomalies (Fig. 3.13a). Lead and Sr isotope data are, however, required to confirm this interpretation. According to Jochum et al. (1991) the fractionation of these elements may be a result of retention of Nb within an unknown residual mineral (s) deep in the mantle; this could account for negative but not positive Nb anomalies.

In summary, it has been demonstrated that the mantle plumes which produced late Cretaceous to modern OPB and OIB (e.g., Ontong Java; Kerguelen, Hikurangi, Hawaii,

and Iceland etc) are characterized by diverse geochemical compositions and multiple mantle components, including those characterized by negative, zero, and positive Nb anomalies (Salters et al., 1992; Wilson, 1993; Mahoney et al., 1993; Hemond et al., 1993; Kerr et al., 1996; Karsten et al., 1996). Like the Schreiber-Hemlo and White River-Dayohessarah greenstone belts, other Archean greenstone belts also have komatiites and associated tholeiitic basalts, with a wide range of trace element characteristics, suggesting that Archean mantle plumes in general may also have contained several mantle source components (Jahn et al., 1982; Condie, 1990; Jochum et al., 1991; Puchtel et al., 1993; Camire et al., 1993; Fan and Kerrich, 1997).

3-5-9. Dynamic melting

Some of the compositional heterogeneity in modern plume lavas has been attributed to dynamic melting processes in a melt column, as well as mixing between plume and upper mantle (Elliot et al. 1991; Campbell and Griffiths, 1992). Based on major and trace element data obtained from modern Iceland lavas, Elliot et al. (1991) suggested that dynamic melting at deeper levels in a melt column of a mantle plume results in higher FeO contents and lower MgO/FeO ratios than at shallower levels. Similarly, for the diverse Gorgona picrites, komatiites, and basalts Arndt et al. (1997) interpreted the most depleted lavas as derived from deepest melting of the most refractory source, whereas less depleted lavas reflect pooling of liquids derived from throughout the melting column. This processes could account for the spectrum of trace element patterns in Al-undepleted komatiites and komatiitic basalts, and some of the compositional variation in the Mg-, and Fe-tholeiites (Fig. 3.16). Nb anomalies ratios do not correlate with MgO/FeO ratios, suggesting that dynamic melting did not control the Th-Nb-La systematics (Fig. 3.16).

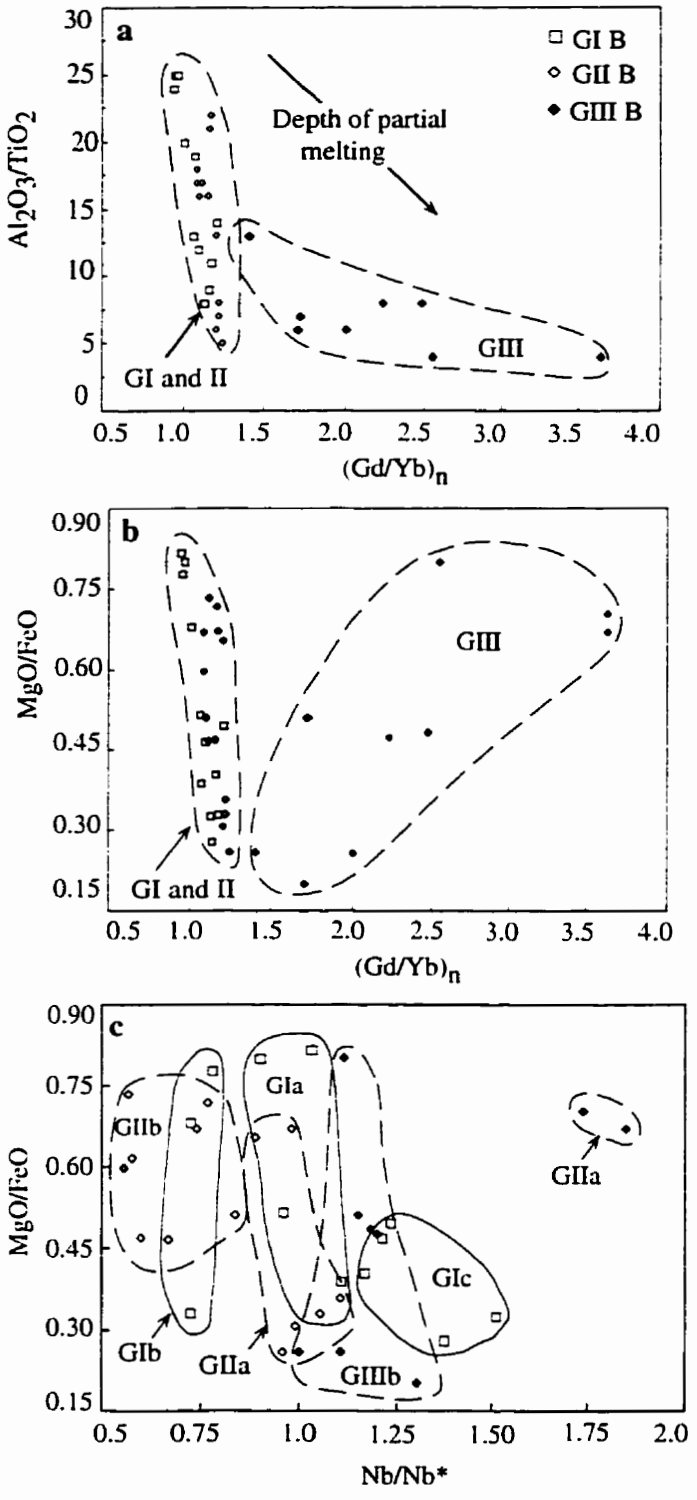

Figure 3.16. Al_2O_3/TiO_2 and MgO/FeO vs Gd/Yb_n and MgO/FeO vs Nb/Nb* variation diagrams for Group I, II, and III basalts.

3-5-10. The Nd-isotope paradox

Archean ultramafic and mafic lavas have positive ε-Nd values mostly in the range of +1 to +4 requiring mantle sources commensurate with long term depletion of incompatible elements. Several authors have pointed out that these depleted mantle sources have been transient, because otherwise the source of the 3.4 Ga and 2.7 G basalts and komatiites with ε-Nd=+2 to +5 would have evolved to have extremely positive values but this is not seen (Jahn et al., 1982; Smith and Ludden, 1989; Shirey, 1990; McCulloch and Bennett, 1992; Wilson, 1993; Blichert-Toft and Albarède, 1994). In the Superior Province Mg-, to Fe-tholeiites with near-flat REE patterns have ε-Nd values averaging +2 (Barrie et al., 1991; Blichert-Toft-Albarède, 1994; Hollings et al., 1996; Xie and Kerrich, 1996). This requires a two stage processes: a long term depleted source with short term enrichment. Erasing the depleted trace element signatures requires recycling of enriched components into the mantle, but clear evidence of this has been lacking. This study suggests that the recycled SDC identified is the source of trace element enrichment.

3-6. Conclusions and implications

High precision ICP-MS trace element data obtained from komatiitic to basaltic volcanic sequences of the late Archean Schreiber-Hemlo and White River-Dayohessarah greenstone belts of the Superior Province reveal diverse geochemical characteristics for these volcanic sequences. Two principal types of komatiite, Al-undepleted and Al-depleted, exist. Group I komatiites and komatiitic basalts are of the Al-undepleted type with variably depleted to flat LREE patterns, and zero to moderately positive Zr(Hf) and negative to minor positive Nb anomalies. Group II Al-undepleted komatiites are characterized by LREE enriched patterns, and zero to moderately negative Zr(Hf) but positive Nb anomalies.

Basalts range from Mg-, and -Fe-tholeiites, to transitional, and alkaline in composition. They are divided into three major groups based on REE fractionation (La/Sm_n=0.7-0.9; La/Sm_n=0.95-1.25; La/Sm_n=1.4-2.7). In each major group two or three sub-populations may be identified based on Th-Nb-La inter-element relations (Appendix 3.3). Group Ia and IIa basalts are characterized by smooth trace element patterns. Groups Ib and IIb basalts possess negative, whereas Groups Ic and IIIa, b basalts have positive Nb anomalies. The enrichment of Nb with respect to La and Th, coupled with positively fractionated LREE patterns, in Group IIIa alkaline basalts is comparable to modern HIMU-type OIB's. Group IIIb transitional basalts may have been derived from the mixture of depleted tholeiites and enriched alkaline magmas.

Field relations suggest that the two major groups of komatiites and three major groups of basalts occur along the same tectonic zone, and have been laterally displaced by strike-slip faults (Polat et al., 1996a; 1998a). Accordingly, these chemically diverse but stratigraphically related ultramafic and mafic volcanic rocks are likely to be the fragments of an Archean oceanic plateau(s) or ocean island(s) derived from a mantle plume(s). The diverse geochemical features of komatiites, komatiitic basalts, and tholeiitic to alkaline basalts cannot be explained by alteration, crustal contamination, fractional crystallization or partial melting of a homogenous mantle plume. Rather, trace element systematics relations suggest that this mantle plume was chemically heterogenous, and contained trace element depleted, undepleted, and enriched source components. The presence of positive and negative Nb anomalies both in komatiites and basalts may have resulted from the incorporation of residual slab (RSC) and slab-derived (SDC) components, respectively, into the plume source through subduction zone processes (Fig. 3.17; cf. Saunders et al., 1988). Dynamic partial melting and magma mixing processes can account for some compositional variations in Al-undepleted komatiites, and the spectrum from Mg-, to Fe-tholeiites. These observations suggest that Archean subduction processes may have played

an important role in the generation of chemically and isotopically heterogeneous mantle (Fig. 3.17; cf. Silver and Carlson, 1988).

Collectively, the coexistence of both Al-depleted and Al-undepleted komatiites and LREE depleted to enriched Mg-, to Fe-tholeiites, with negative to positive Nb anomalies, at similar tectono-stratigraphic horizons of the volcanic sequences of the late Archean Schreiber-Hemlo and Dayohessarah greenstone belts may have resulted from a multicomponent, heterogeneous mantle plume, with melt segregations at different depths. The diverse geochemical characteristics of the belts are comparable to those of other Archean greenstone belts, and of modern oceanic plateaus, and ocean islands derived from large mantle plumes.

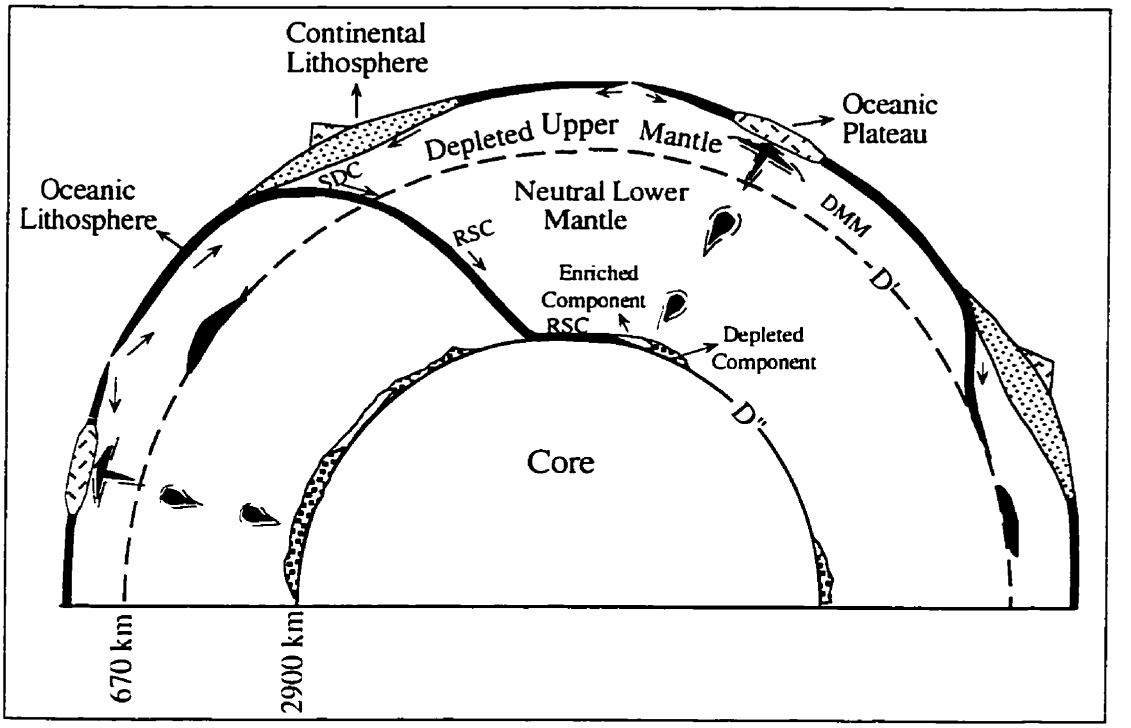

Figure 3.17. A simplified cartoon model for the origin of komatiites and basalts in the Schreiber-Hemlo and White River-Dayohessarah greenstone belts, involving a heterogeneous mantle plume with enriched (SDC) and depleted (RSC) components, and possibly a neutral component, mixing with depleted upper mantle. SDC: Subduction-derived component, RSC: Residual slab component.

CHAPTER 4. PETROGENESIS OF HFSE-DEPLETED THOLEIITIC TO CALC-ALKALINE MAFIC TO FELSIC VOLCANIC ROCKS

4-1. Introduction

Subduction zones are the locations along which two lithospheric plates move towards each other. As the plates converge, the one with a higher density tends to sink beneath the lighter plate, forming a subduction (or Benioff) zone, and the leading edge of the overriding plate becomes a paired forearc and magmatic arc; modern examples are the Andean, Sumatran, Aleutian, and Japanese arcs. Given its higher density oceanic lithosphere subducts underneath continental lithosphere, forming a continental magmatic arc, such as the Andean margin of south America. If two oceanic plates converge, the older, cooler oceanic plate will sink beneath the younger one, generating oceanic island arcs, such as the Marianas, the Caribbean, and the South Sandwich arcs.

Subduction zone are major sites of lithospheric recycling, crustal accretion, low- to high-grade metamorphism, continental growth, and arc magmatism (see Windley, 1995; Condie, 1997a for reviews). The geochemical characteristics of magmatism in a subduction zone are controlled mainly by: (1) the age of the subducting oceanic plate, e.g. young versus old; (2) the nature of overriding plate, e.g.continental versus oceanic; (3) the presence or absence of sediment; (4) the rate, e.g. slow versus rapid and angle of subduction, e.g.shallow versus steep; and (5) the presence or absence of a backarc basin (Wilson, 1989).

Magmatism at modern subduction zones ranges from picritic (Mg#=70-60) through

felsic (Mg#=40-25) in composition, and may generate tholeiitic, through calc-alkaline, to alkaline magma series. Tholeiitic magmatism is dominant between the forearc basin and arc-axis; calc-alkaline magmatism occurs mainly in the central region of the arc; late alkaline igneous rocks tend to occur between the arc axis and backarc region (see Wilson, 1989 for a review).

The depletion of HFSE (Nb, Ta, Hf, Zr, and Ti) relative to LILE (Rb, Ba, Th, U) and LREE is one of the geochemical characteristics that separates subduction zone-derived magmas from mid-ocean ridge (e.g., MORB) and ocean island magmas (e.g., OIB) [Pearce, 1983; Saunders et al., 1991; Hawkesworth et al. 1993; Pearce and Peate, 1995 and references therein]. Slab dehydration and/or slab melting lead to a complex series of fractionations of LILE, REE and HFSE in subduction zone. During dehydration of subducting oceanic crust, LILE and LREE, are lost in aqueous fluids, with preferential solubility of Cs > Rb > K, and of LILE > LREE and LREE > Nb (Ta) and of MREE > Ti. Aqueous fluids and/or melts advect into the subarc mantle, and hence into arc magmas (Kosgio et al., 1997).

In contrast, HFSE and HREE are relatively insoluble in fluids or melts, and are preferentially retained in the dehydrated slab (Saunders et al., 1991; Hawkesworth et al., 1993; McCulloch and Gamble, 1991; Arculus, 1994). The differential solubilities of the trace elements explains not only the LILE/LREE and LREE/HFSE systematics of arc magmas, but also the relative depletion of Cs and Rb over K, and of LILE over LREE, coupled with the relative enrichment of Nb (Ta) over LREE, and Ti over MREE in the dehydrated slab. The complementary geochemical signatures of recycled subducted oceanic lithosphere that is ultimately reflected in the distinctive geochemistry of HIMU-OIB (McDonough, 1991; Kosgio et al., 1997).

It is argued that subduction zone magmatism in the Archean was largely dominated by slab melting as a consequence of elevated mantle temperatures, and subduction of

younger, hotter lithospheric slabs (Drummond and Defant, 1990). In contrast, lower mantle temperatures in the post-Archean resulted in subduction of older, colder lithospheric plates, which mainly underwent dehydration rather than partial melting, suggesting that the metasomatized mantle wedge is the major source of post-Archean subduction zone magmas (Saunders et al., 1991; Pearce and Peate, 1995), albeit exceptions such as the young hot Farralon plate, and associated Peninsula Range Batholith (Gormet and Silver, 1986).

The depletion of HFSE relative to Th and LREE in Archean volcanic rocks, as in their Phanerozoic counterparts, has been interpreted to be the product of arc magmatism (Condie, 1981, 1994, 1997a; Laflèche et al., 1992; Thurston, 1994). These similarities between Phanerozoic and Archean volcanic rocks have lead some geologists to propose similar crustal growth models for the two eons (Condie, 1981; Taylor and McLennan, 1985, 1995). In this chapter, the geochemical characteristics of mafic to felsic sequences (see Thurston and Chievers, 1990; Thurston, 1994 for a review) from the Schreiber-Hemlo and White River-Dayohessarah greenstone belts are discussed in order to better understand the geodynamic evolution of these belts specifically, and the petrogensis of Archean arc magmatism in general, with emphasis on mantle source composition and partial melting processes.

The Schreiber-Hemlo greenstone belt is divided into three lithotectonic assemblages by Williams et al. (1991); the Schreiber, Hemlo-Black River, and Heron Bay. The Schreiber and Hemlo-Black River assemblages are separated by the Proterozoic Coldwell alkali complex (Fig. 4.1). The Hemlo-Black River and Heron Bay assemblages are located to the north and south of the right lateral Lake Superior-Hemlo fault zone, respectively. In comparison to the Schreiber-Hemlo belt, the White River-Dayohessarah greenstone belt is characterized by areally less extensive supracrustal rocks, and has not been subdivided into distinctive lithotectonic assemblages.

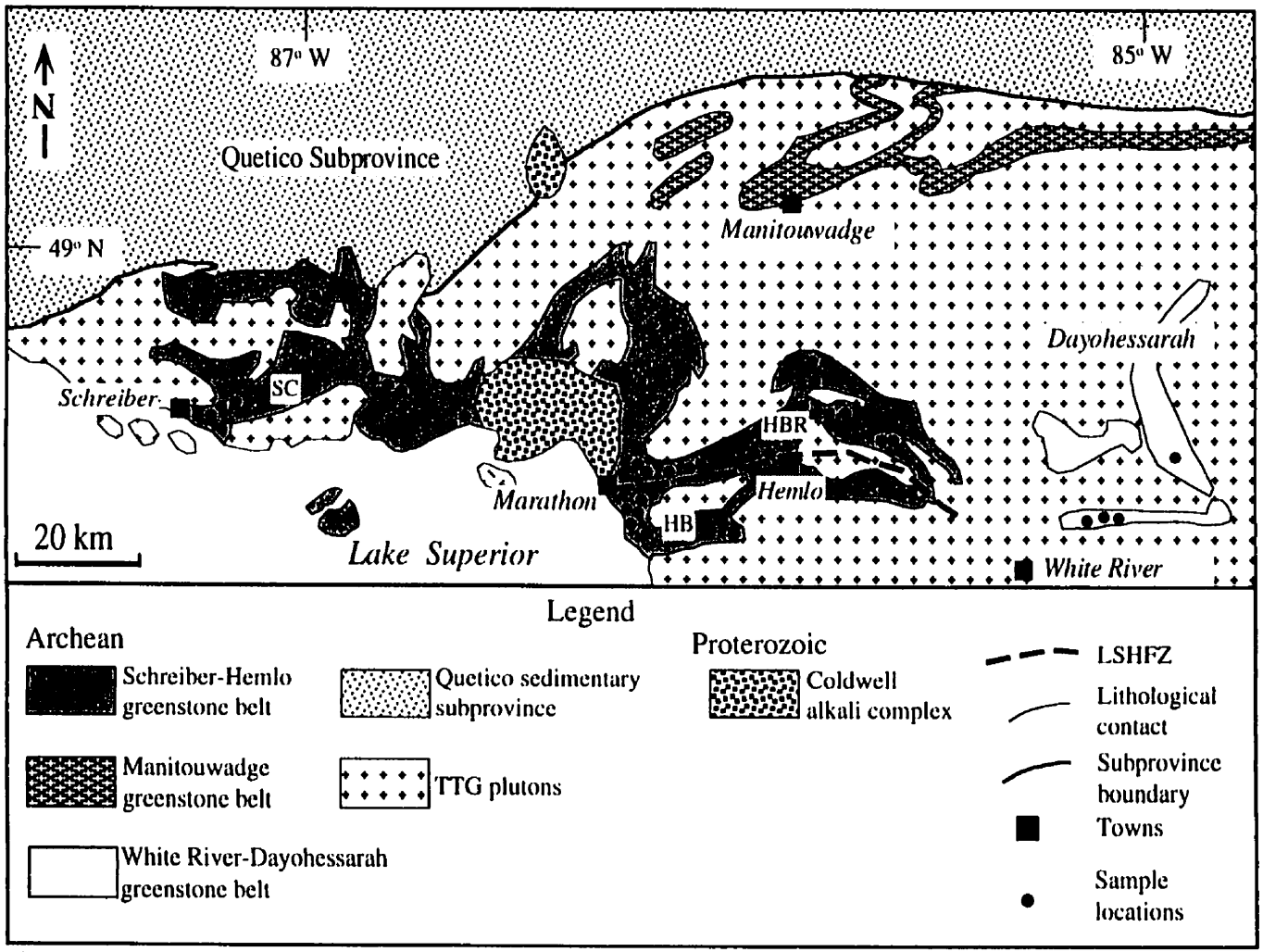

Figure 4.1. Simplified geological map of the Schreiber-Hemlo and White River Dayohessarah greenstone belts. Lithological boundaries may also be tectonic (modified after Williams et al., 1991). TTG: Tonalite trondhjemite-granodiorite; SC: Schreiber assemblage, HBR: Hemlo-Black River assemblage, HB: Heron Bay assemblage.

Based on major and trace element abundances mafic to felsic, arc-related volcanic rocks of the Schreiber-Hemlo and White River Dayohessarah greenstone belts are divided into three major groups: (1) mafic to intermediate tholeiitic flows (Fig. 4.2; Appendices 4.1, 4.2), (2) mafic to intermediate calc-alkaline flows (Fig. 4.2; Appendices 4.3-4.5), and (3) felsic calc-alkaline flows (Fig. 4.9; Appendices 4.6-4.9). Tholeiitic flows are characterized by higher FeO*/MgO ratios than calc-alkaline counterparts (Fig. 4.2; see Miyashiro, 1974). In the following sections the geochemical characteristics of each of the principal rock types will be discussed for the lithotectonic assemblages of the Schreiber-Hemlo and White River-Dayohessarah greenstone belts. Following the presentation of geochemical data, geodynamic characteristics of each magma type will be addressed.

4-2. Geochemical results of tholeiitic volcanic rocks

Mafic to intermediate tholeiitic volcanic rocks of the Schreiber-Hemlo and White River-Dayohessarah greenstone belts are represented by a suite of 17 samples (Figs. 4.1, 4.2; Appendices 4.1 and 4.2). The Schreiber assemblage has the largest population (nine samples), whereas only one sample was collected from the White River-Dayohessarah belt. The Hemlo-Black River and Heron Bay assemblages are represented by two and five samples, respectively. The principal geochemical characteristics of these rocks are as follows:

4-2-1. Schreiber assemblage

Tholeiitic suite from the Schreiber assemblage has ranges of SiO_2=50 to 64 wt.%, MgO=1.1 to 5.3 wt.%, Fe_2O_3= 4.5 to 18 wt.%, Cr=6 to 137 ppm, Ni=2 to 60 ppm, and Mg#=30 to 40 (Table 4.1; Appendix 4.1) Compositionally, they are moderately evolved basalts and andesites. They are characterized by the enrichment of highly incompatible

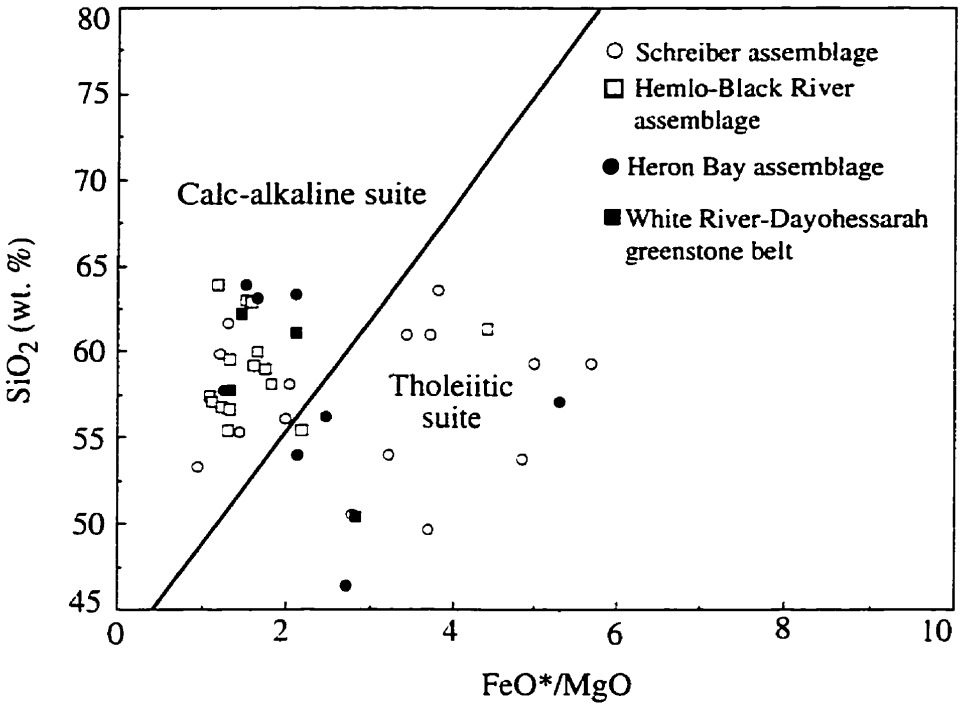

Figure 4.2. SiO_2 vs FeO*/MgO calc-alkaline/tholeiitic discrimination diagram for mafic to intermediate volcanic sequences of the Schreiber-Hemlo and White River-Dayohessarah greenstone belts (Fields after Miyashiro, 1974).

Table 4.1. Summary of significant compositional values and inter-element ratios of mafic to intermediate tholeiitic volcanic rocks of the Schreiber-Hemlo and White River-Dayohessarah greenstone belts.

	Schreiber Assemblage	Hemlo-Black River Assemblage	Heron Bay Assemblage	White River-Dayohessarah Belt
SiO_2 (wt.%)	50-64	56-61	46-63	50.5
MgO	1.1-5.3	1.7-3.8	2.4-5.5	5.3
TiO_2	0.6-2.4	0.5-0.9	0.6-1.1	1.4
Fe_2O_3	4.5-18	8.3-9	5.6-16.4	16.6
Cr (ppm)	6-137	67-148	9-362	217
Ni	2-60	81-90	4-64	32
Th	1.0-8.8	1.4-2.1	0.8-3.7	2.4
La	8.3-44	15.3-16	7.2-45	13
Nb	3.0-19	3.9-7.4	3.2-7	7.3
Zr	99-281	88-145	69-165	116
Y	10-52	10-20	17-31	31
$(La/Yb)_{cn}$	1.9-19.7	5.6-14	2.4-23	2.6
$(La/Sm)_{cn}$	1.5-4.7	2.8-3.3	1.7-3.8	2.1
$(Gd/Yb)_{cn}$	1.3-2.9	1.7-2.5	1.1-3.3	1.2
Al_2O_3/TiO_2	7-28	18-29	14-28	10
Zr/Hf	37-43	37	29-38	36
Th/Nb	0.15-0.50	0.20-0.54	0.2-1.0	0.3
Th/La	0.06-0.13	0.10-0.13	0.10-0.15	0.2
Ti/Zr	21-98	37-39	21-101	69
Zr/Y	3.9-14	7.2-9.3	3.3-9.5	3.8
Nb/Nb*	0.2-0.6	0.2-0.4	0.1-0.5	0.5
Eu/Eu*	0.9-1.1	0.8-0.9	0.8-1.0	0.9
Zr/Zr*	0.6-1.5	0.8-1.2	0.6-1.1	1.0
Hf/Hf*	0.9-1.5	0.8-1.1	0.5-1.3	1.0
Ti/Ti*	0.2-1.1	0.5-0.6	0.2-0.9	0.7

elements such as Th and LREE with respect to moderately incompatible (MREE) and the compatible elements HREE, Y, Cr and Ni (Figs. 4.3-4.5; Table 4.1).

In addition, they have the following compositional features: (1) moderate to large positive fractionation of REE (La/Sm_n=1.5-4.7, Gd/Yb_n=1.3-3, and La/Yb_n=2-20); (2) commensurately high Zr/Y (4-14) ratios; (3) large negative anomalies of Nb with respect to neighbouring elements (Nb/Nb*=0.2-0.6); (4) Ti anomalies are negative to minor positive (Ti/Ti*=0.2-1.1); (5) variably negative to positive anomalies of Zr and Hf (Zr/Zr*=0.6-1.5, Hf/Hf*=0.9-1.5); (6) Eu anomalies are minor (Eu/Eu*=0.9-0.1); and (7) Zr/Hf (37-43) and Nb/Ta (13-22) ratios vary around the primitive mantle values of 36 and 17, respectively (Figs. 4.3-4.6; see Sun and McDonough, 1989). The geological significance of these ratios is given in discussions.

4-2-2. Hemlo-Black River assemblage

Tholeiites of the Hemlo-Black River assemblage are characterized by SiO_2=56-61 wt.%, MgO=1.7-3.8 wt.%, Fe_2O_3=8.3-9.1 wt.%, TiO_2=0.5-0.9 wt.%, Cr=67-148 ppm, and Ni=81-90 ppm contents. There is a total range of Mg# from 52 to 50. These are compositionally basaltic-andesites and andesites (Table 4.1; Appendix 4.2).

On a primitive mantle-normalized diagram, these tholeiites are characterized by: (1) positively fractionated REE patterns (La/Sm_n=2.8-3.3, Gd/Yb_n=1.7-2.5, and La/Yb_n=5.6-14); (2) commensurately high Zr/Y; (3) pronounced negative Nb and Ti anomalies (Nb/Nb*=0.2-0.4, Ti/Ti*=0.5-0.6); (4) minor negative Eu anomalies (Eu/Eu*=0.8-0.9); (5) variably negative to positive Zr and Hf anomalies (Zr/Zr*=0.8-1.2, Hf/Hf*=0.8-1.1); (6) ratios of Zr/Hf (37) and Nb/Ta (15-20) in the range of primitive mantle; and (7) but low Nb/Yb and Sc/Lu ratios (Figs. 4.3-4.6). Collectively, these

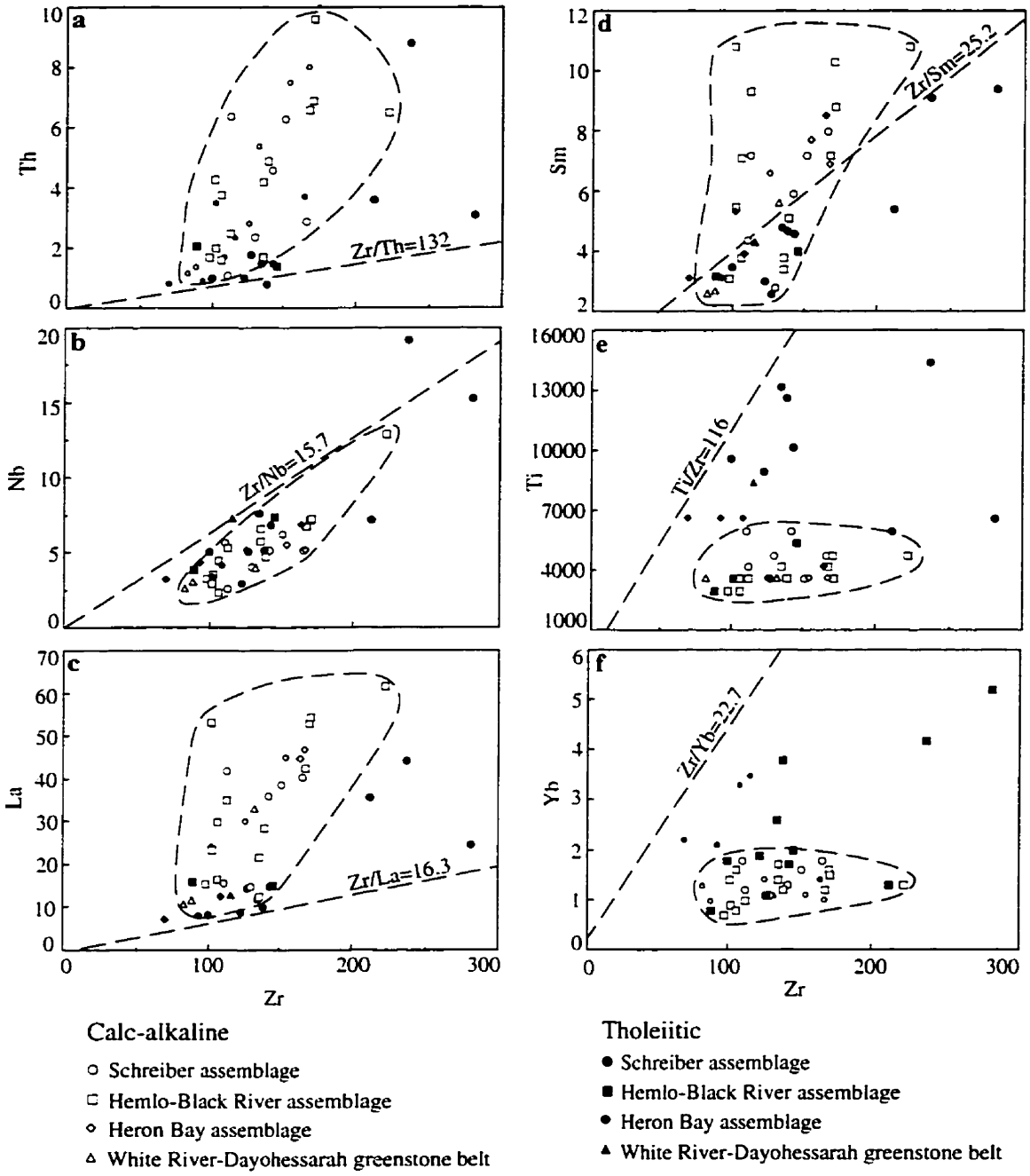

Figure 4.3. Zr (ppm) vs specified element (ppm) variation diagrams for mafic-intermediate tholeiitic and calc-alkaline volcanic rocks. Dashed lines are primitive mantle ratios. Primitive mantle values are from Sun and McDonough (1989). Field for calc-alkaline outlined.

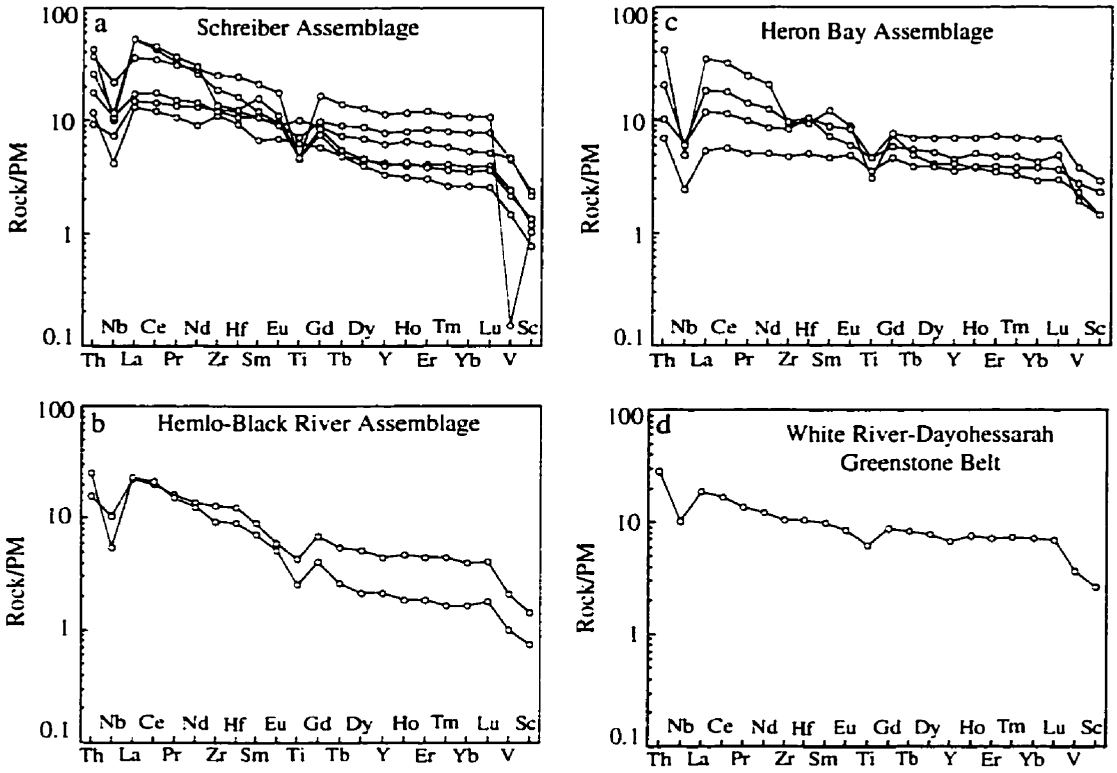

Figure 4.4. Primitive mantle-normalized diagrams for mafic to intermediate tholeiitic volcanic rocks of the Schreiber, Hemlo-Black River, and Heron Bay assemblages, andWhite River-Dayohessarah greenstone belt. Normalizing values are from Sun and McDonough (1989).

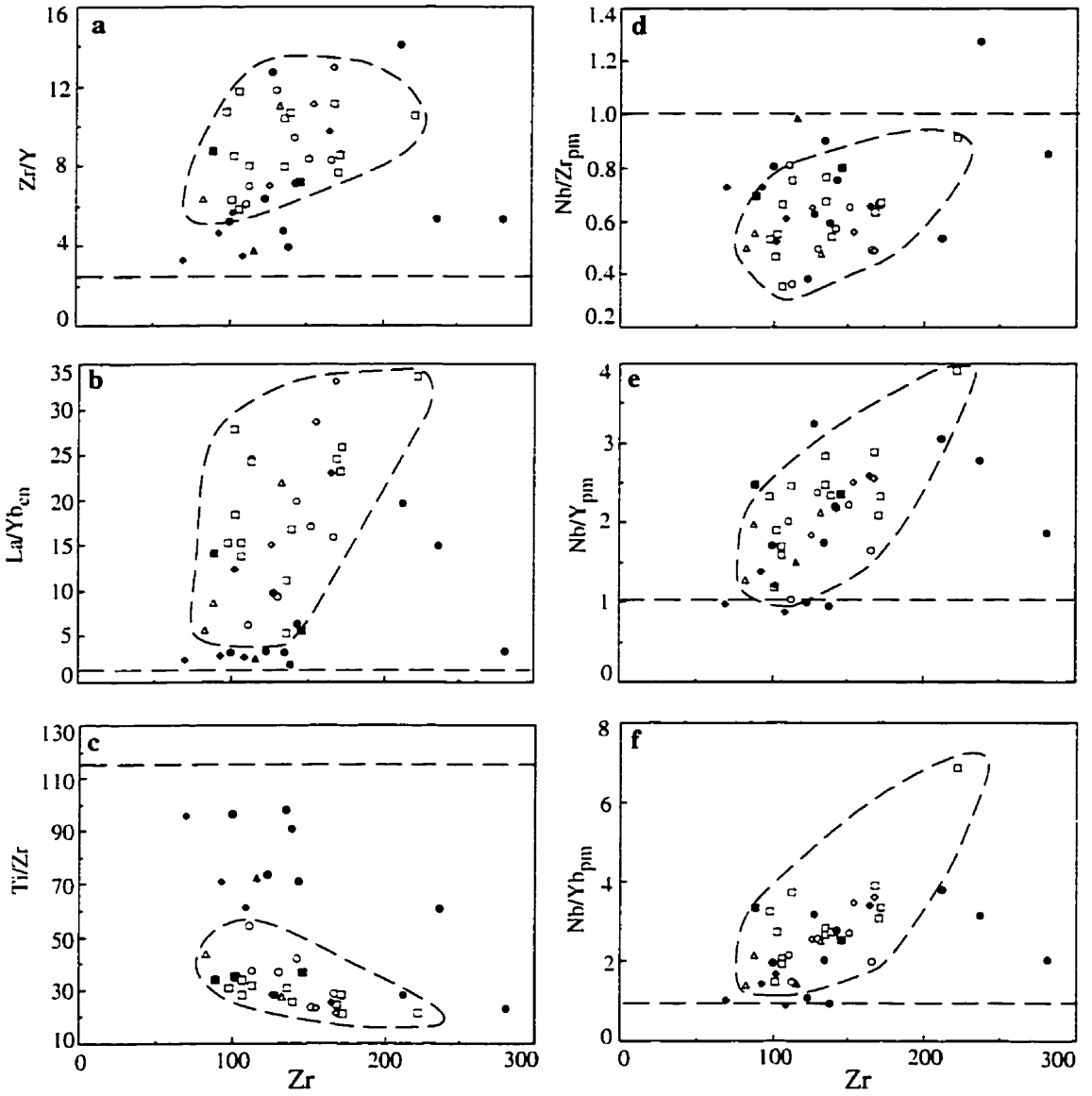

Figure 4.5. Zr (ppm) vs specified ratio diagrams for mafic-intermediate tholeiitic and calc-alkaline volcanic rocks of the Schreiber, Hemlo-Black River, and Heron Bay assemblages, and White River-Dayohessarah greenstone belt. Dashed lines are primitive mantle ratios. Field for calc-akaline outlined. Legend as for in Figure 4. 3.

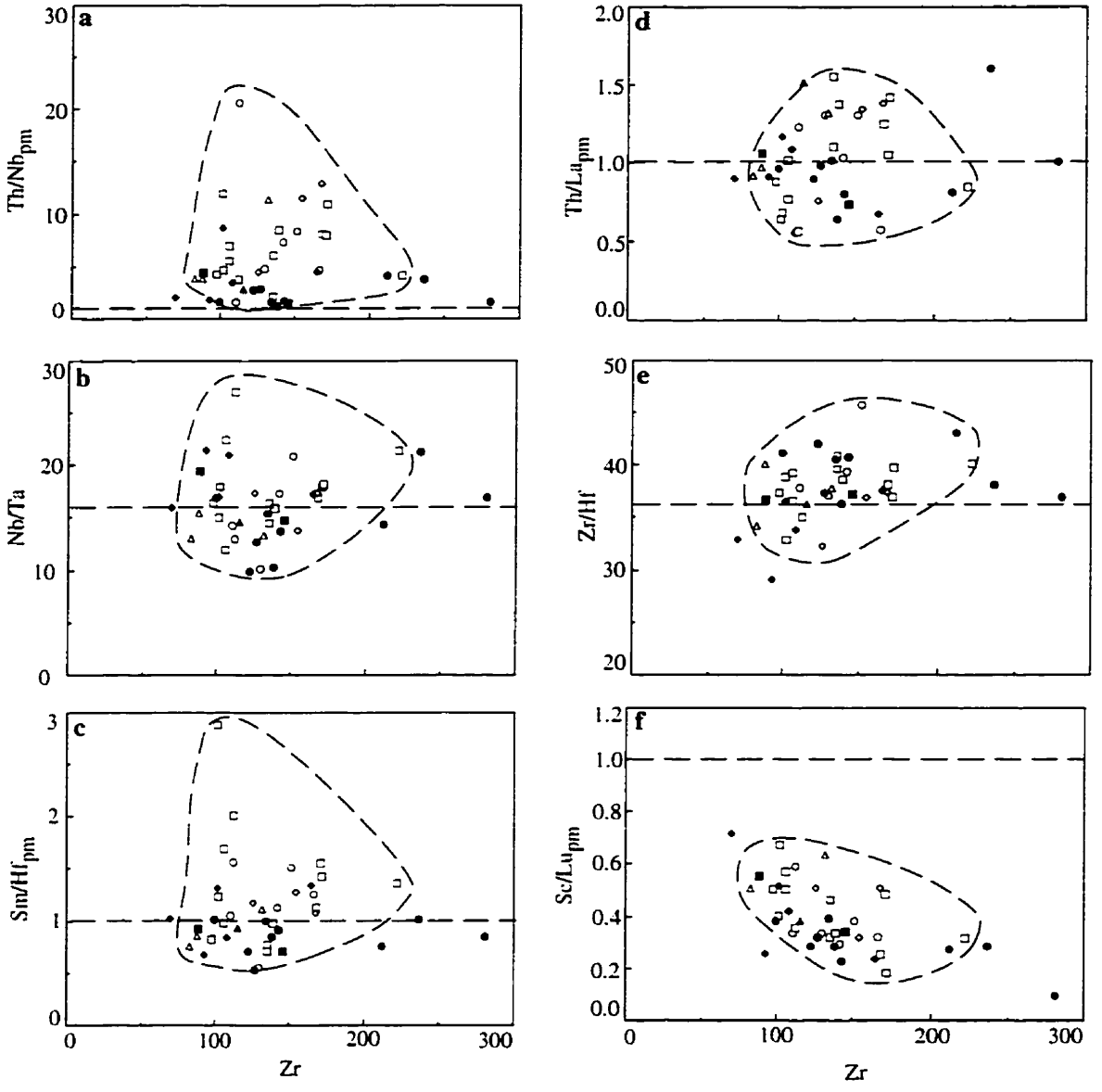

Figure 4.6. Zr (ppm) vs specified ratio diagrams for mafic-intermediate tholeiitic and calc-alkaline volcanic rocks of the Schreiber, Hemlo-Black River, and Heron Bay assemblages, and White River-Dayohessarah greenstone belt. Dashed lines are primitive mantle ratios. Field for calc-alakline outlined. Legend as for in Figure 4. 3.

geochemical results are comparable to those of the Schreiber assemblage, suggesting a similar petrogenetic origin for these two assemblages.

4-2-3. Heron Bay assemblage

Tholeiitic basalts from the Heron Bay assemblage have comparable ranges of major and trace element contents as counterparts from the Schreiber and Hemlo-Black River assemblages (Figs. 4.1-4.6; Table 4.1; Appendix 4.2). In addition, they have the following geochemical features: (1) large positive fractionation of REE (La/Sm_n=1.7-3.8, Gd/Yb_n=1.1-3.3, and La/Yb_n=2.4-23); (2) commensurately high Zr/Y (3.3-9.5) ratios; (3) variably negative anomalies of Nb and Ti (Nb/Nb*=0.1-0.5, Ti/Ti*=0.2-0.9); (4) variably negative to positive anomalies of Zr and Hf (Zr/Zr*=0.6-1.1, Hf/Hf*=0.5-1.3); and (5) with increasing Zr contents thorium and La plot on, to greater than, whereas Nb, Ti and Yb plot on, to less than, primitive mantle values (Figs. 4.2-4.6).

4-2-4. White River-Dayohessarah greenstone belt

Tholeiitic volcanic rocks in the White River-Dayohessarah greenstone belt are represented by only one basalt sample. It is characterized by SiO_2=50 wt.%, MgO=5.3 wt.%, Fe_2O_3=16.6 wt.%, TiO_2=1.4 wt.%, 217 ppm Cr, and 32 ppm Ni (Table 4.1; Appendix 4.3). The primitive mantle-normalized pattern and inter-element ratios are comparable to counterparts of the Schreiber-Hemlo greenstone belt, suggesting a similar petrogentic origin (Figs. 4.2-4.6).

4-3. Discussion of tholeiitic rocks and implications for geodynamic setting

Tholeiitic volcanic rocks of the Schreiber-Hemlo and White River-Dayohessarah greenstone belts are represented by basalts, basaltic andesites and andesites. Compared to

the ocean plateau tholeiites (see Chapter 3), they are distinct in terms of: (1) enrichment in SiO_2, Al_2O_3, Th, LREE, Zr; (2) higher Al_2O_3/TiO_2 ratios; (3) more fractionated patterns; (4) have more pronounced negative Nb and Ti anomalies; and (5) larger and more scattered fields on Zr versus specified trace element and ratio diagrams (Figs. 4.2-4.6).

Fractionated REE patterns, and negative Nb and Ti anomalies with respect to the neighbouring REE are all consistent with a juvenile oceanic island arc origin (cf. McCulloch and Gamble, 1991; Hawkesworth et al., 1993; Pearce and Peate, 1995 and references therein). Mg# values and Cr and Ni contents, together with fractionated incompatible and compatible trace element patterns given weakly fractionated HREE, suggest that they were derived dominantly from a metasomatized mantle wedge, rather than slab melting (cf. Pearce and Peate, 1995; Hawkesworth et al., 1997).

4-4. Geochemical results of calc-alkaline volcanic rocks

The principal geochemical features of mafic to intermediate calc-alkaline volcanic rocks exposed both in the Schreiber-Hemlo and White River-Dayohessarah greenstone belts are as follows:

4-4-1. Schreiber assemblage

Compositionally, calc-alkaline volcanic rocks of the Schreiber assemblage span SiO_2=53-62 wt.%, TiO_2=0.6-1.0 wt.%, MgO=2.9-9.5 wt.%, Fe_2O_3 =6.5-10 wt.%, Cr=136-594 ppm, and Ni=61-326 ppm (Tables 4.2; Appendix 4.3). There is a total range of Mg# from 70 to 50 accompanied by decreasing Cr and Ni contents; however, Co contents (42-25 ppm) are relatively uniform over the total rage of Mg#. Compositionally, they are basalts, basaltic-andesites, and andesites.

Table 4.2. Summary of significant compositional values and inter-element ratios of mafic to intermediate calc-alkaline volcanic rocks of the Schreiber-Hemlo and White River-Dayohessarah greenstone belts.

	Schreiber Assemblage	Hemlo-Black River Assemblage	Heron Bay Assemblage	White River-Dayohessarah Belt
SiO_2 (wt.%)	53-62	56-64	58-64	58-62
MgO	2.9-9.5	3.2-6.4	2.4-6.0	2.5-5.5
TiO_2	0.6-1.0	0.5-0.8	0.6-0.7	0.5-0.6
Fe_2O_3	6.5-10.5	5.5-8.7	5.6-8.3	5.8-8.0
Cr (ppm)	136-594	55-530	9-353	32-245
Ni	61-326	21-230	5-72	22-73
Th	1.1-6.4	1.6-9.6	2.8-8.0	1.2-5.4
La	14-42	12-53	30-47	10.6-33
Nb	2.6-6.3	2.4-13	5.2-6.9	2.6-4.0
Zr	110-166	97-171	126-168	82-132
Y	11-20	9-22	13-18	10-13
$(La/Yb)_{cn}$	6.3-25	5.3-37	15-33	5.7-22
$(La/Sm)_{cn}$	2.6-4.4	2.6-4.2	3.3-4.9	2.9-4.3
$(Gd/Yb)_{cn}$	1.8-3.5	1.5-4.8	3.0-4.2	1.6-3.1
Al_2O_3/TiO_2	15-24	17-30	22-31	25-34
Zr/Hf	35-45	33-41	32-38	34-40
Th/Nb	0.19-2.48	0.26-1.4	0.5-1.55	0.47-1.35
Th/La	0.07-0.16	0.07-0.20	0.09-0.17	0.12-0.16
Ti/Zr	23-57	22-38	20-32	27-46
Zr/Y	6.2-12	6-12	7-13	6.6-10.6
Nb/Nb*	0.1-0.3	0.1-0.4	0.1-0.2	0.1-0.2
Eu/Eu*	0.8-0.9	0.8-0.1	0.8-1.0	0.9-1.1
Zr/Zr*	0.4-1.4	0.3-1.3	0.6-0.7	0.7-1.0
Hf/Hf*	0.5-1.3	0.2-1.1	0.5-0.6	0.6-1.1
Ti/Ti*	0.2-0.6	0.2-0.5	0.2-0.3	0.3-0.6

In addition, they display the following compositional features: (1) fractionated LREE and HREE patterns, yielding high La/Sm_n=2.6-4.4, Gd/Yb_n=1.8-3.5, and La/Yb_n=6.3-24.6 ratios; (2) commensurately high Zr/Y (6-12) ratios; (3) pronounced negative Nb and Ti anomalies (Nb/Nb*=0.1-0.3, Ti/Ti*=0.2-0.6); (4) Zirconium and Hf anomalies are variably negative to positive (Zr/Zr*=0.4-1.4, Hf/Hf*=0.5-1.3); (5) Eu anomalies are minor negative (Eu/Eu*=0.8-0.9); and (6) plot to systematically greater than primitive mantle values on Zr versus Nb/Yb_{pm}, Nb/Y_{pm}, Th/Nb_{pm} variation diagrams (Figs. 4.3-4.7).

4-4-2. Hemlo-Black River assemblage

Calc-alkaline flows of the Hemlo-Black River assemblage display moderate variations in SiO_2 (56-64 wt.%), MgO (3.2-6.4 wt.%), Fe_2O_3 (5.5-8.7 wt.%), TiO_2 (0.5-0.9 wt.%), Cr (55-530 ppm), and Ni (21-230 ppm) contents, forming a coherent suite with a continuous compositional variation from more primitive basalts to evolved andesites (Mg#=62-44; Table 4.2; Appendix 4.4).

Additionally, the suite has the following geochemical characteristics: (1) variably enriched REE patterns (La/Sm_n=2.6-4.2, Gd/Yb_n=1.5-4.8, and La/Yb_n=5.3-34); (2) large negative Nb and Ti anomalies (Nb/Nb*=0.1-0.4, Ti/Ti*=0.2-0.5); (3) Zirconium and Hf anomalies are variably negative to positive (Zr/Zr*=0.3-1.3, Hf/Hf*=0.2-1.1); (4) ratios of Zr/Hf (33-41) and Nb/Ta (13-27) span the chondritic values; and (5) plot to consistently higher than primitive mantle values on Zr versus Th/Nb_{pm}, Nb/Yb_{pm} and Nb/Y_{pm} diagrams (Figs. 4.3-4.7; Table 4.2; Appendix 4.4). Collectively, these geochemical characteristics are comparable to those of the Schreiber assemblage calc-alkaline flows.

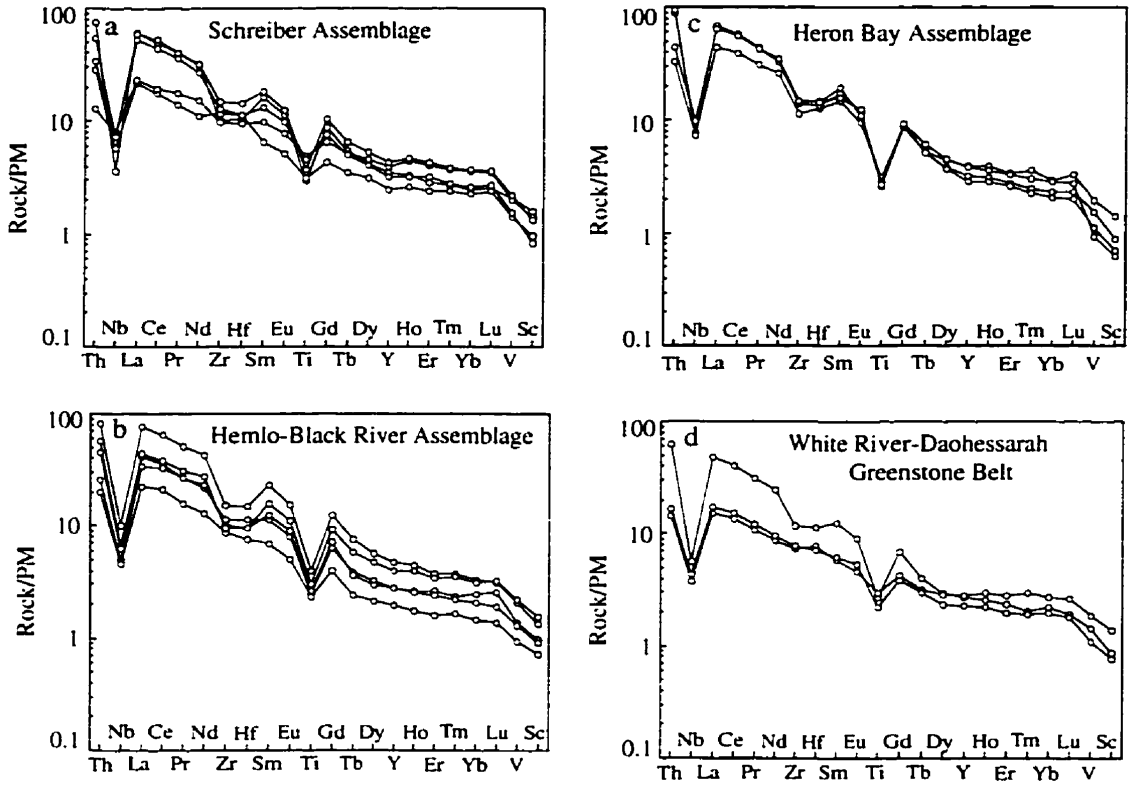

Figure 4.7. Primitive mantle-normalized diagrams for mafic to intermediate calc-alkaline volcanic rocks of the Schreiber, Hemlo-Black River, Heron Bay assemblages, and White River-Dayohessarah greenstone belt. Normalizing values are from Sun and McDonough (1989).

4-4-3. Heron Bay assemblage

Four calc-alkaline andesites were analyzed from the Heron Bay assemblage (Appendix 4.5). They have similar major and transition metal contents as the Schreiber and Hemlo-Black River examples, but have a more restricted range of SiO_2=58-64 wt.%, TiO_2=0.6-0.7 wt.%, Mg#=60-50 (Table 4.2).

On primitive a mantle-normalized diagram, the significant characteristics of these rocks are: (1) positively fractionated REE patterns (La/Sm_n=3.3-4.9, Gd/Yb_n=3.0-4.2, and La/Yb_n=15-33); (2) commensurately high Zr/Y (7-13) ratios; (3) large negative Nb and Ti anomalies (Nb/Nb*=0.1-0.2, Ti/Ti*=0.2-0.3); (4) Zirconium and Hf anomalies (Zr/Zr*=0.6-0.7, Hf/Hf*=0.5-0.6) are moderately negative; and (5) Europium anomalies are minor to absent (Eu/Eu*=0.8-1.0). In addition, on Zr versus selected element and ratios diagrams, they plot consistently close to the Schreiber and Hemlo-Black River counterparts (Figs. 4.3-4.7).

4-4-4. White River-Dayohessarah greenstone belt

Calc-alkaline volcanic rocks in the White River-Dayohessarah greenstone belt are represented by three andesite samples (Appendix 4.5). Major element abundances are comparable to those of the Schreiber-Hemlo greenstone belt (e.g., SiO_2=58-62 wt.%, Fe_2O_3=5.8-8.0 wt.%, MgO=2.5-5.5 wt.%, and TiO_2=0.5-0.6 wt.%) [Table 4.2].

The trace element systematics of the White River-Dayohessarah calc-alkaline flows are similar to those of the Schreiber-Hemlo counterparts in terms of: (1) positively fractionated REE patterns (La/Sm_n=2.9-4.3, Gd/Yb_n=1.6-3.1, and La/Yb_n=5.7-22.0); (2) variably negative Nb and Ti anomalies (Nb/Nb*=0.1-0.2, Ti/Ti*=0.3-0.6); (3) minor Eu anomalies (Eu/Eu*=0.9-1.1); (4) Zr/Y (6.6-11) and Ti/Zr (27-46) ratios; (5) compatible

element abundances (Cr=32-245 ppm, and Ni=22-73 ppm); and (6) Zr versus element and ratio plots (Figs. 4.3-4.7). In summary, these geochemical characteristics are similar to those of the Schreiber-Hemlo greenstone belt, signifying a similar origin for calc-alkaline volcanic sequences in the two belts.

4.5. Discussion of calc-alkaline rocks and implications for geodynamic setting

Calc-alkaline volcanic rocks of the Schreiber-Hemlo and White River-Dayohessarah belts are composed of basalts, basaltic andesites, and andesites. In comparison to tholeiites, they are distinct in terms of: (1) enrichment in MgO, Th and LREE, Cr, Ni (2) higher Al_2O_3/TiO_2 ratios; (3) more fractionated REE patterns; (4) have more pronounced negative Nb and Ti anomalies; and (5) less fractionation between HREE and Sc-V. (Figs. 4.3-4.8). Collectively, these geochemical characteristics suggest different source compositions for the calc-alkaline and tholeiitic suites.

Fractionated REE patterns, and depletion of Nb and Ti with respect to the neighbouring REE, are all consistent with a magmatic arc origin for the calc-alkaline flows (cf. McCulloch and Gamble, 1991; Hawkesworth et al., 1993; Pearce and Peate, 1995 and references therein). Contents of MgO, Cr and Ni together with incompatible/compatible element ratios suggest that the calc-alkaline basalts were derived dominantly from juvenile oceanic island arcs rather than continental arcs (cf. Pearce and Peate, 1995). Highly incompatible/compatible element ratios, specifically Nb/Y, Nb/Yb, La/Yb_n in most basalts are consistent with subduction-enriched mantle wedge source rather than slab melting.

Given the fact that the amount of residual garnet in the source, which is considered as a major repository for HREE and P, increases with the depth of partial melting, the

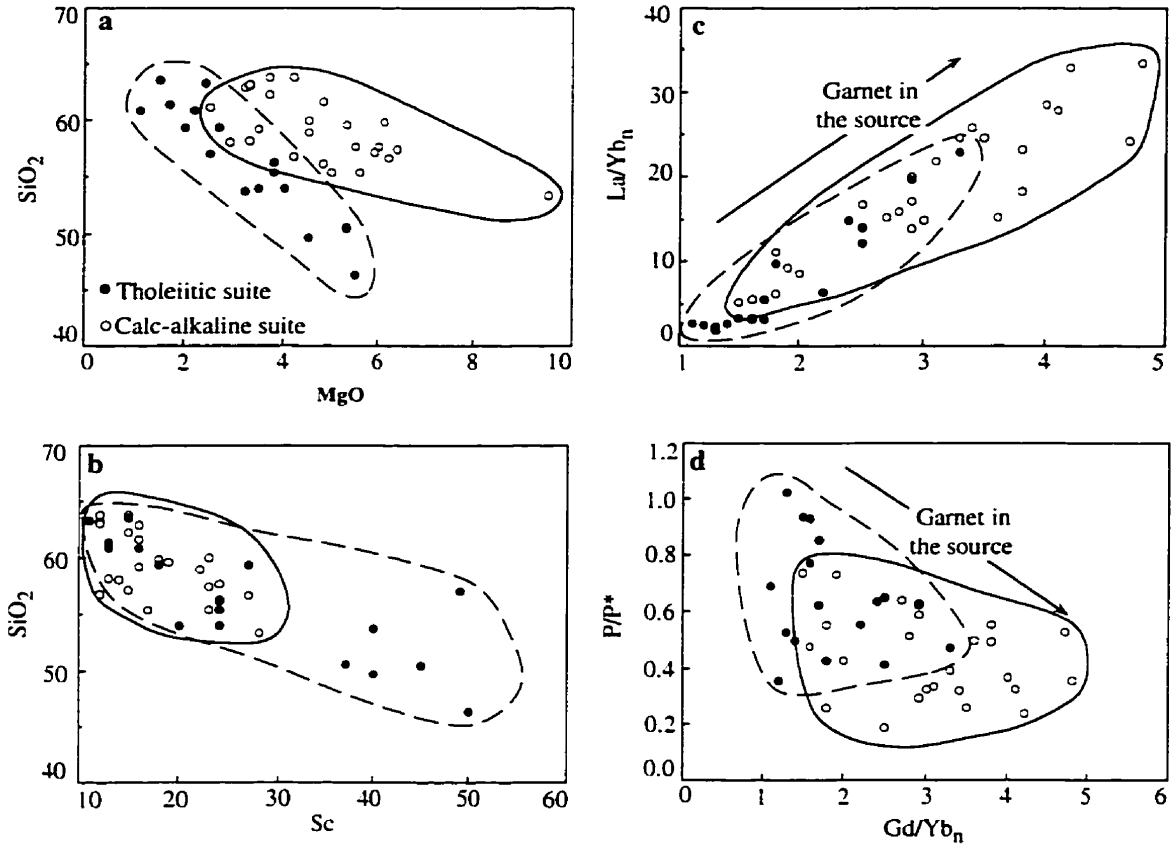

Figure 4.8. (a-b) SiO_2 (wt. %) vs MgO (wt. %) and Sc (ppm), and (c-d) Gd/Yb_n vs La/Yb_n and Gd/Yb_n diagrams for tholeiitic and calc-alkaline, mafic-intermediate volcanic rocks of the Schreiber-Hemlo and White River-Dayohessarah greenstone belts.

primitive mantle-normalized REE patterns and P/P* ratios are consistent with greater depths for the calc-alkaline suite than tholeiitic counterparts (Fig. 4.8; see Plank and Langmuir, 1988; Haggerty et al., 1994; Polat et al., 1997). Field relations indicate that the calc-alkaline and tholeiitic flows of the Schreiber-Hemlo and White River-Dayohessarah greenstone belts are spatially associated. In conclusion, the geochemical characteristics of calc-alkaline and tholeiitic, mafic to intermediate volcanic rocks of the Schreiber-Hemlo and White River-Dayohessarah greenstone belts were consistent with a juvenile oceanic island arc geodynamic setting, and sub-arc mantle wedge sources.

4-6. Geochemical results for felsic volcanic rocks

Felsic volcanic rocks of the Schreiber-Hemlo and White River-Dayohessarah greenstone belts are spatially associated with calc-alkaline volcanic rocks, and have calc-alkaline compositional characteristics (Fig. 4.9). A total of thirty felsic volcanic rock samples were analyzed from these belts for this study.

4-6-1. Schreiber assemblage

Felsic volcanic rocks are relatively rare in the Schreiber assemblage (Fig. 4.1). They have moderate variations in SiO_2 (65-70 wt.%), Fe_2O_3 (1.9-7.0 wt.%), MgO (0.4-3.1 wt.%), Cr (7-92 ppm), Ni (18-71 ppm), and TiO_2 (0.5-0.8 wt.%) contents (Table 4.3; Appendix 4.6).

On a primitive mantle-normalized diagram, felsic rocks of the Schreiber greenstone belt are characterized by: (1) fractionated and enriched REE patterns (La/Sm_n=3.3-4.9, Gd/Yb_n=1.5-2.2, and La/Yb_n=7.1-14.3); (2) large negative Nb and Ti anomalies (Nb/Nb*=0.2-0.3, Ti/Ti*=0.5-0.6); (3) variably positive Zr and Hf anomalies (Zr/Zr*=1.3-1.7, Hf/Hf*=1.2-1.6); and (4) Minor negative to positive Eu anomalies

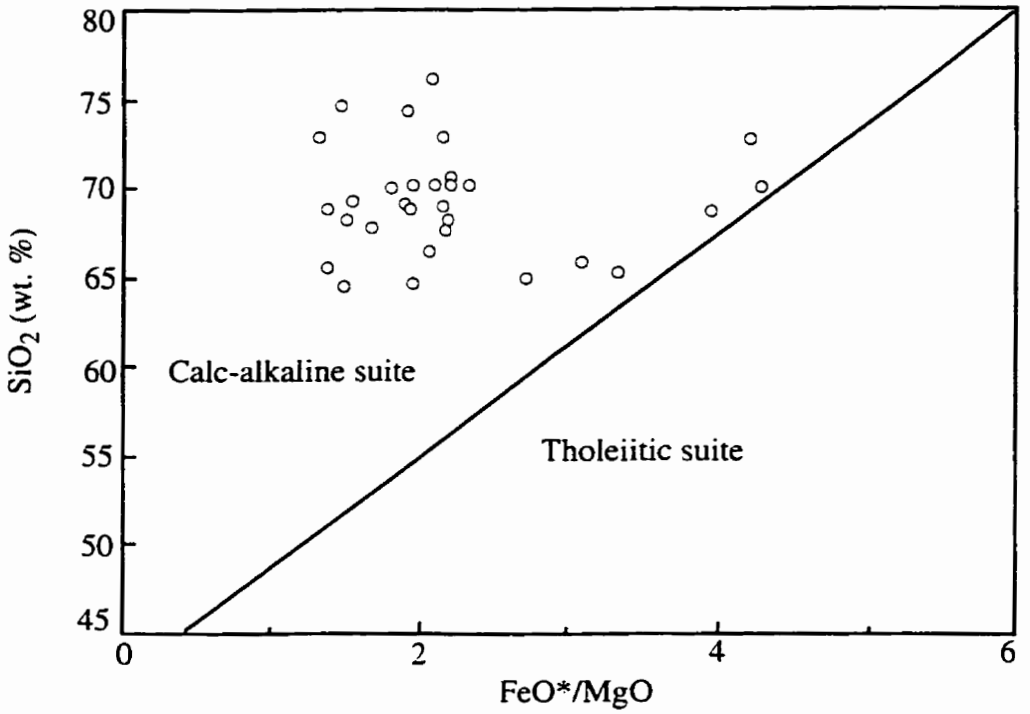

Figure 4.9. SiO_2 vs FeO*/MgO calc-alkaline/tholeiitic discrimination diagram for felsic volcanic rocks of the Schreiber-Hemlo and White River-Dayohessarah greenstone belts (Fields after Miyashiro, 1974).

Table 4.3. Summary of significant compositional values and inter-element ratios of felsic volcanic rocks of the Schreiber-Hemlo and White River-Dayohessarah greenstone belts.

	Schreiber Assemblage	Hemlo-Black River Assemblage	Heron Bay Assemblage	White River-Dayohessarah Belt
SiO_2 (wt.%)	65-70	68-74	66-75	65-76
MgO	0.4-3.1	0.6-1.9	0.9-2.4	1.0-3.1
TiO_2	0.5-0.8	0.3-0.6	0.2-0.5	0.3-0.8
Fe_2O_3	1.9-7.0	1.9-3.5	2.1-4.5	2.3-5.5
Cr (ppm)	7-92	11-126	11-112	17-136
Ni	18-71	8-33	2-33	8-47
Th	2.1-4.3	0.7-6.3	1.2-7.1	2.2-7.6
La	13-18	5.0-25	9-40	13-49
Nb	4.0-7.3	1.6-8.3	2.4-6.0	2.8-4.4
Zr	120-153	84-153	93-148	114-173
Y	8-16	5-14	5-13	5-11
$(La/Yb)_{cn}$	7.1-14	10.7-30	9.7-29	20-50
$(La/Sm)_{cn}$	3.3-4.9	3.7-4.4	3.2-6.6	3.8-6.6
$(Gd/Yb)_{cn}$	1.5-2.2	1.9-4.0	2.2-3.6	2.7-5.2
Al_2O_3/TiO_2	19-30	27-76	35-63	24-52
Zr/Hf	37-42	32-44	29-45	36-38
Th/Nb	0.48-0.64	0.3-1.1	0.5-1.5	0.60-1.95
Th/La	0.17-0.25	0.10-0.25	0.13-0.30	0.15-0.18
Ti/Zr	22-41	13-23	11-29	13-32
Zr/Y	7.7-15.7	11.1-28	12-25	12.1-24
Nb/Nb*	0.2-0.3	0.1-0.3	0.1-0.2	0.1-0.2
Eu/Eu*	0.9-1.1	0.8-1.2	0.8-1.0	0.8-1.1
Zr/Zr*	1.3-1.7	1.1-2.7	0.6-2.3	0.7-2.3
Hf/Hf*	1.2-1.6	1.1-3.1	0.6-2.3	0.7-2.3
Ti/Ti*	0.5-0.6	0.2-0.7	0.2-0.6	0.2-0.7

(Eu/Eu*=0.9-1.1) [Fig. 4.10; Table 4.3).

In addition, they have the following compositional features: (1) relative to primitive mantle ratios, higher Zr/Y (7.7-15.7) ratios; (2) ratios of Zr/Hf (37-42) are near chondritic, but Nb/Ta (9-14) ratios are consistently subchondritic; (3) on Zr versus Th and La diagrams they plot consistently lower than primitive mantle values; (4) compared with primitive mantle ratios, plot to high Th/Nb, Nb/Y, and Nb/Yb; and (5) and feature consistently low Sc/Lu ratios (Figs. 4.11-4.13).

4-6-2. Hemlo-Black River assemblage

Felsics volcanic rocks of the Hemlo-Black River assemblage are compositionally variable at SiO_2=68-74 wt.%, 14-16 wt.% Al_2O_3, 0.3-0.6 wt.% TiO_2, 2-3.5 wt.% Fe_2O_3, 0.9-1.9 wt.% MgO, 10-126 ppm Cr, and 8-33 ppm Ni (Table 4.3; Appendix 4.7). Compositionally, they are evolved rhyolites. They have a comparable range of major and trace element contents, as counterparts from the Schreiber assemblage, but have higher Zr/Y, Al_2O_3/TiO_2, Zr/Zr* and Hf/Hf* ratios. In addition, they have more fractionated REE patterns (La/Sm_n=3.7-4.4, Gd/Yb_n=2-4, and La/Yb_n=11-30), and commensurately higher Zr/Y (11-28) ratios than the Schreiber counterparts (Figs. 4.10-4.13; Table 4.3).

4-6-3. Heron Bay assemblage

Like those in the Schreiber and Hemlo-Black River assemblages, felsic volcanic rocks in the Heron Bay assemblage are spatially associated with calc-alkaline andesites. In comparison to the andesitic flows, felsic flows are characterized by higher SiO_2 (66-75 wt.%), but lower Fe_2O_3 (2.1-4.5 wt.%), MgO (0.9-2.4 wt.%), TiO_2 (0.2-0.5 wt.%), Cr (11-112 ppm), and Ni (2-33 ppm) contents (Tables 4.2, 4.3; Appendix 4.8). One outlier

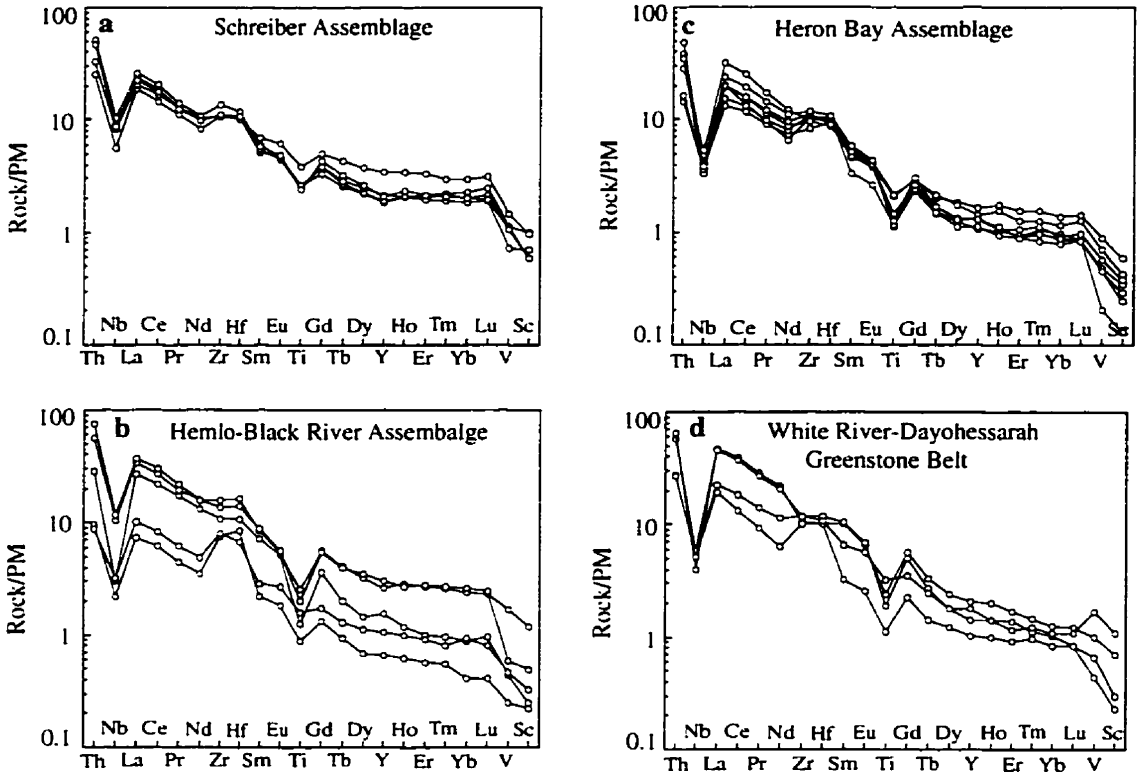

Figure 4.10. Primitive mantle normalized diagrams for felsic volcanic rocks of the Schreiber-Hemlo and White River-Dayohessarah greenstone belts. Normalizing values are from Sun and McDonough (1989).

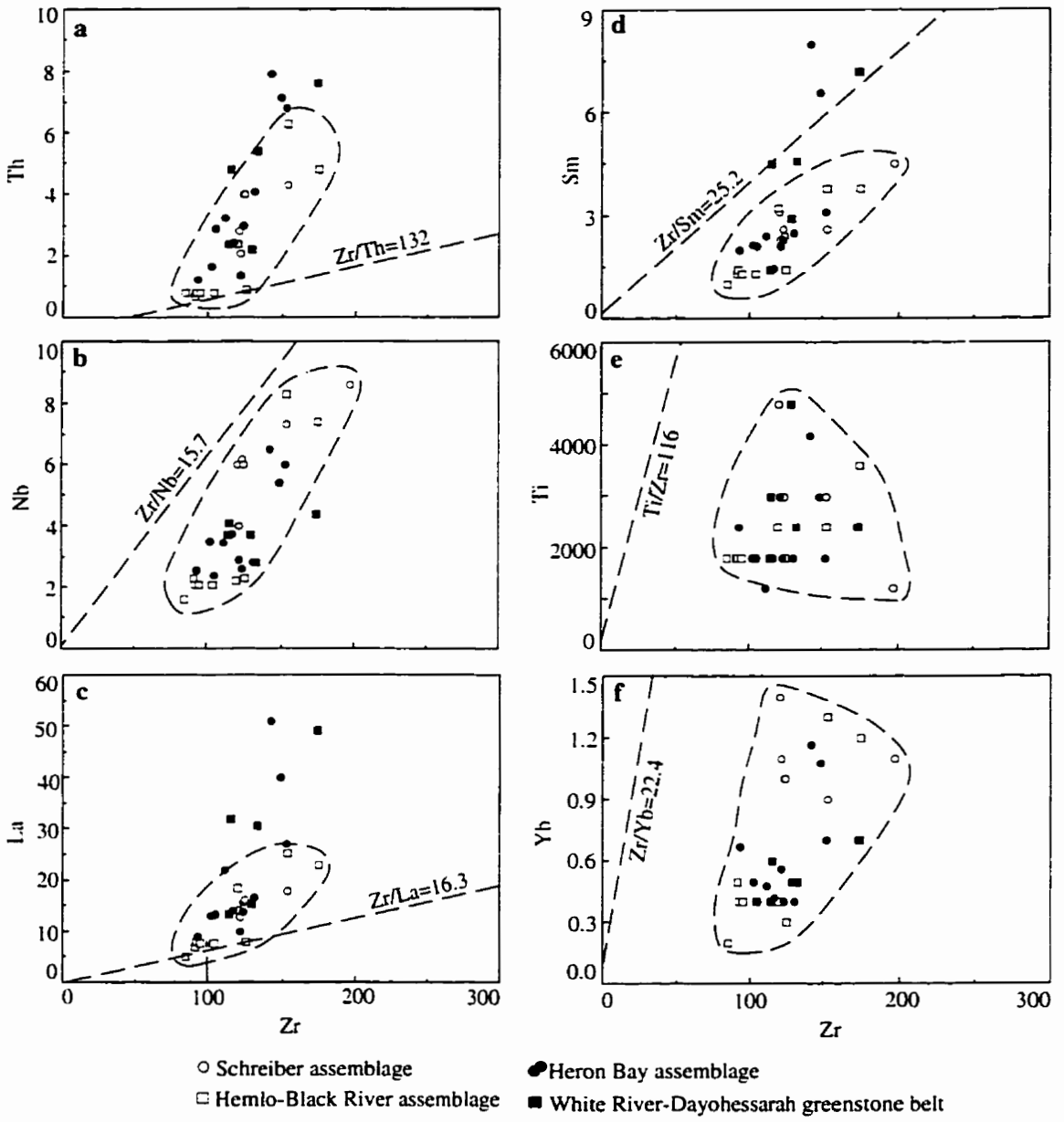

Figure 4.11. Zr (ppm) vs specified element (ppm) variation diagrams for felsic volcanic rocks of the Schreiber-Hemlo and White River-Dayohessrah greenstone belts. Dashed lines are primitive mantle ratios. Field for Schreiber and Hemlo-Black River assemblages outlined. Normalizing values from Sun and McDonough (1989).

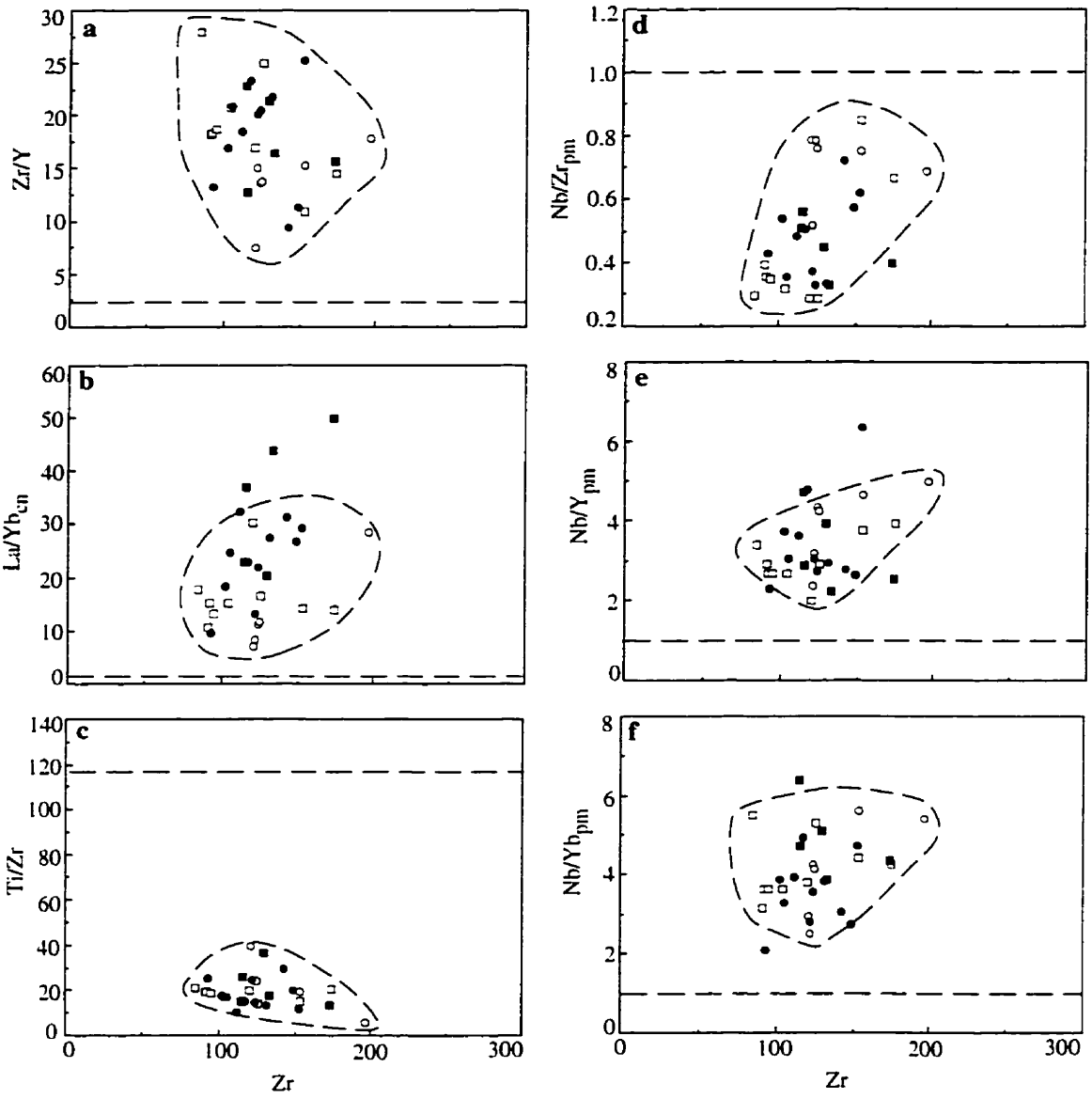

Figure 4.12. Zr (ppm) vs specified ratio diagrams for felsic volcanic rocks of the Schreiber-Hemlo and White River-Dayohessarah greenstone belts. Dashed lines are primitive mantle ratios. Field for Schreiber and Hemlo-Black River assemblages outlined. Legend as for Figure 4.11.

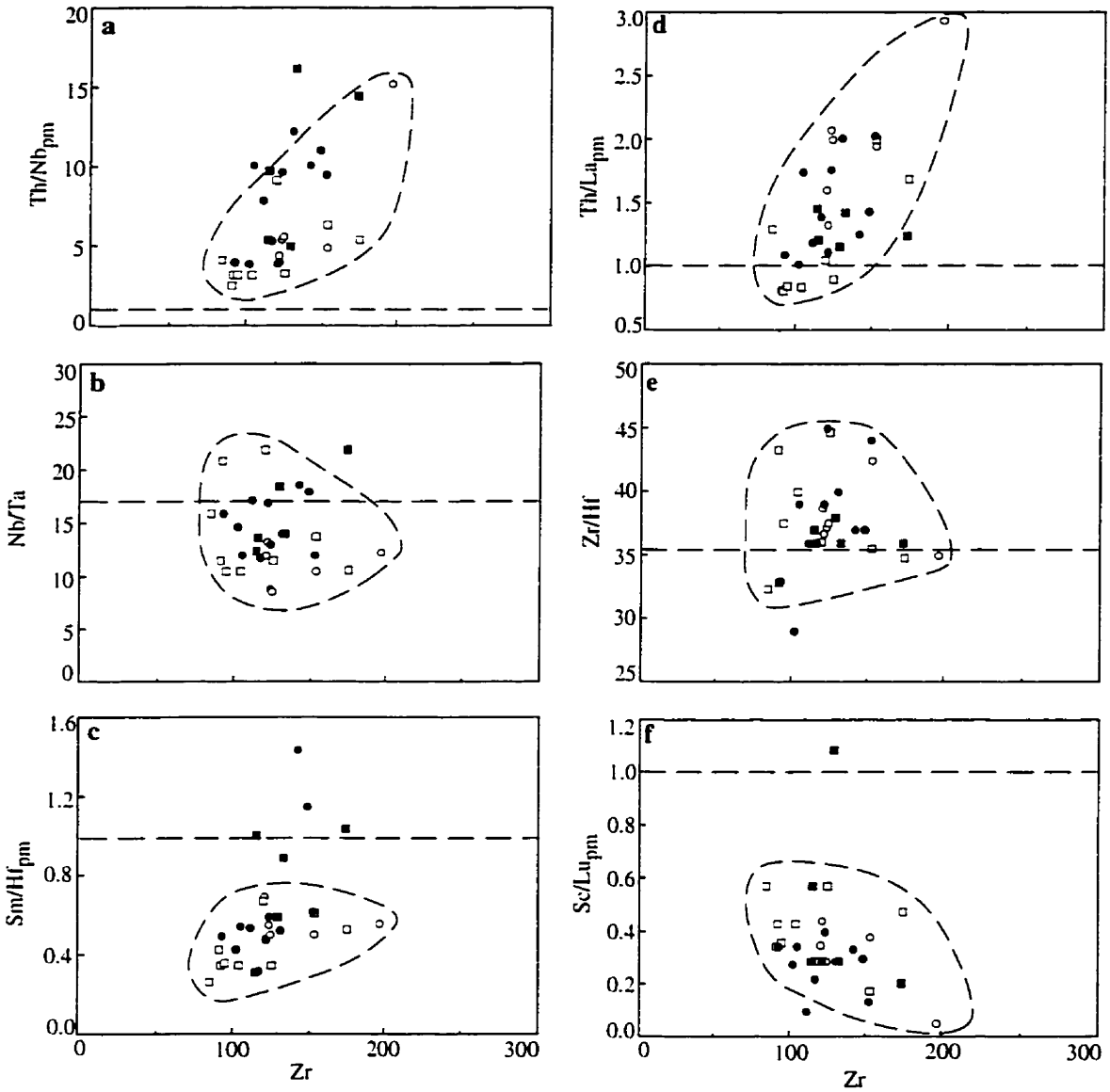

Figure 4.13. Zr (ppm) vs specified ratio diagrams for felsic volcanic rocks of the Schreiber-Hemlo and White River-Dayohessarah greenstone belts. Dashed lines are primitive mantle ratios. Field for Schreiber and Hemlo-Black River assamblage outlined. Legend as for Figure 4.11.

has higher Fe_2O_3 (6.7 wt. %), Cr (166 ppm), and Ni (49 ppm) abundances (HB95-12).

On a primitive mantle-normalized element diagram, the significant features of felsic rocks in the Heron Bay assemblage are: (1) variably LREE enriched patterns, where La/Sm_n=3.2-6.6, Gd/Yb_n=3.2-3.9, and La/Yb_n=10-32; (2) large negative Nb and Ti anomalies (Nb/Nb*=0.1-0.2, Ti/Ti*=0.2-0.6); (3) Zirconium and Hf anomalies are negative to large positive values (Zr/Zr*=0.6-2.3, Hf/Hf*=0.6-2.3); and (4) Europium anomalies are slightly negative to zero (Eu/Eu*=0.8-1.0). Additionally, they have the following compositional characteristics: (1) relative to the primitive mantle ratios, higher Zr/Y (12-25), but lower Ti/Zr (11-29) and Sc/Lu (37-97) ratios; and (2) on Zr versus element and ratio (e.g., Zr/Y, La/Yb_n, Sc/Lu_{pm}) diagrams, they plot coherently along with the Hemlo-Black River assemblage felsics counterparts (Figs. 4.11-4.13; Table 4.3).

4-6-4. White River-Dayohessarah Greenstone Belt

Felsic volcanic rocks of the White River-Dayohessarah greenstone belt are represented by five samples (Appendix 4.9). They are compositionally uniform at 65-76 wt.% SiO_2, 0.3-0.8 wt.% TiO_2, 2.3-5.5 wt.% Fe_2O_3, 1.0-1.6 wt.% MgO, 17-83 Cr ppm, and 8-47 ppm Ni. One outlier consists of higher MgO (3.1 wt.%) and Cr (136 ppm) contents (WR95-9). Felsic volcanic rocks from the White River-Dayohessarah greenstone belt have a comparable range inter-element ratios and primitive mantle-normalized trace element patterns as counterparts from the Schreiber-Hemlo greenstone belt, suggesting a similar origin for the two belts (Figs. 4.9-4.13; Table 4.3).

4-7. Discussion of felsic rocks and implications for tectonic setting

In general, the REE systematics of felsic volcanic rocks of the Schreiber-Hemlo and White River-Dayohessarah greenstone belts are comparable to those of interlayered

tholeiitic to calc-alkaline basalts and andesites albeit at higher absolute abundances. La/Yb_n (>15) ratios coupled with high Al_2O_3 (>15 wt.%) contents suggest slab melting with garnet residual in the source. These geochemical characteristics are comparable to those of high-Al, high La/Yb_n Archean TTGs (see Chapter 5; Fig. 4.15; cf. Martin, 1986, 1993; Drummond and Defant, 1990). On the other hand, La/Yb_n ratios <15 may indicate: (1) slab-dehydration, (2) some combination of slab-dehydration and slab melting, or (3) shallower-level partial melting (cf. Martin, 1986; Drummond and Defant, 1990; Defant and Drummond, 1993; McCulloch, 1993).

Tholeiitic and calc-alkaline mafic to intermediate, and felsic volcanic rocks all share positively fractionated REE patterns, and negative Nb and Ti anomalies (Figs. 4.4, 4.7, 4.11). However, felsic volcanic rocks have larger positive Zr and Hf anomalies than their mafic and intermediate counterparts (Fig. 4.15). There is a general positive correlation between the enrichment of Zr and Hf, relative to MREE, and fractionation of all REE (Fig. 4.15). Additionally, in felsic rocks the enrichment of Zr and Hf, with respect to MREE, correlates negatively with Sc abundances. Collectively, these results are consistent with clinopyroxene residual in the source (see Rollinson, 1993; Skulski et al., 1994). The inferred presence of garnet and clinopyroxene in the source is consistent with an independent argument for eclogitic residue in the slab (see McDonough, 1991).

The existence of overlapping fields between mafic-intermediate and felsic suites on Zr/Zr* versus ratio diagrams suggest that processes controlling the production of these volcanic rocks were more complex than simple slab or wedge melting. This complexity may have resulted from a mixture of slab and wedge melts, second stage melting, magma mixing, fractional crystallization, partial equilibration with sub-arc wedge peridotite crustal contamination, or some combination (Arculus, 1994).

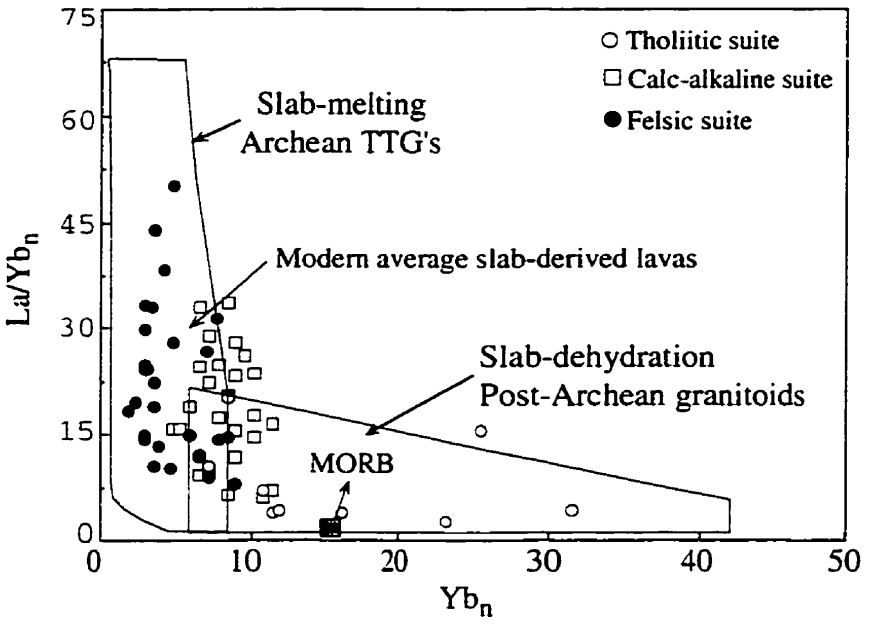

Figure 4.14. La/Yb_n vs Yb_n variation diagrams for subduction related mafic to felsic volcanic rocks of the Schreiber-Hemlo and White River-Dayohessarah greenstone belts (Fields after Martin, 1986; normalizing and MORB values from Sun and McDonough, 1989).

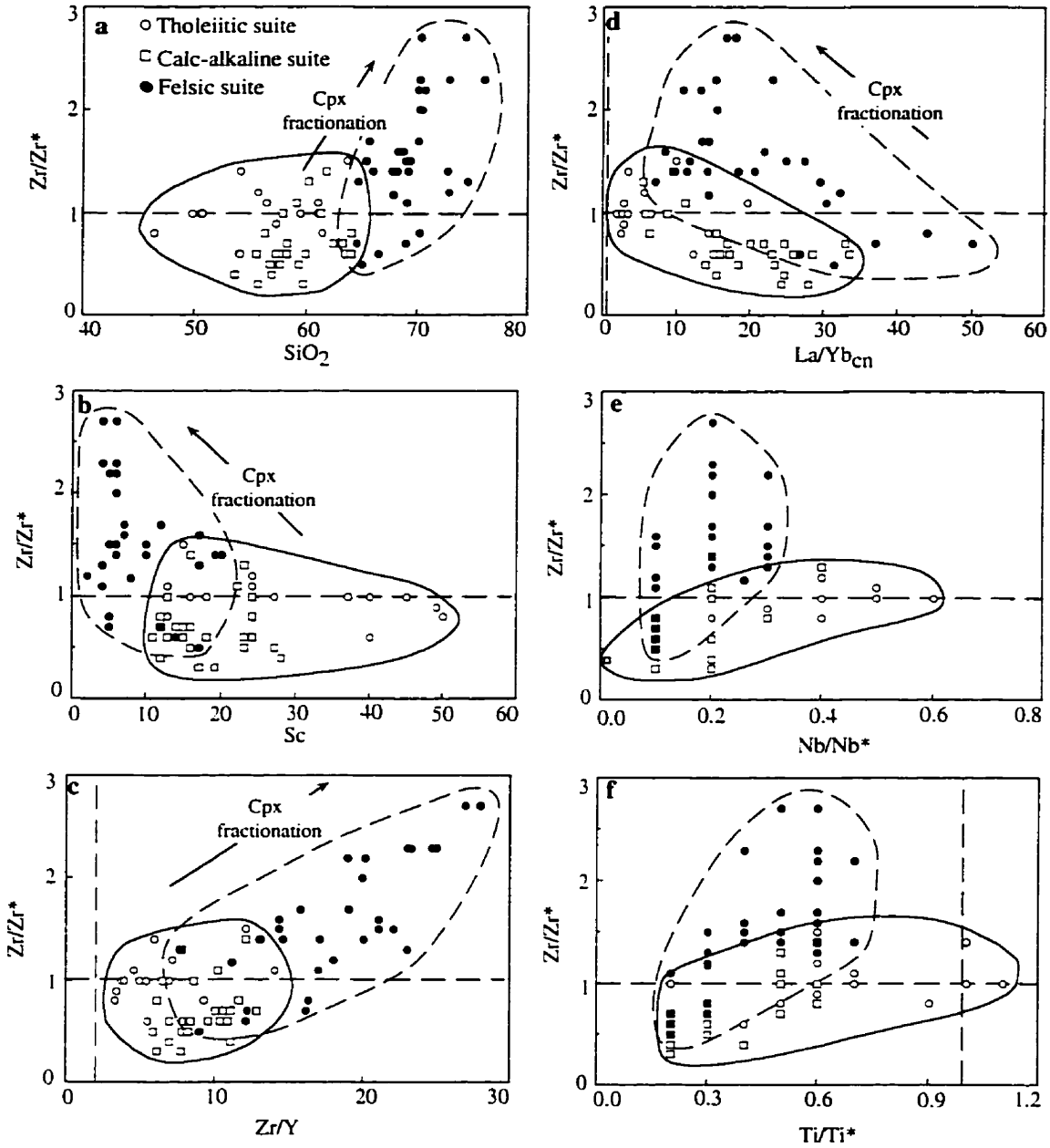

Figure 4.15. Zr/Zr* vs specified element and ratio diagrams for tholeiitic, calc-alkaline, and felsic volcanic rocks of the Schreiber-Hemlo and White River-Dayohessarah greenstone belts. Dashed lines are primitive mantle ratios.

4.8. Summary and synthesis

Both field relations and high-precision ICP-MS trace element data indicate that spatially associated tholeiitic and calc-alkaline suites of mafic through intermediate, to felsic composition of the Schreiber-Hemlo and White River-Dayohessarah greenstone belts were all erupted in an oceanic island arc geodynamic setting. However, in detail major and trace element contents and inter-element ratios are consistent with distinct petrogenetic origins for these two suites (tholeiitic, calc-alkaline) and three populations of arc volcanic rocks. Both the tholeiitic and calc-alkaline suites were derived from the metasomatized mantle wedge: tholeiitic flows were derived from shallower and more depleted mantle sources than calc-alkaline counterparts (cf. Tatsumi et al., 1983; Miller et al., 1992). Slab melting was a major source of felsic rocks with garnet + clinopyroxene ± hornblende residue in the source. High Ni and Cr contents in the felsic suite can be explained by mixing between, or interaction with, slab- and wedge-derived melts (Fig. 4.15). Zr(Hf)/MREE systematics suggest that retention of clinopyroxene in the residual eclogite during slab melting may have fractionated Zr(Hf) from MREE, resulting in positive Zr and Hf anomalies.

Ratios of Zr/Hf and Nb/Ta in most ocean basalts (MORB) are relatively uniform and similar to the primitive mantle values of 36 and 17, respectively. Given the similar mineral-melt partition coefficients for these element pairs, their fractionation during partial melting is not required (see Sun and McDonough, 1989). Recent studies suggest that these element may be fractionated by metasomatizing melts and fluids (Dupuy et al., 1992; Green, 1995; Stolz et al., 1997). Stolz et al. (1997) proposed that higher Nb/Ta (>17) ratios are result of slab-derived silicic melts. Given that slab-derived melts have higher La/Yb_n ratios than mantle wedge-derived counterparts (see Martin, 1986; 1993; Drummond and Defant, 1990), one would expect to see a positive correlation between Nb/Ta ratios and La/Yb_n ratios or SiO_2 contents in Archean arc-related rocks. However,

neither Nb/Ta nor Zr/Hf ratios in mafic to felsic volcanic rocks of the Schreiber-Hemlo and White River-Dayohessarah greenstone belts covary with REE fractionation and SiO_2 contents, suggesting that the fractionation of these element pairs cannot be explain by slab-melting and slab-dehydration processes alone, and requires a more complicated metasomatic process(es) [Figs. 4.14, 4.15; see Woodhead et al., 1993; Green, 1995; Eggins et al., 1997].

Laflèche et al. (1992) reported coeval tholeiitic and calc-alkaline volcanic rocks from the Blake River Group of the late Archean Abitibi greenstone belt. They interpreted the arc-like tholeiites as the product of magma mixing between asthenospheric tholeiites (ocean plateau type; see Chapter 3) and subduction-related calc-alkaline basaltic andesites. They argued that the calc-alkaline suite was generated through subduction of young, hot Archean oceanic lithosphere.

Relative to the Blake River Group arc-related tholeiitic and calc-alkaline volcanic suites, the Schreiber-Hemlo and White River-Dayohessarah counterparts have higher incompatible/compatible trace element ratios (e.g. Zr/Y, Nb/Yb), as signified by more fractionated REE patterns in the latter. However, both the Abitibi and Wawa arc suites have comparable Zr/Hf and Nb/Ta ratios. The trace element systematics of the tholeiitic suite of the Schreiber-Hemlo and White River-Dayohessarah greenstone belts of the Wawa subprovince is inconsistent with a mixture of mantle plume melts (komatiites and ocean plateau tholeiites; see Chapter 3) and subduction-related calc-alkaline basaltic melts. Rather, the Wawa subprovince arc-tholeiites were derived from a shallow-level partial melting of a metasomatized subarc mantle wedge. In contrast to the Blake River Group calc-alkaline volcanic rocks, the Wawa counterparts appear to have been derived dominantly from a deeper-level partial melting of a metasomatized subarc mantle wedge, with some slab melt contributions (Fig. 4.14, 4.15).

Like modern oceanic-island arc basalts, the late Archean Schreiber-Hemlo and

White River-Dayohessarah belt counterparts are characterized by tholeiitic to calc-alkaline magma series, and posses variable REE and HFSE fractionation (Fig. 4.16; see Pearce and Peate, 1995). Similarly, they are comparable to the Phanerozoic counterparts in that the calc-alkaline suite were generated in more enriched mantle wedge than tholeiitic counterparts (Fig. 4.16; Tatsumi et al., 1983; Miller et al., 1992). In contrast, arc volcanic rocks in the late Archean Schreiber-Hemlo and White River-Dayohessarah greenstone belt tend to have more fractionated REE patterns than Phanerozoic counterparts (Miller et al., 1992; Tatsumi et al., 1992; Gamble et al., 1993; Sajona et al., 1996; Hochstaeder et al., 1996), as indicated by higher La/Yb_n ratios in the latter ($La/Yb_n<12$ versus $La/Yb_n>12$). This difference in REE systematics may be attributed to thicker lithosphere in the Archean, resulting in deeper melt segregation (Plank and Langmuir, 1988; McKenzie and O'Nions, 1991; Ellam, 1992).

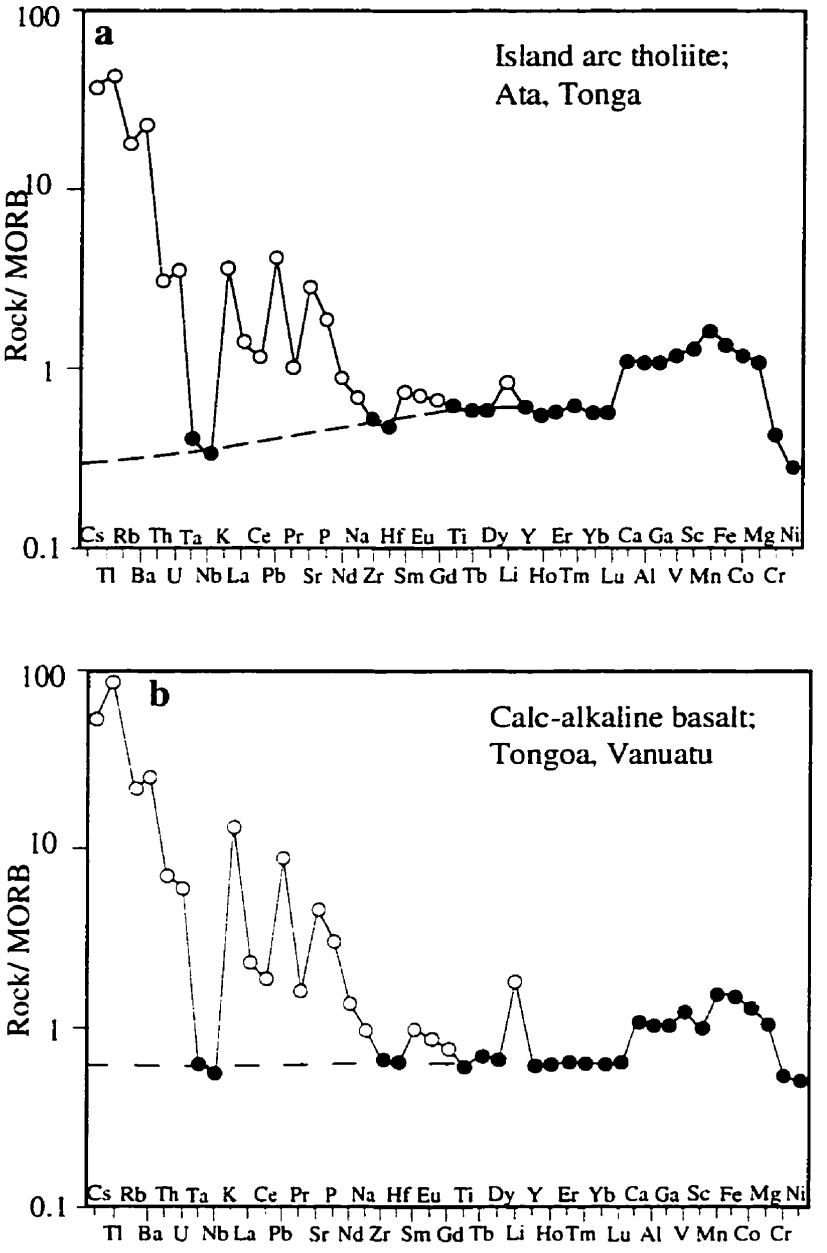

Figure 4.16. MORB-normalized diagrams for oceanic island arc basalts (modified after Pearce and Peate, 1995).

CHAPTER 5. GEOCHEMISTRY OF GRANITOID INTRUSIONS AND SILICICLASTIC TURBIDITES

5-1. Introduction

Syn-kinematic granitoid intrusions and siliciclastic turbidites are important components of greenstone-granitoid terranes in the Archean Superior Province in general, and the Wawa subprovince specifically (Card, 1990; Thurston, 1991). Studies of Archean to modern granitoids have demonstrated that their geochemical of systematics may provide significant information on magmatic source characteristics and tectonic settings. (Pearce et al., 1984; Gromet and Silver, 1987; Sutcliffe et al., 1990; Feng and Kerrich, 1992). Additionally, it has been shown that the geochemical characteristics of granitoids can be used to help understand the mechanisms of continental growth (Gromet and Silver, 1987; Martin, 1993; Taylor and McLennan, 1985; 1995; Tarney and Jones, 1994; Rudnick, 1995).

Based on a number of mineralogical and chemical criteria granitoids have been divided into three major types: (1) I (igneous)-type granitoids, (2) S (supracrustal or sedimentary)-type granitoids, and (3) A (anorogenic)-type granitoids. Pearce et al. (1984) divided Phanerozoic granitoids into four groups on the basis of their tectonic setting: (1) syn-collisional granitoids (Syn-COLG), (2) volcanic arc granitoids (VAG), (3) within-plate granitoids (WPG), and (4) ocean-ridge granitoids (ORG). Archean granitoids are dominated by sodic tonalites, trondhjemites, and granodiorites (TTG suite), whereas post-Archean counterparts are characterized dominantly by K-rich granites (Tarney and Jones,

1994). Using high-precision ICP-MS trace element data Feng and Kerrich (1992) recognized six distinct granitoid magma series in the Archean Abitibi subprovince: (1) TTG (tonalite-trondhjemite-granodiorite), (2) TGGM (tonalite-granodiorite-granite-quartz monzonite), (3) SMG (quartz syenite-monzonite-granite), (4) SS (alkali feldspar syenite-quartz alkali feldspar syenite), (5) MMGS (monzodiorite-monzonite-granodiorite-syenite), and (6) GMG (garnet muscovite granite). The first two and sixth magma series belong to the Archean TTG suite, the third is a K-rich granite, the fourth shoshonitic, fifth S-type.

The geochemistry of siliciclastic sedimentary rocks in Archean and post-Archean orogenic belts have been shown to be useful in providing information concerning the provenance and tectonic settings of these sedimentary rocks (Taylor and Mclennan, 1985; Feng and Kerrich, 1990; Pan et al., 1991; Prame and Pohl, 1994; Garver and Scott, 1995; Polat et al., 1996b). In many cases, the provenance regions of orogenic turbidites have been destroyed and the only record lies in the chemistry of sediments derived from them (Bhatia and Crook, 1986; Polat et al.,1996b). It has been proposed that during clastic sedimentary processes Th, REE, and transition metals, notably Sc, Co, Cr, are transported quantitatively from source regions to sedimentary basins (McLennan and Taylor, 1985; 1991). Moreover, the distribution of these elements is not significantly affected by secondary processes, such as diagenesis, low grade metamorphism, and heavy mineral fractionation. Geochemical studies of siliciclastic sedimentary rocks, particularly those of shales, give a means for estimating average upper crustal composition; and provides a record of how the upper continental crust evolved through time (Taylor and McLennan, 1985, 1995).

Based on REE patterns, McLennan and Taylor (1991) divided Archean siliciclastic turbidites into three major types: (1) Type-1 turbidites that are defined by enriched LREE and flat HREE patterns, with zero to slightly negative Eu anomalies; (2) Type-2 turbidites which are characterized by positively fractionated LREE and HREE patterns, with zero to

minor negative Eu anomalies; and (3) Type-3 turbidites that have essentially flat REE patterns, with or without minor LREE fractionation and negative Eu anomalies. The abundances of these turbidites decrease from Type-1 to Type-3. In general, REE patterns of post-Archean sediments, especially of shales, are found to be quite uniform, possessing enriched LREE and near flat HREE patterns, and moderate negative Eu (Eu/Eu*=0.65) anomalies.

In this chapter, relatively immobile major and trace (HFSE, REE, and transition metals) elements are used in an attempt to better understand the petrogenesis and geodynamic settings of syn-kinematic granitoid intrusions, in the Schreiber-Hemlo and White River-Dayohessarah greenstone belts including the Terrace Bay batholith, Pukaskwa batholith, Cedar Lake plutons (Fig. 5.1), and syn-kinematic mafic to felsic sills and dykes that intruded during mélange formation (see Chapter 6). In addition, the question of the provenance of sliciclastic turbidites is addressed. (For analytical procedures see Chapter 3 and Appendices 1.1, 3.1).

5-2. Petrography

Granitoids and felsic sills and dykes are composed of plagioclase + quartz + alkali feldspar + hornblende + biotite ± titanite ± apatite ± zircon. Mafic sills and dykes have an assemblage mainly of amphibole (likely altered from pyroxene) + plagioclase ± epidote (secondary) ± pyroxene ± quartz (secondary) ± opaques. In general, mafic to felsic sills and dykes are finer-grained and more altered than granitoid intrusions. Sedimentary rocks (graywacke turbidites) are poorly sorted, consisting of angular grains of quartz + plagioclase + amphibole + alkali feldspar (microcline) + mica (biotite) + chlorite + epidote ± zircon ± opaques. The cement of graywackes is dominantly carbonates, with minor silica.

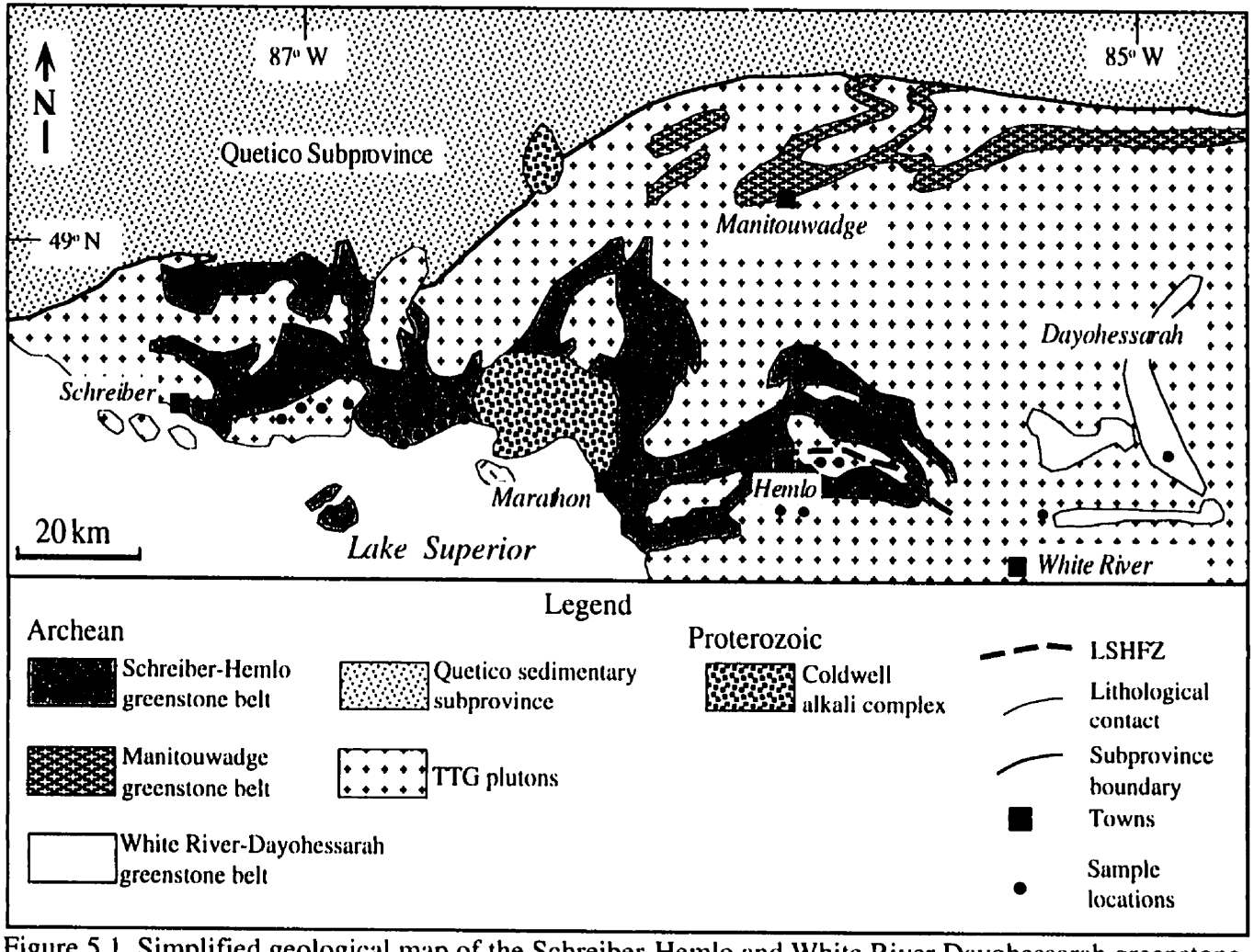

Figure 5.1. Simplified geological map of the Schreiber-Hemlo and White River Dayohessarah greenstone belts. Lithological boundaries may also be tectonic (modified after Williams et al, 1991). TTG: Tonalite trondhjemite-granodiorite.

5-3. Granitoids (tonalites-trondhjemites-granodiorites, TTG)

Granitoids of the Schreiber-Hemlo and White River-Dayohessarah greenstone belts are compositionally uniform at 65-72 wt.% SiO_2, 15-16 wt.% Al_2O_3, 3.7-5.9 wt.% Na_2O, 0.3-0.6 wt.% TiO_2, and Fe_2O_3=2.1-4.2 wt.% (Table 5.1; Appendix 5.1). They are characterized by high Ba (810-1470 ppm), Rb (40-160 ppm), Sr (190-1480 ppm), but low Y (5-14 ppm), Cr (10-42 ppm), and Ni (3-20 ppm) contents (Fig. 5.2; Table 5.1; Appendix 5.1). Compositionally they are typical high-Na, high-Al Archean-type tonalite-trondhjemite-granodiorites.

On a primitive mantle-normalized diagram, the significant features of the Schreiber-Hemlo and White River-Dayohessarah greenstone belt granitoids are: (1) strongly fractionated REE, where La/Yb_n=17-53, La/Sm_n=3.1-7.5, and Gd/Yb_n=2.6-7.9; (2) commensurately high Zr/Y (12-27) ratios; (3) depletion of HFSE (Nb, Ta, and Ti) with respect to Th and neighbouring REE's, as indicated by large negative Nb (Nb/Nb*=0.1-0.2) and Ti (0.15-0.4) anomalies; and (4) enrichment of Th over LREE, generating high Th/La (0.09-0.44) ratios (Figs. 5.3a,b; Table 5.1). Collectively, these geochemical characteristics are comparable to syn-kinematic TTG intrusions of the Abitibi subprovince (see Feng and Kerrich 1992), suggesting that granitoids of the Schreiber-Hemlo and White River-Dayohessarah belts formed by partial melting of mafic to ultramafic magma sources. The highly fractionated REE patterns, high Zr/Y and Sr/Y, but low K/Rb (215-400) ratios, and Th-Nb-La systematics are all consistent with slab-melting with garnet and/or hornblende in the residue (Figs. 5.3a,b; cf. Martin, 1986, 1993; Gromet and Silver, 1986; Drummond and Defant, 1990). Large variations in HREE (Gd/Yb_n=2.6-7.9) may have resulted from either variable amounts of garnet in the residua, or from interaction between HREE-fractionated slab melts and mantle wedge possessing near-flat HREE patterns. Th/La ratios covary with La abundances, suggesting

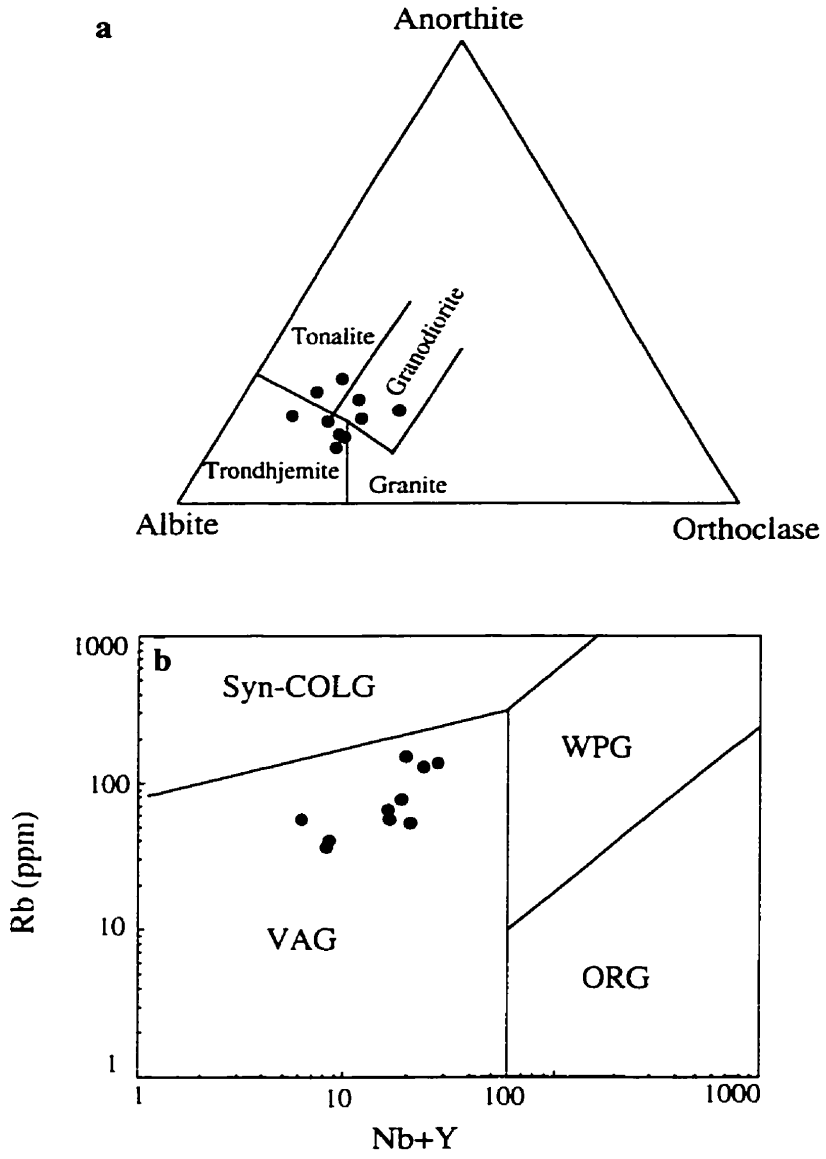

Figure 5.2. (a) Anorthite-Albite-Orthoclase ternary diagram for granitoids of the Schreiber-Hemlo and White River-Dayohessarah greenstone belts, indicating a TTG composition. (b) Rb vs Nb+Y diagram, suggesting a volcanic arc origin. Syn-COLG: Syn-collisional granitoids, VAG: volcanic arc granitoids, WPG: within plate granitoids, ORG: ocean ridge granitoids. Fields after Pearce et al. (1984).

Table 5.1. Summary of significant compositional values and inter-element ratios of granitoids, and mafic- intermediate and felsic sills and dykes of the Schreiber-Hemlo and White River-Dayohessarah greenstone belts.

	Granitoids	Mafic to intermediate sills and dykes	Felsic sills and dykes
SiO_2 (wt. %)	65-72	48-58	61-71
MgO	0.7-2.0	4.9-13.7	0.2-2.5
TiO_2	0.3-0.6	0.6-0.8	0.2-0.6
Fe_2O_3	2.1-4.2	7-10	1.4-4.8
Cr (ppm)	10-42	38-800	7-129
Ni	3-20	18-400	2-52
Th	2.1-22	3.6-12	4.5-16
La	14-55	30-93	24-51
Nb	2-10	5-9	3.3-14
Zr	89-203	108-203	139-240
Y	5-14	13-23	5-12
$(La/Yb)_{cn}$	17-53	13-41	17-190
$(La/Sm)_{cn}$	3.1-7.5	2.8-4.7	4.2-6.8
$(Gd/Yb)_{cn}$	2.6-7.9	2.5-5.4	2.1-21.5
Al_2O_3/TiO_2	33-57	17-27	33-108
Zr/Hf	28-41	38-43	36-50
Th/Nb	0.7-1.9	0.7-1.7	0.8-2.3
Th/La	0.09-0.44	0.1-0.3	0.1-0.4
Ti/Zr	9.5-19	16-44	4.3-20
Zr/Y	12-27	5.7-16	11-32
Nb/Nb*	0.1-0.2	0.1-0.2	0.1-0.2
Eu/Eu*	0.6-1.0	0.8-0.9	0.8-0.9
Zr/Zr*	0.6-1.2	0.3-1.1	0.9-1.6
Hf/Hf*	0.6-1.3	0.3-0.9	0.7-1.2
Ti/Ti*	0.15-0.4	0.1-0.3	0.1-0.3

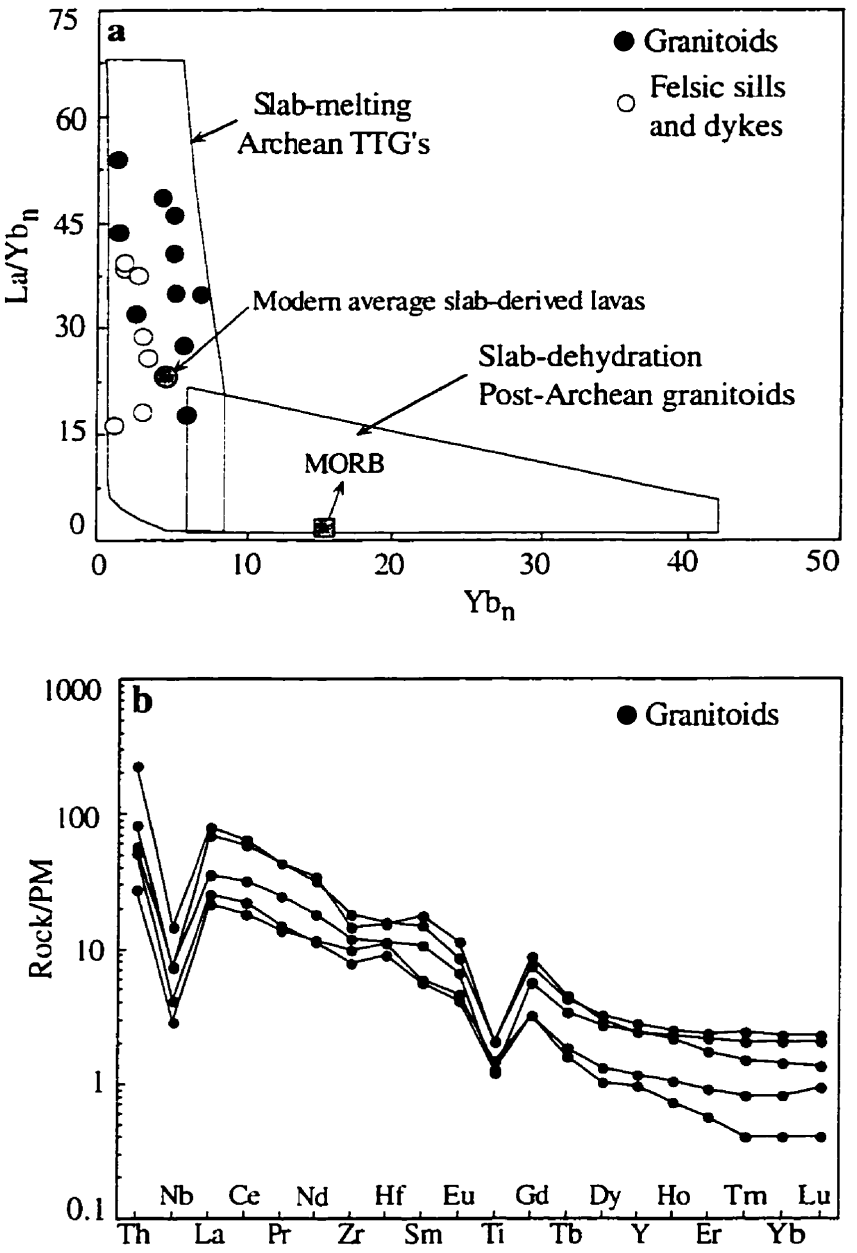

Figure 5.3. (a) La/Yb$_n$ vs Yb$_n$ variation diagram for granitoids and felsic sills (Fields after Martin, 1993). (b) Primitive mantle-normalized diagram for granitoids. Normalzing values from Sun and McDonough (1989).

that Th and LREE behave coherently during slab melting processes. Fractionation of primary melts produced a range of SiO_2 and REE contents. Collectively, HFSE (Nb, Ta, Y, Zr) and LILE (Rb) contents are consistent with a volcanic arc origin (Figs. 5.2b; Table 5.1; Appendix 5.1; see Pearce et al., 1984).

In summary, the geochemical characteristics of granitoids in the Schreiber-Hemlo and White River-Dayohessarah greenstone belts are similar to slab-derived tonalites and adakites (LREE enriched and HREE depleted volcanic rocks that form at modern convergent margins where subducting slab is younger than 30 Ma) volcanic rocks of the late Cenozoic-early Mesozoic Chugach, and the modern Nankai, subduction accretion complexes of southern Alaska and Southern Japan, respectively, which apparently resulted from shallow subduction of hot, young oceanic plates (see Sisson and Hollister, 1988; Morris, 1995).

5-4. Mafic to felsic sills and dykes

The late stages of D_1 and D_2 mélange formation (Chapter 6) were accompanied by the intrusion of syn-kinematic, mafic to felsic sills and dykes ranging from a few centimetres to several hundred metres in thickness, primarily along the D_2 strike-slip faults and S_1 planes (see Chapter 6). The absence of D_1 fabrics in these sills and dykes suggests that their intrusion post-dates tectonic juxtaposition of trench turbidites with oceanic arc and plateau fragments (see Chapter 6; Polat and Kerrich, 1998). Mafic to felsic sills and dykes reported in this chapter were obtained only from the Schreiber assemblage. Based on mineralogical and geochemical compositions, these sills and dykes are divided into two distinctive groups: (1) mafic to intermediate and (2) felsic. The principal geochemical characteristics of these groups are as follows:

5-4-1. Mafic to intermediate sills and dykes

Compositionally, mafic to intermediate sills and dykes are gabbros and diorites. They have moderate variations in SiO_2 (48-58 wt.%), Fe_2O_3 (7-10 wt.%), TiO_2 (0.60-0.85 wt.%), V (160-217 ppm), and Sc (20-26 ppm), and large variations MgO (5-14 wt.%), Cr (67-800 ppm), Co (27-55 ppm), and Ni (18-400 ppm) abundances (Table 5.1; Appendix 5.2). They are calc-alkaline in composition. The geochemistry of gabbroic to dioritic sills and dykes suggest a coherent suite with a continuous compositional variation from more primitive mafic to moderately evolved intermediate melts (Mg#=60-30; Table 5.1).

On a primitive mantle-normalized diagram, the group is characterized by: (1) variably enriched REE patterns (La/Sm_n=2.8-4.7, Gd/Yb_n=2.5-5.4, and La/Yb_n=13-41); (2) commensurately high Zr/Y (5.7-15.5) ratios; (3) large negative Nb and Ti anomalies (Nb/Nb*=0.1-0.2, Ti/Ti*=0.1-0.3); (4) Zirconium and Hf anomalies (Zr/Zr*=0.3-1.1, Hf/Hf*=0.3-0.9) are variably negative to zero; and (5) ratios of Zr/Hf (38-44) are systematically greater than the primitive value of 36 (Figs. 5.4a; Table 5.1; Appendix 5.2). Collectively, these geochemical results indicate a magmatic arc signature, with slab dehydration wedge melting and garnet ± hornblende residue in the source; the arc was likely intraoceanic rather than continental margin based on HFSE/REE inter-element ratios and transition metal contents (cf. McDonough, 1991; Pearce and Parkinson, 1993; Hawkesworth et al., 1993; Pearce and Peate, 1995 and references therein).

5-4-2. Felsic sills and dykes

Felsic sills and dykes from the Schreiber assemblage possess variable SiO_2 (61-71 wt.%), Al_2O_3 (15-19 wt.%), TiO_2 (0.20-0.6 wt.%), Fe_2O_3 (1.4-3.5 wt.%), MgO (0.2-1.3 wt.%), Cr (7-34 ppm), Na_2O (4.5-8.4 wt.%), and Ni (2-17 ppm) contents (Table

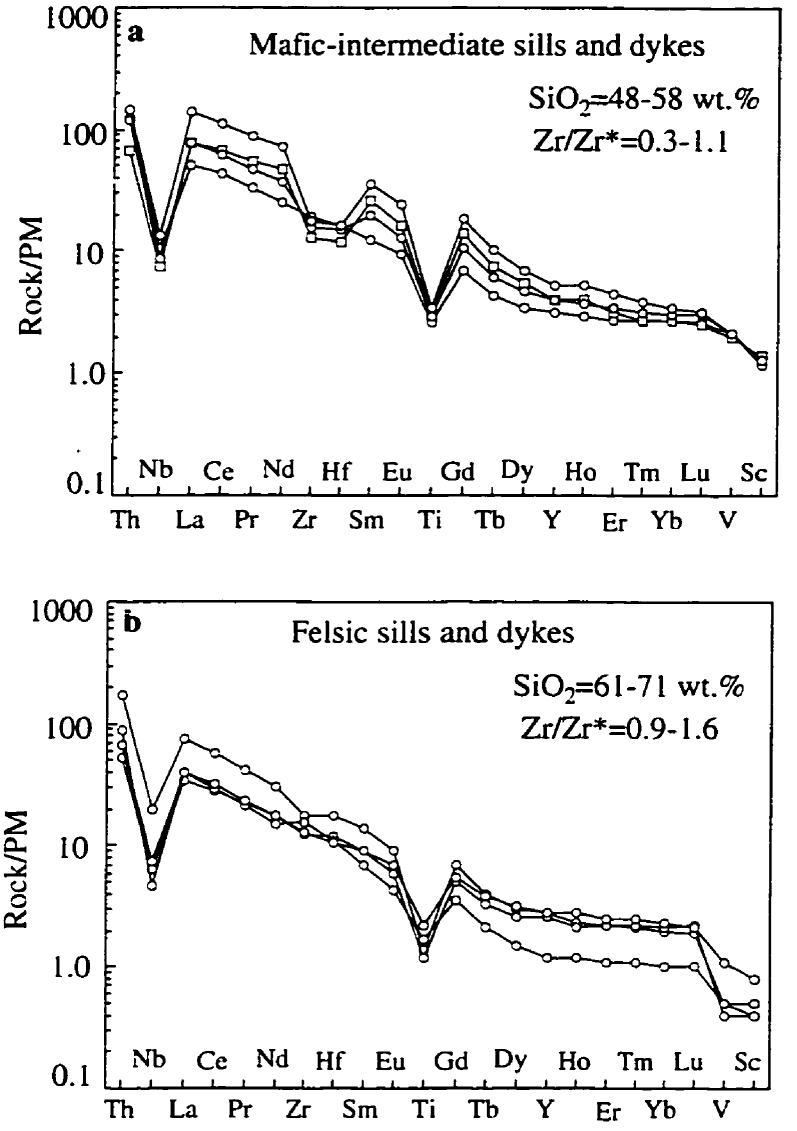

Figure 5.4. (a) Primitive mantle-normalized diagram for mafic-intermediate sills and dykes. (b) Primitive mantle-normalized diagram for felsic sills and dykes. Normalizing values from Sun and McDonough (1989).

5.1; Appendix 5.3). One outlier has higher MgO (4.8 wt.%), Cr (129 ppm) and Ni (52 ppm) contents. Compositionally they are comparable to high-Na, high Al-tonalite-trondhjemite-granodiorites. They are similar to TTG in terms of REE patterns, HFSE/REE, Nb/Nb*, and Ti/Ti* ratios, signifying significant fractionation between incompatible, moderately compatible, and compatible HFSE and REE (Figs. 5.3a, 5.4b; Table 5.1; Appendix 5.3).

Given the smooth patterns from LREE to Th, positive Zr (Hf) anomalies may have resulted from clinopyroxene fractionation (see Chapter 4; Rollinson, 1993; Skulski et al., 1994). In conclusion, excepting pronounced positive Zr and Hf anomalies, these geochemical characteristics are comparable to those of TTG intrusions, and consistent with subduction zone-related magmatism with garnet residual in the source (cf. McDonough, 1991; Pearce and Parkinson, 1993; Hawkesworth et al., 1993; Pearce and Peate, 1995). Collectively, these geochemical characteristics of felsic sills and dykes are similar to those of mafic to intermediate counterparts, but more fractionated to higher SiO_2 but lower mafic element contents.

5.5. Siliciclastic sedimentary rocks

Siliciclastic rocks of the Schreiber-Hemlo and White River-Dayohessarah greenstone belts are dominantly distal turbiditic graywacke sandstones and shales. They are tectonically juxtaposed against volcanic sequences (see Chapter 6).

Graywacke sandstones have narrow variations in SiO_2 (61-69 wt.%), TiO_2 (0.4-0.8 wt.%), Al_2O_3 (15-19 wt.%), and MgO (1.3-3.9 wt.%), but moderate to large variations in Fe_2O_3 (3.1-7.7 wt.%), K_2O (1.4-3 wt.%), Na_2O (2.9-5.1 wt.%), Ni (10-160 ppm), and Cr (10-380 ppm) contents (Table 5.2; Appendix 5.4).

On a primitive mantle-normalized diagram, they are characterized by: (1) strongly

LREE enriched patterns, where La/Sm_n=3.4-5.0, La/Yb_n=15-40, and Gd/Yb_n=2-5; (2) commensurately low Ti/Zr (16-37) ratios; (3) large negative Nb (Nb/Nb*=0.1-0.2) and Ti (Ti/Ti*=0.2-0.8) anomalies; and (4) minor to zero Eu (Eu/Eu*=0.8-1) anomalies (Fig. 5.5a; Table 5.2). Ratios of Zr/Hf (29-40) span the chondritic value of 36.

Shales have lower Na_2O (0.1-4.4 wt.%), but higher Al_2O_3 (13.6-19 wt.%), TiO_2 (0.3-0.8 wt.%), Fe_2O_3 (6.9-9.7 wt.%), K_2O (1.8-3.6 wt.%), Ni (50-120 ppm), and Cr (30-440 ppm) contents than the inter-bedded sandstones (Table 5.2; Appendix 5.5). Primitive mantle-normalized trace element patterns and inter-element ratios of shales are comparable to those of sandstones, suggesting a similar provenance for the two populations (Fig. 5.5a; Table 5.2; cf. Taylor and McLennan, 1985).

The Schreiber-Hemlo and White River-Dayohessarah greenstone belts are composed dominantly of mafic volcanic rocks (~ 70 %); however, the enclosed fine-grained siliciclastic sedimentary rocks in these greenstone belts are geochemically distinct from juxtaposed mafic volcanic rocks of ocean plateau origin (see Chapters 3 and 4). Strongly fractionated LREE patterns and inter-element ratios, with large negative Nb (Nb/Nb*=0.12-0.22) and Ti (Ti/Ti*=0.30-0.43) anomalies signify an oceanic magmatic arc provenance for the turbidites (cf. Feng and Kerrich, 1990; Feng et al., 1993). These geochemical characteristics are similar to those of intermediate to felsic rocks of the Schreiber-Hemlo and White River-Dayohessarah greenstone belts, and high-Al TTG plutons of the Wawa Subprovince. However, transition metal (Ni, Co, Cr and Sc) contents of the sediments are relatively higher than those of felsic volcanics and TTG plutons, suggesting mixed felsic to intermediate and mafic inputs, with a high felsic/mafic ratios (Fig. 5.5b; cf. Taylor and McLennan, 1985).

Collectively, field characteristics and trace element relationships are consistent with the siliciclastic sedimentary rocks of the Schreiber-Hemlo and White River-Dayohessarah

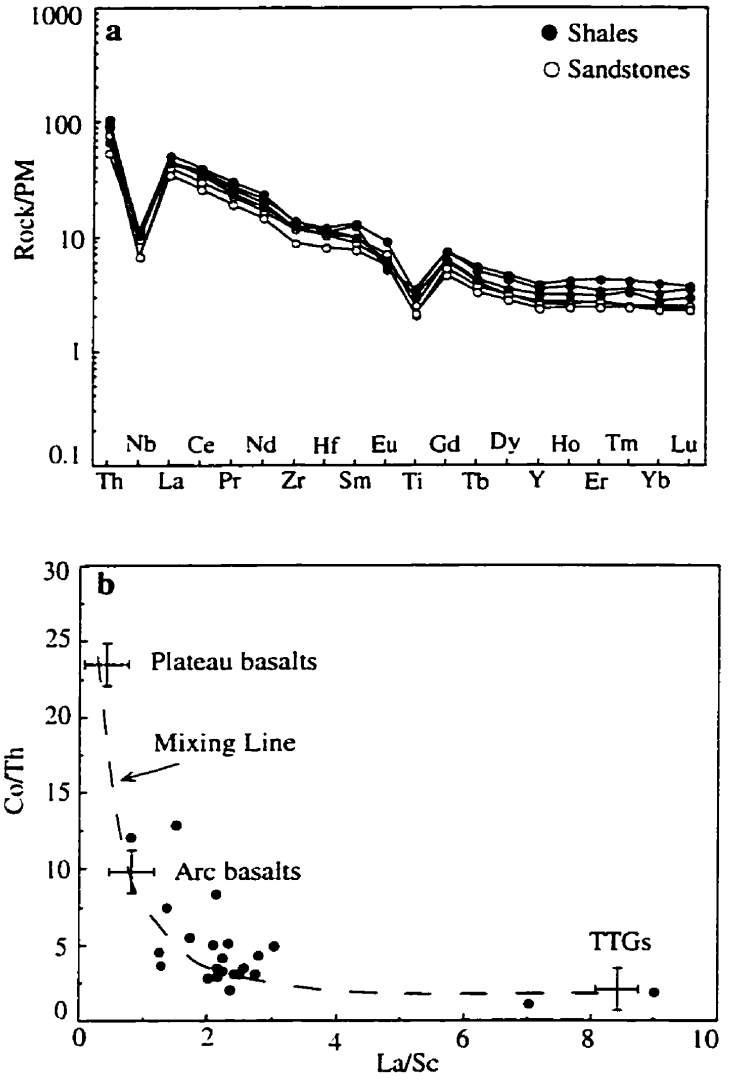

Figure 5.5. (a) Primitive mantle-normalized diagram for turbidites. (b) Co/Th vs La/Sc binary variation diagram, indicating mixed (mafic and felsic) sources for turbidites (shales and sandstones) of the Schreiber-Hemlo and White River-Dayohessarah greenstone belts. Mixing line after Taylor and McLennan (1985).

Table 5.2. Summary of significant compositional values and inter-element ratios for sandstones and shales of the Schreiber-Hemlo and White River-Dayohessarah greenstone belts.

	Sandstones	Shales
SiO_2 (wt.%)	61-69	58.5-71
TiO_2	0.4-0.8	0.25-0.8
Fe_2O_3	3.1-7.7	6.9-9.7
Na_2O	2.9-5.1	0.1-4.4
K_2O	1.4-3	1.85-3.6
Cr (ppm)	10-380	30-440
Co	8-48	9-42
Ni	10-160	50-120
Sc	5-19	3-26
V	48-142	16-200
Rb	40-80	44-97
Sr	390-1070	56-442
Th	1.3-7.8	4.4-9.6
Nb	2.5-7.0	6.1-8.2
La	12-41	27-36
Zr	85-180	116-153
Y	6-18	6-18
Yb	0.5-1.4	0.7-2.0
$(La/Yb)_{cn}$	15-40	11.6-29
$(La/Sm)_{cn}$	3.4-4.7	3.6-6
$(Gd/Yb)_{cn}$	2-5	1.9-2.4
Al_2O_3/TiO_2	20-36	24-52
Zr/Hf	29-40	31-44
La/Nb	4-9	3.7-4.4
Th/Nb	0.5-1.8	0.6-1.2
Th/La	0.11-0.3	0.16-0.3
Zr/Y	6.6-21	7.2-19
Ti/Zr	16-37	13-35
Th/Sc	0.11-0.65	0.2-1.6
La/Sc	0.8-7	1.2-9.0
Eu/Eu*	0.8-1.0	0.8-1.0
Nb/Nb*	0.1-0.2	0.16-0.23
Ti/Ti*	0.2-0.8	0.3-0.4
Zr/Zr*	0.5-1.4	0.7-1.1

belts being orogenic trench turbidites, with a provenance of basalts and intermediate to felsic high Na, high La/Yb_n intrusions, respectively directly comparable to plateau and arc basalts, and Ttg plutons (cf. McLennan et al., 1990; Prame and Pohl, 1994; Garver and Scott, 1995; Polat et al., 1996b; Polat et al., 1998b; Polat and Kerrich, 1998).

5-6. Conclusions and implications

The principal conclusions of this chapter, and tectonic implications, are as follows:

1. High precision ICP-MS trace element data obtained from the syn-kinematic, granitoid intrusions of the Schreiber-Hemlo greenstone belt indicate a high-Na, high-Al TTG suite. LILE enrichment and Nb, Ti depletions consistent with a magmatic arc geodynamic setting. Inter-element ratios (e.g., La/Yb_n) are consistent with hydrous slab melting with garnet in the residue. The geochemical characteristics of the Schreiber-Hemlo TTG intrusions are comparable to those of high-Al TTG intrusions of Cenozoic subduction zones, where the age of subducting oceanic lithosphere is apparently younger than 30 Ma (see Drummond and Defant, 1990).

2. Syn-kinematic, mafic to felsic dykes and sills were intruded primarily along D_2 strike-slip faults and S_1 planes (see Chapter 6). The absence of D_1 fabrics in these dykes and sills suggests that their intrusional post-tectonic juxtaposition of trench turbidites with oceanic arc and plateau fragments. The geochemistry of the dykes and sills is consistent with slab dehydration, mantle wedge-derived melts for mafic and intermediate intrusions, and oceanic slab-derived melts for felsic intrusions. The intrusion of subduction-derived, mafic to felsic igneous rocks into subduction-accretion complexes is an important feature of Phanerozoic subduction-accretion complexes, such the Chugach accretionary complex of Alaska (Page et al., 1986), the

Shimanto accretionary complex of Japan (Hasebe et al., 1993), Altaid accretionary complexes of Central Asia (Sengor and Natal'in, 1996), and Cordilleran accretionary complexes of British Columbia (Hollister and Andronicos, 1997).

3. Trace element systematics of syn-kinematic, siliciclastic, trench turbidites of the Schreiber-Hemlo and White River-Dayohessarah greenstone belts are consistent with a magmatic arc provenance of mixed mafic to felsic source components directly comparable to arc basalts and high-Na, high-Al tonalitic intrusions. Given their tectonic relationships with oceanic plateau sequences, and intrusive relationships with mafic to felsic sills and dykes, the geological characteristics of these turbidites are comparable to those of listed above (see Garver and Scott, 1995; Umhoefer and Schiarizza, 1996).

CHAPTER 6. STRUCTURAL GEOLOGY AND MÉLANGE FORMATION

6-1. Introduction

Deciphering the structural geometry, and using that information to interpret the kinematics and geodynamic evolution of Archean greenstone belts represents one of the least tractable problems in structural geology (Kusky and Vearncombe, 1997). Many chronological tools available for structural interpretation of Phanerozoic greenstone belts, such as fossil-controlled stratigraphic analysis, are absent in Archean counterparts, and the three dimensional exposures of some Phanerozoic mountain belts is lacking. Poly-phase deformation, and greenschist to amphibolite facies metamorphism of Archean greenstone belts are the rule rather than the exception. Several decades of structural studies combined with increased use of U-Pb geochronology have enabled geologists to unravel the tectonic histories of some Archean greenstone belts. These studies have revealed a remarkable structural diversity, that has led in turn to the suggestion that the nature of deformation in many respects is comparable to that of some younger orogenic belts (Kusky and Vearncombe, 1997; Polat and Kerrich, 1998). In this chapter, the structural characteristics of the late Archean Schreiber-Hemlo and White River-Dayohessarah greenstone belts are described. These structural characteristics are compared with those of Phanerozoic orogenic belts in an attempt to understand better the geodynamic evolution of these greenstone belts specifically, and Archean greenstone belts in general.

Previous structural studies in the Schreiber-Hemlo and White River-Dayohessarah greenstone belts have focused primarily on the Hemlo gold deposit and Lake Superior-

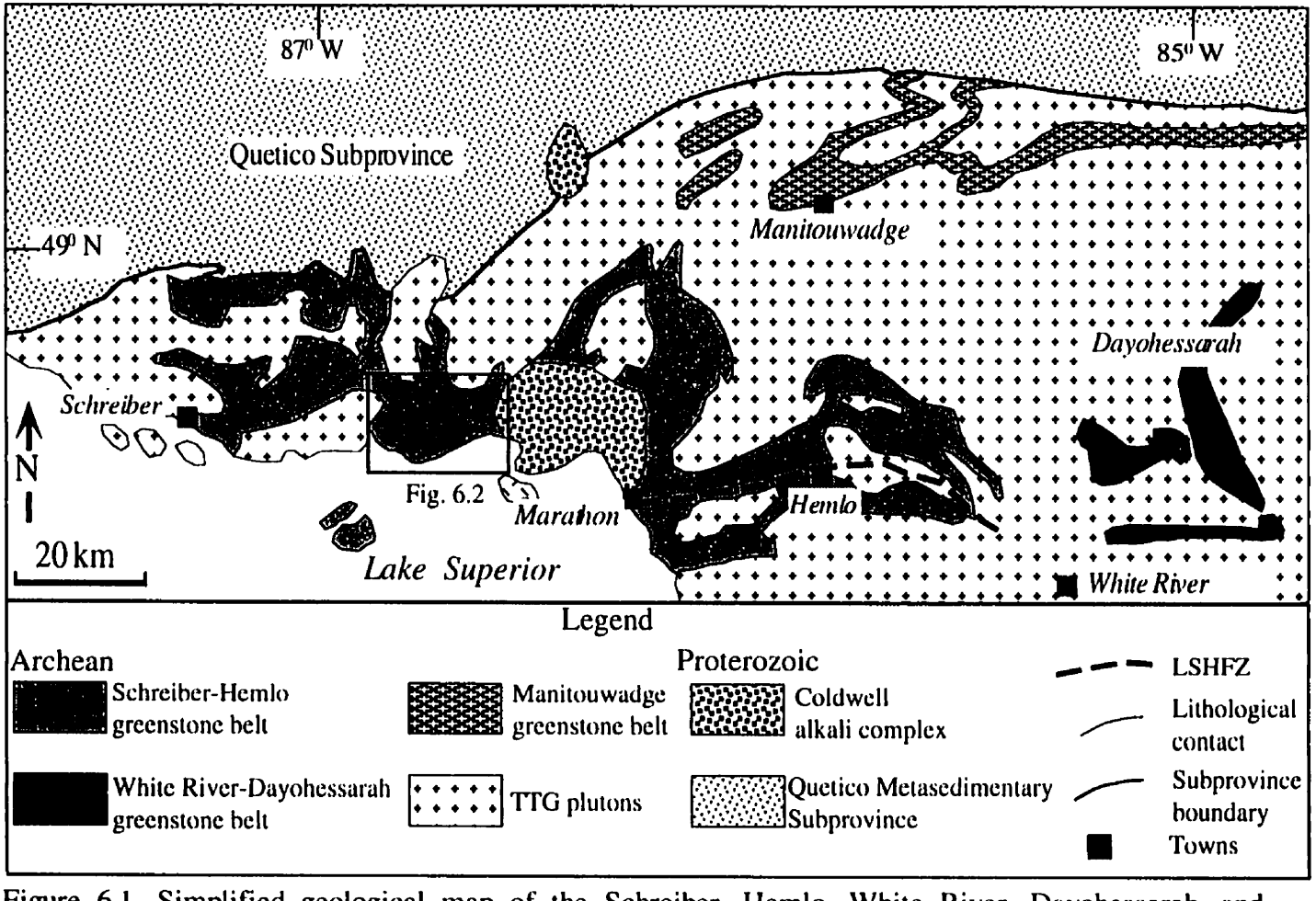

Figure 6.1. Simplified geological map of the Schreiber, Hemlo, White River, Dayohessarah, and Manitouwadge areas of the Wawa subprovince (Modified after Williams et al., 1991). LSHFZ: Lake Superior-Hemlo fault zone. TTG: Tonalite-trondhjemite-granodiorite.

Hemlo fault zone (LSHFZ) [Figs. 6.1; Hugon, 1984; Muir and Elliot, 1987; Muir, 1988; Kuhns et al., 1994]. These studies revealed that the region has undergone complicated, poly-phase deformation. However, inter-relationships between various types of structures, and their significance for interpreting regional tectonics was not addressed in those papers. In this study, new structural data from microscopic to regional scales, obtained mostly from the Schreiber-Hemlo belt, are presented to assess the regional geodynamic evolution. Part of this work provides the first detailed documentation of an Archean tectonic mélange, with proposed mechanisms of its formation (Figs. 6.1, 6.2).

The Schreiber-Hemlo and White River-Dayohessarah greenstone belts are separated by multiple syn- to post-tectonic granitoid intrusions, which impose major difficulties for establishing regional correlations based on large-scale structures (Fig. 6.1). For this reason emphasis is placed on mesoscopic structures, which tend to be localized along highly strained shear zones, rather than being pervasively developed throughout the region. Unlike mesoscopic to regional structures, microscopic structures are rare, and preferentially developed in the turbidites. This is mainly due to the massive isotropic nature of the volcanic flows, and perhaps in part to there having been several episodes of recrystallization.

Overprinting relations between different sets of structures suggest that these greenstone belts underwent three phases of deformation: two probably prior to, and one during the assembly of the southern Superior Province between 2.70 and 2.65 Ga (Fig. 6.3; Polat et al., 1998b, Polat and Kerrich, 1998). The main characteristics of these phases are discussed below.

6-2. Deformation Phase I (D_1)

The earliest deformation phase (D_1) in the Schreiber-Hemlo belt is characterized by

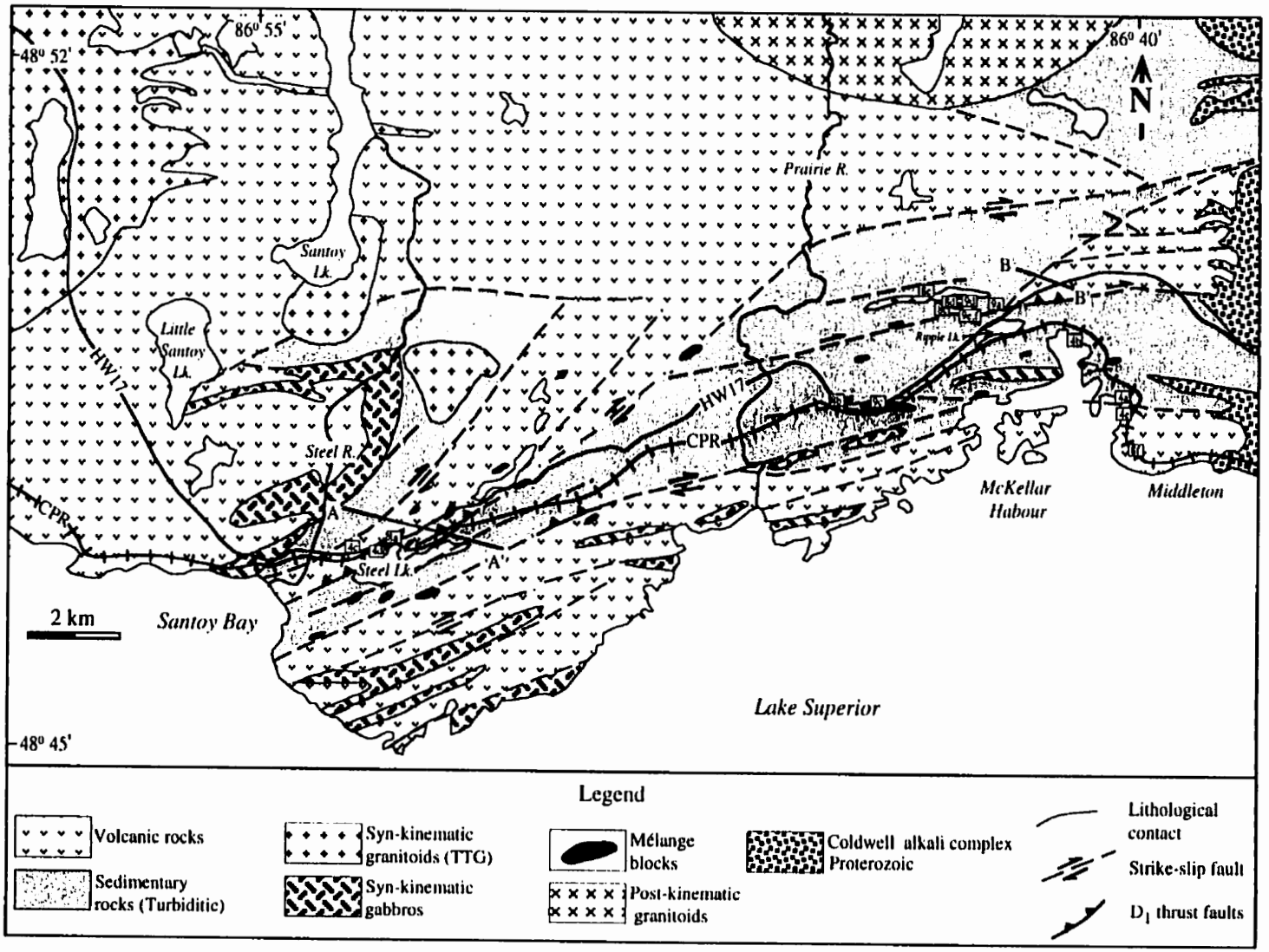

Figure 6.2. Geological map of the Santoy Lake-Middleton area of the Schreiber-Hemlo greenstonebelt. The northern part of the map is modified from Walker (1967). HW17: Highway 17; CPR: Canadian Pacific Railway.

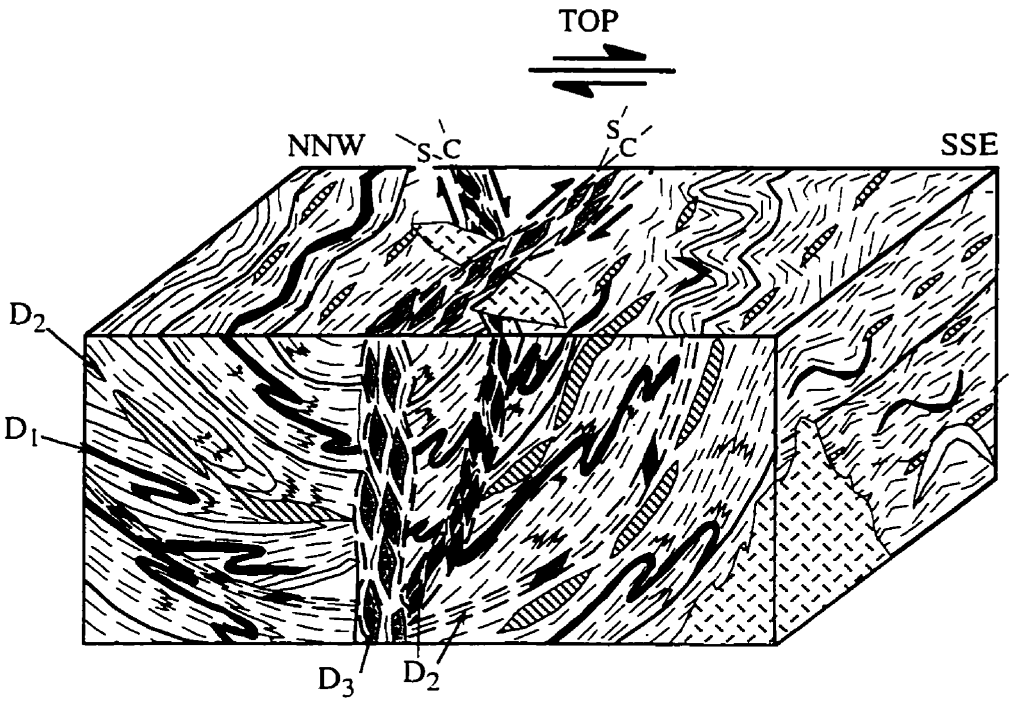

Figure 6.3. A simplified block diagram showing the overprinting relationships between the three phases of deformation recognized in the Schreiber-Hemlo and White River-Dayohessarah greenstone belts.

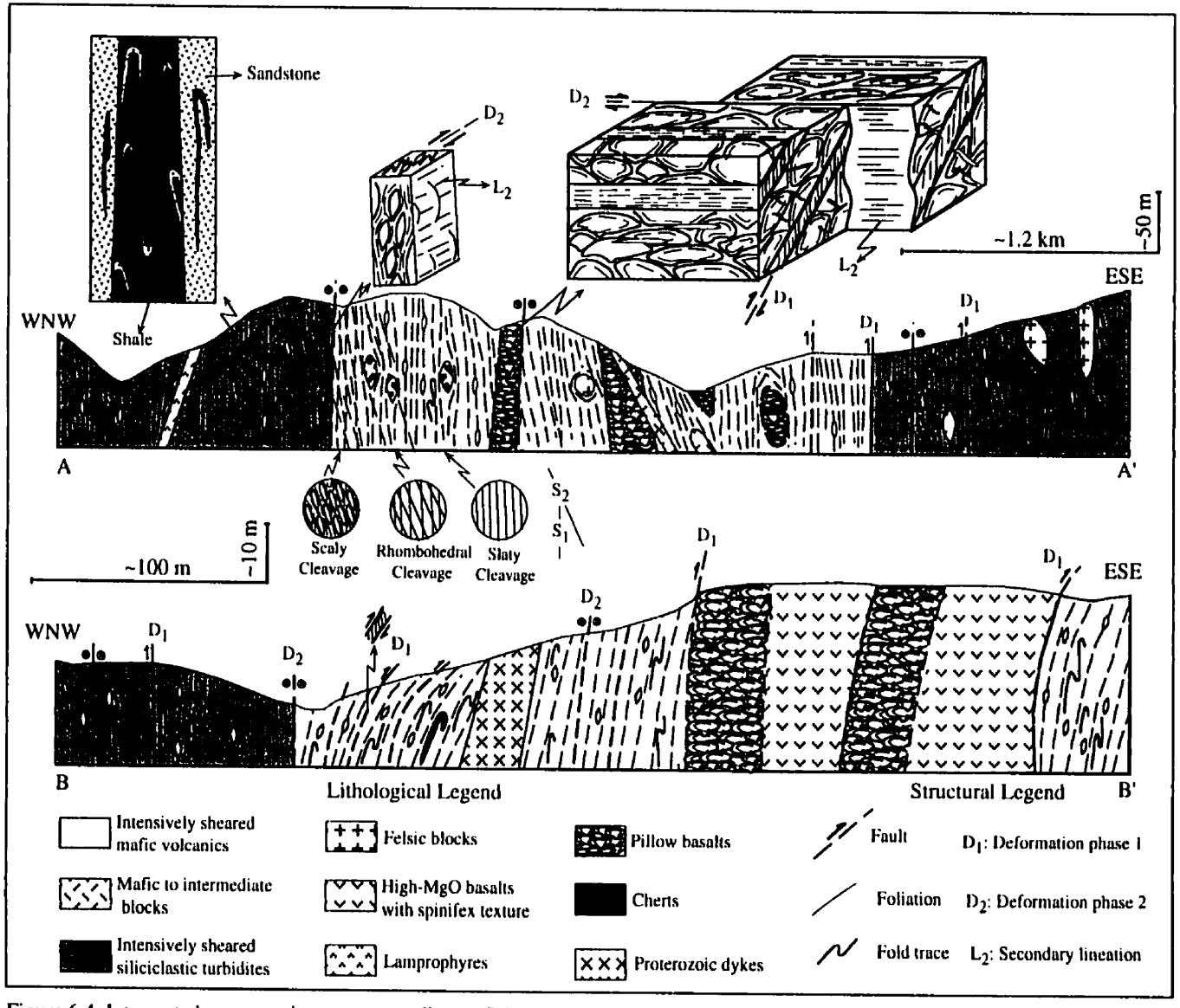

Figure 6.4. Interpreted cross-sections corresponding to field traverses from the Steel Lake (A-A') and Ripple Lake (B-B') area. Inset diagrams are based on detailed field observations. For locations see Figure 6.2.

ENE- striking, rotated thrust faults, and ENE-striking, bedding-parallel slaty cleavage in turbidites and metamorphic layering in volcanic rocks; the foliation dips NNW to SSW (Figs. 6.2, 6.4). The thrust faults occur primarily within sedimentary and volcanic sequences, and locally between them (Fig. 6.4). In addition there are: (1) moderately- to steeply-plunging mineral stretching lineations (L_1); (2) asymmetric, overturned tight to isoclinal folds (F_1) and associated sheath folds; and (3) layer parallel, extensional boudins within turbidites and greenschist to amphibolite facies metavolcanic rocks (Figs. 6.5-6.8).

The L_1 stretching lineations developed within contemporaneous foliation planes are defined by the preferred dimensional orientation of phyllosilicates in metavolcanic rocks, and elongate feldspar and quartz porphyroclasts in sedimentary rocks. The orientation of the F_1 fold hinge lines and axial planes was modified during subsequent deformations; however, the asymmetry of the F_1 overturned folds is consistent throughout the study area, suggesting a regional SSE tectonic vergence during D_1 (Figs. 6.4, 6.5). All primary structures underwent intense transposition during D_1 and subsequent deformation phases: transposition resulted in abrupt lithological changes, for example truncation of sandstones by shales or vice versa; rotation of primary sedimentary structures such as way-up directions; and development of discrete crenulation cleavages, isoclinal fold hooks, and rootless folds (Fig. 6.6).

6-3. Deformation Phase II (D_2)

Second generation structures are well-developed in the Schreiber section of the belt (Figs. 6.1, 6.2). They are dominated by mesoscopic to regional scale, ENE-trending, right-lateral strike-slip fault zones, which are ductile to brittle in character. Faults zones are from about one centimetre- to a metre-thick, and are defined by well-developed, near-

vertical and near-horizontal L_2 slickenlineations (Figs. 6.2-6.4, 6.7a, 6.8, 6.9). Coeval mesoscopic, ENE-striking, thrust shear zones characterized by moderately- to steeply-plunging L_2 slickenside lineations are sporadically developed (Fig. 6.9). The D_1 and D_2 thrust faults are distinguished from one another based on their relationships with the D_2 strike-slip faults: although the D_2 strike-slip and thrust shear zones, and associated lineations, occur close to one another, they never cut each other. In contrast, the D_1 thrust faults are cut by the D_2 strike-slip faults (Fig. 6.4).

The style and intensity of deformation along the strike-slip shear zones varies along strike. They are characterized by a number of structures including: (1) anastomosing (curviplanar) slickensides; (2) rhombohedral and scaly cleavages; (3) sigmoidal quartz, mafic and felsic boudins; (4) reverse kink-bands; (5) microscopic to mesoscopic, NE-striking, asymmetric, upright, steeply- to vertically-plunging folds (including crenulation cleavage); (6) microscopic to mesoscopic mineral elongation and slickenside lineations (L_2), S-C planar fabrics, and sigma (σ) structures; and (7) microscopic mica fish structures (Figs. 6.5-6.9).

The boudins are primarily symmetrical in vertical sections, but show dominantly monoclinic asymmetry on horizontal surfaces (Fig. 6.9). These asymmetric boudins were further deformed, folded and rotated during progressive D_2 strike-slip deformation (Fig. 6.7b). Both the vertical L_1 and horizontal L_2 lineations have limited ranges of orientations throughout the belt (Fig. 6.8b,d). On a microscopic scale, the L_2 lineation is characterized by well-developed quartz, amphibole, and calcite ribbons. The quartz and calcite ribbons are commonly associated with pyrite porphyroclasts. Strike-slip shear zones are more common than thrust counterparts. Collectively, the geometrical relationships of asymmetric boudins and folds, S-C planar fabrics, mica fish structures, and Riedel shears

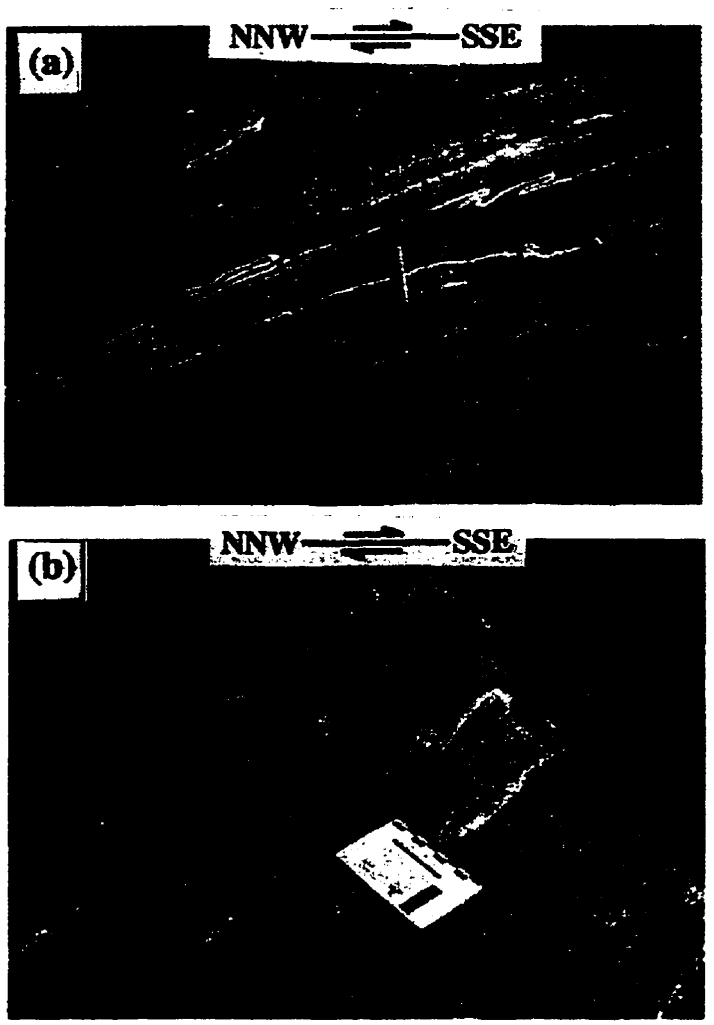

Figure 6.5. Tight to isoclinal, asymmetric F1 folds indicating a SSE tectonic vergence during D1.

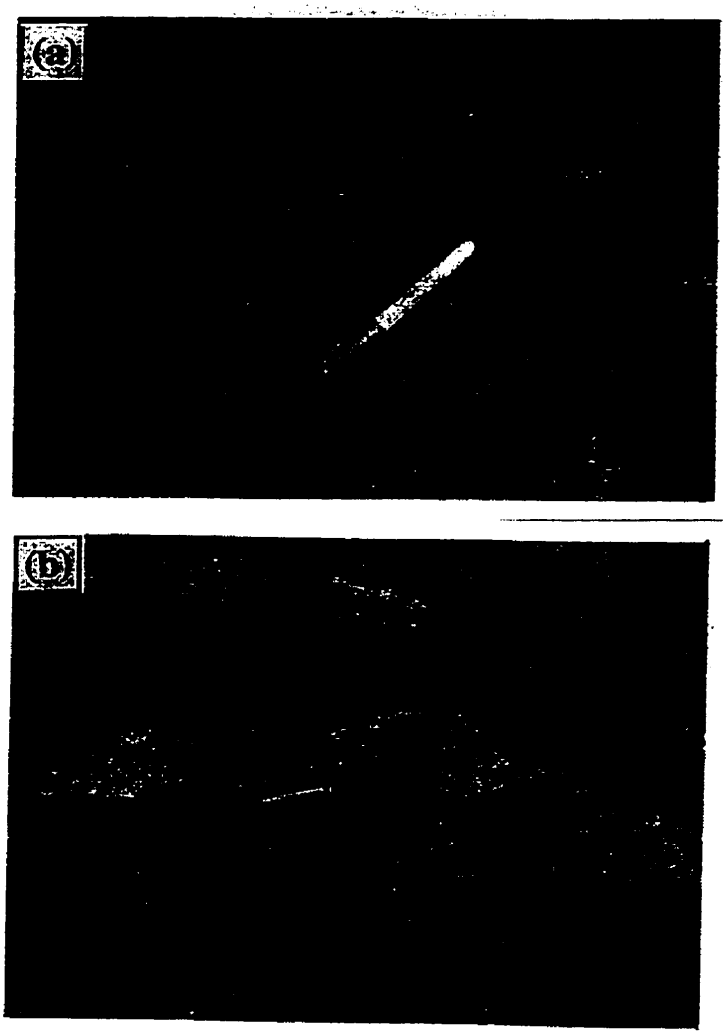

Figure 6.6. Transposed layers, foliations, shear planes, folds, and veins within siliciclastic turbidites.

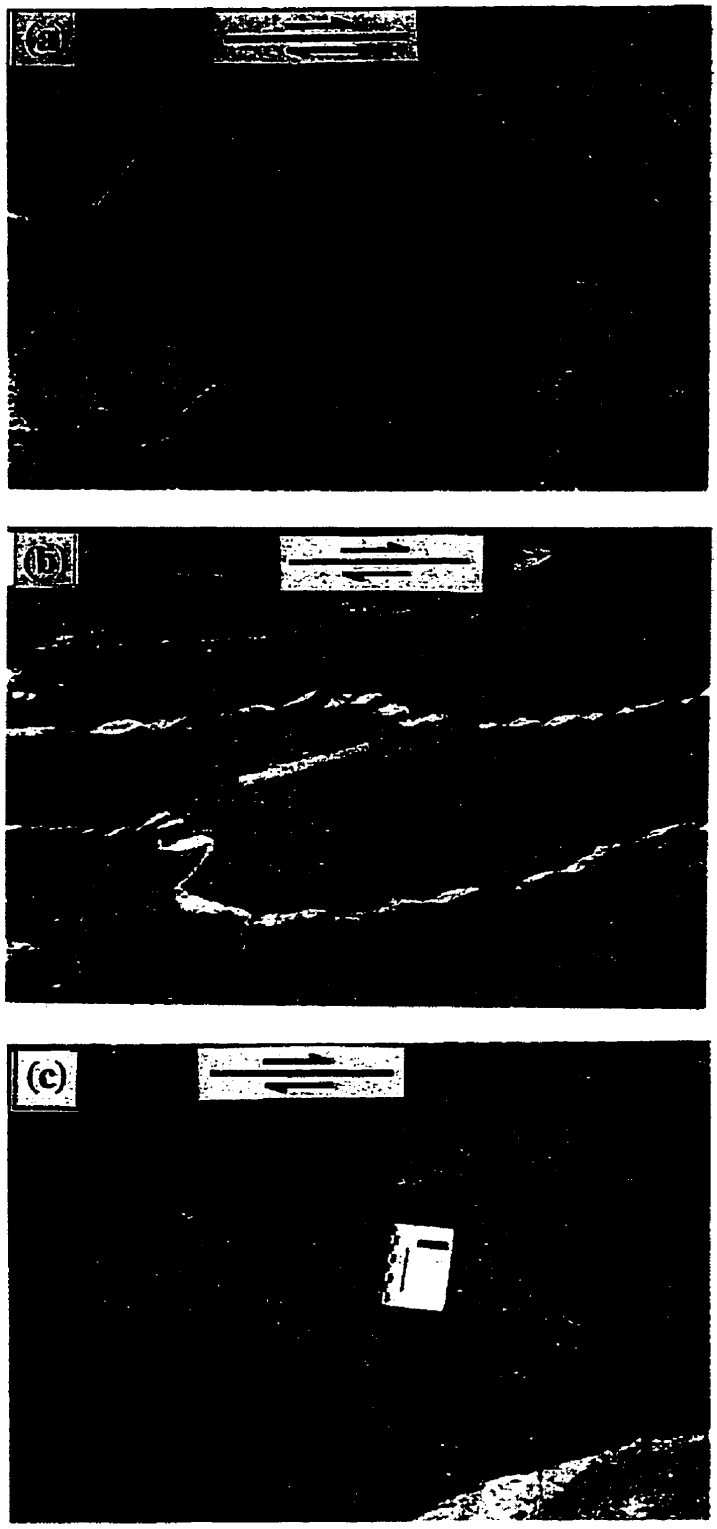

Figure 6.7. (a) Slickenside surfaces and lineations developed within D2 right-lateral strike-slip faults. (b) Sigmoidal quartz veins indicating right-lateral shearing during D2. (c) Delta structures occuring along the Lake Superior-Hemlo fault zone (D3), indicating right-lateral shear-sense.

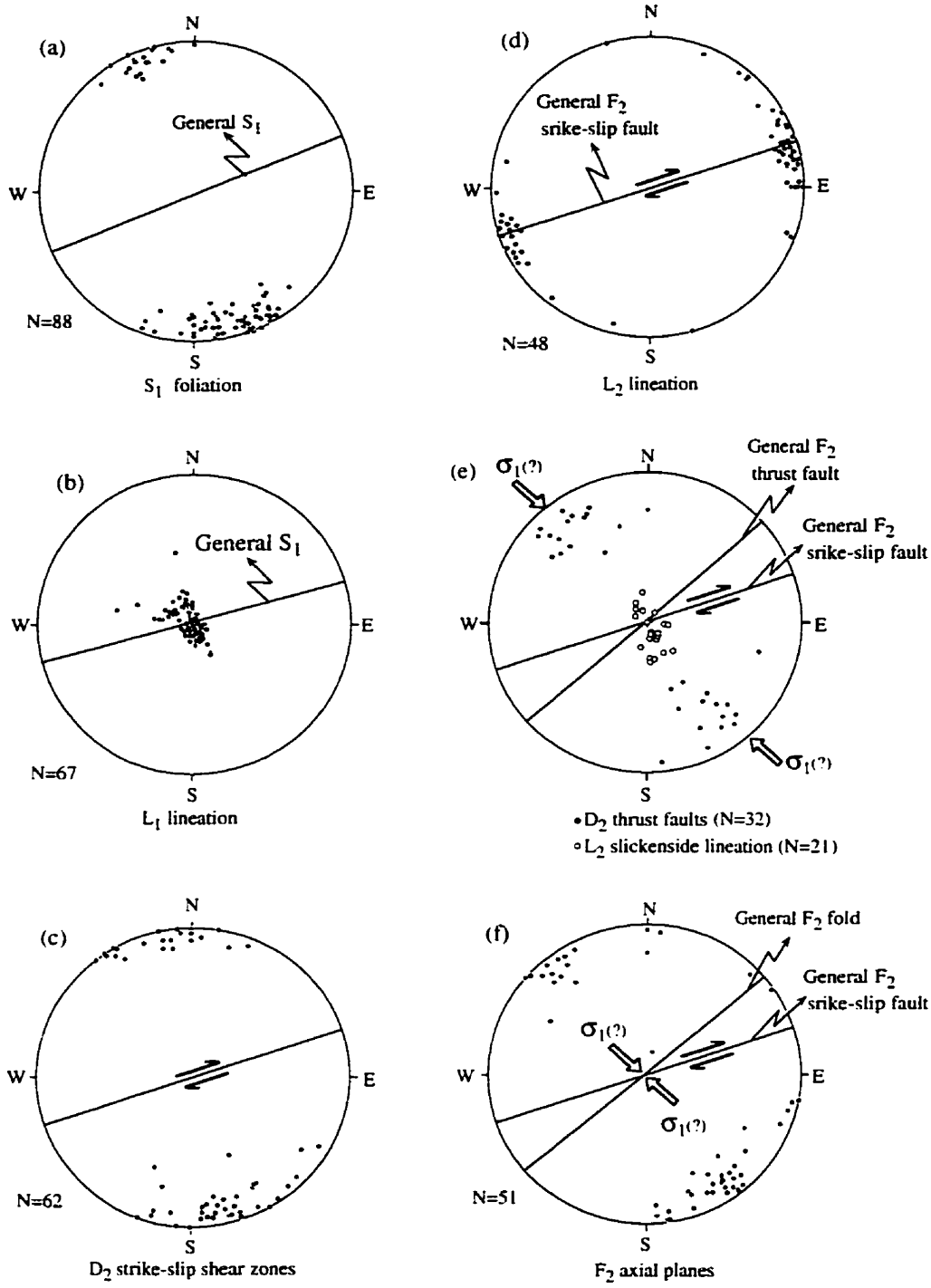

Figure 6.8. Equal area, lower hemisphere projections: (a) Poles to S_1 foliation; (b) L_1 mineral elongation lineation, (c) D_2 strike-slip shear zones, arrows indicate interpreted slip direction; (d) L_2 slickenside lineations, arrows indicate interpreted slip direction; (e) Poles to D_2 thrust faults, arrows indicate interpreted the greatest horizontal compression direction during D_2; (f) Poles to F_2 axial planes, arrows indicate interpreted the greatest horizontal compression direction during D_2.

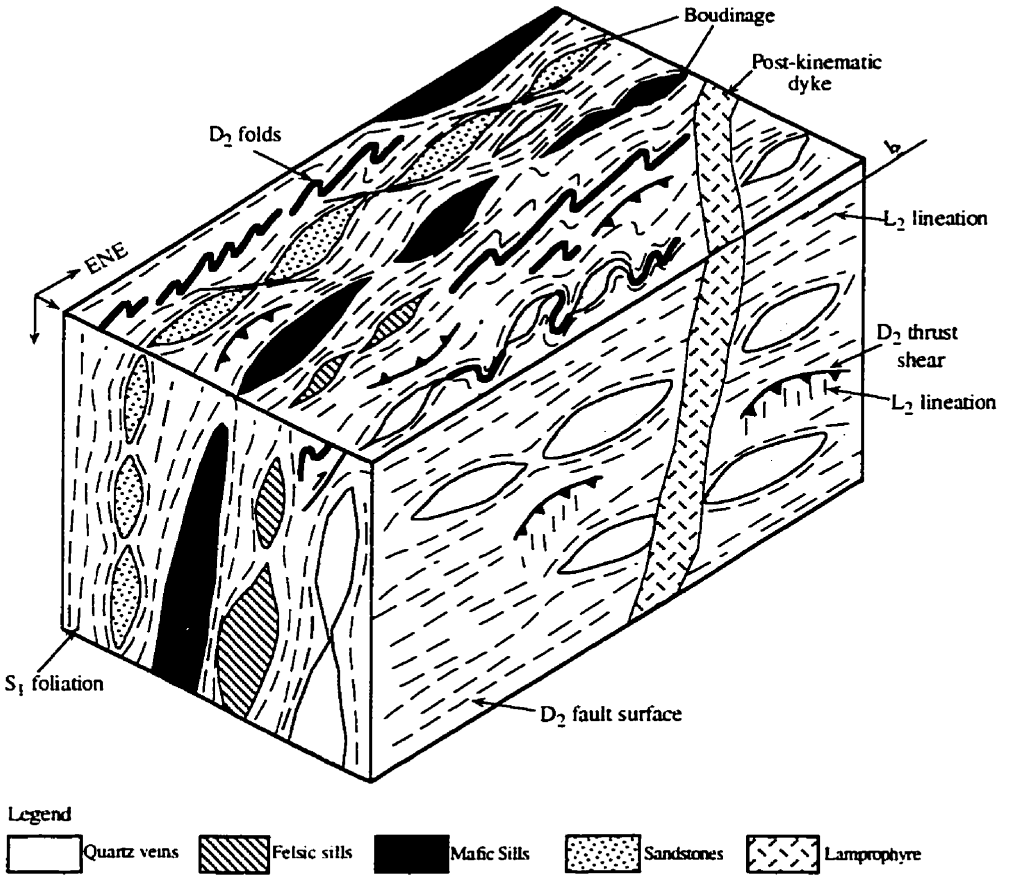

Figure 6.9. A Schematic block diagram, based on field observation and measurements, showing the variety of structures developed during D_2 transpression.

developed within strike-slip shear zones, and are all consistent with a right-lateral shear sense (Fig. 6.9; see Berthé et al., 1979; Lister and Snoke, 1984; Hanmer and Passchier, 1991; Stauffer and Lewry, 1993).

On a mesoscopic scale, three types of cleavages are recognized in the supracrustal assemblages of the Schreiber greenstone belt: slaty (S_1), and rhombohedral and scaly cleavages (S_2). There is a progressive transition from the S_1 slaty (pervasive), to the S_2 rhombohedral and to scaly cleavages in the vicinity of major strike-slip shear zones. As the intensity of strain increases the S_1 slaty cleavage grades into more complex rhombohedral cleavage, which in turn grades into scaly cleavage with further D_2 shearing. This gradational cleavage type has been documented in the Phanerozoic Aladag (Taurides) and Taconic (Appalachian) mélanges (see Bosworth, 1989; Polat and Casey, 1995). Microscopic to mesoscopic crenulation cleavage, as near-vertical folds, are also developed within the strike-slip shear zones.

The co-existence of (1) horizontal and vertical lineations in D_2 strike-slip and thrust shear zones, respectively, and (2) horizontal sense of shear indicators such as asymmetric folds, boudins, porphyroblast/clast structures, and S-C planar fabrics are all consistent with heterogenous transpressional deformation (see Sanderson and Marchini, 1984; Hudleston et al., 1988; Robin and Cruden, 1994; Greene and Schweickert, 1995; Tikoff and Greene, 1997).

6-4. Deformation Phase III (D_3)

The most pronounced D_3 structure in the study area is the Lake Superior-Hemlo fault zone (LSHFZ; Fig. 1; Hugon, 1984; Muir and Elliot, 1987). Delta (δ) structures along the LSHFZ indicate right-lateral shear sense for the fault zone (Fig. 6.7c; Hugon,

1984; Muir and Elliot, 1987; Polat et al., 1998b). The magnitude of off-set along the LSHFZ is not known. The significance of D_3 in the study area is thought to be subprovince accretion (Polat et al., 1998b). Outside the study area D_3 is expressed as faults bounding the Wawa and Quetico subprovinces.

6-5. Mélange Formation

6-5-1. Introduction

In this section combined structural and lithological evidence is presented for formation of an Archean mélange in the Schreiber assemblage of the Schreiber-Hemlo greenstone belt. Mélange is a general term describing a mappable, internally fragmented and mixed rock body containing a variety of blocks, commonly in a pervasively deformed matrix (Silver and Beutner, 1980). Mélanges can be formed by several geological processes in convergent plate boundaries, such as deformation, gravitational sliding (olistostromes), or mud diaprism (see Raymond, 1984; Cowan, 1985). This study deals only with tectonic mélanges that are characterized by inclusions of tectonically mixed fragments or blocks, both exotic and native in nature, in a pervasively sheared, fine-grained, and commonly pelitic to serpentinitic matrix (see Hsü, 1968; Raymond, 1984).

Mélanges are important components of Circum-Pacific subduction-accretion complexes, and the Alpine-Himalayan, Altaid, and Cordilleran orogenic belts (Bailey and McCallian, 1950; Gansser, 1974; Hsü, 1968; Sengor, 1990; Sengor and Natal'in, 1996; Polat et al., 1996b). Their co-existence with high pressure blueschist-eclogite facies metamorphic rocks in Phanerozoic orogenic belts (Okay, 1989) is interpreted as evidence for suture zones, the sites of obliteration of oceanic lithosphere by convergent margin processes (Dickinson, 1972; Dewey, 1977; Sengor, 1990).

Tectonic mélanges in modern convergent plate boundaries, and their Phanerozoic

counterparts, typically originate through the combined processes of off-scraping, folding, faulting, fragmentation and mixing in accretionary wedges above subduction zones (Hsü, 1968; Cowan, 1985; Moore and Silver, 1987; Moore and Byrne, 1987; Polat and Casey, 1995; Needham, 1995). The style of deformation and type of metamorphism in accretionary wedges, and the chemical characteristics of magmatism in the overriding plate, are controlled by a number of factors: (1) the rate and angle of plate convergence; (2) type of lithological material accreted (sedimentary versus igneous); (3) the age and thickness of the subducting oceanic lithosphere; and (4) the volume and migration paths of fluids in the accretionary wedge (Langseth and Moore, 1990). When material enters the subduction zone, it undergoes a sequence of progressive deformation, ranging from thrusting, folding, fragmentation, mixing, and underplating, as well as metamorphism (Moore and Silver, 1987; Moore and Byrne, 1987; Kimura and Mukai, 1991).

Some Archean greenstone belts, especially the Schreiber-Hemlo belt, have geological characteristics similar to Phanerozoic subduction-accretion complexes (Hoffman, 1991; Taira et al., 1992; Windley, 1993; Passchier, 1995; Sengor and Natal'in, 1996; Polat et al., 1996a; Polat et al., 1998b, Polat and Kerrich, 1998). However, Archean greenstone belts are devoid of high-pressure blueschist and eclogite facies metamorphic rocks, and only a few Archean mélanges have been reported (de Wit et al., 1992; Wang et al., 1996; Lin et al., 1996). The absence of abundant carbonate, radiolarian chert, and serpentinite blocks, which are important components of many Phanerozoic mélanges (Gansser, 1974; Kiyokawa, 1992; Saleeby, et al., 1992; Polat and Casey, 1995), combined with prevalent low-pressure greenschist to amphibolite facies metamorphism and polyphase deformation, may obscure the recognition of mélanges in Archean greenstone belts. These observations have been used by some workers to argue against Phanerozoic-style plate tectonics in the Archean (see Hamilton, 1993, 1998). The origin and tectonic setting in which Phanerozoic mélanges evolve are well-established.

Unlike their Phanerozoic counterparts, however, the origin and tectonic significance of Archean mélanges are poorly documented.

Assigning a specific tectonic setting for Phanerozoic mélanges has been based primarily on internal structures, and compositional characteristics of blocks and surrounding matrices (Pollock, 1989; Pavlides, 1989; Kimura and Mukai; 1991; Polat et al., 1996b). In this study, for the first time, structural and lithological evidence for a tectonic mélange formation in the Schreiber section of the late Archean Schreiber-Hemlo greenstone belt is presented (Fig. 6.1; Walker, 1967; Williams, 1991; Polat et al., 1996a, Polat and Kerrich, 1998). An attempt is made here to explain the origin of mélange formation and its tectonic significance for Archean orogens. Based on these characteristics the Archean Schreiber mélange can be compared with Phanerozoic counterparts. This chapter builds on earlier chapters that report chemical data for the diverse volcanic, intrusive, and sedimentary units of the study area.

6-5-2. The Late Archean Schreiber Mélange

Although mélange fabrics are developed over large areas of the Schreiber belt, they can be recognized most readily in extensive outcrops along HW17 (Highway 17; Fig. 6.10), the Canadian Pacific Railroad (CPR), power lines, and the shore of Lake Superior (Fig. 6.2). Elsewhere dense vegetation including lichen, obscure outcrops. Many detailed observations were made at cleaned outcrops (e.g., Figs. 6.7b, 6.11a, 6.11b, 6.12a,b, 6.13a,b, 6.14, 6.15a,b). Like Phanerozoic mélange terranes, the degrees of fragmentation and mixing in the Schreiber belt range from internally intact sedimentary and volcanic sequences, to "broken formations" (usage of Hsü, 1968), through to more intensively deformed tectonic mélanges (see Raymond, 1984). According to Beutner (1975) the concept of "exotic block" should be excluded in the definition of mélanges. However, the existence of exotic blocks in mélanges has important tectonic implications: their presence

may provide critical evidence for large-scale horizontal and vertical displacements, and tectonic juxtaposition of rocks derived from contrasting geodynamic settings (Hsu, 1968).

For these reasons, this study emphasizes the origin of exotic (foreign to the surrounding matrix) as well as native (disrupted lithologies which were once a part of, or inter-layered with, the surrounding matrix) blocks in the Archean Schreiber mélange. The mélange contains a variety of blocks and matrices. Both exotic and native blocks exist within pervasively sheared sedimentary and volcanic matrices. Exotic blocks include arc rhyolites within oceanic plateau basalts (Fig. 6.10a), and ocean plateau basalts within trench turbidites (Fig. 6.2). Native blocks are represented by basalts, komatiites, and gabbros within oceanic plateau sequences, and arc gabbros and tonalities within trench turbidites (Figs. Fig. 6.2, 6.10b). The native blocks are more abundant than exotic counterparts. The blocks are lensoidal to sigmoidal in shape, and range from ten centimetres to kilometres in long dimension (Figs. 6.11a,b, 6.12a,b). The long axes of the blocks tend to be aligned sub-parallel with the S_2 foliation and strike-slip faults (Fig. 6.2). In some places, fragmentation of gabbroic blocks produced tectonic breccia in a cataclastic matrix.

Contacts between blocks and matrices are typically curviplanar, and are marked by diverse structures such as scaly and sigmoidal cleavages, vertical asymmetric folds, near-horizontal slickenside lineations, and Riedel shears (Figs. 6.10b, 11a,b, 6.15a). Because of intense shearing, blocks tend to be rounded and have polished surfaces (Fig. 6.10). In most locations mélange formation is accompanied by sulphide (pyrite, chalcopyrite) mineralization and silicification, signifying that the mélange fabrics acted as hydrothermal conduits.

The geometric relationships between various sizes of blocks indicate that smaller blocks were produced by fragmentation of larger ones. It appears that sills, volcanic flows, and turbidite layers were transformed into asymmetric angular boudins by a

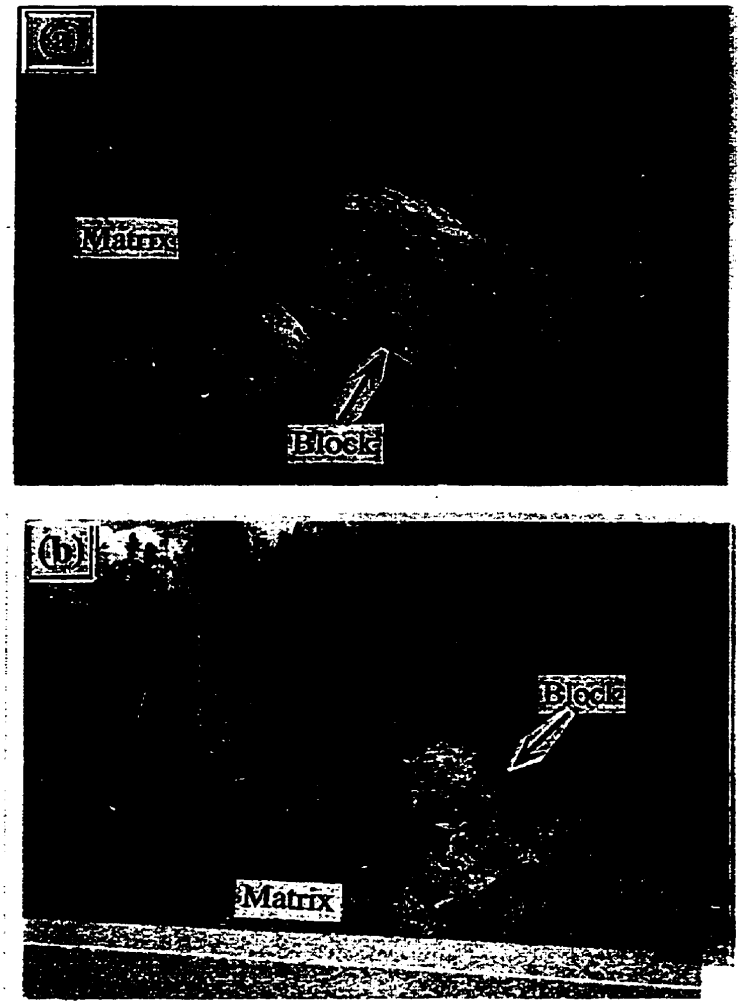

Figure 6.10. (a) A rhyolitic block in a matrix of sheared volcanic rocks (viewed towards north). (b) A gabbroic block in matrix of foliated turbidites (viewed towards north).

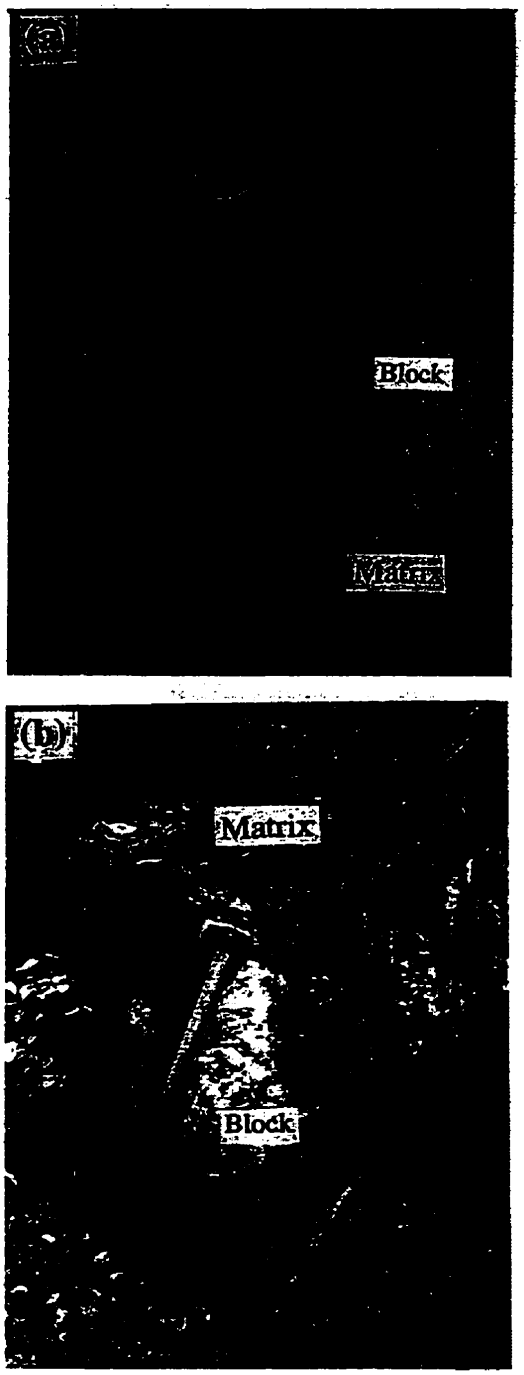

Figure 6.11. (a) A small tonalitic block floating in a matrix of foliated turbidites (plan view). (b) A silicified, epidotized native volcanic block in a matrix of foliated volcanic rocks (viewed towards southwest).

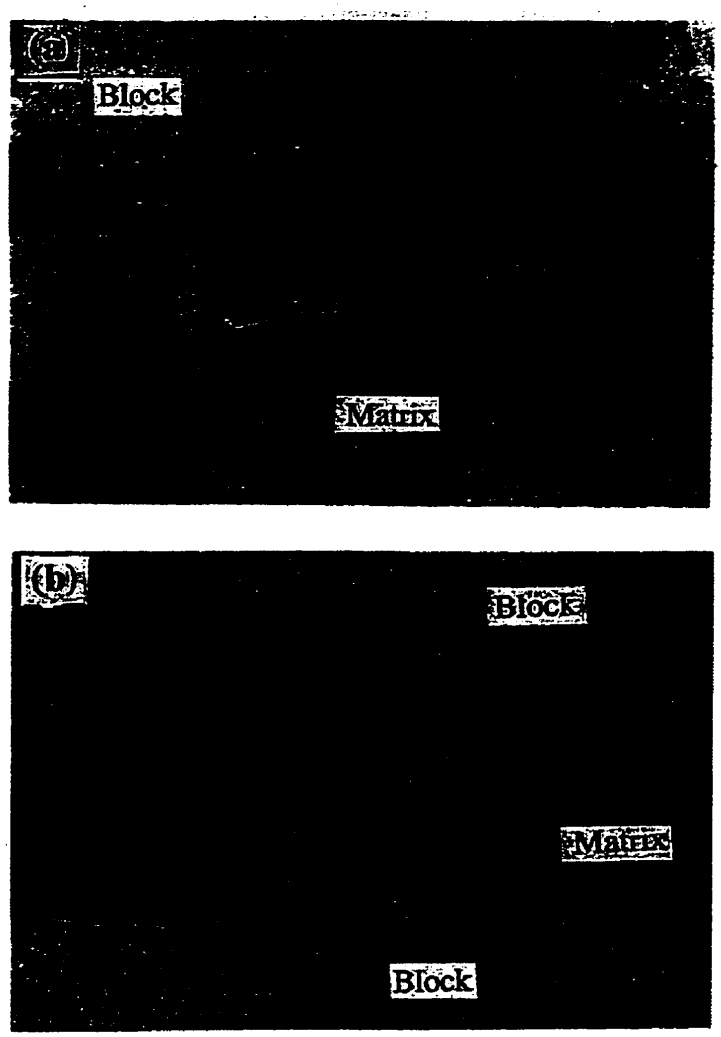

Figure 6.12. (a) Intensely foliated contact between a tonalitic block and sedimentary matrix (plan view). (b) Two tonalitic blocks separated by an intensely foliated sedimentary matrix (plan view).

combination of S-C shearing, Riedel shearing, and shear-fracture boudinage, resulting in broken formations (Figs. 6.13b, 6.15b, Fig. 6.16; see Berthé et al., 1979; Hanmer, 1986; Waldron et al., 1988; Hanmer and Passchier, 1991; Swanson, 1992). These boudins further evolved into lensoidal (sigmoidal) native blocks through tectonic truncation (erosion) at the margins. The propagation of shear planes into the lensoidal blocks resulted in further internal fragmentation, separating large blocks into smaller fragments (Fig. 9.16; see Hanmer, 1986; Swanson, 1992). The formation of mélanges by shear-fracture boudinage was recognized in western Newfoundland by Waldron et al. (1988), and by Riedel shears in Japan (Needham, 1995); however, the author is not aware of any other mélange formation dominated by S-C shearing and strike-slip faulting.

Basalt-komatiite and turbidite sequences, which were juxtaposed during D_1 compression, were further deformed by tectonic wedging during D_2 strike-slip deformation (Fig. 6.2). Strike-slip shearing within volcanic rocks resulted in the development of rhombohedral to scaly cleavages, mylonites, folds, asymmetric quartz boudins, and fragmentation through which large pillows and flows were dismembered into smaller lensoidal fragments. The intense shearing produced centimetre-thick mylonite zones around sigmoidal pillows. In some places weakly deformed lenses of volcanic rocks are surrounded by 50 centimetre- to 1.5 metre-thick curviplanar shear zones, generating broken formations, and native basalt and komatiite blocks (Figs. 6.2, 6.11b). A few native gabbroic blocks were also recognized in the Steel Lake area (Figs. 6.2, 6.4). These blocks are geochemically similar to surrounding basalts, suggesting that they were derived from the lower sections of accreted oceanic plateau fragments. The long axes of these native blocks range from 50 centimetres up to several metres. Although the shearing in turbidites is as intense as in volcanic rocks, the typical occurrence of fine-grained graywackes in these rocks obscures the recognition of native sedimentary blocks. Abrupt

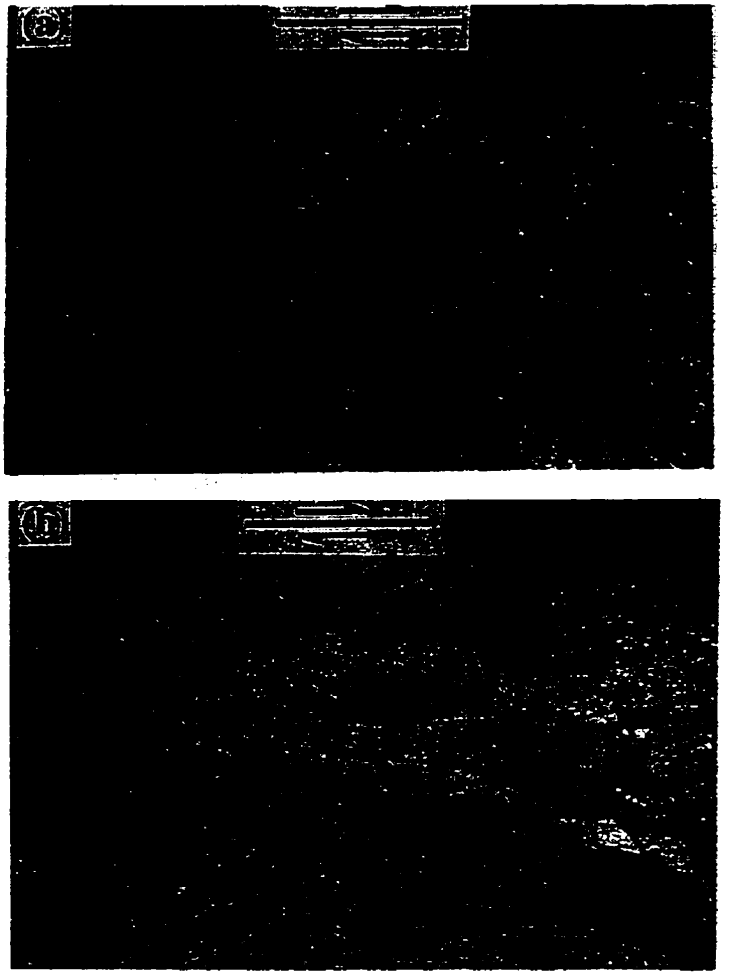

Figure 6.13. (a) An asymmetric boudin developed from a felsic sill, indicating a righ-lateral shear sense (plan view). (b) A sandstone bed derformed through shear-fracture boudinage in turbidites, forming a broken formation (plan view).

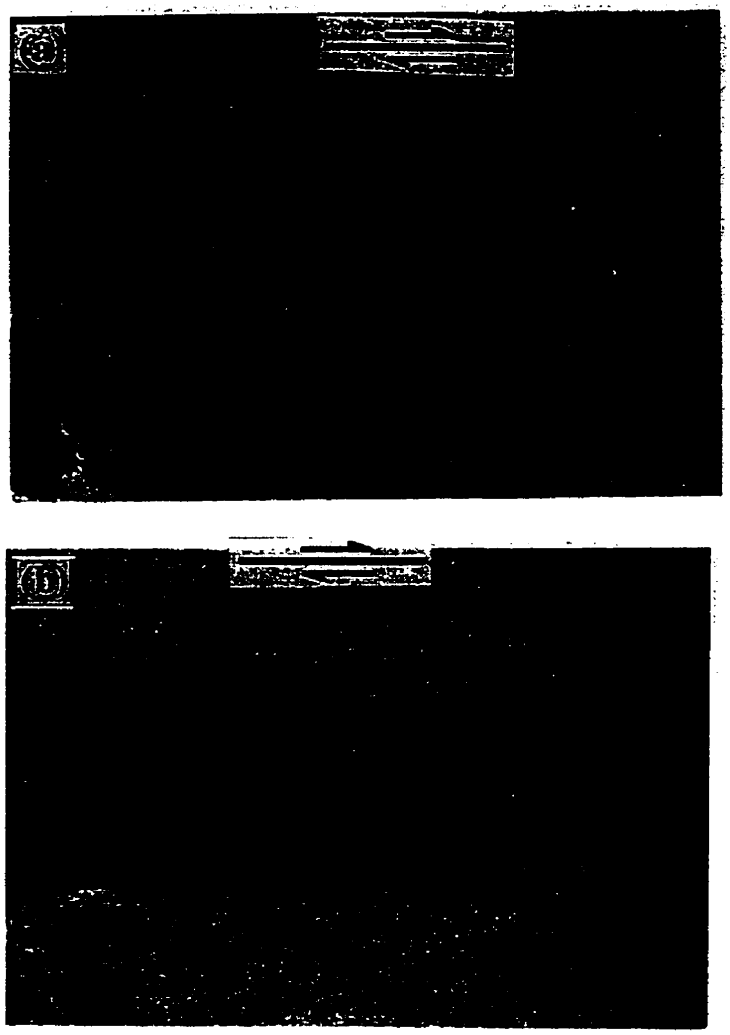

Figure 6.14. (a) Sigmoidal boudins in feldspar veins in the internal shear zones crossing a gabbroic block (plan view). (b) S-C planar fabrics in turbidite matrix between two felsic blocks (plan view).

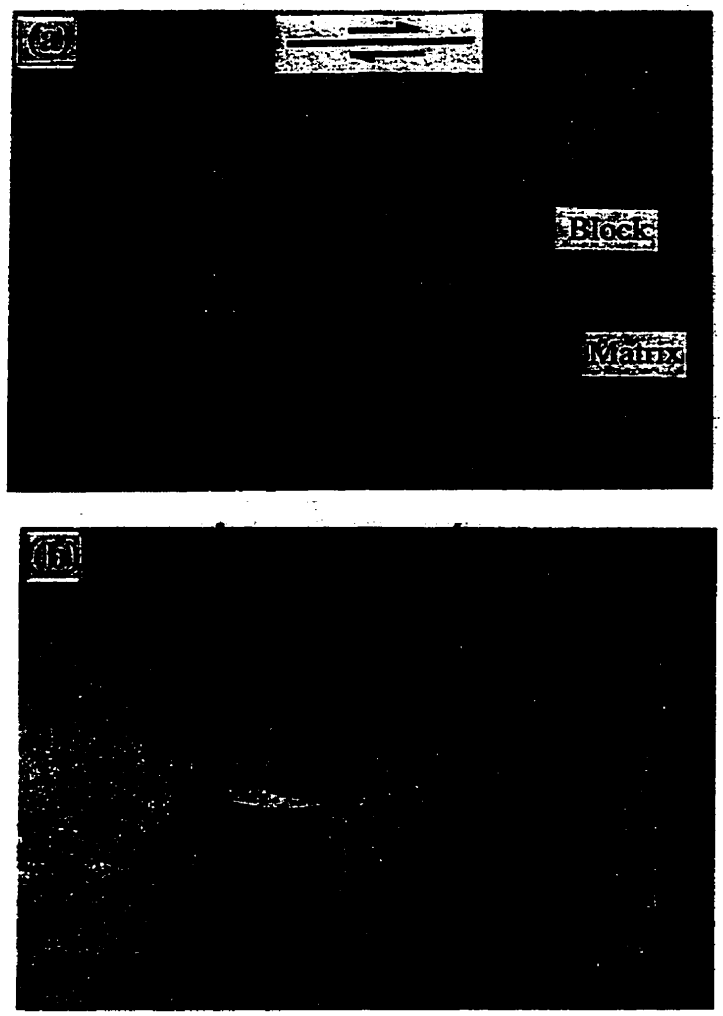

Figure 6.15. (a) sub-vertical folds developed beside a tonalitic block within a sedimentary matrix (plan view). (b) Near-symmetric boudins developed from felsic sills (viewed towards northwest).

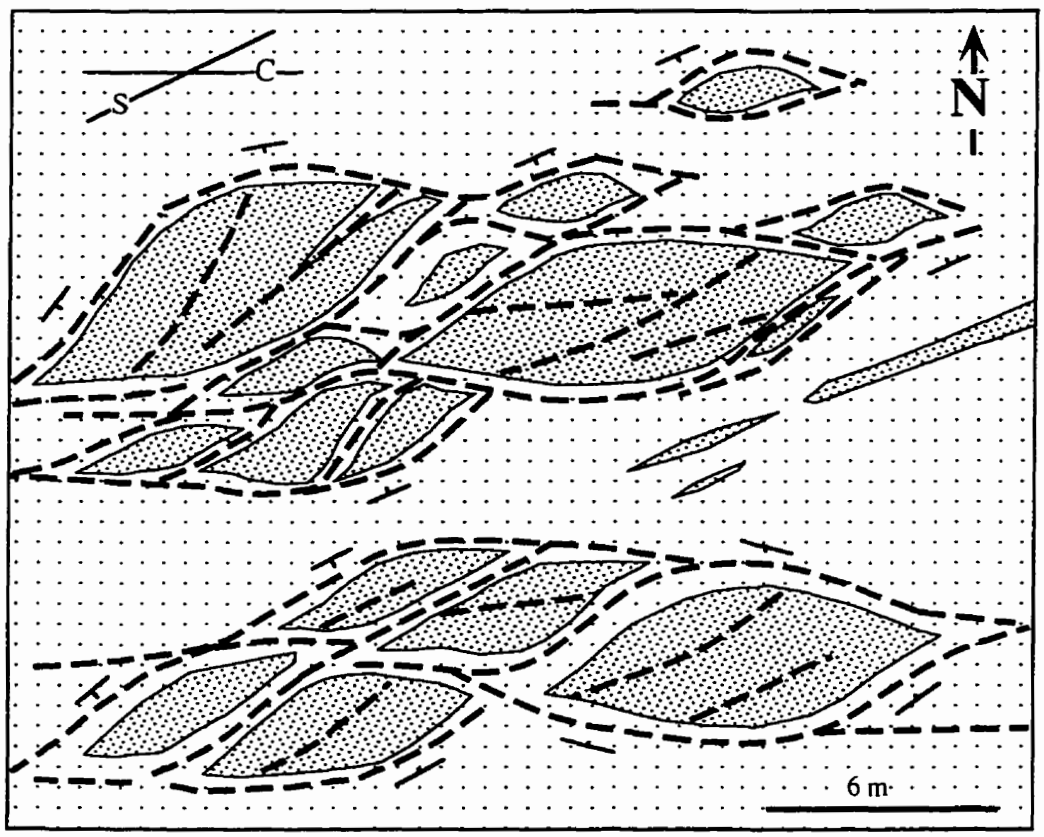

Figure 6.16. A detailed map of a melange outcrop in the Ripple Lake area, indicating that felsic intrusive blocks formed through S-C shearing. The matrix consists of intensely sheared, pelitic sediments. For location see Figure 6.2.

changes in sandstone and shale lithologies, associated with intense shearing and transposition, are consistent with broken formations (see Hsü 1968; Raymond, 1984).

Collectively, oceanic plateau fragments, arc volcanic flows, trench turbidites, syn-kinematic mafic to felsic sills and dykes, and mélange fabrics are all cut by the late-kinematic, lamprophyre dykes (ca. 2690 Ma; see Wyman and Kerrich, 1989). The accretionary mélange complex was intruded by post-kinematic granitoids (ca. 2678-2688 Ma Williams et al., 1991; Fig. 6.17).

In summary, the co-existence of horizontal and vertical L_2 lineations, with measured kinematic indicators including consistent with a right-lateral transpressional tectonic setting for the mélange formation.

6-5-3. Geological evidence for subduction-accretion origin of the Schreiber Mélange

The common orientation of S_1 foliations and L_1 lineations, and the presence of the D_1 thrust faults and tight to isoclinal folds in both volcanic and sedimentary sequences, suggest that turbidites and mafic-ultramafic volcanic sequences were structurally juxtaposed and imbricated during D_1. Contacts between turbidites and volcanic sequences are characterized predominantly by several metre-thick D_2 strike-slip fault zones (Figs. 6.2, 6.4). Along these D_2 strike-slip faults, there are locally preserved D_1 thrust fabrics such as S-C planar fabrics and asymmetric porphyroclasts; these relationships are consistent with the D_1 thrust faults having been overprinted by, and reactivated as, the D_2 strike-slip faults (Figs. 6.2, 6.4).

The occurrence of chert layers between basaltic flows and pillowed lavas suggests intra-oceanic environment for the origin of volcanic sequences (see Isozaki et al., 1990; Ohta et al., 1996). The geochemical characteristics of these basalt-komatiite sequences is

consistent with an intra-oceanic geodynamic setting, suggesting that they are fragments of an Archean oceanic plateau(s) or seamount(s) (Table 6.1; Polat et al., 1998a,b; Chapter 3). Other units of basalt, andesite and rhyolite flows have the geochemical characteristics of intra-oceanic arcs (Table 6.1). Plateau and arc basalts cannot be distinguished in the field, but rather require trace element data to distinguish them. High-precision trace element data obtained from turbidites are consistent with a magmatic arc provenance for the Schreiber-Hemlo siliciclastic sedimentary rocks (Polat et al., 1998b).

In Phanerozoic orogenic belts, the occurrence of tectonically juxtaposed oceanic lithological associations such as mid-ocean ridge basalts, seamounts, oceanic plateaus, with arc-derived trench turbidites is considered as evidence for ancient subduction zones (see Isozaki et al., 1990). Oceanic basalts in Phanerozoic subduction-accretion complexes are often older than turbidites against which they are juxtaposed (Jones et al., 1993). In the late Archean Schreiber belt, the interleaving of fragments of oceanic plateau and arc-derived turbidites occurred by D_1 convergent margin tectonics. These structural and lithological relationships are comparable to Phanerozoic subduction-accretion complexes of Japan (Isozaki et al., 1990; Jones et al., 1993; Kimura et al., 1994). Similarly, tectonically juxtaposed fragments of oceanic crust and arc-derived turbidites in various greenstone belts of the Superior Province have been interpreted as Archean subduction-accretion complexes (Hoffman, 1991; Kimura et al., 1993).

The late stages of D_1 and D_2 were accompanied by the intrusion of syn-kinematic mafic to felsic dykes and sills, ranging from a few centimetres to several hundred metres in thickness; intrusion was primarily along D_2 strike-slip faults and S_1 planes. The absence of D_1 fabrics in these dykes and sills suggest that their intrusion post-dates tectonic juxtaposition of trench turbidites with oceanic arc and plateau fragments. The geochemistry of the dykes and sills is consistent with oceanic crust slab-derived melts for

Table 6.1. Summary of the lithological, geochronological, geodynamic, and structural characteristics of the Schreiber-Hemlo greenstone belt*

Lithological Unit(s)	Age (Ma)	Interpreted Geodynamic Setting	Origin	Tectonostratigraphic Nature	Deformation Phase	Block-Matrix Realtionships
Komatiites, Mg- to Fe-tholeiites, and tholeiitic gabbros	2770-2700	Oceanic plateau(s)	Mantle plumes	Allochthonous	D_1, D_2, D_3	Exotic blocks of ocean plateau basalts in matrix of sheared turbidites. Native blocks of gabbros in sheared basalts
Siliciclastic turbidites	2705-2697	Convergent margin (oceanic island arc)	Island arc trench	Allochthonous	D_1, D_2, D_3	Exotic (?) or native blocks of rhyolites in matrix of sheared turbidites
Tholeiitic to calc-alkaline basalts to rhyolites	2770-2695	Convergent margin (oceanic island arc)	Slab to wedge melting	Allochthonous to autochthonous	D_1, D_2, D_3	Exotic blocks of rhyolites in matrix of sheared oceanic plateau basalts
Mafic to felsic sills and dykes	<2695	Magmatic arc	Slab to wedge melting	Autochthonous	D_2, D_3	Native blocks of felic and mafic sills and dykes in matrices of sheared basalts and turbidites
TTG plutons	2700-2690	Magmatic arc	Slab melting	Autochthonous	D_2, D_3	No block-matrix relations observed
Lamprophyres	2690	Accretion-related extension	Lithospheric mantle	Autochthonous	D_3 ?	No block-matrix relations observed

*Sources Williams et al. 1991; Polat and Kerrich, 1998; Polat et al. 1998b.

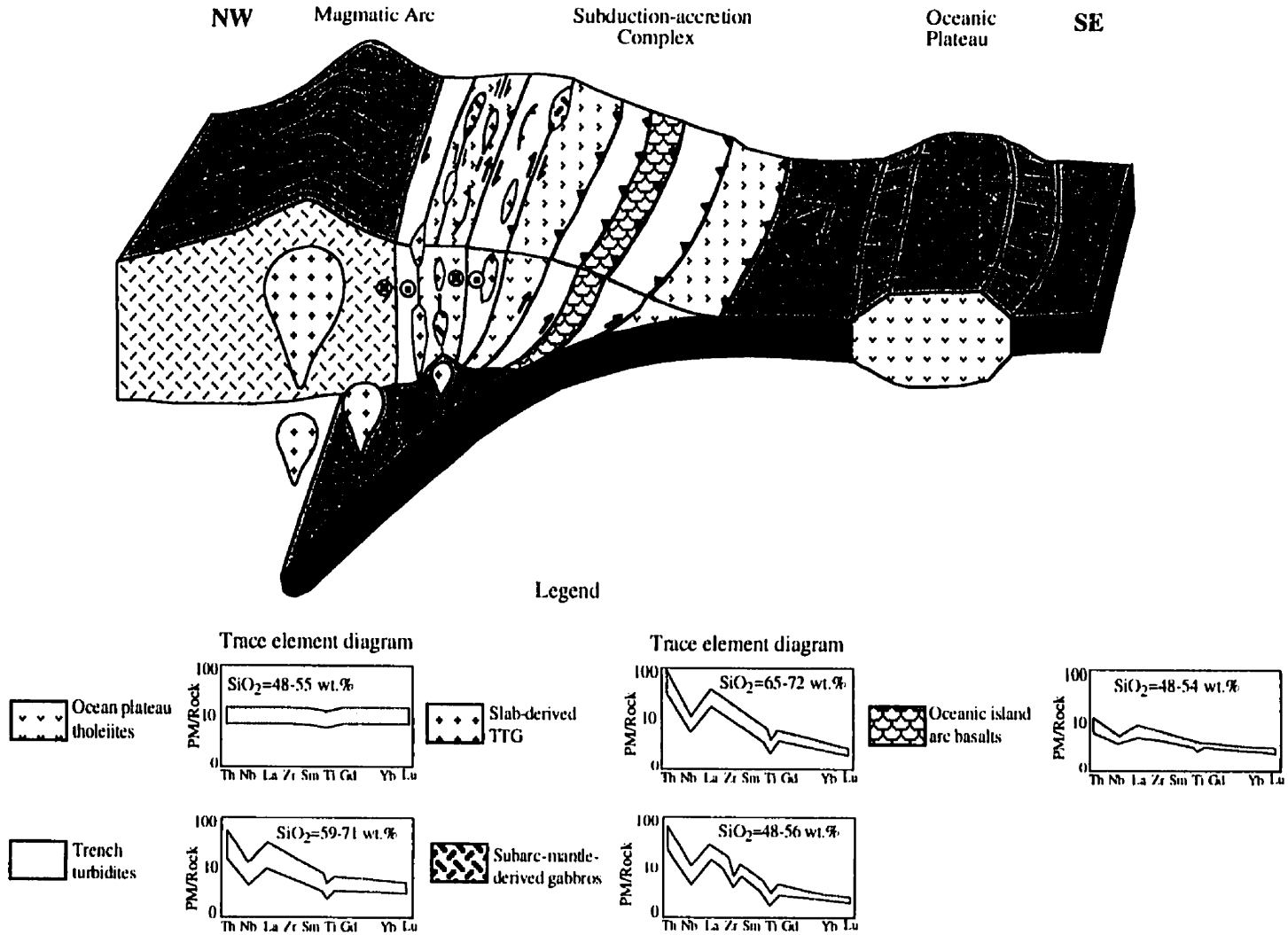

Figure 6.17. Interpreted geodynamic evolution of the Schreiber-Hemlo greenstone belt, and the formation of the melange. See chapters 3, 4, 5 for the sources of primitive mantle-normalized diagrams.

felsic intrusions, and slab-dehydration, mantle wedge-derived melts for mafic and intermediate intrusions (Table 6.1; see Chapter 5). The intrusion of subduction-derived, syn-kinematic mafic to felsic igneous rocks into imbricated turbidite, arc, and oceanic plateau sequences is consistent with the juxtaposition of these contrasting lithologies above an Archean subduction zone. The transition from D_1 to D_2 reflects the evolution from thrust tectonics above a subduction zone to right-lateral transpression. The intrusion of subduction-derived igneous rocks into subduction-accretion complexes is an important feature of Phanerozoic subduction-accretion complexes, such the Chugach accretionary complex of Alaska (Page et al., 1986), Shimanto accretionary complex of Japan (Hasebe et al., 1993), Altaid accretionary complexes of Central Asia (Sengor and Natal'in, 1996), and Cordilleran accretionary complexes of British Columbia (Hollister and Andronicos, 1997).

6-6. Conclusions and implications

The principal conclusions of this chapter, and implications, are as follows:

1. Overprinting relations between different sequences of structures, such as lineations, foliations, shear planes, and folds, suggest that the late Archean Schreiber-Hemlo greenstone belt underwent three phases of deformation.

2. D_1 structures are consistent with a compressional tectonic regime. During D_1 oceanic plateau basalts and associated komatiites, and deep marine turbidites derived from an inboard magmatic arc were all tectonically juxtaposed as they were incorporated into an accretionary complex above a NNW-dipping subduction zone (Fig. 6.17).

3. Following their accretion, volcanic and sedimentary sequences underwent right-lateral

transpressional deformation, and were intruded by syn-kinematic, subduction-derived mafic to felsic sills and dykes. Deformation during right-lateral transpression resulted in fragmentation and mixing of oceanic plateau fragments, trench turbidites, and arc-derived mafic to felsic igneous rocks, forming broken formations and tectonic mélanges (Fig. 6.17).

4. The D_1 to D_2 transition can be interpreted in terms of an oceanward migration of the trench line due to continued accretion and underplating, and an evolution from compression to transpression (Polat et al., 1998b).

5. Based on the new structural observations, distribution of lithologies, and geochemical data, the geological characteristics of the late Archean Schreiber greenstone belt mélange are consistent with a tectonic origin, and right lateral strike-slip deformation. Like Phanerozoic counterparts, the late Archean Schreiber mélange is characterized by various degrees of fragmentation and mixing, ranging from internally intact sedimentary layers and volcanic flows, to broken formations, and intensively sheared, transposed, and mixed tectonic mélanges.

6. Structural transposition is as important a feature of the Schreiber mélange as in Phanerozoic mélanges (see Weiss, 1972; Muller et al., 1989).

7. Most Phanerozoic tectonic mélanges form within shear zones or subduction channels at the base of accretionary prisms during off-scraping of sediments and oceanic crust (Moore and Byrne, 1987; Cloos and Shreve, 1988), whereas formation of the Schreiber mélange postdates the accretion of oceanic crust and trench turbidites into the accretionary prism.

8. Phanerozoic mélanges are characterized by lithologically more diverse blocks, such as carbonates, blueschists, eclogites, serpentinites, gabbros, pillow basalts, radiolarian cherts, than the late Archean Schreiber mélange (Polat and Casey, 1995; Hsü, 1968; Cloos and Shreve, 1988). In addition, many Phanerozoic mélanges have shale matrices, whereas shales are a subordinate component of the Schreiber mélange.

9. The absence of blueschist and eclogite facies metamorphic rocks in Archean subduction-accretion complexes may be attributed to elevated thermal gradients and shallow-angle subduction (Condie, 1997; Polat et al., 1998).

10. D_1 related thrusts and/or D_2 strike-slip faults in the fore-arc region of the Schreiber-Hemlo magmatic arc may have provided conduits for uprising melts from the descending slab and overlying sub-arc wedge, and induced decompressional partial melting in the sub-arc mantle wedge. A close relationship between orogen-parallel strike-slip faulting and magmatism has recently been recognized in several Phanerozoic transpressional orogenic belts, including the North American Cordillera (Tikoff and Saint Blanquat, 1997; Hollister and Andronicos, 1997), Japanese island arcs (Isozaki et al., 1990), British Caledonides (Hutton and Reavy, 1992) suggesting that as in Phanerozoic counterparts, orogen-parallel strike-slip faulting in the Schreiber-Hemlo greenstone belt played an important role in lateral crustal accretion and magma emplacement .

11. The tectonic evolution of the Schreiber belt is comparable to Phanerozoic subduction-accretion complexes that evolved at oblique convergent plate boundaries (see McCaffrey, 1991, 1992; Hansen, 1992; Curtis, 1997; Fuh et al., 1997). The structural characteristics of the Schreiber-Hemlo greenstone belt are similar in many respects to

those of the Vermilion district of the Wawa subprovince to the west, and in the Abitibi greenstone belt to the east, suggesting that oblique plate convergence was a continental-scale phenomenon during the growth of the southern Superior Province in the late Archean over a strike distance of ~400 km (see Hudleston et al., 1988; Bauer et al., 1992; Robin and Cruden, 1994; Mueller et al., 1996).

CHAPTER 7. CONCLUSIONS, IMPLICATIONS, AND FUTURE DIRECTIONS

7-1. Principal conclusions

The principal conclusions of this thesis are as follows:

1. The late Archean (ca. 2.80-2.68 Ga) Schreiber-Hemlo and White River-Dayohessarah greenstone belts of the Superior Province, Canada, are supracrustal lithotectonic assemblages of komatiite to tholeiitic, transitional and alkaline basalt ocean plateau sequences; tholeiitic and calc-alkaline basalt to rhyolite volcanic arc sequences; and syn-kinematic, siliciclastic trench turbidites accreted along a SSE-facing convergent plate margin through compressional and transpressional collisions (Fig. 7.1; Table 7.1). These volcano-sedimentary sequences were collectively intruded by the syn-kinematic high-La/Yb_n, high-Al slab-derived granitoids, syn-kinematic wedge-derived gabbros, and late- to post-kinematic lamprophyres.

2. High precision ICP-MS trace element data obtained from komatiites and associated tholeiitic to alkaline mafic volcanic rocks reveal diverse geochemical characteristics for these oceanic floor volcanic sequences. These chemically diverse but stratigraphically related ultramafic and mafic volcanic rocks are likely to be the fragments of an Archean oceanic plateau(s) and/or ocean island(s) derived from a mantle plume (Fig. 7.1; Table 7.1). The diverse geochemical features of komatiites, komatiitic basalts, and tholeiitic to alkaline basalts cannot be explained by alteration, crustal contamination, fractional crystallization or partial melting of a homogenous mantle plume. Rather, major and

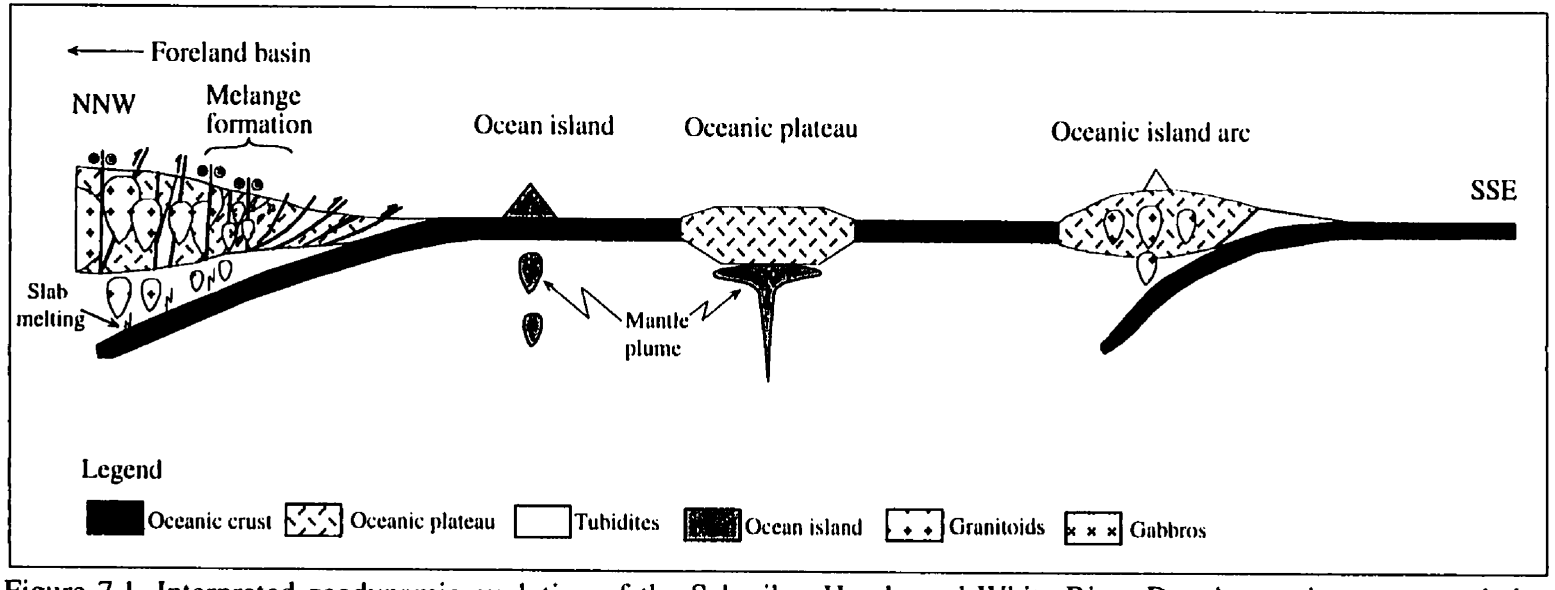

Figure 7.1. Interpreted geodynamic evolution of the Schreiber-Hemlo and White River-Dayohessarah greenstone belts, based on structural and geochemical data.

trace element consistent with a mantle plume that was chemically heterogenous, and contained trace element depleted, undepleted, and enriched source components. The presence of positive and negative Nb anomalies both in komatiites and basalts may have resulted from the incorporation of residual slab (RSC) and slab-derived (SDC) components, respectively, into the plume source through subduction zone recycling processes. Dynamic partial melting and magma mixing processes can account for some compositional variations in Al-undepleted komatiites, and the spectrum from Mg-, to Fe-tholeiites. These observations suggest that Archean subduction processes may have played an important role in the generation of chemically and isotopically heterogeneous mantle. Collectively, the geochemical characteristics of areally extensive ocean floor ultramafic to mafic volcanic sequences in the late Archean Schreiber-Hemlo and White River-Dayohessarah greenstone belts of the Superior Province are comparable to those of Phanerozoic ocean plateaus and ocean islands including Ontong Java, Nauru, Hikurangi, Hawaii, and Iceland.

3. Like modern oceanic-island arc volcanic rocks, the late Archean Schreiber-Hemlo and White River-Dayohessarah belt counterparts are characterized by coeval tholeiitic and calc-alkaline magma series with variable major and trace element systematics. Both the tholeiitic and calc-alkaline suites were derived from metasomatized subarc mantle wedge sources. The calc-alkaline suite was derived from more enriched and deeper-level mantle sources than thoeiitic counterparts. Slab melting was a major source of the felsic suite with garnet + clinopyroxene ± hornblende residual in the source. High Ni and Cr contents in the felsic suite can be explained by mixing between, or interaction with, slab- and wedge-derived melts. Zr(Hf)/MREE systematics suggest that the retention of clinopyroxene in the residual eclogite during slab melting may have fractionated Zr(Hf) from MREE, resulting in positive Zr and Hf anomalies. Volcanic

arc sequences in the late Archean Schreiber-Hemlo and White River-Dayohessarah greenstone belts tend to have more fractionated REE patterns than Phanerozoic and modern counterparts ($La/Yb_n<12$ versus $La/Yb_n >12$). This difference in REE systematics may be attributed to the thicker lithosphere in the Archean, resulting in deeper melt segregation.

4. The trace element characteristics of the syn-kinematic, high-Na, high-Al granitoids (TTG) of the Schreiber-Hemlo and White River-Dayohessarah greenstone belts are consistent with slab melting with garnet ± hornblende in the residue. The geochemical characteristics of the Schreiber-Hemlo TTG intrusions are comparable to those of high-Al TTG intrusions of Cenozoic subduction zones, where the age of subducting oceanic lithosphere is apparently younger than 30 Ma.

5. The geochemistry of the syn-kinematic mafic to felsic dykes and sills is consistent with slab dehydration, mantle wedge-derived melts for mafic and intermediate intrusions, whereas felsic intrusions were slab-derived melts.

6. The trace element systematics of the syn-kinematic, siliciclastic, trench turbidites of the Schreiber-Hemlo and White River-Dayohessarah greenstone belts are consistent with a magmatic arc provenance of mixed mafic to felsic source components, directly comparable to arc and plateau basalts mixed with high-Na, high-Al tonalitic intrusions.

7. The Schreiber-Hemlo and White River-Dayohessarah greenstone belts have undergone three major phases of deformation; two probably prior to, and one during the assembly of the southern Superior Province (Table 7.1). The earliest phase of deformation (D_1) is defined by primarily rotated thrust faults: D_1 reflects tectonic

Table 7.1. Summary of the lithological, geochronological, geodynamic, and structural characteristics of the Schreiber-Hemlo greenstone belt*

Lithological Unit(s)	Age (Ma)	Interpreted Geodynamic Setting	Origin	Tectonostratigraphic Nature	Deformation Phase	Block-Matrix Realtionships
Komatiites, Mg- to Fe-tholeiites, and tholeiitic gabbros	2770-2700	Oceanic plateau(s)	Mantle plumes	Allochthonous	D_1, D_2, D_3	Exotic blocks of ocean plateau basalts in matrix of sheared turbidites. Native blocks of gabbros in sheared basalts
Siliciclastic turbidites	2705-2697	Convergent margin (oceanic island arc)	Island arc trench	Allochthonous	D_1, D_2, D_3	Exotic (?) or native blocks of rhyolites in matrix of sheared turbidites
Tholeiitic to calc-alkaline basalts to rhyolites	2770-2695	Convergent margin (oceanic island arc)	Slab to wedge melting	Allochthonous to autochthonous	D_1, D_2, D_3	Exotic blocks of rhyolites in matrix of sheared oceanic plateau basalts
Mafic to felsic sills and dykes	<2695	Magmatic arc	Slab to wedge melting	Autochthonous	D_2, D_3	Native blocks of felic and mafic sills and dykes in matrices of sheared basalts and turbidites
TTG plutons	2700-2690	Magmatic arc	Slab melting	Autochthonous	D_2, D_3	No block-matrix relations observed
Lamprophyres	2690	Accretion-related extension	Lithospheric mantle	Autochthonous	D_3 ?	No block-matrix relations observed

*Sources Williams et al. 1991; Polat and Kerrich, 1998; Polat et al. 1998a, 1998b.

imbrication of oceanic plateaus, island arcs, and arc-derived turbidites in a subduction-accretion complex. D_2 is dominated by ENE-striking, right-lateral, orogen parallel strike-slip faults, and steeply-dipping thrust shear zones: the presence of coeval strike-slip and compressional structures is consistent with a right-lateral transpressional deformation. Arc-derived mafic to felsic melts intruded D_1 and D_2 structures.

Progressive orogen- parallel D_2 transpression resulted in fragmentation and mixing of ocean plateau sequences, arc volcanics, trench turbidites, and arc intrusions, forming broken formations and a tectonic mélange (Table 7.1). The mélange is characterized by lensoidal native and exotic blocks centimetres to hundreds of metres in diameter, dispersed in intensely sheared, transposed sedimentary and volcanic matrices. It is a part of a continent-scale convergent margin subduction-accretion complex.

Most Phanerozoic tectonic mélanges form within shear zones or subduction channels at the base of accretionary prisms during off-scraping of sediments and oceanic crust (Moore and Byrne, 1987; Cloos and Shreve, 1988), whereas formation of the Schreiber mélange postdates the accretion of oceanic crust and trench turbidites into the accretionary prism. Phanerozoic mélanges are characterized by lithologically more diverse blocks, such as carbonates, blueschists, eclogites, serpentinites, gabbros, pillow basalts, radiolarian cherts, than the late Archean Schreiber mélange (Polat and Casey, 1995; Hsü, 1968; Cloos and Shreve, 1988). In addition, many Phanerozoic mélanges have shale matrices, whereas shales are a subordinate component of the Schreiber mélange. The absence of blueschist and eclogite facies metamorphic rocks in Archean subduction-accretion complexes may be attributed to elevated thermal gradients and shallow-angle subduction (Condie, 1997; Polat et al., 1998).

The most pronounced D_3 structure in the study area is the right-lateral Lake Superior-Hemlo strike-slip fault. The significance of D_3 in the study area is thought to be subprovince accretion. The structural characteristics of the Schreiber-Hemlo greenstone belt are similar in many respects to those of the Vermilion district of the Wawa subprovince to the west, and in the Abitibi greenstone belt to the east, suggesting that oblique plate convergence was a continental-scale phenomenon during the growth of the southern Superior Province in the late Archean.

8. The metasedimentary subprovinces of the Superior Province, the English River and Quetico subprovinces, were previously interpreted as accretionary complexes (see Percival and Williams, 1989; Williams, 1990). They are located between two greenstone-granitoid subprovinces, and are characterized by uniform, greywacke sandstones derived in part from the adjacent granitoid-greenstone subprovinces. These metasedimentary subprovinces are folded and imbricated by progressive SSE-vergent tectonic transportation during the assembly of the Superior Province, and were intruded by post-tectonic high-Al, S-type granitoids (Williams, 1991). The SSE verging nappes were disrupted and complicated by large strike-slip faults as NNW-SSE compression continued.

The age of some sedimentation in the English River and Quetico Subprovinces appears to be 10 to 25 my younger than the youngest arc volcanism in the adjacent granitoid-greenstone subprovinces (Davis and Corfu, 1995; Zaleski, 1995). Some metasedimentary subprovinces such as the Pontiac include older zircons (3.1-2.8 Ga) and have geochemical characteristics including negative ε_{Nd} and negative Eu, anomalies indicative of intra-crustal melting of older continental crust (Feng et al.,

1993).

Collectively, the geological and geochronological characteristics of the metasedimentary subprovinces are more consistent with foreland basins rather than subduction-accretion complexes (cf. Davis and Corfu, 1995). These foreland basins were probably developed in response to lithospheric down flexure under the loading of SSE-verging greenstone-granitoid nappes. Phanerozoic foreland basins of the north American Cordillera may be analogs for the metasedimentary subprovinces of the Superior Subprovince (see Burchfiel, et al., 1992).

7.2. Geological models proposed for Archean greenstone belts

Numerous geological models, including plate tectonic and non-plate tectonic, have been proposed to explain the origin of Archean greenstone belts (Table 7.2). Plate tectonic models, including intra-continental rifts, mid-ocean ridge rifts, back-arc basins, island arcs, ocean plateaus, plumes in a continental setting, and subduction-accretion complexes, can account various structural, lithological, and geochemical characteristics of Archean greenstone belts. These models require a mobile earth, and suggest that Archean greenstone belts, like Phanerozoic counterparts, were derived from various geodynamic settings and involved multiple tectonic processes, including thrusting, folding, strike-slip deformation, and crustal extension (Table 7.2).

In contrast, non-plate tectonic models present a fixist approach for Archean geology (see Davies, 1992; Hamilton, 1993, 1998), and cannot account for the diverse geological features of Archean greenstone belts. The non-plate tectonic models require a coherent, uniform stratigraphy in a given greenstone belt (see Hamilton, 1998). The existence a tectonic mélange, characterized by tectonically juxtaposed and mixed ocean plateau fragments and trench turbidites, broken formations, and intense transposition in

Table 7.2. Models proposed for the origin of various Archean greenstone belts

Intra-continental rift	Goodwin, 1981; Groves and Batt, 1984; Ayres and Thurston, 1985
Intra-oceanic rift-MORB	Helmstaedt et al., 1986; de Wit et al., 1987;
Back-arc basin	Tarney et al., 1976
Collages of oceanic arcs and oceanic plateaus	Burke et al., 1976; Langford and Morin, 1976; Hoffman, 1991; Kimura et al., 1993; Desrochers et al., 1993
Accretionary complex with MORB slices	Kusky, 1990; Otha et al., 1996
Oceanic plateau	Storey et al., 1991; Kusky and Kidd, 1992; Abbott, 1996
Turkic-type subduction-accreation complex	Sengor and Natal'in, 1996
Plume in oceanic or continental setting	Fyfe, 1978; Campbell and Hill, 1988; Abbott, 1996
Non-plate tectonic origin	Park, 1982; Davies, 1992; Hamilton, 1993, 1998

the Schreiber-Hemlo greenstone belt rule out the non-plate tectonic models as applicable geological models for the Schreiber-Hemlo and White River-Dayohessarah greenstone belts specifically, and Archean greenstone evolution in general.

Greenstone belts in the Archean Superior Province are tectonically juxtaposed supracrustal assemblages within composite greenstone-granitoid terranes, with primarily tectonic boundaries (Hoffman, 1991; Polat et al., 1998b; Kusky and Polat, 1998). They have generally undergone greenschist to amphibolite facies metamorphism and poly-phase deformation characterized by isoclinal and sheath folds, thrust and strike-slip faults, and diverse lineations and foliations.

The basic stratigraphy in the Schreiber-Hemlo and White River-Dayohessarah greenstone belts, as well as in many greenstone belts of the Superior Province in which ocean floor volcanic sequences are older than siliciclastic turbidites, is the opposite of typical Phanerozoic continental rift sequences. Similarly, granitoids in the Schreiber-Hemlo and White River-Dayohessarah greenstone belts are younger than the enclosed greenstone belts, suggesting that intra-continental rift models are inconsistent with the geodynamic evolution of these greenstone belts. The trace element systematics of ocean floor volcanic sequences, and the absence of ophiolite-like stratigraphy in the Schreiber-Hemlo and White River-Dayohessarah greenstone belts, are also inconsistent with back-arc and/or mid-ocean ridge geodynamic settings. The presence of diverse geochemical signatures in volcanic rocks, including ocean plateau- and juvenile oceanic island arc-like trace element systematics, suggest that neither ocean plateau nor oceanic island arc accretion alone can account for the geochemical characteristics of the Schreiber-Hemlo and White River Dayohessarah greenstone belts.

Rather, this study demonstrates that the map patterns, and structural, tectono-stratigraphic, magmatic, and sedimentary characteristics of accreted material in the Schreiber-Hemlo and White River-Dayohessarah greenstone belts have pronounced

similarities to certain Phanerozoic subduction-accretion complexes. Several other greenstone belts in the Archean Superior Province have also been interpreted to be Phanerozoic-like subduction-accretion complexes (Hoffman, 1991; Taira et al., 1992; Kimura et al., 1993).

The structural and geochemical characteristics of vertically and laterally dismembered supracrustal units of the Schreiber-Hemlo and White River-Dayohessarah greenstone belts cannot be explained either by a simple tectonic juxtaposition of lithotectonic assemblages with stratified volcanic and sedimentary units, or cyclic mafic to felsic bimodal volcanism models (see Thurston, 1991). A combination of out-of-sequence thrusting, and orogen parallel strike-slip faulting of accreted ocean plateaus, oceanic arcs, and trench turbidites can account for the geological and geochemical characteristics of these greenstone belts.

For Phanerozoic orogens, Sengor (1990) and Sengor and Okurogullari (1991) defined three major types of collisional belts: (1) Alpine-type, (2) Himalayan-type, and (3) Altaid-type. The Alpine- and Himalayan-type belts are characterized by narrow suture zones, the sites of obliteration of oceanic lithosphere by subduction-accretion and collision processes (Dewey, 1977). The Altaid-type (Turkic-type) collisional belts, on the other hand, possess very large sutures up to several hundred km wide, characterized by subduction-accretion complexes and arc-derived granitoid intrusions, similar to the Circum-Pacific accreted terranes (e.g., Alaska, Japan, Canadian Cordillera; Sengor and Natal'in, 1996). These subduction-accretion complexes are often juxtaposed by thrust faults and disrupted orogen parallel strike-slip faults, resulting in bifurcating lithological domains (Sengor and Natal'in, 1996). In these respects, the greenstone-granitoid subprovinces of the Archean Superior Province are similar to the Circum-Pacific, north American Cordillera and Altaid collisional orogens.

Many Phanerozoic subduction-accretion complexes and continental suture zones

typically have ophiolitic fragments and high-pressure metamorphic rocks such as blueschists and eclogites indicative of high-pressure low-temperature conditions in the subduction zone, and slab- dehydration, wedge-melting low-La/Yb_n granitoids. However, Archean greenstone belts are devoid of these associations, but are characterized by abundant, typically high-La/Yb_n granitoids (Martin, 1986). The absence of blueschist and eclogite facies metamorphic rocks in Archean subduction-accretion complexes may be attributed to elevated thermal gradients and shallow angle subduction. The melting of a hotter Archean mantle at ridges and in plumes would generate relatively small, hot, and hence shallowly-subducting oceanic plates, promoting high-temperature metamorphism, migmatization, and slab melting. Larger, colder, Phanerozoic plates typically subduct at a steeper angle, generating high-pressure low-temperature conditions for blueschists and eclogites in the subduction zones, and low La/Yb_n granitoids from slab dehydration, and wedge melting.

In conclusion, field relations, structural characteristics, and high-precision ICP-MS trace element data obtained for representative lithologies of the Schreiber-Hemlo and White River-Dayohessarah greenstone belts suggest that they represent collages of oceanic plateaus, juvenile oceanic island arcs, and trench turbidites, forming an Archean subduction-accretion complex (Fig. 7.1).

7-3. Implications for continental growth

Although the rate of continental growth is a matter of geological debate (Fyfe, 1978; Armstrong, 1991; McCulloch and Bennett, 1994; Taylor and McLennan, 1995), it is generally accepted that the continental crust has been grown by accretionary and magmatic processes taking place at convergent plate boundaries since the early Archean (Burke et al., 1976; Sleep and Windley, 1982; Taylor and McLennan, 1995; Friend et al,

1988; Card, 1990; Condie, 1994, 1997a; Sengor and Natal'in, 1996).

Accretionary processes that have been proposed to contribute to growth of the continental crust in the Archean can be divided into five major groups: (1) oceanic plateau accretion, (2) oceanic island arc accretion, (3) normal ocean crust (mid-ocean ridge) accretion/ophiolite obduction, (4) back-arc basin accretion, and (5) arc-trench migration and/or Turkic (Altaid)-type orogeny accretion (Table 7.3).

The presence of abundant komatiites-high Mg-tholeiite volcanic sequences and slab-derived, high La/Yb_n, high-Al TTGs is consistent with higher average mantle temperatures in the Archean than the post-Archean, resulting in thicker Archean oceanic crust up to 25 km (Sleep and Windley, 1982; McKenzie and Bickle, 1988; Langmuir et al., 1992; Martin, 1993; Drummond and Defant, 1990; Condie, 1997b). In addition, it is believed that higher mantle temperatures in the Archean mantle gave rise to a large number of oceanic plateaus, up to 60-80 km thick, derived from mantle plumes, originating either from the D´ transition zone (670 km seismic discontinuity), or at the D" core-mantle boundary (McDonough and Ireland, 1993; Nisbet et al., 1993; Abbott, 1996; Arndt et al., 1997).

Oceanic plateaus are thicker than normal oceanic crust formed at mid-ocean ridges: they are more buoyant and relatively unsubductable, forming potential sources of accreted oceanic material to the continental crust at convergent plate boundaries (Ben-Avraham et al., 1981; Burke et al., 1978; Desrochers et al., 1993; Abbott, 1996).The average geochemical composition of the continental crust, however, is not consistent with either ocean plateau or andesitic arc accretion alone. For example, modern ocean plateaus such as Ontong Java, Kerguelen, and Nauru Basin have near-flat REE patterns on chondrite-normalized diagrams (see Floyd, 1989; Salters et al., 1992; Mahoney et al., 1993), whereas the bulk continental crust has LREE-enriched patterns. Similarly, areally extensive Mg-, to Fe-tholeiite sequences of the Superior Province and the Arabian-Nubian

Table 7.3. Major accretinary processes that have been proposed for the growth of the continental crust during the Archean.

Oceanic Plateau accetion	Oceanic island arc accretion	Normal (MOR) ocean crust accretion or ophiolite obduction	Back-arc basin acrretion	Arc-trench migration/ Turkic type orogeny accretion
Superior Province greenstone belts (Desrochers et al., 1993; Kimura et al., 1993; Xie et al., 1993; Stein and Hofmann, 1994; Polat et al. 1998b)	Superior Province (Card, 1990; Percival et al., 1994; Polat et al., 1998b)	Isua greenstone belt (Maruyama et al., 1991)	Suo Franciscon Craton (Baars, 1997)	Superior Province (Hoffman, 1991; Jackson and Cruden, 1995)
Belingwe greenstone belt (Kusky and Kidd, 1992)	Kaapvaal Craton (de Ronde and de Wit, 1994; de Wit et al., 1994)	Slave Province (Helmstaedt et al., 1986)	Aldan-Stanovik Shield (Dobretsov et al., 1997)	Yilgarn Craton (Sengor and Natal'in, 1996)
Kostomuksha greenstone belt (Puchtel et al., 1997)	Yilgarn Craton (Myers and Swager, 1997)	Superior Province (Kimura et al. 1993)	Kaapvaal Craton (Brandl and de Wit, 1997)	
General (Condie, 1981, 1997; Abbott, 1996)	Pilbara Craton (Myers, 1993; Kioyokwa and Taira, 1995)	Kaapvaal Craton (de Wit et al., 1987; de Ronde and de Wit, 1994)	Yilgarn Craton (Myers and Swagers, 1997)	
	Aldan-Stanovik Shield (Dobretsov et al., 1997)	Yilgarn Craton (Fripp and Jones, 1997)	Pilbara Craton (Barley, 1997)	
		Pilbara Craton (Ohta et al., 1996)		

Shield, which are interpreted as fragments of Archean and Proterozoic ocean plateaus, respectively, have near-flat, REE patterns (Kroner, 1985; Xie et al., 1993; Desrochers et al., 1993; Polat et al., 1998b).

Many Archean, Proterozoic and Phanerozoic greenstone belts interpreted as oceanic plateau fragments are overprinted by arc magmatism, suggesting that they either formed the base of intra-oceanic island arcs, or they have been intruded by arc magmas following their accretion (see Desrochers et al., 1993; Condie, 1997b). According to Condie (1997b) the upper and lower continental crusts have grown through the accretion of oceanic island arcs and ocean plateaus, respectively. Reymer and Schubert (1986), however, argued that oceanic arc-accretion alone is insufficient to account for the rapid crustal growth of the Precambrian shields. Moreover, most oceanic arcs are characterized by mafic not andesitic bulk compositions (Arculus, 1981; Anderson, 1982), whereas the continental crust is dacitic in composition (Taylor and McLennan, 1995).

Complete Phanerozoic-like ophiolite sequences have not been recognized in Archean greenstone belts. Similarly, many Proterozoic ophiolites are not intact (Kroner, 1985; Berhe, 1990; Dann, 1991). Archean oceanic crust was probably much thicker than Proterozoic and Phanerozoic counterparts, resulting in accretion predominantly of the upper section (basaltic) of the oceanic crust (Burke et al., 1976; Burke, 1995). Thus, a Phanerozoic-like complete ophiolite sequence was very unlikely to be accreted or obducted during Archean orogenies.

Isotopic data from numerous Archean and post-Archean orogenic belts are consistent with the accretion of juvenile material and episodic crustal growth (Reymer and Schubert, 1986; Samson and Pachett, 1991; Boher et al., 1992; Stein and Goldstein, 1994; Taylor and McLennan, 1995 and references therein). Stein and Hofmann (1994) proposed that episodic crustal growth and major orogenic events may have been associated with major plume activities throughout the earth history. They defined this

relationship as mantle overturn and major orogenesis (MOMO). This model can explain global, episodic accretion of 2.7 Ga Archean komatiite-tholeiitic basalt sequences. However, the Archean upper continental crust is composed dominantly of syn- to post-kinematic TTG rather than ultramafic-mafic volcanic sequences (Taylor and McLennan, 1995), requiring the production of voluminous slab, mantle wedge, and crustally-derived calc-alkaline magmas as complementary to ocean plateau accretion (Drummond and Defant, 1991; Feng and Kerrich, 1992; Martin, 1993).

Sengor et al. (1993) and Sengor and Natal'in (1996) proposed a new type of orogeny, so-called "Turkic-type orogeny", for continental growth. The Turkic (Altaid)-type orogenic belts possess very large sutures up to several hundred km wide characterized by subduction-accretion complexes and arc-derived granitoid intrusions, similar to the Circum-Pacific accreted terranes such as Alaska, Canadian Cordillera, and Japan. These subduction-accretion complexes are composed of tectonically juxtaposed fragments of island arcs, back-arc basins, ocean islands/plateaus, trench turbidites, and micro-continents (Sengor, 1993; Sengor and Natal'in, 1996). Another important feature of these orogens is the abundance of orogen-parallel strike-slip fault systems, resulting in lateral stacking and bifurcating of lithological domains (Sengor and Natal'in, 1996). In these respects, the Turkic-type orogeny may be considered as a unified accretionary model for the growth of the continental crust, including the Wawa and Abitibi subprovinces.

7.4. Greenstone belt duality and implications for VMS and gold deposits

This study suggests that the eastern Wawa subprovince greenstone belts have a duality: a subduction-accretion complex, with intra-oceanic plateau sequences and arc-derived turbidites, and rifted-arc and back-arc sequences, coupled to foreland basins (Polat and Kerrich, 1997; Polat et al., 1998b). In this tectonic framework, the gold-prospective Schreiber-Hemlo belt, a subduction-accretion complex formed above a NNW

dipping transpressional subduction zone, is located to the south, whereas the VMS-prospective Manitouwadge and Winston-Big Duck Lake belts are located to the north. This duality may have formed in response to oblique collision and opening of intra-arc and backarc basins in the southern Superior Province. Based on structural style in the southern Superior Province, and the ubiquitous metamorphosed nature of terranes hosting lode-gold deposits, Polat and Kerrich (1997) suggested that those terranes are high-T, low-P type subduction accretion complexes, where subduction-accretion, metamorphism, magmatism, and gold mineralization are closely associated in space and time.

7.5. Resolved and unresolved problems, and future directions

In conclusion, the following points which are highlighted as major geological problems in Chapter 1 for the Schreiber-Hemlo and White River Dayohessarah greenstone belts specifically, and Archean greenstone belts in general, (Chapter I) have been partly or fully resolved by this study:

1. The mantle source characteristics of komatiites and associated Mg-, to Fe-tholeiites;
2. The geodynamic settings of komatiitic and associated basaltic flows;
3. The relationships between komatiites and associated tholeiites;
4. The role of alteration and metamorphism on the trace element characteristics of komatiites and associated tholeiites;
5. The differences and similarities between Archean and Phanerozoic arc magmatism;
6. The differences and similarities between Archean and Phanerozoic subduction zones;
7. The geological relationships between siliciclastic turbidites and interleaved komatiite-basalt sequences;
8. The reasons why there are no high-pressure low temperature (HP/LT) facies metamorphic rocks (blueschist-eclogites) in Archean greenstone belts;

9. The reasons why Archean mélanges are apparently not as abundant as Phanerozoic counterparts;
10. The link between gold mineralization and greenstone belt geodynamics; and
11. The mechanism(s) of the growth of Archean continental crust.

However, the relationship between Archean plume and arc magmatism, and the definite mineralogy of residue during slab and wedge melting in Archean subduction zones have not been resolved by this study.

In addition, there are several first order questions regarding the geological evolution of the Schreiber-Hemlo and White River-Dayohessarah greenstone belts that remain unresolved. In order fully to understand the structural, geochemical, and petrological characteristics of these greenstone belts, the following fundamental questions, amongst others, should be addressed in future studies:

1. Distribution and patterns of structural transposition, and planar and linear fabrics throughout the greenstone belts;
2. Absolute ages of D_1, D_2, and D_3 fabrics;
3. Absolute ages of mafic to felsic sills and dykes;
4. Isotopic (e.g., Sm-Nd, Lu-Hf, Re-Os) compositions of igneous and/or sedimentary rocks;
5. PGE (Ru, Rh, Pd, Os, Ir, Pt) systematics of komatiites and basalts;
6. Mechanisms of slab and wedge melting, mantle metasomatism, and trace element transportation during Archean arc magmatism; and
7. The role of sediment subduction in arc magma compositions.

REFERENCES

Abbott, D., 1996. Plumes and hotspots as sources of greenstone belts. Lithos, **37**: 113-127.

Anderson, A. T., 1982. Parental basalts in subduction zones, implications for continental evolution. J. Geophys. Res., **87**: 7047-7060.

Arculus, R.J., 1981. Island arc magmatism in relation to the evolution of the crust and mantle. Tectonophysics, **75**: 113-133.

Arculus, R. J., 1994. Aspects of magma genesis in arcs. Lithos, **33**: 189-208.

Arias, Z. G. and Helmstaedt, H., 1990. Structural evolution of the Michipicoten (Wawa) greenstone belt, Superior Province: Evidence for an Archean fold and thrust belt. Ontario Geological Survey, Miscellaneous Paper, **150**: 107-117.

Armstrong, R. L., 1991. The persistent myth of crustal growth. Austral. J. Earth. Sci., **38**: 613-630.

Arndt, N. T., 1977. Ultrabasic magmas and high degree melting of the mantle. Contrib. Mineral. and Petrol., **64**: 205-221.

Arndt, N. T. and Nesbitt, R. W., 1982. Geochemistry of Munro Township basalts. In: N. T. Arndt and E. G. Nisbet (Editors), Komatiites, pp. 309-329. Allen and Unwin.

Arndt, N. T. and Jenner, G.A., 1986. Crustally contaminated komatiites and basalts from Kambalda, Western Australia. Chem. Geol., **56**: 229-255.

Arndt. N. T., 1991. High Ni in Archean tholeiites. Tectonophysics, 187: 411-419.
Arndt, N. T., 1994. Archean komatiites. In: K. C. Condie (Editor), Archean crustal evolution, pp. 11-44. Elsevier.

Arndt, N. T., Kerr, A. C., and Tarney, J., 1997a. Dynamic melting in plume heads: the formation of Gorgona komatiites and basalts. Earth Planet. Sci. Letts., **146**: 289-301.

Arndt, N.T., Albarède, F., and Nisbet, E.G., 1997b. Mafic and untramafic magmatism. In: M. de Wit and L. D. Ashwal (Editors), Greenstone belts, Oxford Monogr. On Geol. and Geophys., **35**: 233-254.

Ayres, L. D. and Thurston, P. C., 1985. Archean supracrustal sequences in the Canadian Shield: an overview. Geol. Asso. Can. Spec. Pap., **28**: 343-380.

Baars, F.J., 1997. The Sao Franciscan Craton. In: M. De Wit and L. D. Ashwal (Editors), Greenstone belts. Oxford Monogr. On Geol. and Geophys., **35**: 529-557.

Bach, W., Erzinger, J., Dosso, L., Bollinger, C., Bougnault, H., Etoubleau, J., and Sauerwein, J., 1996. Unusually large Nb-Ta depletion in North Chile ridge

basalts at 36° 50' to 38° 56' S: major element, trace element, and isotopic data. Earth Planet. Sci. Letts., **142**: 223-240.

Bailey, E. B. and McCallian, W. J., 1950. The Ankara mélange and the Anatolian thrusts. Nature, **166**: 938-940.

Barber, A. J., Tjokrosapoetro, S. and Charton, T. R., 1986. Mud volcanoes shale diapirs, wrench faults and mélanges in accretionary complexes, eastern Indonesia. Bull. Amer. Asso. Petrol. Geol., **70**: 1729-1741.

Barley, M.E., 1997. The Pilbara Craton. In: M. de Wit and L. D. Ashwal (Editors), Greenstone belts. Oxford Monogr. on Geol. and Geophys., **35**: 657-664.

Barley, M. E., 1986. Incompatible-element enrichment in Archean basalts: a consequence of contamination by older sialic crust rather than mantle heterogeneity. Geology, **14**: 947-950.

Barrie, C. T., Gorton, M. P., Nalderett, A. J., and Hart, T. R., 1991. Geochemical constraints on the petrogenesis of the Kamiskotia gabbroic complex and related basalts, western Abitibi Subprovince, Ontario, Canada. Precam. Res., **50**: 173-199.

Berhe, S. M., 1990. Ophiolites in north and east Africa: implications for Proterozoic crustal growth. J. Geol. Soc. Lond., **147**: 41-57.

Ben-Avraham, Z., Nur, A., Jones, D., and Cox, A., 1981. Continental accretion: from oceanic plateaus to allochtonous terranes. Science, **213**: 47-54.

Beutner, E. C., 1975. Tectonite and mélange-A distinction: Comment and Reply. Geology, **3**: 358-359.

Berthé, D., Choukroune, P. and Jegouza, P., 1979. Orthogneisses, mylonite and non-coaxial deformation of granites: the example of the south Armorican shear zone. J . Struct. Geol., **1**: 31-42.

Beswick, A. E., 1982. Some geochemical aspects of alteration, and genetic relations in komatiitic suites. In: N. T. Arndt and E. N. Nisbet (Editors), Komatiites, pp. 281-308. Allen and Unwin.

Bhatia, M. R. and Crook, K. A. W., 1986. Trace element characteristics of graywackes and tectonic setting discrimination of sedimentary basins. Contrib. Mineral. and Petrol., **92**: 181-193.

Bickle, M. J. and Nisbet, E. G., 1993. The geology of the Belingwe greenstone belt, Zimbabwe. Balkema, Rorgerdam.

Boher, M., W. Abouchami, Michard, A., Albarède, A., and Arndt, N.T., 1992. Crustal growth in west Africa at 2.1 Ga. J. Geophys. Res., **97**: 345-369.

Bosworth, W., 1989. Mélange fabrics in unmetamorphosed external terranes of northern Appalachians. In: J. W. Horton and N. Rast (Editors), Mélanges and

Olistostromes of the U. S. Appalachians. Geol. Soc. Amer. Spec. Paper, **228**: 6 5-91.

Brenan, J. M., Shaw, H. F., Phinney, D. L., Ryerson, F. J., 1994. Rutile-aqueous fluid partitioning of Nb, Ta, Hf, Zr, U, and Th: implications for high-field strength element depletion in island-arc basalts. Earth Planet. Sci. Letts., **128**: 327-339.

Burke, K., Dewey, J.F. and Kidd, W.S.F., 1976. Dominance of horizontal movements, arc and microcontinental collisions during the later permobile regime. In: B. F. Windely (Editor), The early history of the Earth, pp. 113-129. Wiley.

Burke, K., Fox, P.J., and Sengor, A.M.C., 1978. Buoyant ocean floor and evolution of the Caribbean. J. Geophys. Res., **83**: 3949-3954.

Burke, K., 1995. Did plate tectonics operate in the Archean? Precambrian 95, Program and abstracts, p. 277, Montreal.

Burchfiel, B. C., Cowan, D. S., and Davis, G. A., 1992. Tectonic overview of the Cordilleran orogen in the western United States. In: Burchfiel, B. C., Lipman, P. W., Zoaback, M. I. (Editors), The Geology of North America, The Cordilleran orogen: conterminous U. S., Geol. Soc. Amer., vol. **C-3**: 407-478.

Camire, G. E., Ludden, J. N. Laflèche, M. R., and Burg, J. P., 1993. Mafic and ultramafic amphibolites from the northwestern Pontiac Subprovince: chemical characterization and implication for Tectonic setting. Can. J. Earth Sci., **30**: 1110-1122.

Campbell, I. H. and Hill, R. I., 1988. Two stage model for the formation of the greenstone-granite terrains of Kalgoorlie-Norseman area. Western Australia. Earth. Planet. Sci. Letts., **90**: 11-25.

Campbell, I. H., Griffiths, R. W., and Hill, R. I., 1989. Melting in an Archean mantle plume: Head's its basalts, tails its komatiites. Nature, **339**: 697-699.

Campbell, I. H. and Griffiths, R. W., 1992. The changing nature of mantle hot spots through time: implications for the chemical evolution of the mantle. J. Geol, **92**: 497-523.

Card, K. D. and Ciesielski, A., 1986. DNAG No. 1. Subdivision of the Superior Province of the Canadian Shield. Geosci. Can., **13**: 5-13.

Card, K. D., 1990. A review of the Superior Province of the Canadian Shield, a product of Archean accretion. Precam. Res., **48**: 99-156.

Castillo, P. R., Pringle, M. S., Carson, R. W., 1994. East Mariana basin tholeiites: Cretaceous intra-plate basalts or rift basalts related to the Ontong Java plume. Earth Planet. Sci. Letts., **123**: 139-154.

Cattel, A. and Arndt, N. T., 1987. Low- and high-aluminum komatiites from a late Archean sequence, Newton township, Ontario. Contrib. Mineral. and Petrol., **97**: 218-227.

Chen, C. -Y., Frey, F. A., Garcia, M. O., Dalrymple, G. B., and Hart, S. R., 1991. The tholeiitic to alkaline basalt transition at Heleakala volcano, Maui, Hawaii. Contrib. Mineral. and Petrol., **106**: 183-200.

Corfu, F. and Muir, T. L., 1989a. The Hemlo-Heron Bay greenstone belt and Hemlo Au-Mo deposit, Superior Province, Ontario, Canada. 1. Sequence of igneous activity determined by zircon U-Pb geochronology. Chem. Geol., **79**: 183-200.

Corfu, F. and Muir, T. L., 1989b. The Hemlo-Heron Bay greenstone belt and Hemlo Au-Mo deposit, Superior Province, Ontario, Canada. 2. Timing of metamorphism, alteration and Au mineralization from titanite, rutile, and monozite U-Pb chronology. Chem. Geol., **79**: 201-223.

Cowan, D. S., 1985. Structural analyses in Mesozoic and Cenozoic mélanges in the western Cordillera of north America. Geol. Soc. Amer. Bull., **96**: 451-462.

Condie, K. C., 1981. Archean Greenstone Belts. Elsevier, pp. 434.

Condie, K. C., 1990. Geochemical characteristics of Precambrian basaltic greenstones. In: R. P. Hall and D. J. Hughe (Editors), Early Precambrian basic magmatism, pp. 40-55. Blackie.

Condie, K. C., 1994. Greenstones through time. In: K. C. Condie (Editor), Archean Crustal evolution. Elsevier, pp. 85-121.

Condie, K. C., 1997a. Plate tectonics and crustal evolution.Butterworth-Heinmann, pp. 282.

Condie, K.C., 1997b. Contrasting sources for upper and lower continental crust: the Greenstone connection. J. Geol., **105**: 729-736.

Dann, J.C., 1991. Early Proterozoic ophiolite, central Arizona. Geology, **19**: 590-593.

Davies, G. F., 1992. On the emergence of plate tectonics. Geology, **20**: 963-966.

Davis, D. W. and Corfu, F., 1995. Correlations and contracts among the Superior Province terranes from U-Pb geochronology and Hf isotopes. Precam. inter. conf. on tectonics and metallogeny of early/mid Precambrian orogenic belts, Montreal, Canada, p. 34.

Desrochers, J. P., Hubert, C., Ludden, J. N. and Pilote, P., 1993. Accretion of Archean oceanic plateau fragments in the Abitibi greenstone belt. Geology, **21**: 451-454.

Dewey, J. F. and Bird, J. M., 1971. Origin and emplacement of the ophiolite suite: Appalachian ophiolites in Newfoundland. In: J. M. Bird (Editor), Plate Tectonics. J. Geophys. Res., **76**: 3179-3206.

Dewey, J. F., 1977. Suture zone complexities: A review. Tectonophysics, **40**: 53-67.

de Ronde, E. J., and de Wit, M. J., 1994. Tectonic history of the Barberton greenstone

belt, South Africa: 490 million years of Archean crustal evolution. Tectonics, **13**: 983-1005.

de Wit, M.J., Hart, R.A., and Hart, R.J., 1987. The Jamestown ophiolite complex, Barberton mountain belt: a section through 3.5 Ga oceanic crust. J. African Earth Sci., **6**: 681-730.

de Wit, M.J., Jones, M.G., and Buchanan, D.L., 1992. The geology and tectonic evolution of the Pitersburg greenstone belt, South Africa. Precam. Res., **55**: 123-153.

de Wit, M. J., Roering, C., Hart, J., Armstrong, R.A., de Ronde, C.E.J., Green, R. W. E., Tredoux, M., Peberdy, E., and Hart, R.A., 1994. Formation of an Archean crust. Nature, **357**: 553-562.

Dickinson, W. R., 1972. Evidence for plate-tectonic regimes in the rock record. American Journal of Science, **272**: 551-586.

Dobretsov, N.N., Popov, N.V., Smelov, A.P., Bogomolova, L.M., Moscovchenko, N.I., and Barton, J.M. Jr., 1997. The Aldan-Stanovic Shield. In: M. de Wit and L. D. Ashwal (Editors), Greenstone belts. Oxford Monogr. on Geol. and Geophys., **35**: 710-729.

Dostal, J. and Mueller, W. U., 1997. Komattite flooding of a rifted Archean rhyolitic arc complex: geochemical signature and tectonic significance of the Stoughton-Roquemaure Group, Abitibi greenstone belt, Canada. J. Geol., **105**: 545-563.

Drummond, M. S. and Defant, M. J., 1990. A model for trondhjemite-tonalite-dacite genesis and crustal growth via slab melting: Archean to modern comparisons. J. Geophys. Res., **95**: 21503-21521.

Dupuy, C., Liotard, J. M., and Dostal, J., 1992. Zr/Hf fractionation in intraplate basaltic rocks. Carbonate metasomatism in the mantle source. Geochim Cosmochim. Acta, **56**: 2417-2423.

Eggins, S. M., Woodhead, J. D., Kinsley, L. P. J., Mortimer, G. E., Sylvester, P., McCulloch, M.T., Hergt, J. M., and Handler, M. R., 1997. A simple method for the precise determination of ≥ 40 trace elements in geo;ogical samples by ICPMS using enriched isotope internal standardisation. Chem. Geol., **134**: 311-326.

Ellam, R. M., 1992. Lithospheric thickness as a control on basalt geochemistry. Geology, **20**: 153-156.

Elliot, T. R., Hawkesworth, C. J., and Gronvold, K., 1991. Dynamic melting of Iceland plume. Nature, **351**: 201-106.

Fan., J., 1995. Geochemistry and petrogenesis of unaltered and altered volcanic sequences in the southern Abitibi greenstone belt. Unpublished Ph.D. thesis, University of Saskatchewan, pp.354.

Fan, J. and Kerrich, R., 1997. Geochemical characteristics of Al-depleted and undepleted

komatiites and HREE-enriched tholeiites, western Abitibi greenstone belt: variable HFSE/REE systematics in a heterogeneous mantle plume. Geochim. Cosmochim. Acta, **61**: 4723-4744.

Feng, R. and Kerrich, R., 1990. Geochemistry of fine-grained clastic sediments in the Archean greenstone belt, Canada: implications for provenance and tectonic setting. Geochim. Cosmochim. Acta, **54**: 1061-1081.

Feng, R. and Kerrich, R., 1992. Geochemical evolution of granitoids from the Archean Abitibi Southern Volcanic Zone and Pontiac subprovince, Superior Province, Canada: Implications for tectonic history and source regions. Chem. Geol., **98**: 23-70.

Feng, R., Kerrich, R., and Maas, R., 1993. Geochemical, oxygen, and neodymium isotope compositions of metasediments from the Abitibi greenstone belt and Pontiac Subprovince, Canada: Evidence for ancient crust and Archean terrane juxtaposition. Geochim. Cosmochim. Acta, **57**: 641-658.

Floyd, P. A., 1989. Geochemical features of intra-plate oceanic plateau basalts. In: A. D. Saunders and Norry, M. J. (Editors), Magmatism in the ocean basins.Geol. Soc. Lond. Spec. Publ., **42**: 215-230.

Fralick, P., 1997. Neoarchean Evolution of the Wabigoon Subprovince: Evidence from the sedimentary record. Western Superior Lithoprobe Transect, Third Workshop Report (In press).

Fretzdorff, S., Haase, K. M., and Garbe-Schonberg, C -D., 1996 Petrogenesis of lavas from the Umu volcanic field in the young Hot spot region west of Easter Island, southeastern Pacific. Lithos, **38**: 23-40.

Friend, C. R. L., Nutman, A.P., and McGregor, V.R., 1988. Late Archean terrane accretion in the Godthab region, southern west Greenland. Nature, **335**: 535-538.

Fripp, R.E.P. and Jones, M.G., 1997. Sheeted intrusions and peridotite-gabbro assemblages in the Yilgarn Craton, western Australia: elements of Archean ophiolites. In: M. de Wit and L.D. Ashwal (Editors), Greenstone belts, Oxford Monogr. on Geol. and Geophys. **35**: 422-437.

Fyfe, W. S., 1978. The evolution of Earth's crust: modern plate tectonics to ancient hot spot tectonics? Chemical Geology, **23**: 89-114.

Gamble, J. A., Smith, I. E. M., McCulloch, M. T., Graham, I. J., and Kokelaar, B. P., 1993. The geochemistry and petrogenesis of basalts from the Taupo Volcanic Zone and Kermadec Island Arc, S. W., Pacific. J. Volcanol. and Geother. Res., **54**: 265-290.

Gansser, A., 1974. The ophiolitic mélange, a world wide problem on Tethyan examples. Eclo. Geol. Helve., **67**: 479-507.

Garver, J. I. and Scott, T. J., 1995. Trace elements in shales as indicator of crustal provenance and terrane accretion in southern Canadian Cordillera. Bull. Geol. Soc.

Amer., **107**: 440-453.

Groves, D. I. and Batt, W. D., 1984. Spatial and temporal variations of Archean Metallogenic associations in terms of evolution of granitoid-greenstone belt terranes with particular emphasis on the Western Australian Shield. In: A. Kroner, G. N. Hanson, A. M. Goodwin, (Editors), Archean Geochemistry.pp. 73-98. Springer.

Green, T. H., 1994. Experimental studies of trace element partitioning applicable to igneous petrogenesis-Sedona 16 years later. Chem. Geol., **117**:1-36.

Green, T. H., 1995. Significance of Nb/Ta as an indicator of geochemical processes in the crust-mantle system. Chem. Geol., **120**: 347-359.

Greene, D. C. and Schweickert, R. A., 1995. The Gem Lake shear zone: Cretaceous Dextral transpression in the Northern Ritter pendant, eastern Sierra Nevada, California. Tectonics, **14**: 945-961.

Gromet, L.P. and Silver, L.T., 1987. REE variations across the Peninsular range batholith: implications for batholithic petrogenesis and crustal growth in magmatic arcs. J. Petrol., **28**: 75-125.

Haggerty, S.E., Agnes, T. F., and Burt, D. M., 1994. Apatite, phosphorous and titanium in eclogite garnet from the upper mantle. Geophys. Res. Letts., **21**: 1699-1702.

Hamilton, W. B., 1979. Tectonics of the Indonesian region. United States Geological Survey Professional Paper, **1078**: 1-345.

Hamilton, W. B., 1988. Plate tectonics and island arcs. Geol. Soc. Am. Bull., **100**: 1503-1527.

Hamilton, W.B., 1998. Archean Tectonics and Magmatism. International Geology Review, **40**: 1-39.

Hanan, B. B. and Graham, D. W., 1996. Lead and Helium isotope evidence from oceanic basalts for a common deep mantle plumes. Science, **272**: 991-995.

Hanmer, S., 1986. Asymmetrical pull-aparts and foliation fish as kinematic indicators. J. Struct. Geol., **8**: 111-122.

Hanmer, S. and Passchier, C. W., 1991. Shear sense indicators: A review. Geological Surv. Can. Paper, **90-17**: 1-72.

Hasebe, N., Tagami, T. and Nishimura, S., 1993. Evolution of the Shimanto accretionary complex: A fission-track thermochronologic study. In: M. B. Underwood (Editor), Thermal Evolution of the Tertiary Shimanto Belt, Southwest Japan: An example of Ridge-Trench interaction. Geol. Soc. Amer. Spec. Paper, **273**: 121-136.

Hart, S. R., Hauri, E. H., Oschmann, L. A., and Whitehead, J. A., 1992. Mantle plumes and entrainment: isotopic evidence. Science, **256**: 517-520.

Hawkesworth, C. J., Gallagher, K., Hergt, J. M., and McDermott, F., 1993. Mantle and slab contributions in arc magmas. Ann. Rev. Earth Planet. Sci., **21**: 175-204.

Hawkesworth, C. J. Turner, S. P., McDermott, F., Peate, D. W., and van Calsteren, P., 1997. U-Th isotopes in arc magmas: implications for element transfer from the subducted crust. Science, **276**: 551-555.

Helmstaedt, H. Padgham, W. A., and Brophy, J. A., 1986. Multiple dykes in lower Kam group, Yellowknife greenstone belt: evidence for Archean sea floor spreading? Geology, **14**: 562-566.

Hemond, C., Arndt, N. T., Liechtenstein, U., Hofmann, A. W., Oskarsson, N., and Steinthorsson, S., 1993. The Heterogeneous Iceland plume: Nd-Sr-O isotope and trace element constraints. J. Geophys. Res., **98**: 15833-15850.

Herzberg, C. T. and Ohtani, E., 1988. Origin of komatiites at high pressures. Earth Planet. Sci. Letts., **88**: 321-329.

Herzberg, C. T., 1992. Depth and degree of melting of komatiites. J. Geophys. Res., **97**: 4521-4540.

Hochstaedter, A. G., Kepezhinskas, P., Defant, M., Drummond, M., and Koloskov, A., 1996. Insights into the volcanic arc mantle wedge from magnesian lavas from the Kamchatka arc. J. Geophys. Res., **101**: 697-712.

Hoffman, P. F., 1989. Precambrian geology and tectonic history of North America. In A. W. Bally, and A. R. Palmer (Editors), the Geology of North America. v. A, pp. 447-512. GSA.

Hoffman, P. F., 1991. On accretion of granite-greenstone terranes. In: F. Robert, P. A., Sheahan, and S. B. Green, (Editors), Nuna confer. on greenstone gold and crustal evolution. Val D'or, Geol. Assoc. Can., pp. 32-45.

Hofmann, A.W. and White, W. M., 1982. Mantle plumes from ancient oceanic crust. Earth Planet. Sci. Letts, **57**: 421-426.

Hofmann, A. W., 1997. Mantle geochemistry: the message from oceanic volcanism. Nature, **385**: 219-229.

Hollings, P., Wyman, D., Kerrich R., and Polat, A., 1996. Trace and Sm-Nd systematics of the 3 Ga Lumby Lake greenstone belt, Superior Province, Canada: conjunction of an Archean plateau and oceanic volcanic arc. EOS, **77**: F849.

Hollister, L. S. and Andronicos, C. L., 1997. A candidate for the Baja British Columbia Fault system in the Coast Plutonic Complex. GSA Today, **7**: 1-7.

Hsü, K. J., 1968. The principles of mélanges and their bearing on the Franciscan Knoxville paradox. Geol. Soc. Amer. Bull., **79**: 1063-1074.

Hudleston, P. J., Schultz-Ala, D. and Southwick, D. L., 1988. Transpression in an Archean greenstone belt, northern Minnesota. Can. J. Earth Sci., **25**, 1060-1068.

Hugon, H., 1984. The Hemlo deposit: mineralization within a dextral shear zone. Ont. Geol. Surv. Miscell. Paper, **119**: 212-216.

Hutton, D. H. W. and Reavy, R. J., 1992. Strike-slip tectonics and granite petrogenesis. Tectonics, **11**: 960-967.

Isozaki, Y., Maruyama, S. and Furuoka, F., 1990. Accreted oceanic materials in Japan. Tectonophysics, **181**: 179-205.

Jackson, S. L. and Cruden, R.A. 1995. Formation of the Abitibi greenstone belt by arc-trench migration. Geol., **23**: 471-474.

Jahn, B. M., Gruau, G., Glikson, A. Y., 1982. Komatiites of the Onverwatch Group, S. Africa: REE geochemistry, Sm/Nd age and mantle evolution. Contrib. Mineral. and Petrol., **80**: 25-40.

Jarvis, G. T. and Campbell, I. H., 1983. Archean komatiites and geotherms: solution to an apparent contradiction. Geophys. Res. Letts., **10**: 1133-1136.

Jenner, G. A., Longerich, H. P., Jackson, S. E., and Fryer, B. J., 1990. ICP-MS- a powerful tool for high precision trace element analysis in earth sciences: evidence from analysis of selected U.S.G.S. Reference samples. Chem. Geol., **83**: 133-148.

Jochum, K. P., Seufert, H.M., Thrilwall, M.F., 1990. Multi-element analysis of 15 international standard rocks by isotope dilution spark source mess spectrometry. Geostan. Newslett., **14**: 469-473.

Jochum, K. P., Arndt, N. T., and Hofmann, A. W., 1991. Nb-Th-La in komatiites and basalts: constraints on komatiites petrogenesis and mantle evolution. Earth and Planet. Sci. Letts., **107**: 272-289.

Jochum, K.P., Rehkamper, M., Seufert, H.M., 1994. Trace element analysis of basalt BIR-1 by ID-SSMS, HPLC and LIMS. Geostan. Newslett., **18**: 43-51.

Jones, G., Sano, H. and Valsami-Jones, E., 1993. Nature and tectonic setting of accreted basalts from the Mino terrane, central Japan. J. Geol.Soc, Lond., **150**: 1167-1181.

Joron, J. L. and Treuil, M., 1989. Hygromagmaphile element distribution in oceanic basalts as fingerprints of partial melting and mantle heterogeneities: a specific approach and proposal on an identification and modelling method. In: A. D. Saunders and M. J. Norry (Editors), Magmatism in the ocean basins. Geol. Soc. Lond. Spec. Publ., **42**: 277-299.

Karsten, J. L., Klein, E. M., and Sherman, S. B., 1996. Subduction zone geochemical signature in ocean ridge basalts from the southern Chile Ridge: implications of modern ridge subduction systems for Archean. Lithos, **37**: 143-161.

Kerr, A. C., Marriner, G. F., Arndt, N. T., Tarney, J., Nivia, A., Saunders, A. D., and

Duncan, R. A., 1996. The petrogenesis of Gorgona komatiites, picrites and basalts: new field and petrographic and geochemical constraints. Lithos, **37**: 2 4 5-260.

Kerrich, R., Polat, A., Wyman, D. and Hollings, P., 1996. Trace element systematics of TTG plutons of the late Archean Schreiber-Hemlo greenstone belt, Canada: Implications for petrogenesis. Amer. Geophys. Union Fall Meeting Abstracts, EOS **77**, F849.

Kerrich, R. And Wyman, D. A., 1996. The trace element systematics of igneous rocks in mineral exploration, an overview. In: D. A. Wyman (Editor), Trace Element Geochemistry of Volcanic Rocks: Application for Massive Sulphide Exploration. Geol. Asso. Mineral. Asso. Can, Short Course Notes, 12: 1-50.

Kimura, G., Ludden, J. L., Desrochers, J-P., and Hori, R., 1993. A model of ocean-crust accretion for the Superior Province, Canada. Lithos, **30**: 337-355.

Klein, E. M. and Karsten, J. L., 1995. Ocean-ridge basalts with convergent-margin affinities from the Chile Ridge. Nature, **374**: 52-57.

Kogiso, T., Tatsumi, Y., and Nakano, S., 1997. Trace element transport during dehydration processes in the subducted oceanic crust: 1. Experiments and implications for the origin of ocean island basalts. Earth Planet. Sci. Letts., **148**: 193-205.

Kimura, G. and Mukai, A., 1991. Underplated units in an accretionary complex: mélange of the Shimanto belt of eastern Shikoku, southwest Japan. Tectonics, **10**: 31-50.

Kimura, G., Ludden, J. L., Desrochers, J-P., and Hori, R., 1993. A model of ocean-crust accretion for the Superior Province, Canada. Lithos, **30**: 337-355.

Kimura, G., Sakakibara, M. and Okamura, M., 1994. Plumes in central Panthalassa? Deduction from accreted oceanic fragments in Japan. Tectonics, **13**: 905-916.

Kiyokawa, S., 1992. Geology of the Idonappu belt, central Hokkaido, Japan: Evolution of a Cretaceous accretionary complex. Tectonics, **11**: 1180-1206.

Kiyokawa, S. and Taira, A., 1995. Obducted island arc origin for a middle Archean greenstone belt: west Pilbara coastal greenstone belt, western Australia. Precambrian, 95, Program and abstracts, p. 75, Montreal.

Kroner, A., 1985. Ophiolites and the evolution of tectonic boundaries in the late Proterozoic Arabian-Nubian Shield of north east Africa and Arabia. Precam. Res., **27**: 277-300.

Kuhns, R. J., Sawkins, F. J., and Ito, E., 1994. Magmatism, metamorphism, and deformation at Hemlo, Ontario, and the timing of Au-Mo mineralization in the golden giant mine. Econ. Geol., **89**: 720-756.

Kusky, T. M., 1990. Evidence for Archean ocean opening and closing in the southern Slave Province. Tectonics, **9**: 1533-1563.

Kusky, T. M. and Kidd, 1992. Remnants of an Archean oceanic plateau, Belingwe greenstone belt, Zimbabwe. Geology, **20**: 43-46.

Kusky, T. M. and Vearncombe, J. R., 1997. Structure of Archean greenstone belts. In: M. de Wit, and L. Ashwal, (Editors), Tectonic evolution of greenstone belts. Oxford Monogr. on Geol. and Geophys., pp. 91-24.

Kusky, T. M. and Polat, A., 1998. Arhean greenstone belt evolution: implications for continental growth, Tectonophysics (in review).

Lacroix, S. and Sawyer, E. W., 1995. An Archean fold-thrust belt in the northwestern Abitibi greenstone belt:structural and seismic evidence. Can. J. Earth. Sci., **32**: 97-112.

Laflèche, M. R., Dupuy, C., and Dostal, J., 1992. Tholeiitic volcanic rocks of the late Archean Blake River Group, southern Abitibi greenstone belt: origin and geodynamic implications. Can. J. Earth Sci., **29**: 1448-1458.

Lahaye, Y., Arndt, N. T., Byerly, G., Chauvel, C., Fourcade, S., and Gruau, G., 1995. The influence of alteration on trace element and neodymium isotopic compositions of komatiites. In: J. N. Ludden and N. T. Arndt (Editors), Mafic magmatism through time. Chem. Geol., **126**: 43-64.

Langford, F. F. and Morin, J. A., 1976. The development of the Superior Province of northwestern Ontario by merging island arc. Amer. J. Sci., **276**: 1023-1034.

Langmuir, C.H., Klein, E.M., and Planl, T., 1992. Petrological constraints of mid-ocean ridge basalts: constraints on melt generation beneath ocean ridge. In: J.P. Morgan, D.K.Blackman, and J. M. Sinton (Editors), Mantle flow and melt generation at mid-Ocean ocean ridges. Trans. Amer. Geol. Uni., **71**: 183-280.

Lin, S., Percival, J. A. and Skulski, T., 1996. Structural constraints on the tectonic evolution of a late Archean greenstone belt in the northeastern Superior Province, northern Quebec (Canada). Tectonophysics, **256**: 151-167.

Lister, G. S. and Snoke, A. W., 1984. S-C mylonites. J. Struct. Geol., **6**: 617-638.

Longerich, H. P., Jenner, G. A., Fryer, B. J., and Jackson, S. E., 1990. Inductively coupled plasma-mass spectroscopic analysis of geological samples: a critical evaluation based on case studies. Chem. Geol., **83**: 105-118.

Ludden, J., Gelienas, L., and Trudel, P., 1982. Archean metavolcanics from the Rouyn-Noranda district, Abitibi greenstone belt, Quebec. 2. Mobility of trace elements and petrogenetic constraints. Can. J. Earth Sci., **19**: 2276-2287.

Martin, H., 1986. Effect of steeper Archean geothermal gradient on geochemistry of subduction zone magmas. Geology, **14**: 753-756.

Martin, H., 1993. The mechanisms of petrogenesis of the Archean continental crust-comparison with modern processes. Lithos, **30**: 373-388.

Mahoney, J. J., Storey, M., Duncan, R. A., Spencer, K. J., and Pringle, M., 1993. 1. Geochemistry and geochronology of leg 130 basement lavas: Nature and origin of the Ontong-Java Plateau. Proceedings of the Ocean Drilling Program, Scientific Results, **130**: 3-22.

Mahoney, J. J., Jones, W. B., Frey, F. A., Salters, V. J. M., Pyle, D. G., and Davies, H. L., 1995. Geochemical characteristics of lavas from Broken Ridge, the Naturaliste Plateau and southernmost Kerguelen Plateau: Cretaceous plateau volcanism in the southeast Indian Ocean. Chem. Geol., **120**: 315-345.

Martin, H., 1993. The mechanisms of petrogenesis of the Archean continental crust-comparison with modern processes. Lithos, **30**: 373-388.

Maruyama, S., Masuda, T., Appel, P., 1991. The oldest accretionary complex on the Earth, Isua, Greenland. GSA Abs. and Prog., A429.

McCulloch, M. T. and Gamble, J. A., 1991. Geochemical and geodynamic constrains on subduction zone magmatism. Earth Planet. Sci. Letts., **102**: 358-374.

McCulloch, M. T. and Bennett, V. C., 1994. Progressive growth of the Earth's crust and depleted mantle: Geochemical constraints. Geochim. Cosmochim., Acta, **58**: 4717-4738.

McCuaig, T. C., Kerrich, R., and Xie, Q., 1994. Phosphorus and high field strength anomalies in Archean high magnesian magmas as possible indictors of source mineralogy and depth. Earth. Planet. Sci. Letts., **124**: 221-239.

McDonough, W. F., 1991. Partial melting of subducted oceanic crust and isolation of its residual eclogitic lithology. Philos. Trans. R. Soc. Lond. **A335**: 407-418.

McDonough, W. F. and Ireland, T. R., 1993. Intra-plate origin of komatiites inferred from trace element in glass inclusions. Nature, **365**: 432-434.

McKenzie, D. And Bickle, M.J., 1988. The volume and composition of melts generated by extension of lithosphere. J. Petrol., **29**: 624-679.

McKenzie, D., and O'Nions, R. K., 1991. Partial melt distribution from inversion of rare earth element concentrations. J. Petrol., **32**: 1021-1091.

McLennan, S. M., Taylor, S. R., McCulloch, M. T., and Maynard, J. B., 1990. Geochemical and Sm-Nd isotopic composition of deep sea turbidites: crustal evolution and plate tectonic associations. Cosmochim. Geochim. Acta, **54**: 2015-2050.

McLennan, S.M. and Taylor, S.R., 1991. Sedimentary rocks and crustal evolution: tectonic setting and secular trends. Journal of Geology, **99**: 1-21.

Miller, G. H., Stopler, E. M., and Ahrens, T. J., 1991. The equation of state of molten komatiite, 2. application to komatiite petrogenesis and Hadean mantle. J. Geophys. Res., **96**: 11849-11864.

Miller, D. M., Langmuir, C. H., Goldstein, S. T., Franks, A. L., 1992. The importance of parental magma composition to calc-alkaline and tholeiitic evolution: Evidence from Umnak Island in the Aleutians. J. Geophys. Res., **97**: 321-343.

Miyashiro, A., 1974. Volcanic rock series in island arcs and active continental margins. Amer. J. Sci., **274**: 321-355.

Moore, J. C. and Silver, E. A., 1987. Continental margin tectonics: submarine accretionary prisms. Reviews of Geophysics, **25**: 1305-1312.

Moore, J. C. and Byrne, T., 1987. Thickening of fault zones: a mechanism of mélange formation in accreting sediments. Geology, **15**: 1040-1043.

Morris, P. A., 1995. Slab melting as an explanation of Quaternary volcanism and aseismicity in southwest Japan. Geology, **23**: 395-398.

Mueller, W. U., Daigneault, R., Mortensen, J. K. and Chowen, E. H., 1996. Archean terrane docking: upper crust collision tectonics, Abitibi greenstone belt, Quebec, Canada. Tectonophysic, **265**: 127-150.

Muir, T. L., 1982. The Geology of the Heron Bay area, District of Thunder Bay. Ont. Geol. Serv. Rep. **218**, pp. 89.

Muir, T. L., 1986. Geology of the Hemlo area, District of Thunder Bay. Ont. Geol. Serv., **217**, pp. 65.

Muir, T. L. and Elliott, C. G., 1987. Hemlo tectono-stratigraphic study, district of Thunder Bay. Ont. Geol. Surv. Miscell. Pap., **137**: 117-129.

Myers, J.S., 1993. Precambrian history of the west Australian craton and adjacent orogens. Annu. Rev. Earth. Planet. Sci., **21**: 453-485.

Myers, J.S. and C. Swagers, 1993. The Yilgarn Craton. In: M. de Wit and L. D. Ashwal (Editors), Greenstone belts. Oxford Monogr. on Geol. and Geophys., **35**: 640-656.

Needham, D. T., 1995. Mechanisms of mélange formation: examples from SW Japan and southern Scotland. Journal of Structural Geology, **17**: 971-985.

Nesbitt, R. W and Sun, S. -S., 1976. Geochemistry of Archean spinifex textured peridotites and magnesian and low magnesian tholeiites. Earth Planet. Sci. Letts., **31**: 433-453.

Nesbitt, R. W., Sun, S. -S., and Purvis, A. C., 1979. Komatiites: geochemistry and genesis. Can. Mineral., **17**: 165-186.

Nisbet, E. G., 1982. The tectonic setting and petrogenesis of komatiites In: N. T. Arndt and E. G. Nisbet (Editors), Komatiites, pp. 501-520. George Allen and Unwin.

Nisbet, E. G., Cheadle, M. J., Arndt, N. T., and Bickle, M. J., 1993. Constraining the potential temperature of the Archean mantle: A review of the evidence from

komatiites. Lithos, **30**: 291-307.

Nisbet, E. G. and Walker, D., 1982. Komatiites and structure of the Archean mantle. Earth. Planet. Sci. Letts., **60**: 105-113.

Ohta, H., Maruyama, S., Takahashi, E., Watanebe, Y. and Kato, Y., 1996. Field occurrence, geochemistry and petrogenesis of the Archean Mid-oceanic ridge basalts (AMORBs) of the Cleaverville area, Pilbara Craton, Western Australia. Lithos, **37**: 199-221.

Okay, A. I., 1989. Alpine-Himalayan blueschists. Annu Rev. Earth and Planet. Sci., **17**: 55-87.

Page, R. A., Plafker, G., Fuis, G.S., Nokleberg, W.J., Ambos, E. L., Mooney, W. D. and Campbell, D. L., 1986. Accretion and subduction tectonics in the Chugach Mountains and Copper River Basin, Alaska: Initial results of the Trans-Alaska Crustal Transect. Geology, **14**: 501-505.

Pan, Y. and Fleet, M. E., 1989. Cr-rich calc-silicates from the hemlo area, Ontario. Can. Mineral., **27**: 565-577.

Pan, Y., Fleet, M. E., and Stone, W.E., 1991. Geochemistry of metasedimentary rocks in the late Archean Hemlo-Heron Bay greenstone belt, Superior Province, Ontario: implications for provenance and tectonic setting. Precam. Res., **52**: 53-69.

Park, R. G., 1982. Archean tectonics. Geol. Rund., **71**: 22-37.

Pavlides, L., 1989. Early Palaeozoic composite mélange terrane, central Appalachian Piedmont, Virginia and Maryland; its origin and tectonic history. In: J. W. Horton, and N. Rast (Editors), Mélanges and olistostromes of the Appalachians. Geol. Soc. Amer. Spec. Paper, **228**: 135-193.

Pearce, J.A., 1983. Role of the sub-continental lithosphere in magma genesis at active continental margins. In: C. J. Hawkesworth, and M. J. Norry (Editors), Continental basalts and mantle xenoliths: Shiva, Nantwich, England, p. 230-249.

Pearce, J. A., Harris, N. B. W., and Tindle, A. G., 1984. Trace element discrimination diagrams for the tectonic interpretation of granitic rocks. J. Petrol., **25**: 956-983.

Pearce, J. A. and Parkinson, I. J., 1993. Trace element models for mantle melting: application to volcanic arc petrogenesis. In: H. M. Pichard, T. Alabaster, N. B. W. Harris, and C. R. Neary (Editors), Magmatic Processes and Plate Tectonics. Geol. Soc. Lond. Spec. Publ., **76**: 373-403.

Pearce, J. A. and Peate, D. W., 1995. Tectonic implications of the composition of volcanic arc magmas. Annu. Rev. Earth. Planet. Sci., **23**: 251-285.

Percival, J. A. and Williams, H. R., 1989. The Quetico accretionary complex, Superior Province, Canada. Geology, **17**: 23-25.

Percival, J. A., Stern, R. A., Skulski, T., Card, K. D., Mortensen, J. K., and Begin, N.

J., 1994. Minto block, Superior province: Missing link in deciphering assembly of the Craton at 2.7 Ga. Geology, **22**: 839-842.

Perring, C. S., Barnes, S. J., and Hill, R. E. T., 1996. Geochemistry of komatiites from Forrestania, southern Cross Province, western Australia: evidence for crustal contamination. Lithos, **37**: 181-197.

Plank, T. and Langmuir, C. H., 1988. An evaluation of the global variations in the major element chemistry of arc basalts. Earth and Planetary Science Letters, **90**: 349-370.

Polat, A. and Casey, 1995. A structural record of the emplacement of the Pozanti-Karsanti ophiolite onto the Menderes-Taurus block in the late Cretaceous, eastern Taurides Turkey. J. Struct. Geol., **17**: 1673-1688.

Polat, A., Kerrich, R., Wyman, D., and Hollings, P., 1996a. Plume and magmatic arc accretion in the late Archean Schreiber Hemlo greenstone belt: evidence from trace element systematics, Superior Province, Canada. EOS., **77**: F849.

Polat, A., Casey, J. F., and Kerrich, R., 1996b. Geochemical characteristics of accreted material beneath the Pozanti-Karsanti ophiolite, Turkey: Intra-oceanic detachment, assembly and obduction. Tectonophysics, **263**: 249-276.

Polat, A. and Kerrich, R., 1997. Geodynamic controls on gold mineralization in greenstone belts of the Archean Superior Province, GSA Annual meeting, Abstracts with Programs, **29**: 444.

Polat, A., Kerrich, R., and Casey, J.F., 1997. Geochemistry of Quaternary basalts erupted along the east Anatolian Dead Sea fault zones of southern Turkey: implications for mantle sources. Lithos, **40**: 55-68.

Polat, A., Kerrich, R., and Wyman, D., 1998a. Geochemical diversity in oceanic komatiites and basalts from the late Archean Wawa Subprovince greenstone belts, Superior Province, Canada: Evidence for multiple mantle components in heterogeneous plume. Precam. Res. (in press).

Polat, A., Kerrich, R., and Wyman, D.A., 1998b. The late Archean Schreiber-Hemlo and White River-Dayohessarah greenstone belts, Superior Province: collages of Oceanic plateaus, oceanic arcs, and subduction-accretion complexes. Tectonophysics (in press).

Polat, A. P. and Kerrich, R., 1998. Formation of an Archean tectonic melange in a transpressional subduction-accretion complex: The Schreiber greenstone belt, Superior Province, Canada. Tectonics (In review).

Pollock, S. G., 1989. Mélanges and olistostrome associated with ophiolitic metabasalts and their significance in Cambro-Ordovician forearc accretion in the Appalachians. In: J. W. Horton, J. W and N. Rast (Editors), Mélanges and olistostromes of the Appalachians. Geological Society of America Special Paper, **228**: 43-64.

Potts, P. J., 1987. A handbook of silicate rock analysis. Blackie.

Potts, P. J., Tindle, A. G., and Webb, P. C., 1992. Geochemical reference material compositions. Whittles Publishing, pp. 313.

Prame, W. K. N. and Pohl, J., 1994. Geochemistry of pelitic and psammopelitic Precambrian metasediments from southwestern Sri Lanka: implications for two contrasting source-terrains and tectonic settings. Precam. Res., **66**: 223-244.

Puchtel, I. S., Zhuravlev, D. Z., Samsonov, A. V., and Arndt, N. T., 1993. Petrology and geochemistry of metamorphosed komatiites and basalts from the Tungurcha greenstone belt, Aldan Shield. Precam. Res., **62**: 399-417.

Puchtel, I. S., Hofmann, A.W. Jochum, K.P., Mezger, K., Shchippansky, A.A., and Samsanov, A.V., 1997. The Kostomuksha greenstone belt, NW Baltic Shield: remnant of a late Archean oceanic plateau? Terra Nova, **9**: 87-90.

Purdon, R. H., 1995. Lithostratigraphy and provenance of the Neoarchean McKellar Harbour Sequence, Superior Province, Ontario, Canada. Unpublished M. Sc. Thesis, Lakehead University, p. 103.

Raymond, L. A., 1984. Classification of mélanges. In: L. A. Raymond (Editor) Mélanges: Their Nature, Origin, and Significance. Geol. Soc. Amer. Spec. Paper, **198:** 7-20.

Redman, B. A. and Keays, R. R., 1985. Archean volcanism in the eastern Goldfields Province, Western Australia. Precam. Res., **30**: 113-152.

Reymer, A. and Schubert, G., 1986. rapid growth of some major segments of continental crust. Geology, **14**: 299-302.

Richard, D., Marty B., Chaussidon, M., and Arndt, N. T., 1996. Helium isotopic evidence for a lower mantle component in depleted Archean mantle. Science, **273**: 93-95.

Robin, P-Y, F. and Cruden, A. R., 1994. Strain and vorticity in ideally ductile transpression zones. J. Struct. Geol., **16**: 447-466.

Rollinson, H. R. and Lowry, D., 1992. Early basic magmatism in the evolution of the northern marginal zone of the Archean Limpopo belt. Precam. Res., **55**: 33-45.

Rollinson, H., 1993. Using Geochemical Data: Evaluation, presentation, interpretation. Longman, pp. 352.

Rudnick, R. L., 1995. Making continental crust. Nature, **378**: 571-578.

Sajona, F. G., Maury, R. C., Bellon, H., Cotten, J., and Defant, M., 1996. High field strength element enrichment of Pliocene-Pliostecene island arc basalts, Zamboanga Peninsula, Western Mindano (Philippines). J. Petrol., **37**: 639-726.

Saleeby, J. B., 1984. Tectonic significance of serpentinitic mobility and ophiolitic mélange. In: L. A. Raymond (Editor), Mélanges: their nature, origin, and significance. Geol. Soc. Amer. Spec. Paper, **198**: 153-168.

Saleeby, J. B. and seven others, 1992. Early Mesozoic tectonic evolution of the western U. S. Cordillera. In: B. C. Burchfiel, P. W. Lipman and M. L. M (Editors), The Cordilleran Orogen. Geol. Soc. Amer. The geology of north America **G-3**: 107-168.

Salters, V. J., Storey, M., Seving, J. H., and Whitechurch, H., 1992. 3. Trace element characteristics of Kerguelen-Head plateau basalts. Proceed. of the Ocean Drill. Prog. Sci. Res., **120**: 55-62.

Samson, S.D. and Pachett, P.J., 1991. The Canadian Cordilleran as a modern analogue of Proterozoic crustal growth. Austral. J. Earth Sci., **38**: 595-611.

Sanderson, D. J. and Marchini, W. R., 1984. Transpression. Journal of Structural Geology, **6**: 449-458.

Saunders, A. D., Norry, M. J., and Tarney, J., 1988. Origin of MORB and chemically-depleted mantle reservoirs: trace element constraints. J. Petrol. Spec. Lithosphere Issue: 415-445.

Saunders, A. D. Norry, M. J., and Tarney, J., 1991b. Fluid influence on the trace element compositions of subduction zone magmas. Phil. Trans. R. Soc. Lond. A, **335**: 377-392.

Schiano P., Clocchiatti, R., Shimuzu, N., Maury, R. C., Jochum, K. P., and Hofmann, A. W., 1994. Hydrous, silica rich melts in the sub-arc mantle and their relation with erupted arc lavas. Nature, **377**: 595-600.

Sengor, A. M. C., 1990. Plate tectonics and orogenic research after 25 years: A Tethyan perspective. Earth Science Reviews, **27**: 1-201.

Sengor, A. M. C. and Okurogullari, A. H., 1991. The role of accretionary wedges in the growth of continents: Asiatic examples from Argan to plate tectonics. Eclo. Geol. Helve., **84**: 535-597.

Sengor, A.M.C., 1993. Turkic-type orogeny in the Altaids: implications for the evolution of continental crust and methodology of regional tectonics. Transactions of the Leicester Literary and Philos. Soc., **87**: 37-51.

Sengor, A. M. C., Natal'in, B. A., and Burtman, V. S., 1993. Evolution of the Altaid tectonic collage and Palaeozoic crustal growth in Eurasia. Nature, **364**: 299-307.

Sengor, A. M. C. and Natal'in B. A., 1996. Turkic-type orogeny and its role in the making of the continental crust. Annu. Rev. Earth. Planet. Sci., **24**: 263-337.

Shirey, S. B. and Hanson, G. N., 1986. Mantle heterogeneity and crustal recycling in Archean greenstone belts; evidence from Nd isotopes and trace elements in the Rainy Lake area, Superior Province, Ontario, Canada. Geochim. Cosmochim. Acta, **50**: 2631-2651.

Shirey, S. B., 1991. The Rb-Sr, Sm-Nd, and Re-Os isotopic systems: A summary and comparison of their applications to the cosmochronology and geochemistry of

igneous rocks. In: L. Heaman, L. and J. N. Ludden (Editors), Applications of radiogenic isotope systems to problems in geology, MAC Short course hand book, Mineral. Asso. Can., pp. 103-166.

Silver, E. A. and Beutner, E. C., 1980. Mélanges. Geology, **8**: 32-34.

Silver, P. G., Carlson, R. W., and Olson, P., 1988. Deep slabs, chemical heterogeneity, and structure of mantle convection: investigation of an enduring paradox. Annu. Rev. Earth. Planet. Sci., **16**: 477-541.

Sisson, V. B. and Hollister, L. S., 1988. Low pressure facies series metamorphism in an accretionary sedimentary prism, southern Alaska. Geology, **16**: 358-361.

Skulski, T., Minarik, W., Watson, E. B., 1994. High-pressure experimental trace-element partitioning between clinopyroxene and basaltic melts. Chem. Geol., **117**: 127-147.

Sleep, N. and Windley, B. F., 1982. Archean Tectonics: constraints and inferences. J. Geol., **90**: 363-379.

Sleep, N., 1992. Archean plate tectonics: what can we leaned from continental geology? Can. J. Earth Sci., **29**: 2066-2071.

Smith, A. D. and Ludden, J. N., 1990. Nd isotopic evolution of the Precambrian mantle. Earth. Planet. Sci. Letts., **93**: 14-22.

Stauffer, M. R. and Lewry, J. F., 1993. Regional setting and kinematic features of the Needle Falls Shear Zone, Trans-Hudson Orogen. Can. J. Earth Sci., **30**: 1338-1354.

Stein, M. and Hofmann, A.W., 1994. Mantle plumes and episodic crustal growth. Nature, **372**: 63-68.

Stern, R. A., Syme, E. C., Lucas, S. B., 1995. Geochemistry of 1.9 Ga MORB- and OIB basalts like from the Amisk collage, Flin Flon belt, Canada: evidence for an intra-oceanic origin. Geochim. Cosmochim. Acta, **59**: 3131-3154.

Stolz, A. J., Jochum, K. P., Spettel, B., and Hofmann, A. W., 1996. Fluid- and melt related enrichment in the subarc mantle: Evidence from Nb/Nb variations in island-arc basalts. Geology, **24**: 587-590.

Storey, M., Mahoney, J. J., Kroenke, L. W., and Saunders, A. D., 1991. Are oceanic plateaus sites of komatiite formation? Geology, **19**: 376-379.

Sun, S. -S. and Nesbitt, R. W., 1977. Chemical heterogeneity of the Archean mantle, composition of the Earth and mantle evolution. Earth. Planet. Sci. Letts., **35**: 429-448.

Sun, S. -S., and Nesbitt, R. W., 1978. Petrogenesis of Archean ultrabasic and basic volcanics: Evidence from rare earth elements. Contrib. Mineral. and Petrol., **65**: 301-325.

Sun, S. -S and McDonough, W. F., 1989. Chemical and isotopic systematics of oceanic basalts: implications for mantle composition and processes. In: A. D. Saunders and M. J. Norry (Editor), Magmatism in the ocean basins. Geol. Soc. Lond. Spec. Publ., **42**: 313-345.

Sun, S- S., Nesbitt, R. W., and McCulloch, M. T., 1989. Geochemistry and petrogenesis of Archean and early Proterozoic siliceous high magnesian basalts. In: A. J. Crawford (Editor) Bononites and related rocks, pp. 149-173. Unwin Hyman.

Sun, S. -S., Wallace, D. A., Hoatson, D. M., Glikson, A. Y., and Keasy, R. R., 1991. Use of trace element potential of mafic-ultramafic rocks: examples from the west Pilbara Block and Halls Creek Mobile zone, western Australia. Precam. Res., **50**: 1-35.

Sutcliffe, R.H., Smith, A.R., Doherty, W., and Barnett, L.R., 1990. Mantle derivation of Archean amphibole bearing granitoid and associated mafic rocks: evidence from the southern Superior Province, Canada. Contrib. Mineral. and Petrol., **105**: 255-274.

Swanson, M., 1992. Late Acadian-Alleghenian transpressional deformation: evidence from asymmetric boudinage in the Casco Bay area, coastal Maine. J. Struct. Geol., **14**: 323-341.

Sylvester P. J. And Ghaderi, M., 1997. Trace element analysis of scheelite by exciter laser ablation-inductively coupled plasma mass spectrometry (ELA-ICP-MS) using a synthetic silicate glass standard. Chem. Geol., **141**: 49-65.

Snyder, G. L., Hall, R. P., Hughes, D. J., and Ludwig, K., 1990. Early Precambrian basic rocks of The USA. In: R. P. Hall and D. J. Hughes (Editors), Early Precambrian magmatism, pp. 191-220. Blackie.

Taira, A., Pickering, K. T., Windley, B. F. and Soh, W., 1992. Accretion of Japanese Island arcs and implications for the origin of Archean greenstone belts. Tectonics, **11**: 1224-1244.

Tajda, M. L. G., Mahoney, J. J., Duncan, R. A., and Hawkins, M. P., 1996. Age and geochemistry of Basement and alkalic rocks of Malatia and Santa Isabel, Solomon Islands, southern margin of Ontong Java plateau. J. Petrol., **37**: 361-394.

Tarney, J., Dalziel, I., and de Wit, M. J., Marginal basins Rocas Verdes complex from Southern Chile: a model for Archean greenstone belt evolution. In: B. F. Windley, (Editor), The Archean history of the Earth, pp.131-146. Wiley.

Tarney, J. and Jones, C.E., 1994. Trace element geochemistry of orogenic igneous rocks and crustal growth models. J. Geol. Soc. Lond., **151**: 855-868.

Tatsumi, Y., Sakuyama, M., Fukuyama, H., and Kushiro, I., 1983. Generation of basalt magmas and thermal structure of the mantle wedge in subduction zones. J. Geophys. Res., **88**: 5815-5825.

Taylor, S. R. and McLennan, S. M., 1985. The continental crust: its composition and evolution. Blackwell, Oxford, pp. 1-312.

Taylor, S. R. and McLennan, S. M., 1988. The significance of the rare earths in the geochemistry and cosmochemistry. In: K. A. Gscheindner and L. Eyring, (Editors), Handbook on the Physics and Chemistry of Rare Earths, pp. 485-578. Elsevier.

Taylor, S. R. and McLennan, S. M., 1995. The geochemical evolution of the continental crust. Rev. Geophys, **33**: 241-265.

Thurston, P. C., 1990. The Superior Province-emphasizing greenstone belts. In: Gold and base-metal mineralization in the Abitibi Subprovince, Canada, with emphasis on the Quebec segment. Geol. Dept (Key Centre) and University Extension, The Univ. Western Australia, Publ. **24**, pp. 1-52.

Thurston, P. C. and Chivers, K. M., 1990. Secular variations in greenstone sequence development emphasizing Superior Province, Canada. Precam. Res., **46**: 21-58.

Thurston, P. C., 1991. Archean geology of Ontario: introduction. In: P. C. Thurston, H . R., Williams, H. R. Sutcliffe, G.M. Stott, (Editors), Geology of Ontario. Ont. Geol. Surv., Spec. vol. **4/1**: 73-78.

Thurston P. C., Osmani, I. A., and Stone, D., 1991. Northwestern Superior Province: Review and Terrane analysis. In: P.C. Thurston, H. R. Williams, H. R.Sutcliffe, G. M. Stott (Editors), Geology of Ontario. Ont. Geol. Surv., Spec. vol. **4/1**: 81-141.

Thurston, P. C., 1994. Archean volcanic patterns. In: Condie, K.C. (Editor), Archean crustal evolution. Elsevier, pp. 45-84.

Tikoff, B., Greene, D., 1997. stretching lineations in transpressional shear zones: an example from the Sierra Nevada Batholith California. J. Struct. Geol., **19**: 29-39.

Tikoff, B. and Saint Blanquat, M. S., 1997. Transpressional shearing and strike-slip partitioning in the late Cretaceous Sierra Nevada magmatic arc, California. Tectonics, **16**: 442-459.

Umhoefer, P. J. and Schiarizza, P., 1995. Latest Cretaceous to early Tertiary dextral strike-slip faulting on the southern Yalakom fault system, southeastern Coast Belt. Geol. Asso. Amer. Bull., **108**: 768-785.

Viljoen, R. P. and Viljoen, M. J., 1969. Evidence for the composition of the primitive mantle and its products of patrial melting from a study mafic and ultramafic rocks of the Barberton Mountain Land. Spec. Public. Geol. Soc. S. Africa, **2**: 275-295.

Walker, J. W. R., 1967. Geology of the Jackfish-Middleton area. Ontario Depart. Mines, Geol. Rep. **50**, pp. 41.

Wang, K., Li, J., Hao, J., Li, J. and Zhou, S., 1996. The Wutaishan orogenic belt within the Shanxi Province, northern China: a record of late Archean collision

tectonics. Precam. Res., **78**: 95-103.

Weaver, B. L., 1991. Trace element evidence for the origin of ocean-island basalts. Geology, **19**: 123-126.

West, H. B., Garcia, M. O., Gerlach, D. C., Romano, J., 1992. Geochemistry of tholeiites from Lanai, Hawaii. Contrib. Mineral. and Petrol., **112**: 520-542.

Williams, H. R., 1990. Subprovince accretion tectonics in the south-central Superior Province. Can. J. Earth Sci., **27**: 570-581.

Williams, H. R., 1991. Quetico Subprovince. In: P. C. Thurston, H. R. Williams, H. R. Sutcliffe, G. M. Stott (Editors), Geology of Ontario, Ont. Geol. Surv., Spec. vol. **4/1**: 383-403.

Williams, H. R., Stott, G. M., Heather, K. B., Muir, T. L., and Sage, R. P., 1991. Wawa Subprovince.In: P. C. Thurston, H. R. Williams, H. R. Sutcliffe, G. M. Stott (Editors), Geology of Ontario, Ont. Geol. Surv., Spec. vol. **4/1**: 485- 539.

Wilson, M., 1989. Igneous Petrogenesis.Unwin Hyman, pp. 466.

Wilson, M., 1993. Geochemical signature of oceanic and continental basalts: a key to mantle dynamics. J. Geol. Soc. Lond., **150**: 977-990.

Winchester, J. A. and Floyd, P. A., 1977. Geochemical discrimination of different magma series and their differentiation products using immobile elements. Chem. Geol., **20**: 325-343.

Windley, B. F., 1993. Uniformitarianism today: plate tectonics is the key to the past. In: M. J. Le Bas (Editor), Milestone in Geology. Geol. Soc. Lond. Memoir **16**: 11-23.

Windley, B. F., 1995. The Evolving Continents. Wiley, pp. 526.

Waldron, J. W. F., Turner, D., and Stevens, K. M., 1988. Stratal disruption and development of mélange, western Newfoundland: effect of high fluid pressure in a accretionary terrane during ophiolite emplacement. J.Struct. Geol., **10**: 861-873.

Woodhead, J., Eggins, S., and Gamble, J., 1993. High field strength and trasition element systematics in island arc and back-arc basin basalts: evidence for multi-phase melt extraction and depleted mantle wedge. Earth Planet. Sci. Letts., **114**: 491-504.

Wyman, D.A. and Kerrich, R., 1989. Archean Lamprophyre dikes of the Superior Province, Canada: distribution, petrology, and geochemical characteristics. J. Geophys. Res., **94**: 4667-4696.

Xie, Q., Kerrich, R. and Fan, J., 1993. HFSE/REE fractionations recorded in three komatiite-basalt sequences, Archean Abitibi greenstone belt: implications for multiple plume sources and depths. Geochim. Cosmochim. Acta., **57**: 4111-4118.

Xie, Q. and Kerrich, R., 1994. Silicate-perovskite and majorite signature komatiites from

the Archean Abitibi Greenstone belt: Implications for early mantle differentiation and stratification. J. Geophys. Res., **99**: 15799-15812.

Xie, Q. and Kerrich, R., 1995. Application of isotope for precise measurements of Zr and Hf in low-abundance samples and international reference materials by inductively coupled plasma mass spectrometry: implications for Zr (Hf)/REE fractionations in komatiites. Chem. Geol., **123**: 17-27.

Zaleski, E., Peterson, V. L., and van Breeman, O., 1995. Geological and age relationships of the margins of the Manitouwadge greenstone belt and the Wawa-Quetico subprovince boundary, northwestern Ontario, Current Res. 1995-C, Geol. Surv. Can., pp. 35-44.

Zindler, A. and Hart, S., 1986. Chemical Geodynamics. Annu. Rev. Earth. Planet. Sci., **14**: 493-571.

Appendix 1-1. Rationale behind ICP-MS analyses

As pointed out in Chapter 1 there are only limited high precision trace element data for turbidites and felsic intrusive rocks of the Hemlo and Heron Bay areas (Pan and Fleet, 1991). Accordingly, the magma source characteristics and geodynamic settings of volcanic rocks of in the Schreiber-Hemlo and White River-Dayohessarah greenstone belts are unknown. Similarly, the provenance characteristics of siliciclastic turbidites in the Schreiber area have not been studied. The main reasons for the requirement of high-precision ICP-MS data to understand the petrogenesis and geodynamic setting of igneous, and the source characteristics of siliciclastic sedimentary rocks in the Schreiber-Hemlo and White River-Dayohessarah greenstone belts can be outlined as follows:

(1) Incomplete data;

(2) Detection limits;

(3) Calibration strategies;

(4) Spike equilibration;

(5) International reference materials;

(6) Data forcing; and

(7) Failure of prediction

Each of these is addressed briefly in turn below

1. Incomplete data

Interpretation of the origin of komatiites and related problems such as early stratified magma oceans, or the depth of plume melting, requires accurate and precise analysis of all HFSE and REE (Xie et al., 1993; Xie and Kerrich, 1994; Fan and Kerrich, 1997). Similarly, understanding of the petrogenesis of arc magmatism, such as slab melting

versus slab-dehydration subarc-mantle wedge melting, and sediment input into magma source, requires accurate and precise analysis of all REE, HFSE and transition metals (McCulloch and Gamble, 1991; Brenan et al., 1994; Sachiano et al., 1995; Pearce and Peate, 1995; Hawkesworth et al., 1997). In addition, REE/HFSE and REE/transition metal inter-element relations are critical for determination of the source characteristics of siliciclastic turbidites (Feng and Kerrich, 1992; Taylor and Mclennan, 1995; Polat et al., 1996).

2. Detection limits

Given the low levels of REE and HFSE in komatiites and associated basalts, there are problems with detection limits for some of these elements by XRF (X-ray fluorescence) and INAA (Instrumental neutron activation analysis).

3. Calibration strategies

Prior to the development of ICP-MS, the analysis of all HFSE, REE and transition metals required some combination of analytical instrumentation. The instrument of choice for major elements, Zr and Nb was XRF, whereas Hf, Ta, and REE have been analyzed using INAA or TIMS (thermal ionization mass spectrometry). Unknowns run by XRF are calibrated against an international reference material of similar composition and therefore matrix, and the reference material calibrated against yet another standard that may or may not have a comparable matrix. Similarly, for INAA unknowns are calibrated against reference materials that may in turn have been calibrated against a primary standard with a differing matrix. Hence, critical element-element ratios such La/Nb, Nb/Ta, Zr/Hf, Zr/Sm, Zr/Y analyzed by different techniques may be systematically in error.

4. Spike Equilibration

A requirement of isotope dilution is that the sample and spike attain chemical equilibration. Spark source mass spectrometry (SSMS), with isotope dilution, has been used for low level multi-element analyses of rocks, including komatiites (Jochum et al., 1991). Rock powders are mixed with graphite, and isotopic spike 91Zr added to the powder in an aqueous acid matrix, than dried down (Jochum et al., 1990). In this technique, Zr in the sample and spike are clearly in different chemical forms; in the rock, Zr may be present in a refractory oxide such as baddeleyite (ZrO_4), or substituting in silicates such as pyroxene, whereas the spike will be present as dried down chlorite or nitrate.

The observation that values of Zr and Hf in international reference material BIR analyzed by isotope dilution-spark source mass spectrometry (ID-SSMS), have shifted by +30 % and + 56 % respectively, signifing that caution is warranted in using values of Zr and Hf either in standards or unknowns as determined by this technique (Jochum et al., 1990; 1994).

5. International reference materials

Accurate and precise analysis of trace elements in unknowns presupposes that concentrations of the elements in question are known in the reference material used for calibration. For analysis by ICP-MS, pure elemental standards in solution, e.g., 99.9999% Zr can be used for calibration, such that both elemental standards, unknowns, and reference materials are all in the same dilute aqueous matrix. As a corollary, pure elemental standards cannot be used to calibrate XRF or INAA, because the standard and unknown present such contrasting matrices to in the incident X-ray or neutrons respectively.

Jenner et al. (1990), using ICP-MS and pure elemental standards for calibration, showed that the accepted values for several elements in international rock standards

including BIR-1 were in error. These standards are now more properly termed reference materials (Potts et al., 1992).

6. Data forcing

Some geochemical studies of igneous rocks requires accurate Zr/Hf and Nb/Ta ratios (Dupuy et al., 1992; Stolz et al., 1996; Polat et al., 1997). Most igneous rocks have these ratios invariably close to the chondritic or primitive mantle values, e.g. Zr/Hf=36±2 and Nb/Ta=17±2 (Sun and McDonough, 1989; McDonough and Sun, 1995). A possible corollary of these premises is that one can test the quality of data by comparing these ratios with chondritic or primitive mantle inter-element ratios.

7. Failure of prediction

High pressure experimental studies show systematic HFSE/REE fractionations for pyrope garnet-, majorite garnet,-and Mg silicate perovskite-liquid. The komatiite data of Jochum et al. (1991) do not show HFSE/REE fractionation, yet for some komatiites there is independent evidence for HREE depletion, low Al_2O_3 content, and low Al_2O_3/TiO_2 ratios, for melting in the garnet stability field (Xie et al., 1993). Herzberg (1992) predicted on the basis the experimental data that some komatiites should have the trace element signature of high pressure phases. For these reasons high precision trace element data are required for characterizing the depth of partial melting in some komatiites.

Appendix 3.1. Results of the analyses of trace elements in BIR-1 by various techniques at the University of Saskatchewan.

	University of Saskatchewan (n=90)						Compiled values
	HF-HNO3			Na2O2 sinter			
	x	σ	RSD(%)	x	σ	RSD(%)	Potts et al. (1992)
Sc	46.1	1.4	3				44
V	346	11	3				313
Rb	0.172	0.03	17				0.27
Sr	112	2.07	2	143	6.7	5	108
Y	14.6	0.25	2	14.7	0.67	5	16
Nb	0.738	0.07	10	0.648	0.07	11	2
Zr	15.7	0.5	3	15.1	0.44	3	22
Hf	0.639	0.04	6	0.62	0.06	9	0.58
La	0.614	0.02	3	0.628	0.04	6	0.88?
Ce	1.93	0.05	3	1.92	0.08	4	2.5?
Pr	0.382	0.01	3	0.357	0.02	5	0.5?
Nd	2.47	0.07	3	2.29	0.15	7	2.5
Sm	1.14	0.06	5	1.08	0.06	6	1.08
Eu	0.524	0.03	6	0.516	0.04	8	0.54
Gd	1.91	0.06	3	1.81	0.12	7	1.9
Tb	0.351	0.01	3	0.353	0.02	5	0.41
Dy	2.63	0.08	3	2.53	0.13	5	2.4
Ho	0.567	0.02	4	0.57	0.03	5	0.5
Er	1.72	0.04	2	1.68	0.08	5	1.8
Tm	0.26	0.01	4	0.252	0.02	7	0.27
Yb	1.71	0.05	3	1.59	0.08	5	1.7
Lu	0.259	0.01	4	0.248	0.02	8	0.26
Cs	0.007	0.01	14				0.45
Ba	6.47	0.15	2	7.46	0.48	6	7.7?
Pb	3.13	0.14	5	2.19	0.33	15	3.2
Th	0.06	0.01	17	0.04	0.01	25	0.031
U	0.011	0.002	18				0.01

Appendix 3.2. Major (wt. %) and trace (ppm) element data for komatiites and komatiitic basalts of the Schreiber-Hemlo and Dayohessarah greenstone belts.

	Al-undepleted Komatiites and Komatiitic Basalts								
	Komatiites					Komatiitic Basalts			
Samples	HEG-1	SC95-80	HEG-2	DH96-9	SC96-6	SC95-7	SC96-8	SC95-53	DH96-10
SiO2	47.3	50.4	44.2	47.1	48.3	51.4	47.1	49.1	51.1
TiO2	0.4	0.4	0.5	0.4	0.4	0.6	0.9	0.6	0.8
Al2O3	8.0	6.6	10.2	8.8	7.8	11.4	10.8	10.6	10.7
Fe2O3	11.9	11.2	14.4	13.5	12.7	11.7	15.8	13.9	12.8
MnO	0.2	0.2	0.3	0.2	0.2	0.2	0.2	0.2	0.2
MgO	24.9	23.9	23.3	20.4	22.9	13.3	15.4	16.3	14.3
CaO	7.2	7.1	6.7	8.8	7.6	8.9	8.2	8.2	9.0
K2O	0.01	0.07	0.04	0.09	0.02	0.54	0.63	0.08	0.13
Na2O	0.22	0.25	0.34	0.78	0.09	1.95	0.95	1.01	0.87
P2O5	0.02	0.03	0.03	0.04	0.03	0.04	0.09	0.05	0.08
LOI	5.2	1.0	5.4	3.1	5.0	2.5	1.1	3.9	0.7
Mg#	82	82	78	77	80	72	68	72	71
Cr	3028	1494	2474	1142	1631	1304	1229	1770	775
Co	102	77	107	97	105	73	90	92	65
Ni	972	1017	598	461	804	399	504	546	209
Sc	26	37	36	38	28	42	30	40	47
V	154	250	203	167	171	262	234	252	252
Ta	0.10	0.06	0.05	0.09	0.06	0.11	0.24	0.14	0.13
Nb	0.58	0.57	0.83	1.49	1.08	1.68	4.03	1.81	1.96
Zr	20	26	28	27	38	41	66	49	57
Hf	0.56	0.59	0.65	0.77	0.81	1.18	1.89	1.37	1.63
Th	0.07	0.12	0.14	0.13	0.19	0.23	0.51	0.38	0.32
Y	8	9	12	11	9	15	21	15	20
La	0.62	0.78	0.93	1.51	1.59	2.20	5.01	2.37	3.26
Ce	2.17	2.34	2.46	4.10	4.21	5.80	13.00	6.37	8.93
Pr	0.36	0.40	0.41	0.61	0.61	0.87	1.86	0.91	1.38
Nd	1.89	2.24	2.25	3.16	3.12	4.50	9.00	4.63	6.95
Sm	0.74	0.87	0.98	1.02	1.00	1.50	2.73	1.66	2.24
Eu	0.25	0.12	0.49	0.35	0.33	0.86	0.93	0.75	0.66
Gd	1.10	1.19	1.59	1.54	1.31	1.99	3.30	2.29	3.11
Tb	0.22	0.21	0.28	0.25	0.24	0.36	0.57	0.38	0.53
Dy	1.49	1.41	2.05	1.82	1.60	2.49	3.67	2.58	3.71
Ho	0.33	0.30	0.46	0.36	0.36	0.50	0.83	0.58	0.80
Er	0.98	0.85	1.40	1.18	1.01	1.50	2.38	1.65	2.33
Tm	0.15	0.13	0.20	0.17	0.16	0.23	0.36	0.25	0.36
Yb	0.99	0.80	1.30	1.16	0.96	1.40	2.21	1.48	2.21
Lu	0.16	0.12	0.20	0.15	0.12	0.20	0.36	0.18	0.33
(La/Sm)n	0.54	0.58	0.60	0.96	1.04	0.95	1.20	0.93	0.94
(Gd/Yb)n	0.92	1.23	1.01	1.10	1.12	1.18	1.23	1.28	1.16
(La/Yb)n	0.45	0.70	0.52	0.93	1.18	1.13	1.62	1.14	1.06
(Nb/La)n	0.90	0.70	0.86	0.95	0.65	0.74	0.78	0.74	0.58
(Nb/Th)n	0.98	0.57	0.70	1.36	0.67	0.87	0.94	0.57	0.73
(Th/La)n	0.91	1.24	1.20	7.00	0.96	0.84	0.83	1.30	0.79
Nb/Nb*	0.95	0.63	0.78	1.14	0.66	0.80	0.85	0.65	0.65
Zr/Zr*	1.20	1.30	1.30	1.00	1.30	1.00	0.93	1.20	1.00
Hf/Hf*	1.20	1.10	1.10	1.10	1.10	1.10	0.96	1.20	1.00
Eu/Eu*	0.85	0.40	1.20	0.85	0.88	1.50	0.95	1.20	0.77
Ti/Zr	105	81	103	95	60	88	79	73	86
AL2O3/TiO2	23	19	20	20	20	19	12	18	13
Zr/Hf	36	44	43	35	47	35	35	36	35
Nb/Ta	14	10	17	17	18	15	17	13	15
Zr/Y	2.5	2.8	2.3	2.5	4.4	2.7	3.1	3.3	2.9
Ti/Sm	2835	2411	2936	2527	2301	2398	1910	2167	2194

Appendix 3.2. continues

Al-depleted Komatiite and Komatiitic Basalts

Komatiites			K. Basalts
HB96-15	DH96-11	DH96-12	DH95-2
41.3	42.1	41.6	49.2
0.9	0.6	0.6	1.1
2.8	4.1	3.6	6.0
22.0	20.7	19.9	14.9
0.3	0.3	0.2	0.2
29.3	30.3	28.2	17.5
3.3	1.9	5.7	10.3
0.01	0.01	0.01	0.09
0.11	0.10	0.05	0.66
0.05	0.04	0.04	0.07
7.8	7.1	7.7	1.6
75	76	76	72
3022	2250	2271	1081
175	158	169	99
1734	1544	1822	845
22	15	26	45
158	132	149	259
0.51	0.20	0.15	0.34
8.58	3.42	2.56	5.89
71	40	29	59
1.90	1.02	0.79	1.80
0.73	0.28	0.23	0.44
7	6	5	14
7.39	3.31	3.03	4.17
17.28	8.48	7.48	12.86
2.33	1.19	1.08	1.97
9.91	5.60	5.23	9.28
2.30	1.57	1.32	2.79
0.63	0.32	0.50	0.98
2.06	1.62	1.40	3.14
0.27	0.22	0.20	0.45
1.67	1.36	1.26	2.69
0.32	0.27	0.24	0.51
0.75	0.77	0.58	1.37
0.11	0.10	0.09	0.19
0.72	0.61	0.50	1.07
0.11	0.10	0.10	0.16
2.07	1.36	1.48	0.97
2.36	2.19	2.32	2.42
7.36	3.89	4.34	2.80
1.11	0.99	0.81	1.36
1.40	1.45	1.32	1.60
0.80	0.68	0.61	0.85
1.25	1.20	1.04	1.47
1.00	0.94	0.76	0.85
1.00	0.86	0.75	0.90
0.89	0.62	1.26	1.00
76	93	120	113
3	7	6	5
37	39	37	33
17	17	17	17
10.1	6.7	5.8	4.2
2345	2367	2634	2385

Appendix 3.3. Major (wt. %) and trace (ppm) element data for basalt of the Schreiber-Hemlo and Dayohessarah greenstone belts.

	Group I Basalts							Basalt Group I				
	Group Ia				Group Ib			Group Ic				
Samples	HEG-12	HEG-14	SC95-106	WA95-22	WA95-15	HEG-17	SC95-85	DH95-7	DH95-8	MW95-16	WR95-8	DH95-4
SiO2	50.4	47.1	49.5	50.8	48.6	53.0	52.1	46.6	51.3	49.7	52.8	49.5
TiO2	0.6	0.6	1.1	0.8	0.8	0.6	1.5	1.6	1.7	1.5	1.1	1.2
Al2O3	14.3	14.1	14.8	15.7	15.7	15.2	16.6	13.3	13.4	13.8	15.5	15.3
Fe2O3	12.0	14.4	14.4	13.1	13.3	10.8	12.4	20.1	16.5	16.1	11.3	14.7
MnO	0.2	0.3	0.2	0.3	0.2	0.2	0.2	0.3	0.3	0.2	0.2	0.2
MgO	8.7	10.6	6.7	4.6	8.2	7.5	3.7	5.9	4.2	5.9	5.1	6.2
CaO	12.2	10.9	10.4	12.0	10.2	8.5	10.0	7.9	9.6	9.6	9.8	10.7
K2O	0.4	0.4	0.5	0.3	0.3	0.7	0.5	0.7	0.5	0.5	0.8	0.2
Na2O	1.1	1.5	2.4	2.4	2.6	3.4	2.9	3.5	2.4	2.5	3.3	2.1
P2O5	0.03	0.04	0.08	0.05	0.05	0.04	0.12	0.10	0.12	0.12	0.07	0.08
LOI	0.9	0.7	1.1	1.5	0.8	1.0	0.7	0.6	1.1	0.5	0.5	0.3
Mg#	61	61	50	43	57	60	40	39	36	44	50	48
Cr	638	667	627	327	283	682	231	85	82	90	359	194
Co	66	76	58	46	55	71	66	74	71	57	48	60
Ni	129	153	133	162	161	178	129	73	59	62	98	76
Sc	50	52	51	40	39	61	47	49	50	46	52	41
V	292	310	371	277	250	336	289	405	412	390	381	326
Ta	0.09	0.09	0.13	0.13	0.11	0.10	0.14	0.19	0.24	0.31	0.21	0.24
Nb	1.47	1.50	3.15	2.30	1.64	1.60	2.06	3.79	3.86	4.91	3.70	4.22
Zr	34	31	66	44	46	36	69	73	70	101	58	68
Hf	1.0	0.9	2.2	1.3	1.3	1.0	1.8	2.3	2.2	3.2	1.8	2.1
Th	0.16	0.14	0.36	0.21	0.27	0.23	0.27	0.17	0.23	0.49	0.31	0.38
Y	16	17	25	18	19	16	24	35	30	34	22	27
La	1.94	1.74	3.43	2.45	2.19	2.07	3.52	4.25	3.94	4.16	3.34	3.70
Ce	5.00	4.83	9.24	6.87	6.54	5.66	9.26	12.67	11.11	12.74	9.57	10.40
Pr	0.82	0.77	1.34	1.03	1.03	0.88	1.53	2.07	1.83	2.06	1.47	1.64
Nd	4.21	4.16	8.17	5.58	5.44	4.42	8.30	10.79	10.17	11.56	7.54	8.91
Sm	1.46	1.43	2.69	1.86	1.86	1.51	2.86	3.73	3.26	3.85	2.52	3.15
Eu	0.53	0.51	0.96	0.72	0.69	0.55	0.99	1.35	1.32	1.41	0.91	1.09
Gd	2.11	2.17	3.64	2.42	2.75	2.04	3.88	5.15	4.91	5.31	3.59	4.20
Tb	0.38	0.37	0.63	0.45	0.49	0.38	0.66	0.87	0.83	0.90	0.59	0.71
Dy	2.68	2.70	4.45	2.87	3.40	2.65	4.45	6.06	5.66	6.21	3.99	4.95
Ho	0.60	0.62	0.99	0.66	0.76	0.62	1.00	1.37	1.18	1.36	0.87	1.09
Er	1.90	1.91	2.94	1.89	2.31	1.80	2.83	3.96	3.55	3.94	2.44	3.11
Tm	0.28	0.29	0.43	0.30	0.35	0.27	0.43	0.60	0.56	0.58	0.33	0.48
Yb	1.81	1.91	2.84	1.86	2.26	1.76	2.74	3.79	3.57	3.83	2.47	3.17
Lu	0.27	0.28	0.41	0.27	0.33	0.27	0.43	0.57	0.51	0.57	0.35	0.51
(La/Sm)n	0.86	0.78	0.82	0.85	0.76	0.88	0.80	0.73	0.78	0.69	0.86	0.76
(Gd/Yb)n	0.96	0.94	1.06	1.07	1.00	0.95	1.17	1.12	1.13	1.15	1.20	1.09
(La/Yb)n	0.77	0.65	0.87	0.94	0.70	0.84	0.92	0.80	0.79	0.78	0.97	0.83
(Nb/La)n	0.73	0.83	0.88	0.90	0.72	0.74	0.56	0.86	0.94	1.13	1.06	1.10
(Nb/Th)n	1.09	1.27	1.00	1.30	0.72	0.83	0.90	2.65	2.00	1.20	1.42	1.32
(Th/La)n	0.66	0.65	0.85	0.70	0.99	0.89	0.62	0.32	0.47	0.95	0.75	0.83
Nb/Nb*	0.90	1.03	0.96	1.10	0.72	0.78	0.72	1.50	1.37	1.16	1.23	1.20
Zr/Zr*	0.95	0.88	0.98	0.95	1.00	0.97	1.00	0.80	0.84	1.00	0.93	0.89
Hf/Hf*	1.10	1.00	1.20	0.80	1.00	1.00	0.97	0.93	0.95	1.10	1.10	1.00
Eu/Eu*	0.93	0.90	0.94	1.00	0.94	0.96	0.91	0.94	1.00	0.96	0.93	0.92
Ti/Zr	100	112	101	113	102	100	127	134	146	92	117	109
AL2O3/TiO2	25	24	13	19	20	25	11	8	8	9	14	12
Zr/Hf	33	33	30	44	34	35	38	31	32	34	32	32
Nb/Ta	16	17	24	17	15	16	15	20	16	16	18	18
Zr/Y	2.1	1.9	2.6	2.4	2.4	2.3	2.9	2.1	2.3	2.9	2.7	2.5
Ti/Sm	2340	2431	2473	2675	2514	2382	3060	2619	3126	2413	2688	2360

Appendix 3.3. continues

	Basalts Group II													
	Group IIa						Group IIb							
Samples	HE4-2	HE13	HE96-3	SC95-119	SC95-126	WA95-18	HE19	HE95-9	HE95-25	HB95-17	WA95-13	WA95-4	HB96-12	SC95-81
SiO2	48.7	48.0	54.6	52.6	50.3	51.2	52.6	50.5	50.5	49.5	52.6	49.3	48.3	48.3
TiO2	0.8	2.1	2.3	2.4	1.9	0.9	0.8	0.8	1.0	0.8	1.0	1.2	0.7	0.9
Al2O3	15.1	14.1	12.5	12.3	14.4	14.8	12.8	14.1	15.7	17.5	17.8	15.6	15.2	16.0
Fe2O3	12.2	17.3	15.5	16.6	15.7	14.4	13.0	13.2	14.0	11.6	10.5	14.1	11.5	13.4
MnO	0.2	0.2	0.2	0.1	0.2	0.2	0.2	0.2	0.2	0.2	0.2	0.1	0.2	0.2
MgO	7.4	5.1	4.3	4.9	5.9	6.6	7.2	7.1	5.9	7.0	4.4	8.3	7.4	8.8
CaO	12.2	8.7	7.4	5.3	8.5	10.4	10.0	11.3	9.7	9.8	10.4	8.7	10.7	9.1
K2O	0.2	0.2	0.3	0.4	0.2	0.2	0.4	0.5	0.6	0.7	0.2	0.4	0.2	0.3
Na2O	1.6	3.4	2.8	4.9	3.5	1.1	1.9	2.3	2.3	2.7	2.7	2.1	2.8	2.8
P2O5	0.07	0.19	0.30	0.32	0.21	0.07	0.07	0.06	0.08	0.06	0.07	0.09	0.06	0.07
LOI	1.5	0.4	0.3	2.4	1.4	3.4	1.3	1.1	1.3	1.0	0.5	3.2	1.9	2.3
Mg#	51	48	37	40	41	50	42	50	48	57	48	56	58	59
Cr	435	237	20	27	153	220	724	215	239	412	262	229	282	293
Cu			41	49	48	53		51	58	51	61	55	49	46
Ni	147	72	18	30	40	122	231	92	124	215	169	157	126	118
Sc	43	42	27	46	44	39	37	49	55	39	48	41	29	55
V	266	362	188	351	307	293	251	277	308	275	314	322	201	401
Ta	0.16	0.39	0.73	0.76	0.44	0.21	0.14	0.15	0.16	0.17	0.20	0.26	0.14	0.17
Nb	3.04	7.12	12.23	13.32	7.22	2.94	2.57	2.39	2.31	2.61	2.88	3.89	2.34	2.17
Zr	54	113	220	244	133	51	50	51	59	46	56	73	46	57
Hf	1.4	3.5	5.6	6.3	3.3	1.9	1.6	1.6	1.9	1.5	1.9	2.2	1.3	1.7
Th	0.37	0.76	1.40	1.54	0.62	0.39	0.55	0.55	0.46	0.44	0.50	0.50	0.39	0.50
Y	20	35	62	66	37	21	18	19	23	18	23	26	16	23
La	3.00	6.95	12.60	14.40	7.41	3.61	4.06	3.74	3.65	3.20	4.27	4.36	2.67	3.29
Ce	8.30	19.41	35.47	40.20	20.42	9.62	10.37	9.76	9.39	8.65	11.04	12.06	7.14	8.38
Pr	1.22	2.79	5.30	5.63	3.05	1.45	1.46	1.35	1.42	1.30	1.60	1.83	1.05	1.30
Nd	5.74	14.11	26.67	28.75	15.41	7.18	7.57	6.46	6.95	6.38	7.99	9.21	5.39	6.52
Sm	2.06	4.48	7.77	8.67	4.67	2.32	2.11	1.92	2.34	2.04	2.51	2.91	1.78	1.95
Eu	0.76	1.59	2.38	2.52	1.66	0.88	0.67	0.74	0.90	0.83	0.97	1.03	0.66	0.75
Gd	2.60	5.61	10.30	10.73	5.52	3.13	2.85	2.70	3.45	2.77	3.54	3.98	2.29	2.78
Tb	0.44	0.90	1.70	1.80	0.95	0.56	0.46	0.48	0.57	0.47	0.62	0.66	0.39	0.49
Dy	3.09	6.11	11.49	12.28	6.08	3.73	3.09	3.32	3.84	3.15	4.12	4.50	2.71	3.38
Ho	0.66	1.27	2.50	2.60	1.30	0.83	0.60	0.73	0.84	0.74	0.88	0.98	0.59	0.71
Er	2.14	3.89	7.24	7.35	3.70	2.45	1.77	2.12	2.38	2.02	2.58	2.84	1.75	2.14
Tm	0.32	0.55	1.11	1.12	0.55	0.36	0.27	0.31	0.39	0.29	0.39	0.45	0.25	0.32
Yb	1.98	3.80	7.10	7.12	3.72	2.34	1.74	2.07	2.47	1.95	2.63	2.76	1.63	2.06
Lu	0.28	0.52	1.07	1.09	0.55	0.33	0.24	0.30	0.40	0.29	0.38	0.15	0.23	0.31
(La/Sm)n	0.95	1.00	1.05	1.07	1.00	1.00	1.24	1.25	1.00	1.00	1.09	0.97	0.97	1.09
(Gd/Yb)n	1.10	1.22	1.20	1.24	1.22	1.10	1.35	1.08	1.15	1.17	1.11	1.20	1.16	1.11
(La/Yb)n	1.09	1.31	1.30	1.45	1.42	1.19	1.67	1.50	1.06	1.17	1.16	1.13	1.17	1.14
(Nb/La)n	0.97	0.98	0.93	0.90	0.94	0.79	0.61	0.62	0.61	0.78	0.65	0.86	0.84	0.63
(Nb/Th)n	0.98	1.11	1.04	1.00	1.38	0.89	0.56	0.52	0.60	0.71	0.68	0.93	0.72	0.51
(Th/La)n	0.99	0.88	0.90	0.86	0.70	0.87	1.09	1.20	1.00	1.11	0.94	0.93	1.18	1.22
Nb/Nb*	0.98	1.05	1.00	0.96	1.10	0.84	0.58	0.56	0.60	0.74	0.67	0.89	0.77	0.57
Zr/Zr*	1.10	1.00	1.00	1.00	1.10	0.87	1.00	1.00	1.00	0.89	0.90	0.98	1.00	1.10
Hf/Hf*	1.00	1.00	0.97	1.00	0.98	1.10	1.00	1.10	1.10	1.10	1.10	1.10	1.00	1.20
Eu/Eu*	1.00	0.97	0.82	0.80	1.00	1.00	0.84	1.00	0.97	1.00	1.00	0.93	1.00	0.98
Ti/Zr	92	109	62	60	85	109	81	96	99	104	109	98	94	99
AL2O3/TiO2	18	7	6	5	8	16	16	17	16	22	17	13	21	17
Zr/Hf	39	33	40	39	40	27	37	31	31	30	29	33	36	33
Nb/Ta	18	18	17	18	16	14	18	16	14	15	14	15	17	13
Zr/Y	2.7	3.2	3.6	3.7	3.6	2.4	3.3	2.6	2.6	2.6	2.4	2.8	2.9	2.5
Ti/Sm	2415	2743	1732	1680	2426	2404	2273	2560	2485	2351	2436	2472	2425	2889

Appendix 3.3. continues

	Basalts Group III							
	Group IIIa		Group IIIb					
Samples	HE10-1	HE10-2	HB96-13	HE95-1	SC95-23	SC95-35	SC95-56	SC95-83	HE11-1
SiO2	47.0	47.8	49.0	47.6	51.1	43.8	51.3	52.7	49.7
TiO2	2.1	2.2	1.7	1.7	2.6	2.0	1.4	2.4	1.7
Al2O3	8.2	8.2	6.8	13.2	14.8	14.7	17.5	14.3	14.1
Fe2O3	17.7	15.7	15.7	12.8	15.5	15.1	8.4	10.3	12.7
MnO	0.2	0.2	0.2	0.3	0.4	0.2	0.2	0.2	0.3
MgO	11.2	9.5	11.3	5.5	4.8	6.9	5.0	4.4	5.5
CaO	8.7	11.4	13.6	10.6	4.6	8.4	8.3	8.0	12.4
K2O	1.3	0.1	0.2	0.3	0.4	0.2	0.6	0.3	0.2
Na2O	2.4	2.7	1.4	2.9	3.0	2.3	3.6	3.8	1.9
P2O5	0.14	0.14	0.09	0.17	0.41	0.27	0.20	0.43	0.16
LOI	0.6	2.4	3.3	2.2	1.1	6.3	0.6	1.6	1.1
Mg#	48	52	61	48	41	50	43	44	42
Cr	1238	925	608	176	618	218	175	131	260
Co			52	70	52	66	55	48	
Ni	419	508	244	105	70	163	114	115	96
Sc	39	41	41	35	36	35	37	34	38
V	270	295	415	378	338	301	252	285	367
Ta	1.71	1.97	0.58	0.72	0.48	0.44	0.42	0.71	0.68
Nb	30.41	34.55	10.30	13.27	14.57	7.86	7.27	14.40	13.38
Zr	109	120	83	127	206	107	129	188	120
Hf	2.8	3.2	2.0	3.5	4.8	2.6	3.5	5.3	4.1
Th	1.58	1.76	0.92	1.07	0.89	0.36	0.60	1.12	1.10
Y	15	16	18	26	36	22	26	32	26
La	22.14	22.62	10.70	12.92	16.47	8.60	10.12	17.89	13.43
Ce	51.39	54.02	26.83	34.36	44.63	22.53	26.43	51.18	32.92
Pr	6.18	6.75	3.85	4.76	5.90	3.35	3.80	6.90	4.40
Nd	25.16	28.19	17.77	21.73	29.35	15.86	17.16	30.94	21.92
Sm	5.20	5.70	4.50	5.90	6.93	4.08	4.40	7.29	5.77
Eu	1.43	1.71	1.40	1.90	2.10	1.55	1.52	2.42	1.86
Gd	4.26	4.92	4.51	5.87	7.09	4.24	4.72	7.00	5.82
Tb	0.51	0.59	0.64	0.93	1.09	0.65	0.74	1.01	0.81
Dy	3.04	3.41	3.82	4.93	6.85	4.10	4.76	6.27	4.98
Ho	0.50	0.56	0.71	0.95	1.37	0.83	1.00	1.22	0.90
Er	1.24	1.41	1.82	2.49	3.77	2.28	2.85	3.17	2.41
Tm	0.18	0.20	0.25	0.41	0.56	0.32	0.42	0.47	0.34
Yb	0.97	1.12	1.46	2.17	3.45	2.00	2.77	2.89	1.94
Lu	0.15	0.15	0.49	0.32	0.49	0.30	0.43	0.43	0.27
(La/Sm)n	2.73	2.55	1.54	1.42	1.53	1.36	1.48	1.60	1.50
(Gd/Yb)n	3.63	3.63	2.55	2.23	1.70	1.72	1.40	2.00	2.48
(La/Yb)n	16.40	14.50	5.30	4.30	3.42	3.04	2.62	4.40	4.96
(Nb/La)n	1.32	1.47	0.93	1.00	0.85	0.88	0.70	0.77	0.96
(Nb/Th)n	2.29	2.34	1.33	1.48	1.95	2.60	1.40	1.53	1.45
(Th/La)n	0.57	0.63	0.69	0.67	0.43	0.33	0.47	0.50	0.66
Nb/Nb*	1.74	1.85	1.11	1.20	1.30	1.15	1.00	1.10	1.18
Zr/Zr*	0.66	0.65	0.65	0.78	1.00	0.92	1.00	0.87	0.78
Hf/Hf*	0.61	0.64	0.57	0.76	0.84	0.82	1.00	0.88	0.78
Eu/Eu*	0.93	0.98	0.96	1.00	0.92	1.14	1.00	1.00	0.98
Ti/Zr	114	110	121	80	74	113	64	76	81
AL2O3/TiO2	4	4	4	8	6	7	13	6	8
Zr/Hf	39	37	41	37	43	41	37	36	36
Nb/Ta	18	18	18	18	30	18	17	20	20
Zr/Y	7.3	7.5	4.6	4.9	5.7	4.9	5.0	5.5	4.9
Ti/Sm	2384	2301	2239	1723	2214	2968	1862	1957	1787

Appendix 4.1. Major (wt. %) and trace (ppm) element data for mafic to intermediate tholeiitic volcanic rocks of the Schreiber assemblage.

Sample#	SC95-87	SC95-24	SC95-102	SC95-20	SC95-89	SC95-130	SC95-123	SC95-36	SC95-29
SiO2	50.6	54.0	53.8	49.7	59.4	63.6	61.0	59.4	61.0
TiO2	2.2	1.5	2.4	2.1	1.6	0.6	1.7	1.1	1.0
Al2O3	14.7	15.3	12.6	12.9	13.7	16.5	14.6	14.3	18.8
Fe2O3	16.2	12.4	17.2	18.3	14.9	6.3	8.3	12.6	4.5
MnO	0.2	0.2	0.1	0.3	0.2	0.1	0.2	0.2	0.2
MgO	5.3	3.5	3.2	4.5	2.7	1.5	2.2	2.0	1.1
CaO	7.2	9.4	5.4	9.0	4.6	3.8	5.9	5.8	5.9
K2O	1.3	0.7	2.5	0.2	0.3	4.5	0.4	1.3	2.1
Na2O	2.0	2.7	2.3	2.7	2.4	3.1	5.4	2.6	5.1
P2O5	0.3	0.2	0.5	0.3	0.2	0.1	0.2	0.5	0.4
LOI	5.2	1.2	2.6	1.1	4.4	2.3	4.9	1.4	3.3
Mg#	40	40	30	40	30	30	40	30	40
Cr	22	64	36	14	69	74	137	6	20
Co	42	33	59	41	45	15	32	18	11
Ni	24	53	20	27	45	23	60	2	13
Rb	28	29	65	2	13	102	13	52	37
Sr	297	306	305	133	184	204	129	173	472
Cs	2.2	1.3	1.9	0.2	0.3	1.0	0.3	1.8	1.6
Ba	297	132	803	23	63	624	125	331	522
Sc	37	20	40	40	27	15	16	18	13
V	386	203	407	368	297	90	116	13	124
Ta	0.5	0.3	0.9	0.5	0.3	0.4	0.5	0.9	0.5
Nb	7.7	3.0	19.2	5.2	5.1	5.1	6.9	15.3	7.2
Zr	134	122	236	138	99	127	143	281	211
Hf	3.3	2.9	6.2	3.8	2.4	3.4	3.5	7.6	4.9
Th	1.5	1.0	8.8	0.8	1.0	1.8	1.5	3.1	3.6
U	0.3	0.2	1.4	0.2	0.2	0.6	0.3	0.7	0.7
Y	28	19	44	35	19	10	20	52	15
La	11.9	9.0	44.3	10.0	8.3	14.7	15.0	24.7	35.7
Ce	31.6	21.2	94.9	25.7	22.5	28.7	38.0	62.0	75.9
Pr	4.2	2.9	11.0	3.8	3.0	3.3	4.9	8.6	9.1
Nd	19.3	12.3	44.2	17.7	14.3	12.9	20.6	38.0	35.2
Sm	4.8	3.0	9.1	4.7	3.5	2.6	4.6	9.4	5.4
Eu	1.5	1.1	2.4	1.6	1.1	0.8	1.6	3.0	1.6
Gd	5.2	3.5	8.9	5.9	3.6	2.3	4.4	9.8	4.5
Tb	0.8	0.5	1.2	1.0	0.6	0.3	0.7	1.5	0.5
Dy	5.1	3.3	7.6	6.4	3.6	1.9	3.7	9.5	2.9
Ho	1.1	0.6	1.5	1.3	0.7	0.4	0.7	1.9	0.5
Er	2.9	1.9	4.4	3.9	2.0	1.1	1.8	5.7	1.4
Tm	0.4	0.3	0.6	0.6	0.3	0.2	0.3	0.8	0.2
Yb	2.6	1.9	4.2	3.8	1.8	1.1	1.7	5.2	1.3
Lu	0.4	0.3	0.6	0.6	0.3	0.2	0.3	0.8	0.2
(La/Yb)cn	3.3	3.4	15.0	1.9	3.3	9.9	6.4	3.4	19.7
(La/Sm)cn	1.8	2.2	3.7	1.5	1.7	4.1	2.3	1.9	4.7
(Gd/Yb)cn	1.6	1.5	2.4	1.3	1.7	1.8	2.2	1.6	2.9
(Eu/Eu*)cn	0.9	1.1	0.9	0.9	1.0	1.0	1.1	0.9	1.0
AL2O3/TiO2	7	11	16	8	8	28	10	14	18
Zr/Hf	41	43	40	37	41	37	41	37	43
La/Nb	1.5	3.0	4.2	1.9	1.6	2.9	2.2	1.6	5.0
Th/Nb	0.19	0.33	0.26	0.15	0.20	0.35	0.21	0.20	0.50
Th/La	0.13	0.11	0.06	0.08	0.12	0.12	0.10	0.13	0.10
Zr/Y	5	6	8.3	3.9	5	12	7	5	14
Ti/Zr	97	66	41	66	98	27	58	21	29
Ti/Sm	2718	2733	891	1930	2787	1322	1805	636	1130
P/Nd	60	64	48	41	62	42	38	47	49
Sc/Lu	98	70	86	70	97	90	65	22	72
Nb/Nb*	0.6	0.3	0.2	0.5	0.6	0.3	0.4	0.6	0.2
Zr/Zr*	1.0	1.4	0.6	1.0	1.0	1.5	1.0	1.0	1.1
Hf/Hf*	0.9	1.2	0.6	1.0	0.9	1.5	0.9	1.0	0.9
Ti/Ti*	1.0	1.0	0.4	0.7	1.1	0.6	0.7	0.2	0.5

Appendix 4.2. Major (wt. %) and trace (ppm) element data for mafic to intermediate tholeiitic volcanic rocks of the Hemlo-Black River, Heron Bay assemblages, and White River-Dayohessarah greenstone belt.

	Hemlo-Black River assemblage		Heron Bay assemblage					W. River belt
Sample#	**HE6-3**	**HEG-9**	**HB95-15**	**HB95-31**	**HB95-9**	**HB95-29**	**HB96-11**	**WR95-1**
SiO2	61.4	55.5	54.0	46.4	56.3	57.1	63.4	50.5
TiO2	0.5	0.9	0.6	1.1	1.1	1.1	0.7	1.4
Al2O3	15.3	17.1	15.7	16.6	16.5	14.1	16.6	13.1
Fe2O3	8.3	9.1	9.4	16.4	10.4	14.7	5.6	16.6
MnO	0.2	0.1	0.2	0.2	0.2	0.2	0.1	0.2
MgO	1.7	3.8	4.0	5.5	3.8	2.5	2.4	5.3
CaO	5.7	8.4	11.8	11.2	7.0	6.1	4.5	9.5
K2O	2.0	0.3	0.6	0.5	2.8	0.3	1.5	0.8
Na2O	2.9	4.6	3.5	2.1	1.8	3.7	4.8	2.4
P2O5	0.2	0.2	0.2	0.1	0.1	0.2	0.4	0.1
LOI	1.5	0.3	3.7	1.2	10.4	0.4	2.1	0.9
Mg#	52	50	50	40	40	30	50	40
Cr	148	67	117	362	138	165	9	217
Co		41	36	52	34	44	15	43
Ni	81	90	64	37	32	4	5	32
Rb	54	3	15	12	72	5	45	64
Sr	639	351	913	279	142	288	1061	154
Cs	2.3	0.1	0.6	0.4	5.7	0.7	5.5	17
Ba	497	20	155	207	611	75	637	243
Sc	13	24	24	50	24	49	11	45
V	84	175	187	344	159	308	78	306
Ta	0.2	0.5	0.2	0.2	0.2	0.2	0.4	0.5
Nb	3.9	7.4	3.4	3.2	4.3	4.2	6.9	7.3
Zr	88	145	102	69	93	108	165	116
Hf	2.4	3.9	2.8	2.1	3.2	3.2	4.4	3.2
Th	2.1	1.4	3.5	0.8	0.9	1.7	3.7	2.4
U	0.8	0.3	0.6	0.1	0.2	0.3	0.8	0.5
Y	10	20	18	21	20	31	17	31
La	16.0	15.3	24.2	7.2	8.0	12.6	44.6	12.8
Ce	36.9	35.4	55.7	18.3	20.1	30.9	98.0	30.0
Pr	4.3	4.4	6.7	2.5	2.7	3.9	11.8	3.8
Nd	17.1	18.3	27.4	11.1	11.6	16.7	47.4	16.2
Sm	3.2	4.0	5.3	3.1	3.1	3.9	8.5	4.3
Eu	0.9	1.0	1.5	1.1	1.0	1.4	1.9	1.4
Gd	2.5	4.1	4.3	3.5	3.5	4.5	5.5	5.2
Tb	0.3	0.6	0.5	0.5	0.6	0.7	0.7	0.9
Dy	1.6	3.7	3.0	3.5	3.8	5.1	3.4	5.8
Ho	0.3	0.8	0.6	0.8	0.8	1.1	0.6	1.2
Er	0.9	2.2	1.6	2.1	2.3	3.4	1.6	3.5
Tm	0.1	0.3	0.2	0.4	0.4	0.5	0.2	0.5
Yb	0.8	2.0	1.4	2.2	2.1	3.3	1.4	3.5
Lu	0.1	0.3	0.2	0.3	0.4	0.5	0.2	0.5
(La/Yb)cn	14.2	5.6	12.3	2.4	2.8	2.7	22.9	2.6
(La/Sm)cn	3.3	2.8	3.3	1.7	1.9	2.3	3.8	2.1
(Gd/Yb)cn	2.5	1.7	2.5	1.3	1.4	1.1	3.3	1.2
(Eu/Eu*)cn	0.9	0.8	0.9	1.0	0.9	1.0	0.8	0.9
AL2O3/TIO2	29	18	24	14	16	14	28	10
Zr/Hf	37	37	36	33	29	33	38	36
La/Nb	4.1	2.1	7.1	2.3	1.9	3.0	6.5	1.8
Th/Nb	0.54	0.2	1.02	0.26	0.20	0.41	0.5	0.34
Th/La	0.13	0.1	0.15	0.11	0.11	0.14	0.1	0.19
Zr/Y	9.3	7.2	5.6	3.3	4.6	3.4	9.5	3.8
Ti/Zr	37	39	39	101	65	56	21	69
Ti/Sm	1048	1426	744	2286	1924	1553	416	1857
P/Nd	38	36	43	75	81	51	30	44
Sc/Lu	100	81	112	144	68	97	52	87
Nb/Nb*	0.2	0.4	0.1	0.4	0.5	0.3	0.1	0.5
Zr/Zr*	0.8	1.2	0.6	0.8	1.1	0.9	0.6	1.0
Hf/Hf*	0.8	1.1	0.6	0.9	1.3	1.0	0.5	1.0
Ti/Ti*	0.5	0.6	0.3	0.9	0.7	0.6	0.2	0.7

Appendix 4.3. Major (wt. %) and trace (ppm) element data for mafic to intermediate calc-alkaline volcanic rocks of the Schreiber assemblage.

Sample#	SC95-25	SC95-93	SC95-42	SC95-43	SC95-94	SC95-26
SiO2	53.4	55.4	59.9	56.2	58.1	61.7
TiO2	0.7	0.8	0.6	1.0	1.0	0.8
Al2O3	13.7	15.3	13.9	15.8	18.2	15.7
Fe2O3	9.8	8.9	8.0	10.5	6.5	6.9
MnO	0.2	0.1	0.1	0.2	0.1	0.1
MgO	9.5	5.6	6.1	4.8	2.9	4.8
CaO	9.1	6.8	5.9	6.8	6.3	5.0
K2O	0.2	1.8	1.1	1.0	1.8	0.9
Na2O	3.0	4.9	4.2	3.4	4.6	3.9
P2O5	0.2	0.4	0.2	0.2	0.4	0.2
LOI	10.6	6.3	1.2	1.2	4.0	4.0
Mg#	70	60	60	50	50	60
Cr	594	136	590	106	136	147
Co	42	31	32	39	28	25
Ni	326	46	126	61	72	123
Rb	5	47	48	47	35	18
Sr	186	904	330	309	477	480
Cs	0.9	5.2	1.3	2.1	2.1	1.1
Ba	181	699	283	211	510	335
Sc	28	23	18	24	14	16
V	172	186	135	169	128	119
Ta	0.2	0.3	0.3	0.4	0.3	0.4
Nb	2.6	5.2	6.3	5.7	5.2	4.1
Zr	112	166	151	110	142	130
Hf	3.2	4.4	3.3	2.9	3.6	3.5
Th	6.4	2.9	6.3	1.1	4.6	2.4
U	1.3	0.6	4.9	0.3	0.9	0.5
Y	16	20	18	18	15	11
La	42.0	40.4	38.8	15.9	35.9	14.8
Ce	88.2	93.1	79.0	33.8	77.5	31.4
Pr	11.0	11.1	9.1	4.9	9.9	3.9
Nd	42.1	42.8	39.2	20.7	36.1	15.0
Sm	7.2	8.0	7.2	4.4	5.9	2.8
Eu	1.9	2.1	1.7	1.3	1.7	0.9
Gd	5.3	6.2	5.6	3.9	4.5	2.6
Tb	0.6	0.7	0.6	0.6	0.5	0.4
Dy	3.1	3.9	3.5	3.4	3.0	2.3
Ho	0.5	0.8	0.7	0.7	0.5	0.4
Er	1.4	2.0	1.8	2.0	1.5	1.2
Tm	0.2	0.3	0.3	0.3	0.2	0.2
Yb	1.2	1.8	1.6	1.8	1.3	1.1
Lu	0.2	0.3	0.2	0.3	0.2	0.2
(La/Yb)cn	24.6	16.0	17.2	6.3	20.0	9.4
(La/Sm)cn	4.2	3.6	3.9	2.6	4.4	3.7
(Gd/Yb)cn	3.5	2.8	2.9	1.8	2.9	1.9
(Eu/Eu*)cn	0.9	0.9	0.8	0.9	0.9	0.9
AL2O3/TIO2	21	19	24	15	18	23
Zr/Hf	35	38	45	38	40	37
La/Nb	16	8	6.21	2.81	6.95	3.62
Th/Nb	2.48	0.55	1.00	0.19	0.89	0.59
Th/La	0.15	0.07	0.16	0.07	0.13	0.16
Zr/Y	7	8	8.34	6.20	10	12
Ti/Zr	34	29	23	57	42	31
Ti/Sm	533	604	482	1433	996	1427
Sc/Lu	147	85	74	92	73	93
Nb/Nb*	0.1	0.1	0.1	0.3	0.1	0.2
Zr/Zr*	0.4	0.6	0.6	0.8	0.7	1.4
Hf/Hf*	0.5	0.6	0.5	0.8	0.6	1.3
Ti/Ti*	0.2	0.3	0.2	0.6	0.5	0.6

Appendix 4.4. Major (wt. %) and trace (ppm) element data for intermediate calc-alkaline volcanic rocks of the Hemlo-Black River assemblage.

Sample#	HE1A	HE1B	HE2	HE6-1	HE6-2	HE6-5	HE95-29	HEG-8	HEG-15	HEG-20	HEG-11	HEG-19	HEG-21
SiO2	59.0	63.0	58.2	55.5	59.3	56.8	60.1	57.2	57.5	56.7	63.1	59.6	63.9
TiO2	0.7	0.6	0.6	0.6	0.6	0.5	0.7	0.8	0.8	0.6	0.7	0.6	0.5
Al2O3	17.1	17.0	15.8	15.4	15.9	14.1	15.3	15.6	14.9	13.6	16.3	14.9	15.2
Fe2O3	8.7	5.6	6.6	7.2	6.2	5.7	8.2	7.2	7.7	9.1	5.5	7.7	5.5
MnO	0.1	0.1	0.1	0.1	0.1	0.1	0.1	0.1	0.1	0.1	0.1	0.1	0.1
MgO	4.5	3.2	3.3	5.0	3.5	4.2	4.5	5.9	6.4	6.2	3.3	5.3	4.2
CaO	2.7	2.8	5.9	8.2	7.3	9.0	5.5	7.5	6.8	7.0	4.7	7.2	5.6
K2O	2.1	2.3	1.0	1.7	1.4	1.3	0.5	0.6	1.5	2.8	2.1	0.8	2.2
Na2O	3.0	3.8	4.9	3.2	3.8	2.9	4.8	4.7	3.8	3.4	4.0	3.3	2.7
P2O5	0.1	0.1	0.3	0.5	0.3	0.2	0.2	0.4	0.5	0.4	0.3	0.4	0.2
LOI	2.1	1.4	3.2	2.3	1.6	5.4	0.9	0.4	0.7	4.1	0.5	4.1	3.2
Mg#	61	44	59	62	48	62	55	60	60	60	60	60	60
Cr	531	236	84	399	338	206	148	158	205	251	55	192	279
Co							29	32	37	33	21	29	25
Ni	229	93	24	119	95	80	77	110	66	21	35	60	87
Rb	67	72	26	49	39	38	14	20	52	90	69	20	54
Sr	503	566	1043	435	760	528	214	1374	1181	936	1125	744	667
Cs	4.6	5.2	0.7	4.2	3.0	4.4	0.5	2.9	3.1	7.8	8.2	1.7	6.4
Ba	665	561	664	264	374	246	119	617	1028	675	1112	195	381
Sc	22	16	13	17	16	12	23	15	23	27	12	19	12
V	155	114	92	119	108	78	145	123	172	185	111	166	103
Ta	0.4	0.3	0.4	0.2	0.2	0.2	0.4	0.6	0.4	0.2	0.4	0.2	0.2
Nb	5.8	4.8	7.3	5.4	3.6	3.3	6.6	12.9	7.2	4.5	6.8	3.0	2.4
Zr	135	139	171	112	102	97	135	221	170	106	168	101	106
Hf	3.4	3.6	4.3	3.2	3.1	2.6	3.3	5.5	4.6	2.9	4.4	2.6	2.7
Th	4.2	4.9	9.6	2.5	2.0	1.7	1.7	6.5	6.9	3.8	6.6	4.3	1.6
U	0.9	1.1	2.0	0.5	0.6	0.2	0.4	1.9	1.4	1.2	1.4	0.7	0.4
Y	13	13	20	14	12	9	17	21	22	18	15	16	9
La	21.8	28.7	54.5	35.2	23.4	15.5	12.4	61.6	52.9	30.0	42.7	53.4	16.7
Ce	47.7	63.6	115.9	94.2	58.0	37.0	27.8	134.4	115.8	66.9	91.2	130.2	41.3
Pr	5.5	7.4	13.0	12.6	7.4	4.4	3.8	15.8	14.0	8.5	10.8	16.9	5.6
Nd	20.8	29.4	52.2	55.9	30.8	17.3	15.2	63.2	57.4	36.8	42.0	69.3	22.6
Sm	3.8	5.1	8.8	9.3	5.5	3.1	3.4	10.8	10.3	7.1	7.2	10.8	3.8
Eu	1.1	1.4	2.3	2.3	1.5	0.9	1.0	2.7	2.5	1.8	1.8	2.7	1.1
Gd	3.1	3.7	6.1	5.9	4.2	2.3	3.1	7.6	7.5	5.5	5.0	6.9	3.4
Tb	0.4	0.4	0.6	0.6	0.4	0.3	0.5	0.8	0.8	0.6	0.5	0.7	0.4
Dy	2.2	2.4	3.5	3.0	2.2	1.6	2.8	3.9	4.1	3.5	2.9	3.4	1.8
Ho	0.4	0.4	0.6	0.5	0.4	0.3	0.6	0.7	0.7	0.6	0.5	0.6	0.3
Er	1.2	1.2	1.7	1.2	1.0	0.8	1.6	1.6	1.8	1.6	1.3	1.6	0.9
Tm	0.2	0.2	0.2	0.2	0.2	0.1	0.3	0.2	0.3	0.3	0.2	0.2	0.1
Yb	1.4	1.2	1.5	1.0	0.9	0.7	1.7	1.3	1.6	1.6	1.2	1.4	0.8
Lu	0.2	0.2	0.3	0.2	0.1	0.1	0.3	0.2	0.2	0.2	0.2	0.2	0.1
(La/Yb)cn	11.2	16.9	25.9	24.3	18.4	15.4	5.3	33.6	23.3	13.9	24.6	27.9	15.4
(La/Sm)cn	3.7	3.6	4.0	2.4	2.7	3.3	2.6	4.1	3.7	3.0	4.2	3.5	3.2
(Gd/Yb)cn	1.8	2.5	3.4	4.7	3.8	2.7	1.5	4.8	3.8	2.9	3.3	4.1	3.6
(Eu/Eu*)cn	1.0	0.9	1.0	1.0	1.0	1.0	0.9	0.9	0.8	0.9	0.9	0.9	0.9
AL2O3/TiO2	24	30	25	24	28	30	21	19	17	20	22	23	30
Zr/Hf	40	39	40	35	33	37	41	40	37	36	38	39	40
La/Nb	3.75	6.04	7.44	6.55	6.49	4.69	1.89	4.8	7.3	6.7	6.3	18.0	7.0
Th/Nb	0.72	1.02	1.31	0.46	0.56	0.51	0.26	0.5	1.0	0.9	1.0	1.4	0.7
Th/La	0.19	0.17	0.18	0.07	0.09	0.11	0.14	0.1	0.1	0.1	0.2	0.1	0.1
Zr/Y	10.2	10.6	8.4	7.8	8.2	11.0	7.8	10.4	7.9	5.9	11.0	6.2	11.6
Ti/Zr	33	23	25	36	33	31	33	22	30	38	26	38	29
Ti/Sm	1177	631	492	435	609	991	1285	455	498	565	598	356	813
Sc/Lu	115	84	52	113	114	120	86	83	100	111	69	102	104
Nb/Nb*	0.2	0.1	0.1	0.2	0.1	0.2	0.4	0.2	0.1	0.1	0.1	0.1	0.1
Zr/Zr*	1.1	0.7	0.6	0.3	0.5	0.4	1.3	0.6	0.5	0.5	0.7	0.3	0.8
Hf/Hf*	1.0	0.7	0.5	0.4	0.6	0.4	1.1	0.5	0.5	0.5	0.6	0.2	0.7
Ti/Ti*	0.5	0.3	0.2	0.2	0.3	0.4	0.5	0.2	0.2	0.3	0.3	0.2	0.3

Appendix 4.5. Major (wt. %) and trace (ppm) element data for intermediate calc-alkaline volcanic rocks of the Heron Bay assemblage and White River-Dayohessarah greenstone belt.

	Heron Bay Assemblage				White River-Dayohessarah belt		
Sample#	**HB956**	**HB9513**	**HB9514**	**HB96-11**	**WR9510**	**DH96-5**	**WR956**
SiO2	57.8	63.9	63.2	63.4	57.8	61.2	62.3
TiO2	0.6	0.6	0.6	0.7	0.6	0.5	0.6
Al2O3	15.0	16.7	17.5	16.6	16.2	16.3	15.2
Fe2O3	8.3	6.2	6.0	5.6	8.0	5.8	6.0
MnO	0.1	0.1	0.1	0.1	0.1	0.1	0.1
MgO	6.0	3.7	3.3	2.4	5.5	2.5	3.7
CaO	6.8	2.9	2.6	4.5	5.4	9.0	5.3
K2O	1.7	1.4	1.7	1.5	2.4	0.4	2.2
Na2O	3.3	4.3	4.9	4.8	3.9	4.0	4.5
P2O5	0.2	0.3	0.2	0.4	0.1	0.1	0.2
LOI	5.9	1.8	1.4	2.1	1.0	0.4	0.8
Mg#	60	60	50	50	60	50	60
Cr	353	155	183	9	245	32	166
Co	32	23	19	15	32	29	21
Ni	61	72	57	5	73	22	40
Rb	52	43	45	45	148	4	70
Sr	765	866	775	1061	359	361	904
Cs	8.7	3.7	3.3	5.5	25	0.6	4
Ba	808	499	674	637	393	46	948
Sc	24	15	12	11	24	13	15
V	164	128	94	78	155	91	116
Ta	0.3	0.4	0.3	0.4	0.2	0.2	0.3
Nb	5.2	5.5	5.2	6.9	2.6	3.1	4.0
Zr	126	155	168	165	82	88	132
Hf	3.9	4.2	4.5	4.4	2.4	2.2	3.5
Th	2.8	7.5	8.0	3.7	1.2	1.4	5.4
U	0.7	1.6	1.5	0.8	0.3	0.3	1.1
Y	18	14	13	17	13	10	12
La	30.0	45.0	46.9	44.6	10.6	11.7	33.1
Ce	69.3	100.2	101.8	98.0	23.9	27.1	70.5
Pr	8.4	11.9	12.1	11.8	2.9	3.3	8.4
Nd	35.3	44.7	44.9	47.4	11.9	13.0	32.6
Sm	6.6	7.7	6.9	8.5	2.6	2.7	5.6
Eu	1.6	2.0	2.1	1.9	0.8	0.9	1.5
Gd	5.3	5.4	5.2	5.5	2.5	2.3	4.1
Tb	0.6	0.5	0.6	0.7	0.3	0.3	0.4
Dy	3.2	2.9	2.7	3.4	2.1	1.7	2.2
Ho	0.6	0.5	0.5	0.6	0.5	0.4	0.4
Er	1.6	1.3	1.3	1.6	1.3	0.9	1.1
Tm	0.3	0.2	0.2	0.2	0.2	0.1	0.1
Yb	1.4	1.1	1.0	1.4	1.3	1.0	1.1
Lu	0.2	0.2	0.1	0.2	0.2	0.1	0.1
(La/Yb)cn	15.0	28.6	33.0	22.9	5.7	8.7	21.9
(La/Sm)cn	3.3	4.2	4.9	3.8	2.9	3.1	4.3
(Gd/Yb)cn	3.0	4.0	4.2	3.3	1.6	2.0	3.1
(Eu/Eu*)cn	0.8	0.9	1.0	0.8	0.9	1.1	0.9
AL2O3/TIO2	22	27	31	28	25	34	25
Zr/Hf	32	37	37	38	34	40	38
La/Nb	5.72	8.13	9.06	6.5	4.0	3.8	8.3
Th/Nb	0.53	1.35	1.55	0.5	0.47	0.5	1.35
Th/La	0.09	0.17	0.17	0.1	0.12	0.12	0.16
Zr/Y	7.0	10.8	12.8	9.5	6.6	8.6	10.6
Ti/Zr	32	24	20	21	46	33	27
Ti/Sm	617	483	485	416	1475	1065	634
Sc/La	100	88	81	52	122	99	106
Nb/Nb*	0.2	0.1	0.1	0.1	0.2	0.2	0.1
Zr/Zr*	0.6	0.6	0.7	0.6	1.0	1.0	0.7
Hf/Hf*	0.6	0.6	0.6	0.5	1.1	0.9	0.6
Ti/Ti*	0.3	0.2	0.2	0.2	0.6	0.5	0.3

Appendix 4.6. Major (wt. %) and trace (ppm) element data for felsic volcanic rocks of the Schreiber assemblage.

Sample#	SC95-109	SC95-111	SC95-112	SC95-90	SC95-32
SiO2	65.3	70.0	68.2	64.6	68.7
TiO2	0.5	0.5	0.5	0.8	0.5
Al2O3	15.8	16.8	15.6	15.8	15.8
Fe2O3	7.4	1.9	4.6	6.7	7.0
MnO	0.1	0.0	0.0	0.1	0.1
MgO	2.0	0.4	1.9	3.1	1.6
CaO	2.7	1.1	1.8	4.0	1.0
K2O	1.9	0.5	1.3	1.6	2.0
Na2O	4.3	8.7	6.0	3.2	3.2
P2O5	0.1	0.1	0.1	0.2	0.1
LOI	4.4	1.0	2.7	3.6	2.3
Mg#	40	30	50	50	30
Cr	7	13	9	38	92
Co	23	9	19	22	27
Ni	44	18	25	31	71
Rb	55	13	30	63	55
Sr	162	190	175	236	231
Cs	1.5	0.4	1.3	1.3	3.5
Ba	363	123	774	215	276
Sc	10	12	10	17	17
V	92	59	89	124	94
Ta	0.7	0.7	0.7	0.5	0.3
Nb	6	7.32	6.16	6	4
Zr	124	153	123	120	121
Hf	3.3	3.6	3.3	3.1	3.3
Th	4.0	4.3	4.0	2.8	2.1
U	1.4	1.5	1.3	1.0	0.7
Y	9	10	9	16	8
La	16.2	17.9	15.6	14.1	12.8
Ce	33	37	31	30	26
Pr	3.5	3.9	3.4	3.5	3.0
Nd	13.3	14.6	13.4	14.0	11.3
Sm	2.4	2.6	2.6	3.1	2.3
Eu	0.7	0.8	0.8	1.0	0.8
Gd	2.3	2.3	2.6	2.9	2.0
Tb	0.3	0.3	0.3	0.5	0.3
Dy	1.7	1.8	2.0	2.8	1.6
Ho	0.3	0.3	0.4	0.6	0.3
Er	1.0	0.9	1.0	1.6	1.0
Tm	0.2	0.1	0.2	0.2	0.2
Yb	1.0	0.9	1.0	1.4	1.1
Lu	0.2	0.1	0.1	0.2	0.2
(La/Yb)cn	11.7	14.3	11.3	7.1	8.3
(La/Sm)cn	4.8	4.9	4.3	3.3	4.0
(Gd/Yb)cn	1.9	2.1	2.2	1.7	1.5
(Eu/Eu*)cn	0.9	0.9	0.9	1.0	1.1
AL2O3/TIO2	29	29	30	19	28
Zr/Hf	38	42	37	39	37
La/Nb	2.6	2.4	2.5	2.4	3.2
Th/Nb	0.63	0.58	0.64	0.48	0.53
Th/La	0.25	0.24	0.25	0.20	0.17
Zr/Y	14.3	15.7	13.1	7.7	14.3
Ti/Zr	26	22	25	41	28
Ti/Sm	1328	1280	1207	1600	1458
Sc/Lu	65	84	69	73	92
Nb/Nb*	0.3	0.3	0.3	0.3	0.2
Zr/Zr*	1.5	1.7	1.4	1.3	1.6
Hf/Hf*	1.5	1.5	1.4	1.2	1.6
Ti/Ti*	0.5	0.5	0.5	0.6	0.6

Appendix 4.7. Major (wt. %) and trace (ppm) element data for felsic volcanic rocks of the Hemlo-Black River assembalge.

Sample#	HE3	HE96-1	HE96-2	HE96-5	HE96-9	HEG-4	HEG-5	HEG-6	HEG-7
SiO2	67.8	74.3	69.0	70.6	72.7	70.0	70.1	70.1	70.2
TiO2	0.4	0.3	0.4	0.3	0.6	0.3	0.3	0.3	0.3
Al2O3	14.1	14.4	16.1	16.0	15.3	16.0	16.0	15.9	16.0
Fe2O3	3.5	1.9	3.1	2.7	2.8	2.8	2.6	2.7	2.8
MnO	0.1	0.0	0.0	0.0	0.1	0.0	0.0	0.0	0.0
MgO	1.9	0.9	1.3	1.1	0.6	1.4	1.2	1.1	1.2
CaO	3.5	1.1	3.4	3.1	2.7	2.7	2.1	3.7	2.4
K2O	1.6	1.4	1.3	1.1	2.0	1.2	0.8	1.4	1.2
Na2O	4.5	5.6	5.3	5.1	3.2	5.4	6.7	4.7	5.9
P2O5	0.1	0.1	0.1	0.1	0.1	0.1	0.1	0.1	0.1
LOI	2.4	1.0	1.8	0.4	1.3	1.3	1.1	1.0	1.1
Mg#	50	50	50	50	30	50	50	50	50
Cr	110	29	11	10	126	52	37	17	24
Co		8	9	9	9	10	10	10	11
Ni	33	19	8	11	24	24	20	12	14
Rb	43	25	29	26	42	29	18	32	24
Sr	298	260	1234	464	165	402	464	438	350
Cs	1.38	0.59	1.95	1.01	2.69	1.37	0.78	1.14	1.23
Ba	658	354	760	288	386	343	384	306	252
Sc	8	4	4	6	20	5	6	6	6
V	48	21	36	38	143	38	38	39	41
Ta	0.6	0.1	0.1	0.2	0.7	0.2	0.2	0.1	0.2
Nb	8.3	1.6	2.2	2.3	7.4	2.1	2.1	2.1	2.3
Zr	153	84	119	91	174	94	104	92	125
Hf	4.3	2.6	3.3	2.1	5.0	2.5	2.6	2.8	2.8
Th	6.3	0.8	2.4	0.7	4.8	0.8	0.8	0.8	0.9
U	1.0	0.3	0.4	0.2	1.2	0.3	0.3	0.3	0.3
Y	14	3	7	5	12	5	5	5	5
La	25.4	5.0	18.5	6.9	23.0	7.6	7.7	8.0	8.0
Ce	54	11	38	14	48	16	16	16	16
Pr	5.9	1.2	4.7	1.7	5.4	1.8	1.9	1.9	1.8
Nd	21.5	4.7	18.1	6.5	21.2	6.8	7.5	7.1	7.3
Sm	3.8	1.0	3.2	1.3	3.8	1.3	1.3	1.4	1.4
Eu	0.9	0.3	0.9	0.5	0.9	0.5	0.4	0.5	0.5
Gd	3.2	0.8	2.1	1.0	3.3	1.2	1.2	1.2	1.2
Tb	0.4	0.1	0.2	0.1	0.4	0.1	0.1	0.2	0.2
Dy	2.6	0.5	1.1	0.8	2.4	0.8	0.8	0.8	0.8
Ho	0.4	0.1	0.2	0.2	0.5	0.2	0.2	0.2	0.2
Er	1.3	0.3	0.5	0.4	1.3	0.4	0.4	0.4	0.5
Tm	0.2	0.0	0.1	0.1	0.2	0.1	0.1	0.1	0.1
Yb	1.3	0.2	0.4	0.5	1.2	0.4	0.4	0.4	0.3
Lu	0.2	0.0	0.1	0.1	0.2	0.1	0.1	0.1	0.1
(La/Yb)cn	14.2	17.9	30.4	10.7	14.1	13.2	15.2	15.3	16.6
(La/Sm)cn	4.3	3.7	4.2	3.9	4.4	4.1	4.4	4.0	4.0
(Gd/Yb)cn	2.1	3.3	4.0	1.9	2.3	2.3	2.6	2.7	2.8
(Eu/Eu*)cn	0.8	1.1	1.0	1.2	0.8	1.1	1.1	1.1	1.0
AL2O3/TIO2	34	76	60	46	27	53	52	52	50
Zr/Hf	35	32	36	44	35	37	40	33	44
La/Nb	3.1	3.2	8.6	3.1	3.1	3.6	3.8	3.8	3.5
Th/Nb	0.76	0.5	1.1	0.3	0.6	0.4	0.4	0.4	0.4
Th/La	0.25	0.2	0.1	0.1	0.2	0.1	0.1	0.1	0.1
Zr/Y	11.07	28.0	16.9	18.9	14.5	20.1	23.0	19.9	26.9
Ti/Zr	17	13	14	23	19	19	18	20	15
Ti/Sm	688	1172	511	1627	879	1348	1473	1280	1346
Sc/La	40	125	61	92	118	107	109	110	122
Nb/Nb*	0.26	0.2	0.1	0.3	0.2	0.2	0.2	0.2	0.2
Zr/Zr*	1.17	2.7	1.1	2.2	1.4	2.2	2.3	2.0	2.7
Hf/Hf*	1.20	3.1	1.1	1.8	1.4	2.1	2.1	2.2	2.2
Ti/Ti*	0.30	0.5	0.2	0.7	0.4	0.6	0.6	0.6	0.6

Appendix 4.8. Major (wt. %) and trace (ppm) element data for felsic volcanic rocks of the Heron Bay assemblage.

Sample#	HB96-3	HB96-5	HB96-8	HB96-10	HB954	HB955	HB957	HB958	HB9510	HB9511	HB9512
SiO2	69.3	68.2	74.6	68.9	72.8	72.8	69.1	67.7	65.6	66.4	64.9
TiO2	0.3	0.3	0.3	0.3	0.2	0.3	0.3	0.4	0.5	0.5	0.7
Al2O3	15.3	15.5	13.7	15.4	15.3	15.1	15.1	16.6	17.7	17.1	17.7
Fe2O3	2.9	3.0	2.6	2.9	2.1	2.5	2.8	4.0	3.6	4.5	6.7
MnO	0.03	0.03	0.03	0.03	0.01	0.01	0.05	0.03	0.04	0.01	0.07
MgO	1.7	1.8	1.6	1.9	0.88	1.71	1.33	1.66	2.36	1.97	2.21
CaO	3.3	3.7	2.3	3.6	2.20	2.51	5.34	5.79	3.14	0.77	1.50
K2O	1.6	1.7	1.7	1.8	1.14	2.67	1.61	1.19	2.02	2.47	3.02
Na2O	5.5	5.6	3.1	4.9	5.33	2.20	4.18	2.60	4.92	6.00	2.95
P2O5	0.09	0.10	0.16	0.10	0.07	0.11	0.10	0.09	0.12	0.20	0.20
LOI	1.6	1.9	1.3	2.2	0.76	3.57	5.77	3.68	4.17	1.83	2.30
Mg#	60	60	60	60	48	60	51	48	59	49	42
Cr	49	53	11	52	32	17	21	26	21	112	166
Co	12	12	6	11	3	8	9	14	14	13	24
Ni	28	31	5	33	2	8	13	22	24	30	49
Rb	44	51	35	48	30	67	34	30	45	50	68
Sr	531	565	480	656	464	88	169	335	133	161	442
Cs	3.3	4.3	4.1	2.7	0.7	2.8	2.3	1.6	2.2	0.4	1.5
Ba	539	498	689	557	427	725	343	253	354	469	909
Sc	6	7	4	5	2	4	6	10	7	14	17
V	40	47	26	38	17	37	40	73	58	107	138
Ta	0.2	0.2	0.5	0.2	0.20	0.32	0.24	0.16	0.17	0.30	0.35
Nb	2.4	2.6	6.0	2.8	3.44	3.76	3.51	2.55	2.88	5.41	6.53
Zr	105	123	152	131	111	117	102	93	121	148	142
Hf	2.7	2.7	3.5	3.3	3.11	3.23	3.49	2.83	3.07	3.98	3.88
Th	2.9	3.0	6.8	4.1	3.25	2.42	1.64	1.22	1.38	7.13	7.90
U	0.89	1.04	1.33	1.27	0.56	0.53	0.40	0.30	0.38	1.59	1.60
Y	5	6	6	6	6	5	6	7	6	13	15
La	13.4	13.7	27.0	16.5	21.6	13.6	12.7	9.1	10.5	40.2	51.5
Ce	28	28	57	34	44	24	26	21	23	89	110
Pr	3.1	3.4	6.4	3.9	5	3	3	2	3	10	13
Nd	11.7	12.8	22.4	15.0	16.1	8.7	11.2	9.8	10.9	39.2	48.4
Sm	2.1	2.3	3.1	2.5	2.4	1.5	2.2	2.0	2.1	6.6	8.0
Eu	0.6	0.7	0.7	0.7	0.7	0.4	0.7	0.7	0.7	1.6	1.8
Gd	1.4	1.5	1.9	1.8	1.6	1.4	1.9	1.8	1.7	4.7	5.6
Tb	0.2	0.2	0.2	0.2	0.2	0.2	0.2	0.2	0.2	0.5	0.6
Dy	0.8	1.0	1.1	1.0	0.9	0.9	1.2	1.4	1.3	2.5	3.1
Ho	0.2	0.2	0.2	0.2	0.2	0.2	0.2	0.3	0.3	0.5	0.6
Er	0.4	0.5	0.6	0.4	0.4	0.4	0.5	0.7	0.6	1.3	1.5
Tm	0.1	0.1	0.1	0.1	0.1	0.1	0.1	0.1	0.1	0.2	0.2
Yb	0.4	0.4	0.7	0.4	0.5	0.4	0.5	0.7	0.6	1.1	1.2
Lu	0.1	0.1	0.1	0.1	0.1	0.1	0.1	0.1	0.1	0.2	0.2
(La/Yb)cn	24.8	21.9	29.4	27.5	32.3	23.0	18.3	9.7	13.3	26.8	31.5
(La/Sm)cn	4.6	4.3	6.2	4.6	6.4	6.6	4.2	3.2	3.6	4.4	4.6
(Gd/Yb)cn	3.0	2.9	2.4	3.5	2.8	2.7	3.2	2.2	2.5	3.6	3.9
(Eu/Eu*)cn	1.0	1.0	0.9	1.0	1.0	0.9	1.0	1.0	1.1	0.8	0.8
AL2O3/TIO2	53	49	49	56	63	61	41	37	39	35	26
Zr/Hf	39	45	44	40	36	36	29	33	39	37	37
La/Nb	5.6	5.3	4.5	6.0	6.3	3.6	3.6	3.6	3.6	7.4	7.9
Th/Nb	1.2	1.2	1.1	1.5	0.95	0.64	0.47	0.48	0.48	1.32	1.21
Th/La	0.2	0.2	0.3	0.2	0.15	0.18	0.13	0.13	0.13	0.18	0.15
Zr/Y	21	21	23	22	18	25	17	13	19	12	9
Ti/Zr	16	15	11	12	13	13	21	29	23	19	29
Ti/Sm	826	831	535	643	595	1011	1010	1326	1309	433	507
Sc/Lu	95	91	42	82	37	66	79	97	77	87	97
Nb/Nb*	0.1	0.1	0.2	0.1	0.1	0.2	0.2	0.2	0.2	0.1	0.1
Zr/Zr*	1.5	1.6	1.3	1.5	1.2	2.3	1.4	1.4	1.7	0.6	0.5
Hf/Hf*	1.4	1.3	1.0	1.3	1.3	2.3	1.8	1.6	1.6	0.6	0.5
Ti/Ti*	0.4	0.4	0.3	0.3	0.3	0.4	0.4	0.6	0.6	0.2	0.2

Appendix 4.9. Major (wt. %) and trace (ppm) element data for felsic volcanic rocks of the White River-Dayohessarah greenstone belt.

Sample#	DH96-1	DH955	WR954	WR957	WR959
SiO2	65.9	76.1	68.9	64.5	70.1
TiO2	0.8	0.3	0.4	0.5	0.4
Al2O3	16.8	12.6	16.0	16.5	15.8
Fe2O3	5.5	2.3	3.0	5.1	2.6
MnO	0.1	0.0	0.0	0.1	0.0
MgO	1.6	1.0	1.4	3.1	1.0
CaO	3.1	2.7	3.1	2.9	3.4
K2O	2.0	2.2	2.9	1.2	2.1
Na2O	4.2	2.7	4.0	6.0	4.4
P2O5	0.09	0.07	0.19	0.15	0.12
LOI	0.8	0.91	0.55	1.32	0.50
Mg#	40	50	50	57	47
Cr	83	17	49	136	45
Co	27	8	7	16	8
Ni	47	8	8	38	8
Rb	62	65	200	96	118
Sr	493	86	1193	539	915
Cs	15	3	21	1	26
Ba	379	706	1547	533	942
Sc	19	4	5	12	5
V	143	36	45	83	55
Ta	0.2	0.3	0.2	0.3	0.2
Nb	3.7	3.7	4.4	4.1	2.8
Zr	129	114	173	115	132
Hf	3.4	3.1	4.8	3.1	3.6
Th	2.2	2.4	7.6	4.8	5.4
U	0.5	0.51	1.48	0.76	1.73
Y	6	5	11	9	8
La	15.3	13.3	49.2	32.0	30.7
Ce	32	24	105	68	65
Pr	3.9	2.6	11.9	7.8	7.4
Nd	15.2	8.5	45.0	29.0	28.0
Sm	2.9	1.4	7.2	4.5	4.6
Eu	0.9	0.4	1.7	1.1	1.1
Gd	2.1	1.3	4.5	3.3	2.9
Tb	0.3	0.2	0.4	0.4	0.3
Dy	1.3	0.9	2.0	1.7	1.3
Ho	0.2	0.2	0.3	0.3	0.2
Er	0.6	0.4	0.8	0.8	0.6
Tm	0.1	0.1	0.1	0.1	0.1
Yb	0.5	0.4	0.7	0.6	0.5
Lu	0.1	0.1	0.1	0.1	0.1
(La/Yb)cn	20.5	23.0	50.0	37.1	43.8
(La/Sm)cn	3.8	6.6	4.9	5.1	4.8
(Gd/Yb)cn	3.2	2.7	5.2	4.5	4.8
(Eu/Eu*)cn	1.1	0.9	0.9	0.8	0.9
AL2O3/TiO2	24	52	35	31	38
Zr/Hf	38	36	36	37	36
La/Nb	4.1	3.6	11.2	7.8	11.1
Th/Nb	0.6	0.64	1.72	1.18	1.95
Th/La	0.15	0.18	0.15	0.15	0.18
Zr/Y	20.0	24.6	16.1	12.1	16.3
Ti/Zr	32	13	16	27	19
Ti/Sm	1443	1011	384	691	537
Sc/La	232	66	59	130	84
Nb/Nb*	0.2	0.2	0.1	0.1	0.1
Zr/Zr*	1.4	2.3	0.7	0.7	0.8
Hf/Hf*	1.3	2.3	0.7	0.7	0.8
Ti/Ti*	0.7	0.4	0.2	0.3	0.3

Appendix 5.1. Major (wt. %) and trace (ppm) element data for granitoid (TTG) intrusions of the Schreiber-Hemlo and White River-Dayohessarah greenstone belts.

Sample#	SC95-95	SC95-96	SC95-97	SC95-98	HE95-10	HE95-11	HE95-12	HE95-19	HE95-23	WR95-5
SiO2	67.0	71.6	69.0	70.1	71.9	69.7	68.7	66.5	64.8	72.1
TiO2	0.46	0.32	0.31	0.28	0.26	0.32	0.35	0.45	0.56	0.31
Al2O3	15.2	14.8	15.6	15.1	15.0	15.8	16.1	16.2	16.4	15.0
Fe2O3	4.15	2.31	2.86	2.55	2.10	2.18	2.75	3.26	4.16	2.23
MnO	0.05	0.02	0.03	0.03	0.02	0.01	0.01	0.04	0.05	0.03
MgO	1.92	0.86	1.54	1.35	0.72	0.89	1.01	1.70	2.00	0.71
CaO	3.04	1.51	2.34	2.98	2.38	2.77	3.19	2.84	4.01	2.63
K2O	3.87	4.07	3.06	2.72	2.47	2.74	2.21	2.87	2.47	3.13
Na2O	4.18	4.34	5.12	4.79	5.16	5.47	5.54	5.93	5.27	3.72
P2O5	0.20	0.11	0.14	0.12	0.08	0.10	0.10	0.23	0.27	0.09
LOI	1.11	1.27	1.27	0.60	0.55	1.52	0.50	0.86	0.45	0.76
Mg#	50	45	54	54	43	47	45	53	52	41
Cr	19	15	30	34	10	13	12	25	42	39
Co	11	6	9	7	8	6	7	9	13	5
Ni	9	4	17	18	5	5	5	16	20	3
Rb	134	157	80	65	62	59	38	59	55	143
Sr	617	472	727	766	604	784	1102	1176	1487	191
Cs	3.7	4.5	1.7	1.6	2.8	1.0	1.3	0.6	1.9	4.4
Ba	1349	845	1076	969	811	1017	993	1449	1472	842
Sc	9	4	6	5	4	4	4	6	10	4
V	63	33	47	38	31	35	41	53	70	23
Ta	1.0	1.0	0.4	0.4	0.2	0.1	0.2	0.3	0.4	2.3
Nb	10.4	8.9	6.0	5.3	2.9	2.1	2.8	5.2	5.5	17.6
Zr	203	141	141	133	89	110	109	164	180	194
Hf	4.9	4.5	5.0	3.5	2.8	3.5	3.5	4.7	4.8	5.7
Th	19.3	16.8	6.3	5.0	4.4	2.3	2.1	7.0	5.2	21.6
U	4.1	3.4	1.8	1.2	0.8	0.5	0.6	1.2	1.0	1.5
Y	13	10	12	11	5	4	5	11	14	9
La	55	41	37	25	18	15	14	48	54	49
Ce	114	86	79	56	39	33	34	104	115	89
Pr	12.0	8.9	8.6	6.8	4	4	4	12	13	9
Nd	44	31	33	25	15	16	15	46	51	28
Sm	6.7	4.8	5.4	4.7	2.5	2.7	2.9	7.8	8.5	4.2
Eu	1.4	1.0	1.3	1.1	0.7	0.8	0.8	1.9	2.1	0.7
Gd	4.5	3.2	3.9	3.3	1.9	1.9	1.9	5.3	5.8	3.1
Tb	0.5	0.3	0.4	0.4	0.2	0.2	0.2	0.5	0.5	0.3
Dy	2.4	1.8	2.2	2.0	1.0	0.8	0.8	2.2	2.6	1.7
Ho	0.4	0.3	0.4	0.4	0.2	0.1	0.2	0.4	0.4	0.3
Er	1.1	0.8	1.1	1.1	0.4	0.3	0.3	0.8	1.0	0.8
Tm	0.2	0.1	0.2	0.2	0.1	0.0	0.1	0.1	0.2	0.1
Yb	1.1	0.8	1.0	1.0	0.4	0.2	0.2	0.7	0.8	0.9
Lu	0.2	0.1	0.2	0.2	0.1	0.0	0.1	0.1	0.1	0.1
(La/Yb)cn	34.9	35.7	27.6	17.4	31.4	52.5	42.1	48.9	45.7	40.4
(La/Sm)cn	5.9	6.1	5.0	3.8	5.0	4.0	3.4	4.4	4.5	8.3
(Gd/Yb)cn	3.3	3.1	3.3	2.7	3.9	7.8	6.9	6.2	5.7	3.0
(Eu/Eu*)cn	0.8	0.8	0.9	0.8	0.9	1.0	1.0	0.9	0.9	0.6
AL2O3/TiO2	33	45	47	56	53	49	43	36	30	47
Zr/Hf	41	32	28	38	32	32	31	35	37	34
La/Nb	5.3	4.7	6.1	4.6	6.0	7.2	4.8	9.2	9.7	2.8
Th/Nb	1.9	1.9	1.0	0.9	1.5	1.1	0.8	1.3	0.9	1.2
Th/La	0.4	0.4	0.2	0.2	0.2	0.2	0.2	0.1	0.1	0.4
Zr/Y	16	15	12	12	16	25	23	15	13	21
Ti/Zr	13	14	14	12	19	17	20	16	18	10
Sc/Lu	52	28	37	31	52	117	73	60	81	36
Nb/Nb*	0.1	0.2	0.1	0.2	0.1	0.1	0.2	0.1	0.1	0.2
Zr/Zr*	0.8	0.8	0.7	0.8	1.0	1.2	1.1	0.6	0.6	1.2
Hf/Hf*	0.7	0.9	0.9	0.8	1.1	1.3	1.3	0.6	0.6	1.3
Ti/Ti*	0.2	0.2	0.2	0.2	0.3	0.3	0.4	0.2	0.2	0.2

Appendix 5.2. Major (wt. %) and trace (ppm) data for mafic-intermediate sills and dykes of the Schreiber-Hemlo greenstone belt.

Sample	SC97-21	SC97-22	SC97-27	SC97-28	SC97-49	SC97-56	SC97-65
SiO2	55.7	50.9	57.4	53.1	56.4	57.5	47.6
TiO2	0.6	0.7	0.6	0.8	0.6	0.6	0.8
Al2O3	14.2	10.8	14.3	15.3	14.1	14.0	15.2
Fe2O3	7.0	8.0	7.2	7.7	7.2	7.0	10.0
MnO	0.1	0.1	0.1	0.1	0.1	0.1	0.2
MgO	8.6	13.7	6.0	4.9	5.9	5.8	5.2
CaO	2.9	8.9	6.0	5.8	6.5	6.3	7.8
K2O	0.6	1.9	2.4	3.4	2.6	3.1	0.7
Na2O	3.8	1.6	4.1	4.2	3.9	3.6	3.8
P2O5	0.3	0.4	0.4	0.6	0.4	0.4	0.4
LOI	6.3	1.6	1.5	3.7	1.3	1.5	8.3
Mg#	51	60	42	36	41	42	31
Cr	232	801	291	38	260	266	67
Co	31	55	36	27	34	34	36
Ni	66	399	88	18	80	79	26
Rb	19	56	84	176	77	85	25
Sr	404	275	1340	773	1331	1005	861
Cs	0.8	1.9	7.1	22.2	3.1	3.6	1.4
Ba	386	924	1084	486	1204	1131	278
Sc	20	24	21	21	21	21	26
V	168	163	170	166	168	158	217
Ta	0.4	0.3	0.4	0.5	0.4	0.4	0.3
Nb	6.9	5.2	6.1	9.2	6.7	6.7	4.9
Zr	204	144	174	187	168	190	108
Hf	4.8	3.6	4.7	4.8	4.0	4.8	2.6
Th	10.2	5.7	10.1	12.0	9.7	10.3	3.6
U	2.4	1.2	2.1	2.5	2.0	2.5	0.9
Y	13	18	18	23	18	18	19
La	32	54	54	93	54	53	30
Ce	72	119	109	192	110	111	67
Pr	8.7	15.2	13.0	23.5	13.2	13.1	8.9
Nd	32	62	49	93	48	50	38
Sm	5.3	11.4	8.6	15.5	8.3	8.7	7.5
Eu	1.5	2.7	2.1	3.9	1.9	2.0	2.0
Gd	3.8	8.1	6.1	10.6	5.5	5.7	5.7
Tb	0.4	0.8	0.7	1.1	0.6	0.6	0.7
Dy	2.4	3.9	3.4	5.0	3.1	3.3	3.5
Ho	0.4	0.6	0.6	0.8	0.6	0.6	0.6
Er	1.2	1.5	1.6	2.0	1.5	1.6	1.7
Tm	0.2	0.2	0.2	0.3	0.2	0.2	0.3
Yb	1.3	1.3	1.5	1.6	1.4	1.5	1.6
Lu	0.2	0.2	0.2	0.2	0.2	0.2	0.2
(La/Yb)cn	18.4	29.4	26.1	41.3	27.7	25.7	13.3
(La/Sm)cn	4.4	3.4	4.5	4.3	4.7	4.4	2.8
(Gd/Yb)cn	2.5	5.1	3.4	5.4	3.2	3.2	2.9
(Eu/Eu*)cn	0.9	0.8	0.8	0.9	0.8	0.8	0.9
AL2O3/TiO2	27	17	23	22	25	23	19
Zr/Hf	43	40	37	39	42	39	42
La/Nb	4.7	10.3	8.9	10.2	8.1	8.0	6.2
Th/Nb	1.5	1.1	1.7	1.3	1.4	1.5	0.7
Th/La	0.3	0.1	0.2	0.1	0.2	0.2	0.1
Zr/Y	15.5	8.0	9.8	8.1	9.1	10.8	5.7
Ti/Zr	16	27	22	23	20	19	44
Sc/Lu	110	134	96	92	96	88	115
Nb/Nb*	0.2	0.1	0.1	0.1	0.1	0.1	0.1
Zr/Zr*	1.1	0.4	0.6	0.3	0.6	0.6	0.4
Hf/Hf*	0.9	0.3	0.6	0.3	0.5	0.6	0.4
Ti/Ti*	0.3	0.2	0.2	0.1	0.2	0.2	0.3

Appendix 5.3. Major (wt. %) and trace (ppm) data for felsic sills and dykes of the Schreiber-Hemlo greenstone belt.

Sample	SC97-12	SC97-13	SC97-16	SC97-20	SC97-43	SC97-46	SC97-66	SC97-74
SiO2	69.2	69.6	71.3	65.4	61.1	65.8	65.1	70.7
TiO2	0.4	0.4	0.2	0.5	0.4	0.6	0.3	0.3
Al2O3	16.0	16.1	15.5	14.5	19.0	16.2	16.8	15.1
Fe2O3	2.1	2.4	1.4	4.8	2.6	2.9	3.5	2.4
MnO	0.0	0.0	0.0	0.1	0.1	0.0	0.1	0.0
MgO	1.0	0.9	0.2	2.5	0.7	1.0	1.3	1.1
CaO	0.9	1.6	0.8	2.4	3.1	3.1	3.2	2.9
K2O	0.4	2.0	3.8	1.1	0.9	1.7	2.9	2.3
Na2O	8.4	5.6	5.1	4.9	9.4	6.0	4.5	5.0
P2O5	0.1	0.1	0.0	0.1	0.2	0.2	0.2	0.1
LOI	0.9	1.5	1.3	3.2	2.3	2.0	2.0	0.3
Mg#	28	24	10	31	19	23	24	28
Cr	17	14	7	129	13	34	10	31
Co	8	10	3	23	8	9	11	9
Ni	7	9	2	52	5	17	5	14
Rb	11	51	117	33	26	44	61	55
Sr	101	84	337	435	796	986	916	830
Cs	0.2	0.9	2.7	1.1	0.8	1.2	1.3	0.9
Ba	58	298	757	317	560	986	1125	920
Sc	11	7	2	14	8	5	6	7
V	52	45	12	89	38	42	45	37
Ta	0.2	0.2	0.7	0.4	1.0	0.3	0.6	0.3
Nb	4.1	3.3	10.2	5.2	14.1	6.6	7.4	4.5
Zr	173	171	198	139	193	240	162	141
Hf	3.6	3.4	5.5	3.2	5.3	5.7	4.3	3.7
Th	7.3	7.4	16.4	5.4	14.2	5.2	6.2	4.5
U	1.7	1.7	4.7	1.4	5.1	1.1	1.3	1.1
Y	6	5	11	12	13	7	12	12
La	26	27	44	27	50	50	43	24
Ce	49	52	86	54	99	105	82	51
Pr	5.4	5.7	9.4	6.3	11.1	12.8	9.2	6.2
Nd	19	20	32	23	40	49	31	24
Sm	3.0	3.1	4.9	3.9	6.1	7.8	4.5	4.1
Eu	0.7	0.7	1.1	1.1	1.5	1.9	1.2	1.0
Gd	1.9	2.1	3.5	3.1	4.1	5.0	3.0	3.0
Tb	0.2	0.2	0.4	0.4	0.4	0.4	0.3	0.4
Dy	1.0	1.1	1.9	2.3	2.2	1.6	1.9	1.9
Ho	0.2	0.2	0.3	0.5	0.4	0.2	0.4	0.4
Er	0.5	0.5	0.9	1.1	1.0	0.4	1.0	1.0
Tm	0.1	0.1	0.2	0.2	0.2	0.0	0.2	0.2
Yb	0.5	0.5	1.1	1.1	1.0	0.2	1.2	1.0
Cu	29.9	31.6	3.2	43.4	11.9	15.1	9.1	2.3
(La/Yb)cn	39.3	40.5	28.9	17.6	38.1	189.7	26.0	16.5
(La/Sm)cn	6.4	6.4	6.5	5.0	5.9	4.6	6.8	4.2
(Gd/Yb)cn	3.3	3.7	2.6	2.4	3.6	21.5	2.1	2.4
(Eu/Eu*)cn	0.9	0.8	0.8	0.9	0.8	0.9	0.9	0.8
AL2O3/TiO2	46.6	45.7	108.2	31.1	63.1	32.5	53.8	56.0
Zr/Hf	47	50	36	43	36	43	38	38
La/Nb	6	8	4	5	4	8	6	5
Th/Nb	1.8	2.3	1.6	1.0	1.0	0.8	0.8	1.0
Th/La	0.3	0.3	0.4	0.2	0.3	0.1	0.1	0.2
Zr/Y	27.5	32.5	17.3	11.4	15.4	32.5	13.2	12.1
Ti/Zr	11.9	12.4	4.3	20.1	9.3	12.4	11.5	11.5
Sc/Lu	159	96	10	92	59	182	31	45
Nb/Nb*	0	0	0	0	0	0	0	0
Zr/Zr*	1.6	1.5	1.1	1.0	0.9	0.9	0.9	1.0
Hf/Hf*	1.2	1.1	1.1	0.9	0.9	0.7	0.9	0.9
Ti/Ti*	0.3	0.3	0.1	0.3	0.1	0.2	0.2	0.2

Appendix 5.4. Major (wt. %) and trace (ppm) data for sandstones of the Schreiber-Hemlo and White River-Dayohessarah greenstone belts.

Sample	SC95-63	SC95-64	SC95-65	SC95-66	SC95-69	SC95-72	SC95-74	SC95-75	HB95-20
SiO2	65.2	64.3	65.9	64.2	66.5	67.7	66.7	65.4	61.2
TiO2	0.60	0.57	0.54	0.58	0.57	0.49	0.53	0.54	0.6
Al2O3	15.4	15.8	15.4	15.9	15.6	15.7	15.2	15.5	16.43
Fe2O3	6.37	6.13	5.61	6.73	5.91	4.94	5.40	5.55	7.7
MnO	0.09	0.08	0.07	0.09	0.07	0.06	0.11	0.07	0.06
MgO	2.90	3.21	2.97	3.12	3.20	2.50	2.57	3.31	3.85
CaO	3.64	3.56	3.28	3.43	2.33	2.05	3.70	3.21	3.26
K2O	1.73	2.18	1.82	2.08	1.29	1.29	2.30	1.64	2.95
Na2O	3.89	3.98	4.29	3.72	4.42	5.12	3.36	4.62	3.62
P2O5	0.16	0.16	0.14	0.18	0.15	0.17	0.13	0.16	0.33
LOI	2.72	2.25	3.47	2.41	3.57	2.83	5.60	4.11	1.11
Mg#	50	54	54	51	54	53	51	57	52
Cr	169	192	113	181	334	133	128	177	388
Co	27	24	16	27	23	19	19	23	48
Ni	66	84	50	68	65	48	62	78	166
Rb	63	77	48	79	38	40	69	45	77
Sr	479	597	488	690	385	579	394	577	698
Cs	3.2	4.3	1.5	5.1	1.0	1.0	2.4	1.5	4.7
Ba	449	721	552	662	391	465	458	661	1166
Sc	14	13	12	13	14	11	12	11	17
V	112	92	83	108	106	75	86	84	164
Ta	0.50	0.46	0.47	0.45	0.31	0.44	0.41	0.44	0.25
Nb	6.98	6.79	6.81	6.65	6.72	6.50	6.79	6.65	6.29
Zr	124	134	131	106	134	146	99	130	121
Hf	3.24	3.31	3.21	3.05	3.56	3.64	2.47	3.35	3.36
Th	6.46	6.66	7.77	6.17	7.73	7.79	6.73	6.56	5.80
U	2.09	1.47	1.91	2.02	2.10	3.18	2.01	1.63	1.51
Y	13	12	12	14	12	10	11	13	18
La	31	30	28	36	30	33	24	28	36
Ce	62	63	54	74	60	67	47	59	80
Pr	7.0	7.2	6.2	8.3	6.1	7.5	5.4	6.7	9.4
Nd	26	27	23	32	25	28	20	25	35
Sm	4.3	4.4	4.0	5.3	4.4	4.5	3.4	4.4	6.6
Eu	1.2	1.2	1.0	1.4	1.3	1.1	1.0	1.3	1.6
Gd	3.5	3.6	3.2	4.1	3.3	3.2	2.7	3.6	5.0
Tb	0.5	0.4	0.4	0.5	0.4	0.4	0.4	0.4	0.6
Dy	2.6	2.3	2.3	2.6	2.4	2.0	2.1	2.5	3.3
Ho	0.5	0.5	0.4	0.5	0.5	0.4	0.4	0.5	0.7
Er	1.4	1.3	1.3	1.3	1.3	1.0	1.2	1.3	1.8
Tm	0.2	0.2	0.2	0.2	0.2	0.1	0.2	0.2	0.3
Yb	1.4	1.2	1.2	1.2	1.2	1.0	1.1	1.2	1.7
Lu	0.2	0.2	0.2	0.2	0.2	0.1	0.2	0.2	0.3
(La/Yb)cn	16	18	16	21	17	25	15	17	16
(La/Sm)cn	5.2	4.9	5.0	4.9	4.9	5.3	4.9	4.4	3.9
(Gd/Yb)cn	2.1	2.5	2.2	2.8	2.2	2.8	2.0	2.5	2.5
(Eu/Eu*)cn	0.9	0.9	0.8	0.9	1.0	0.8	0.9	1.0	0.8
AL2O3/TiO2	25	29	34	25	27	32	33	30	28
Zr/Hf	38	40	41	35	38	40	40	39	36
La/Nb	4.4	4.4	5.8	5.5	4.5	5.1	5.0	4.2	8.5
Th/Nb	0.9	0.7	1.6	0.9	1.1	0.6	1.4	1.0	1.4
Th/La	0.21	0.15	0.28	0.17	0.26	0.11	0.28	0.24	0.16
Zr/Y	9.5	10.9	11.1	7.8	11.2	14.9	9.2	10.0	6.8
Ti/Zr	30	24	20	35	26	20	28	23	29
Sc/La	64	72	63	70	76	76	71	64	62
Nb/Nb*	0.2	0.2	0.1	0.1	0.2	0.1	0.1	0.2	0.1
Zr/Zr*	0.8	0.9	1.0	0.6	0.9	0.9	0.8	0.9	0.5
Hf/Hf*	0.8	0.8	0.8	0.6	0.9	0.8	0.8	0.8	0.6
Ti/Ti*	0.4	0.3	0.3	0.3	0.4	0.3	0.4	0.3	0.2

Appendix 5.4. Continues

Sample	HB95-21	HB95-26	HE95-15	HE95-18	DH96-1
SiO2	68.6	64.4	68.9	62.7	65.9
TiO2	0.4	0.6	0.5	0.5	0.8
Al2O3	15.15	18.87	16.12	15.43	16.78
Fe2O3	3.7	5.7	3.1	5.5	5.5
MnO	0.04	0.05	0.02	0.08	0.06
MgO	2.16	2.84	1.27	3.80	1.62
CaO	4.52	1.85	3.13	4.81	3.12
K2O	1.41	2.55	2.66	2.32	1.96
Na2O	3.88	2.91	4.14	4.65	4.21
P2O5	0.12	0.20	0.20	0.24	0.09
LOI	0.45	2.56	2.09	0.40	0.76
Mg#	56	52	47	60	39
Cr	53	146	10	173	83
Co	17	23	9	21	27
Ni	38	89	10	63	47
Rb	36	62	56	70	62
Sr	471	547	958	871	493
Cs	1.7	2.1	1.7	2.0	14.7
Ba	291	716	900	920	379
Sc	8	17	5	14	19
V	64	130	49	107	143
Ta	0.16	0.39	0.25	0.38	0.24
Nb	2.54	6.12	3.88	5.05	3.72
Zr	85	144	182	144	129
Hf	2.64	3.60	5.14	4.92	3.36
Th	1.33	7.39	7.15	6.71	2.25
U	0.69	1.93	1.86	1.75	0.47
Y	7	14	10	13	6
La	12	42	35	38	15
Ce	26	93	79	83	32
Pr	3.0	10.8	9.3	9.5	3.9
Nd	12	42	36	37	15
Sm	2.3	7.0	6.0	6.4	2.9
Eu	0.7	1.8	1.5	1.6	0.9
Gd	2.0	5.0	3.8	4.6	2.1
Tb	0.2	0.6	0.4	0.5	0.3
Dy	1.2	2.9	1.9	2.3	1.3
Ho	0.2	0.5	0.3	0.4	0.2
Er	0.7	1.4	0.8	1.1	0.6
Tm	0.1	0.2	0.1	0.2	0.1
Yb	0.5	1.2	0.6	1.1	0.5
Lu	0.1	0.2	0.1	0.2	0.1
(La/Yb)cn	17	25	40	26	20
(La/Sm)cn	3.7	4.3	4.2	4.2	3.8
(Gd/Yb)cn	3.3	3.5	5.0	3.6	3.2
(Eu/Eu*)cn	0.9	0.9	0.9	0.9	1.1
AL2O3/TiO2	36	32	32	32	24
Zr/Hf	32	40	35	29	38
La/Nb	4.8	6.9	9.1	7.6	4.1
Th/Nb	0.5	1.2	1.8	1.3	0.6
Th/La	0.11	0.18	0.20	0.18	0.15
Zr/Y	11.9	10.0	18.2	10.9	20.0
Ti/Zr	29	24	16	20	32
Sc/La	104	83	64	76	232
Nb/Nb*	0.2	0.1	0.1	0.1	0.2
Zr/Zr*	1.1	0.6	0.9	0.6	1.4
Hf/Hf*	1.3	0.5	0.9	0.8	1.3
Ti/Ti*	0.5	0.2	0.2	0.2	0.7

Appendix 5.5. Major (wt. %) and trace (ppm) data for shales of the Schreiber-Hemlo and White River-Dayohessarah greenstone belts.

Sample	SC95-61	SC95-68	SC95-70	SC95-78	SC95-113	SC95-122	HB96-7
SiO2	62.0	58.5	62.0	63.4	64.1	60.6	71.3
TiO2	0.70	0.80	0.65	0.69	0.64	0.77	0.26
Al2O3	17.7	19.2	16.1	16.8	16.5	18.5	13.61
Fe2O3	7.32	9.67	7.38	7.45	6.88	8.66	7.20
MnO	0.06	0.11	0.12	0.08	0.07	0.09	0.05
MgO	3.95	4.86	3.17	3.93	3.30	3.84	1.91
CaO	1.82	0.98	4.99	1.57	2.61	1.31	2.66
K2O	1.85	3.64	2.14	2.32	2.03	3.13	2.82
Na2O	4.35	2.10	3.24	3.50	3.68	2.83	0.12
P2O5	0.20	0.16	0.18	0.18	0.16	0.18	0.10
LOI	2.62	4.28	5.60	3.25	2.99	3.41	4.66
Mg#	1	1	0	1	1	0	0
Cr	200	195	183	237	179	438	3
Co	32	42	28	33	28	36	10
Ni	108	119	80	108	80	110	5
Rb	47	104	67	78	70	97	46
Sr	337	113	442	290	401	282	59
Cs	0.9	3.0	2.0	2.4	4.5	4.2	1.2
Ba	741	892	574	634	535	879	221
Sc	21	25	14	20	13	26	3
V	126	203	130	127	118	178	17
Ta	0.56	0.56	0.51	0.50	0.47	0.38	0.52
Nb	8.13	8.20	7.48	7.36	7.04	8.11	6.33
Zr	151	153	138	130	144	130	122
Hf	3.74	3.44	3.62	3.64	3.37	4.13	3.04
Th	5.80	9.08	8.42	4.35	7.82	9.57	4.94
U	1.89	2.02	2.12	1.38	1.92	2.29	1.08
Y	16	17	14	14	15	18	6
La	36	31	31	27	28	33	28
Ce	71	67	63	56	62	68	57
Pr	8.4	7.6	6.7	6.5	6.5	7.4	6.0
Nd	32	30	25	24	25	31	21
Sm	5.8	5.5	4.4	4.4	4.4	5.5	3.0
Eu	1.5	0.9	1.1	1.1	1.3	1.4	0.7
Gd	4.4	4.5	3.7	3.5	3.6	4.7	2.1
Tb	0.6	0.6	0.5	0.4	0.4	0.6	0.2
Dy	3.1	3.5	2.6	2.7	2.6	3.5	1.2
Ho	0.6	0.7	0.5	0.5	0.5	0.7	0.2
Er	1.6	2.0	1.5	1.5	1.4	2.0	0.6
Tm	0.3	0.3	0.2	0.2	0.2	0.3	0.1
Yb	1.6	1.9	1.3	1.4	1.4	2.0	0.7
Lu	0.3	0.3	0.2	0.2	0.2	0.3	0.1
(La/Yb)cn	16	11	16	13	15	12	29
(La/Sm)cn	4.5	4.0	5.0	4.4	4.6	4.3	6.6
(Gd/Yb)cn	2.3	1.9	2.3	2.0	2.2	2.0	2.4
(Eu/Eu*)cn	0.9	0.5	0.8	0.8	0.9	0.8	0.9
AL2O3/TiO2	25	25	25	24	26	24	85
Zr/Hf	41	45	38	36	43	32	40
La/Nb	4.4	3.7	4.1	3.6	4.0	4.1	4.4
Th/Nb	0.7	1.1	1.1	0.6	1.1	1.2	0.8
Th/La	0.16	0.30	0.28	0.16	0.28	0.29	0.2
Zr/Y	9.5	8.9	9.8	9.5	9.3	7.2	21
Ti/Zr	28	30	28	33	26	36	8
Sc/La	81	91	65	87	68	88	27
Nb/Nb*	0.2	0.2	0.2	0.2	0.2	0.2	0.2
Zr/Zr*	0.8	0.8	0.9	0.9	1.0	0.7	1.1
Hf/Hf*	0.7	0.7	0.9	0.9	0.8	0.8	1.0
Ti/Ti*	0.3	0.4	0.4	0.4	0.4	0.4	0.2

IMAGE EVALUATION
TEST TARGET (QA-3)

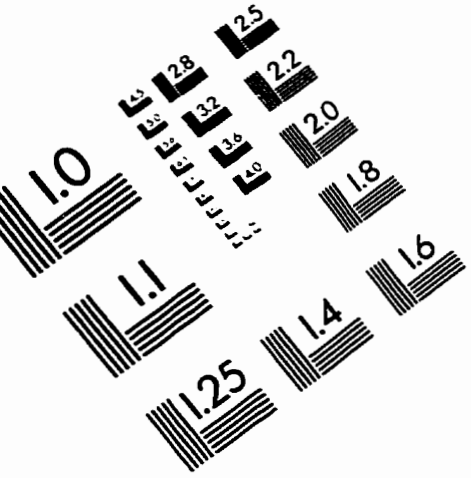

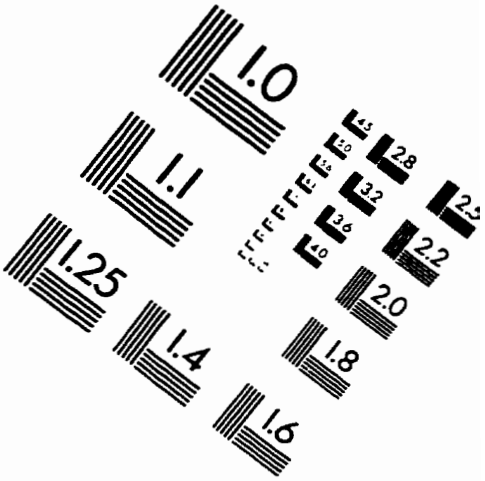

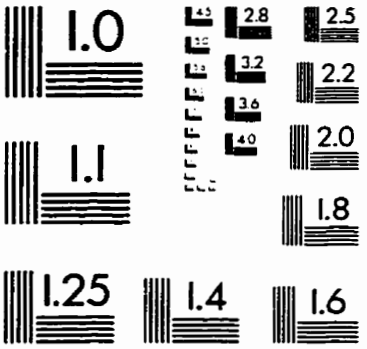

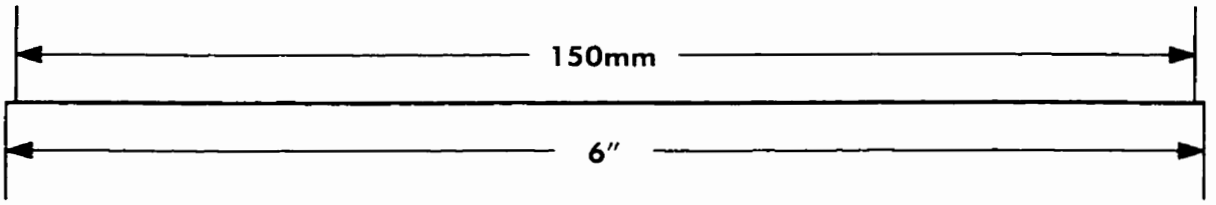

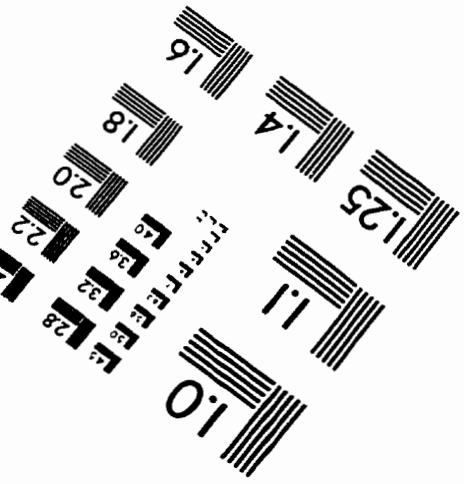

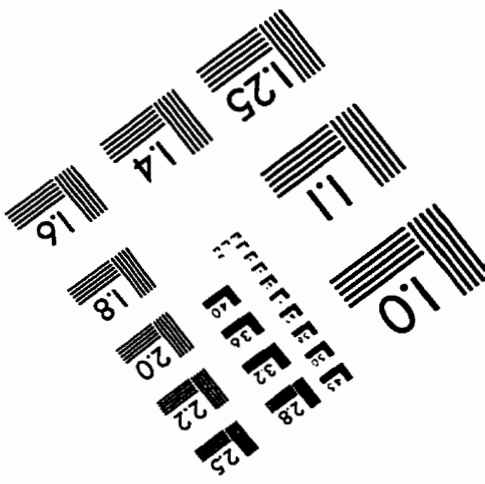

APPLIED IMAGE, Inc
1653 East Main Street
Rochester, NY 14609 USA
Phone: 716/482-0300
Fax: 716/288-5989